

## Imaging and control of magnetic islands in tokamaks

**Citation for published version (APA):**

Classen, I. G. J. (2007). *Imaging and control of magnetic islands in tokamaks*. [Phd Thesis 1 (Research TU/e / Graduation TU/e), Applied Physics and Science Education]. Technische Universiteit Eindhoven.  
<https://doi.org/10.6100/IR627226>

**DOI:**

[10.6100/IR627226](https://doi.org/10.6100/IR627226)

**Document status and date:**

Published: 01/01/2007

**Document Version:**

Publisher's PDF, also known as Version of Record (includes final page, issue and volume numbers)

**Please check the document version of this publication:**

- A submitted manuscript is the version of the article upon submission and before peer-review. There can be important differences between the submitted version and the official published version of record. People interested in the research are advised to contact the author for the final version of the publication, or visit the DOI to the publisher's website.
- The final author version and the galley proof are versions of the publication after peer review.
- The final published version features the final layout of the paper including the volume, issue and page numbers.

[Link to publication](#)

**General rights**

Copyright and moral rights for the publications made accessible in the public portal are retained by the authors and/or other copyright owners and it is a condition of accessing publications that users recognise and abide by the legal requirements associated with these rights.

- Users may download and print one copy of any publication from the public portal for the purpose of private study or research.
- You may not further distribute the material or use it for any profit-making activity or commercial gain
- You may freely distribute the URL identifying the publication in the public portal.

If the publication is distributed under the terms of Article 25fa of the Dutch Copyright Act, indicated by the "Taverne" license above, please follow below link for the End User Agreement:

[www.tue.nl/taverne](http://www.tue.nl/taverne)

**Take down policy**

If you believe that this document breaches copyright please contact us at:

[openaccess@tue.nl](mailto:openaccess@tue.nl)

providing details and we will investigate your claim.

**Imaging and Control  
of  
Magnetic Islands  
in  
Tokamaks**



**Ivo Classen**

# **Imaging and Control of Magnetic Islands in Tokamaks**

## **Proefschrift**

ter verkrijging van de graad van doctor aan de Technische  
Universiteit Eindhoven, op gezag van de Rector Magnificus,  
prof.dr.ir. C.J. van Duijn, voor een commissie aangewezen  
door het College voor Promoties in het openbaar te  
verdedigen op dinsdag 12 juni 2007 om 14.00 uur

door

**Ivo Godefridus Johannes Classen**

geboren te Herkenbosch

Dit proefschrift is goedgekeurd door de promotoren:

prof.dr. N.J. Lopes Cardozo  
en  
prof.dr. F.C. Schüller

Copromotor:  
dr. R.J.E. Jaspers

CIP-DATA LIBRARY TECHNISCHE UNIVERSITEIT EINDHOVEN

Classen, Ivo

Imaging and Control of Magnetic Islands in Tokamaks/ by Ivo Classen.-

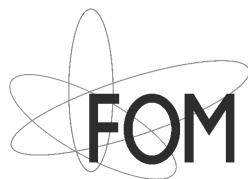
Eindhoven : Technische Universiteit Eindhoven, 2007.- Proefschrift.

ISBN: 978-90-386-1028-3

NUR 926

Trefwoorden: plasmafysica / kernfusie / tokamaks / magnetohydrodynamica /  
magnetische eilanden / plasmadiagnostiek

Subject headings: plasma physics / nuclear fusion / tokamaks / magneto-  
hydrodynamics / magnetic islands / plasma diagnostics



The work described in this thesis was performed as part of a research programme of Stichting voor Fundamenteel Onderzoek der Materie (FOM) with financial support from the Nederlandse Organisatie voor Wetenschappelijk Onderzoek (NWO), the Forschungszentrum Jülich GmbH and EURATOM. It was carried out at the Forschungszentrum Jülich GmbH in collaboration with the FOM-Institute for Plasma Physics Rijnhuizen. The views and opinions expressed herein do not necessarily reflect those of the European Commission.

*To my parents.*



# Contents

<b>Contents</b>		<b>v</b>
<b>1</b>	<b>Introduction</b>	<b>1</b>
1.1	The need for alternatives to fossil fuels	1
1.2	Nuclear fusion and the tokamak concept	2
1.3	Magnetic islands	4
1.4	This thesis	6
1.5	List of publications	8
<b>2</b>	<b>The theory of magnetic islands</b>	<b>11</b>
2.1	The island topology	12
2.2	The effect of an island on $T_e$ and $n_e$	14
2.3	The island evolution equation	16
2.3.1	The Rutherford equation	18
2.4	Other contributions to the helical current	19
2.4.1	Perturbed bootstrap current: Neoclassical Tearing Modes	19
2.4.2	The effect of an external perturbation field	21
2.4.3	Heating and current drive	24
2.5	Mode rotation	26
2.6	Conclusion	27
<b>3</b>	<b>TEXTOR and its auxiliary systems</b>	<b>29</b>
3.1	The TEXTOR tokamak	29
3.2	Auxiliary heating systems	30
3.2.1	The neutral beam injectors	30
3.2.2	ECRH	30
3.3	Main diagnostics used in this thesis	31
3.3.1	ECE-Imaging	31

---

3.3.2	Charge exchange recombination spectroscopy	31
3.3.3	Thomson Scattering	32
3.3.4	O-mode reflectometer	32
3.4	The Dynamic Ergodic Divertor	33
<b>4</b>	<b>Electron Cyclotron Emission</b>	<b>35</b>
4.1	ECE as a local electron temperature measurement	35
4.2	The principle of an ECE radiometer	38
4.3	ECE-Imaging	40
4.4	Radial resolution of an ECE diagnostic	44
4.5	Thermal noise	48
4.6	Radiation temperature versus electron temperature	49
<b>5</b>	<b>2D edge temperature profile during DED 12/4 operation</b>	<b>51</b>
5.1	Introduction	51
5.2	The vacuum field edge properties.	52
5.3	Edge transport during DED operation	55
5.4	Experimental results	56
5.5	Summary and discussion	61
<b>6</b>	<b>Fluctuation measurements with ECE-Imaging</b>	<b>63</b>
6.1	Noise reduction by correlation	64
6.2	The Quasi Coherent mode	67
6.3	Alfvén-like modes	72
6.4	Conclusions and discussion	74
<b>7</b>	<b>Experimental determination of the island parameters</b>	<b>77</b>
7.1	Calibration and filtering	77
7.2	Poloidal reconstruction of the island	78
7.3	The fitting procedure	80
<b>8</b>	<b>Dynamics of tearing modes in the presence of a perturbation field</b>	<b>83</b>
8.1	Introduction	83



## Imaging and Control of Magnetic Islands in Tokamaks

---

8.2	Experimental setup	85
8.2.1	The DED perturbation field	85
8.2.2	Diagnostics: ECE-Imaging and CXRS	86
8.2.3	Discharge scenario and data analysis	87
8.3	Theoretical framework	90
8.3.1	The interaction of islands with a perturbation field	90
8.3.2	Mode rotation	92
8.3.3	Torque balance and viscosity	93
8.3.4	Complications	95
8.4	Comparison of experiment with theory	95
8.4.1	The numerical simulation	96
8.4.2	Mode penetration	98
8.4.3	Mode growth	99
8.4.4	Mode unlocking	101
8.5	Summary and discussion	105
<b>9</b>	<b>The effect of heating on the suppression of tearing modes</b>	<b>107</b>
<b>10</b>	<b>Conclusions and Outlook</b>	<b>115</b>
10.1	2D structures and fluctuations	115
10.2	Magnetic islands	117
10.3	Outlook	118
	<b>Summary</b>	<b>121</b>
	<b>Samenvatting</b>	<b>125</b>
	<b>Curriculum Vitae</b>	<b>129</b>
	<b>Acknowledgements</b>	<b>131</b>
	<b>Bibliography</b>	<b>133</b>



# 1 Introduction

## 1.1 The need for alternatives to fossil fuels

Global warming is a fact. According to the recently published UN climate report [IPCC 2007], the average temperature has already increased by about 0.7 degrees since 1950. A variety of climate models all point to the conclusion that this temperature increase is *very likely* due to the increased concentrations of the greenhouse gases carbon dioxide, methane and nitrous oxide caused by human activity. More alarming, without drastically reducing the emission of greenhouse gases (mainly CO<sub>2</sub>), the global average temperature is expected to rise another 1.8 to 4 degrees by the end of the century. Locally, in particular in the Arctic, even a rise of more than 6 degrees is likely. This will cause more frequent extreme weather events and rising sea levels. Figure 1-1a shows the CO<sub>2</sub> concentration in the atmosphere over the last 10.000 years. The pronounced increase over the last century is mainly due to the increased use of fossil fuels.

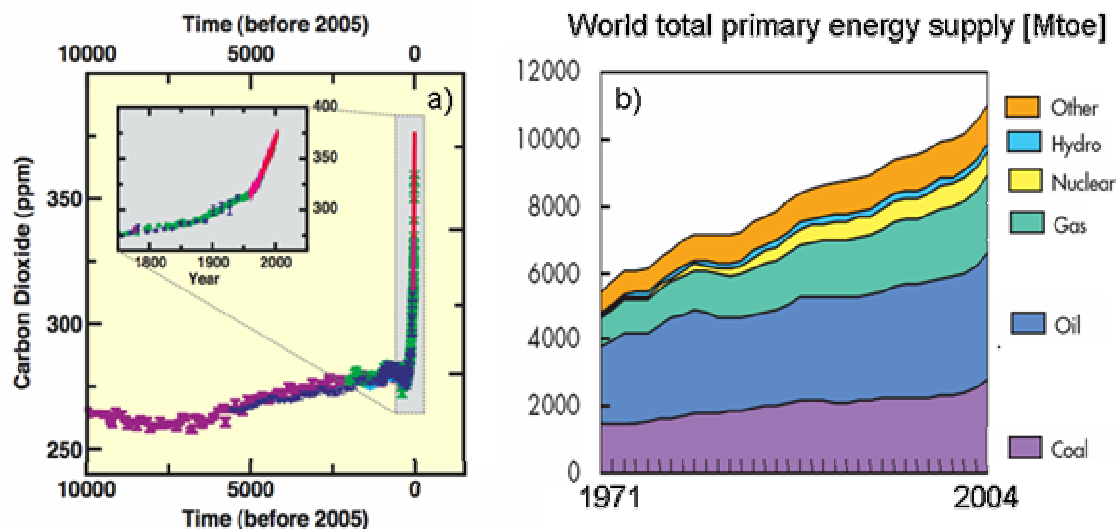


**Figure 1-1:** a) The concentration of CO<sub>2</sub> in the earth atmosphere over the last 10.000 years. An ever faster increase over the last century is visible, due to the ever increasing use of fossil fuels. Source: [IPCC 2007]. b) The composition of the world supply of primary energy between 1971 and 2004. The use of fossil fuels accounts for about 80% of the total amount of energy. The total energy production and the use of fossil fuel have almost continuously increased over this period. Source: [IEA 2006].

The most dramatic effects of the climate change can only be averted if the use of fossil fuels is drastically reduced. Figure 1-1b shows that currently about 80% of the world energy is produced by burning coal, oil and gas. Moreover, the use of fossil fuel

# 1 Introduction

---

has almost doubled over the period 1971-2004, and is still growing. To change this trend, the development of (CO<sub>2</sub>-free) alternative energy sources is needed.

An equally important argument for developing alternative energy sources is the limited reserve of fossil fuels. Although there is still a large coal reserve, oil and gas are expected to become scarce over the course of this century. Sooner or later, the ever scarcer supply of fossil fuels will no longer balance against the ever increasing energy demand. If by that time no alternatives are available, this will be devastating for the world economy.

Examples of currently available renewable (so, practically inexhaustible and environmentally friendly) energy sources are bio, hydro, geothermal, wind and solar energy. These are currently responsible for respectively 3.6, 2.2, 0.4, 0.05 and 0.04 percent of the world energy production [IEA 2003]. For large-scale CO<sub>2</sub>-free energy generation, only four options are presently known of. These are nuclear fission, solar power, carbon sequestration (so burning fossil fuels, but capturing the emitted CO<sub>2</sub>) and fusion [Llewellyn-Smith 2005]. To develop a sustainable energy infrastructure, all four options are needed as fast as possible. Fusion would be a practically inexhaustible and safe source of energy. Moreover, fusion is CO<sub>2</sub>-free and the fuels can not be used for the production of nuclear weapons. Although fusion will produce a limited amount of radioactive waste products, these are contaminated only for a short period of time (50-100 years).

The social acceptance of nuclear fission is variable but low in a number of countries. This is mainly due to accidents that happened (Chernobyl), the long-lived nuclear waste and the proliferation of fissile material. Moreover, the reserves of fission fuel are limited, too. Some of these problems could be overcome with modern reactor designs and fuel cycles, but these are not yet ready for large-scale implementation. Fission could, however, be used to bridge the period between losing the fossil fuels and the installation of a sufficiently large renewable energy infrastructure.

In the long term energy mix, nuclear fusion could play a large role. Fusion has very attractive characteristics as a energy source, but it has one drawback: it is an extremely difficult technology. Fifty years of fusion research has given a very rapid progress, though. The figure of merit of fusion reactors, the power multiplication factor (equivalent  $Q$ ), was doubled every 1.8 years over a period of 40 years, reaching unity in the present generation of large fusion test reactors such as JET. The world-wide collaborative fusion test reactor ITER, of which construction is starting in Cadarache (France), is designed to produce 500 MW of fusion power, ten times more than the power needed to sustain the reaction.

## 1.2 Nuclear fusion and the tokamak concept

A chemical process, like the burning of oil, taps its energy [typically in the order of an electronvolt ( $1 \text{ eV} = 1.6 \cdot 10^{-19} \text{ J}$ ) per reaction] from the binding energy of the electrons. Nuclear fission and fusion tap their energy from the binding energy of nucleons (protons and neutrons) inside the atomic cores (typically in the order of a MeV per reaction). Iron has the strongest bound nucleus, and is hence in the most favourable energy state. By splitting larger (fission), or merging smaller (fusion) nuclei, resulting

in more iron-like reaction products, energy is released. For nuclear fusion, the reaction between the hydrogen isotopes deuterium ( $D=^2_1H$ ) and tritium ( $T=^3_1H$ ) is foreseen, resulting in helium and a neutron. In this reaction 17.6MeV of energy is released, mainly (14.1MeV) as kinetic energy of the lighter neutron.



Although this reaction is exothermic, it does not happen spontaneously. The two positively charged  $D$  and  $T$  nuclei repel each other due to the Coulomb force. One way to overcome this barrier is to raise the temperature of the reacting gases, so that their thermal energy is sufficient to overcome the Coulomb barrier. For the  $D$ - $T$  reaction, the temperature needed is about 10 keV (as a measure of temperature, 1eV=11600K, so 10keV is more than 100 million K!). At such high temperatures, electrons can no longer be bound to the atoms. The resulting ‘gas’ of free electrons and stripped nuclei is called a plasma.

Contrary to a gas, where all particles are electrically neutral, a plasma responds to a magnetic field. For charged particles, motion parallel to the field lines is unrestricted, while perpendicular motion results in a gyration with (cyclotron) frequency  $\omega_c = eB/m$  and (Larmor) radius  $\rho_L = v_{\perp}/\omega_c$ . This can be used to confine the plasma. Confinement is the ability to keep energy and particles in the plasma, and hence to limit the outward energy and particle fluxes. A high confinement is absolutely necessary for a fusion plasma to efficiently reach the required high temperature and density.

To date, the best confinement has been achieved by a magnetic configuration called the tokamak. A toroidal vacuum vessel contains the plasma, see Figure 1-2. This plasma is confined by both a toroidal  $B_{\phi}$  and a poloidal magnetic field  $B_{\theta}$ , giving a resultant helical field. The toroidal field is produced by external coils, the poloidal field by a current in the plasma. This plasma current is produced by making the plasma the secondary winding of a transformer. The poloidal field (so the plasma current) is necessary to avoid the loss of the plasma due to curvature  $B$  and  $\nabla B$  drifts, occurring if only a toroidal field is present. The plasma current also heats the plasma. Additional heating can be applied by injecting high-energy particles (NBI, Neutral Beam Injection) or through the resonant absorption of electromagnetic radiation (ICRH or ECRH, Ion or Electron Cyclotron Resonance Heating).

Current tokamaks (like TEXTOR) are too small to have a positive energy balance, so more energy has to be put in than fusion energy is produced. However, the energy balance improves with the size of a tokamak. The future ITER tokamak ( $R_0=6.2\text{m}$   $a=2\text{m}$ ), being build in southern France, is the first tokamak designed to produce significantly (10 times) more energy than has to be put in.

Although the tokamak has proven to be successful in confining a fusion plasma, and our understanding of tokamak plasmas enables a quite accurate prediction of the performance of ITER, many questions remain. In this thesis we focus on phenomena leading to an enhanced loss of energy and particles from the plasma. In particular, the unwanted, spontaneous occurrence of magnetic field disturbances, the so called magnetic islands, is investigated.

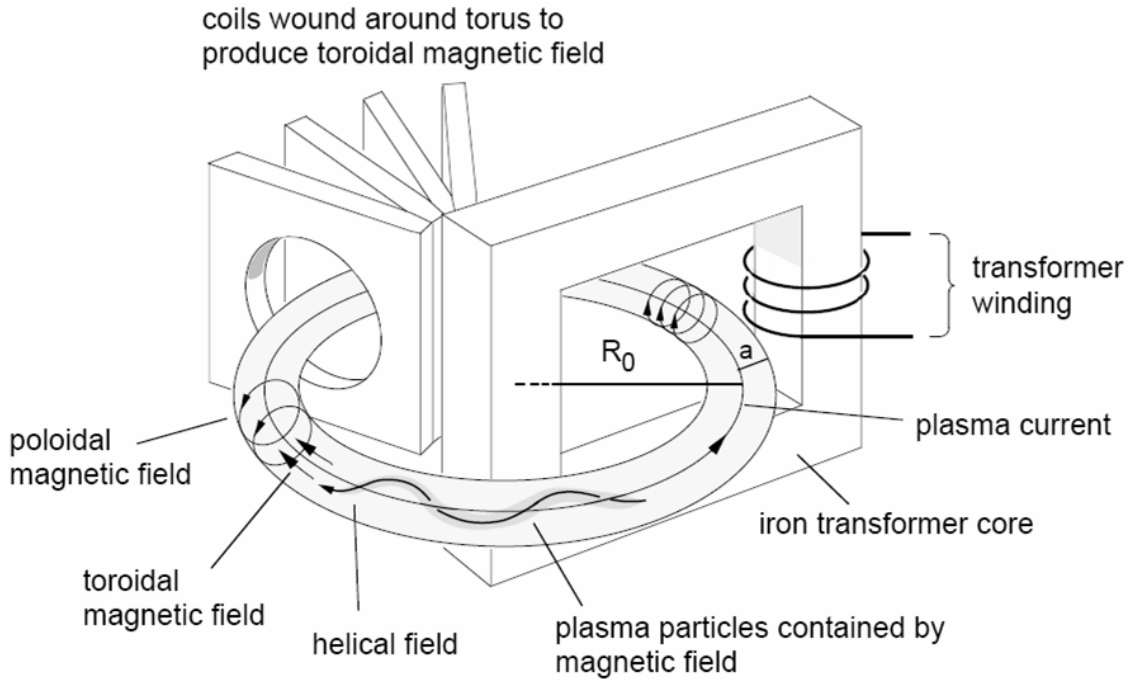


**Figure 1-2:** Schematic representation of a tokamak, showing the main constituents: the toroidal-field coils, the transformer to induce the plasma current and the resulting field components. Also, the major radius  $R_0$  and minor radius  $a$  are indicated.

### 1.3 Magnetic islands

The helicity of a field line can be expressed by the safety factor  $q$ , defined as the number of toroidal turns needed to make one poloidal turn, and depends on the ratio between the toroidal and poloidal magnetic fields. In a cylindrical plasma,  $q$  is approximated by [Wesson 1997]

$$q = \frac{rB_\phi}{R_0B_\theta} \tag{Eq. 1-2}$$

For normal tokamak operation, the value of  $q$  increases with minor radius, being about 1 at the magnetic axis and 2-10 (depending on total plasma current) at the edge. A rational  $q$  surface is a flux surface where  $q$  can be written as  $q=m/n$ ,  $m$  and  $n$  being the (natural) poloidal and toroidal mode numbers. At such a rational  $q$  surface, the individual field lines close on themselves after  $m$  toroidal turns.

Ideally, in a tokamak the helical field lines define a set of nested flux surfaces, see Figure 1-3a. Outward (so radial) heat and particle transport is then only possible perpendicular to the field lines, for instance by collisions. In reality, however, a variety of instabilities can lead to less ideal magnetic topologies.

One of the most common instabilities is the tearing mode or magnetic island. Magnetic islands occur at rational  $q$  surfaces. The presence of a perturbed radial magnetic field with a Fourier component resonant with the  $q=m/n$  surface results in the formation of a magnetic island in the magnetic field topology. A magnetic island

can be seen as a closed, helical flux tube, with helicity  $m/n$ , meaning it closes on itself after going  $m$  times around the torus, while going  $n$  times around poloidally. Figure 1-3b shows the non-axisymmetric flux surfaces in the presence of magnetic islands (in this case both a  $m/n=1/1$  and a  $2/1$  island). The original  $q=m/n$  surface, now forms the boundary of the island flux tube and is called the island separatrix, with its typical X-point in the poloidal cross section. The magnetic axis of the island flux tube is called the O-point. Magnetic islands (so a radial magnetic perturbation) develop either due to the introduction of an external resonant magnetic perturbation field, or by a (energetically favourable) non-axisymmetric redistribution of the plasma current.

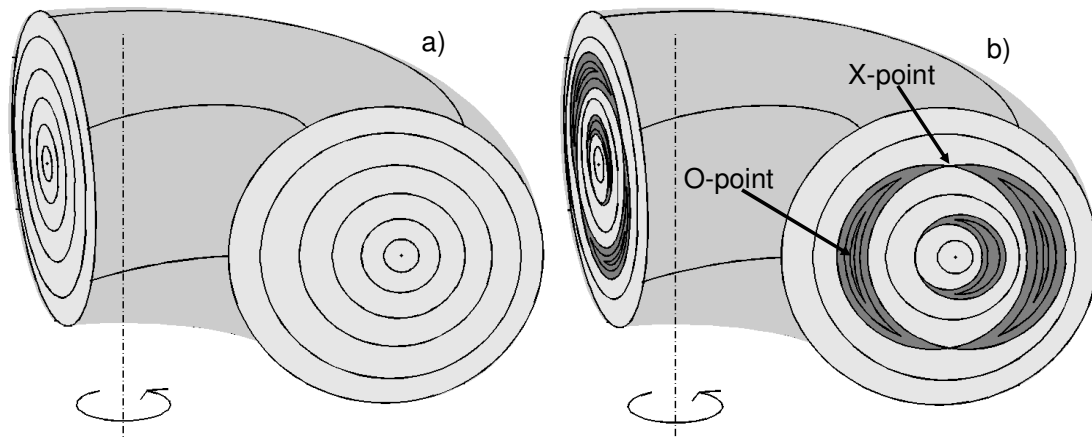


**Figure 1-3:** *Magnetic field topology in a) the ideal case, with nested flux surfaces, and b) in the presence of magnetic islands. Both an  $m/n=1/1$  and a  $2/1$  island are shown. The X and O-points of the  $2/1$  island are indicated.*

Although tokamak operation is possible with (not too large, saturated) magnetic islands, they do have a deleterious effect on the confinement. The island flux surfaces make radial excursions, offering a shortcut along the field lines for radial transport. This results in flattened temperature and density profiles over the island region.

In larger tokamaks, like the future ITER tokamak, a type of magnetic island called the neoclassical tearing mode (NTM) will pose a limit on the parameter range for efficient operation. This mode is destabilised by the loss of bootstrap current (which is a thermo-electric current driven by the density gradient) inside the island, due to the flattened pressure profile. As the bootstrap current depends on the ratio between the plasma pressure and the poloidal magnetic pressure ( $\beta_\theta$ ), NTMs occur in high performance (high pressure) plasmas.

Also, magnetic islands play an important role in disruptions. A (major) disruption is a fast, total loss of confinement, terminating the plasma. The resulting large forces and heat loads on the walls make a disruption an unwanted event that may even lead to damage to the reactor. Normally, magnetic islands rotate with the same velocity as the electrons. Disruptions can occur when a magnetic island locks to the static error field. In that case the mode comes to a standstill, and grows rapidly. Small error fields are present in all tokamaks, for instance due to a slight coil misalignment. Also a locking (and subsequent growth) of two island chains can lead to a loss of the plasma.

In summary, the presence of magnetic islands deteriorates the confinement of a plasma, and makes it more susceptible to disruptions. Hence, magnetic islands should generally be avoided. The control of magnetic islands is the main subject of this thesis. To control islands, both a good knowledge of the theory of island evolution, and tools to influence this evolution are needed. To compare experiment with theory, diagnostics measuring the key parameters are needed.

## 1.4 This thesis

The theory of magnetic islands is known to a large extent. The evolution of the island width is described by the (modified) Rutherford equation, relating island growth to the various sources of helical current in the island region. Each current source is represented by a different term in the Rutherford equation, and represents a way to control (normally suppress) magnetic islands. This thesis focuses on the experimental verification of two terms in the Rutherford equation that are normally difficult to evaluate; the heating term and the perturbation field term. On TEXTOR, the combination of available tools puts us in a unique situation to study these two terms. The three main tools used in this thesis are:

- The electron temperature diagnostic ECE-Imaging (Electron Cyclotron Emission Imaging) [Park 2003] to visualize magnetic islands in 2D with a high spatial and temporal resolution.
- The Dynamic Ergodic Divertor (DED), to generate magnetic islands in a very controlled way by applying a perturbation field of known amplitude and phase [Special Issue 1997].
- A 140 GHz gyrotron [Westerhof 2003] to locally heat magnetic islands by Electron Cyclotron Resonance Heating (ECRH) or drive current by Electron Cyclotron Current Drive (ECCD).

ECE-Imaging enables the accurate measurement of the island width, phase and temperature profile. The island width and phase are important parameters in the theory of the interaction of islands with a perturbation field. The island width and temperature profile are the main parameters for the theory of island suppression by heating. The experiments on magnetic islands are presented in chapters 8 and 9. Before coming to the core of the thesis, however, first the capabilities of the ECE-Imaging diagnostic are explored in chapters 5 and 6. In these chapters ECE-Imaging will be used to study two phenomena that are, like magnetic islands, (thought) responsible for enhanced transport: A perturbed magnetic field at the plasma edge to purposely enhance the edge transport, and high frequency fluctuations thought responsible for the anomalously high transport observed in tokamaks. In these chapters, ECE-Imaging and (in chapter 5) the DED are the main tools used.

In chapter 5, the 2D nature of the ECE-Imaging measurements is exploited in measurements at the plasma edge during DED operation. Apart from a tool to investigate magnetic islands, the DED was designed to alter the edge transport properties. During DED operation, the plasma edge shows a pronounced 2D structure, caused by field lines intersecting the wall. This chapter tries to find answers to the questions:



- What is the effect of the DED perturbation field on the 2D edge temperature profile?
- How does the transport at the edge change during DED operation?
- Can the DED be used to influence the plasma surface interaction?

In chapter 6, the possibilities of measuring high frequency fluctuations with ECE-Imaging are investigated. In principle, ECE-Imaging is capable of measuring high frequency fluctuations with a high spatial resolution, using correlation to suppress the thermal noise inherent to all ECE diagnostics. This chapter tries to find answers to the questions:

- Is ECE-Imaging indeed capable of detecting fluctuation with amplitudes far below the noise level, as expected when using correlation techniques?
- Which types of fluctuations can we see at TEXTOR, and what properties do they have?
- Can we see the fluctuations generally thought responsible for the experimentally observed high transport levels?

After having explored the capabilities of ECE-Imaging, the main subject of this thesis, magnetic islands, is treated in chapters 8 and 9. But before that, the procedure to experimentally determine the island parameters is developed in chapter 7.

In chapter 8, experiments are described investigating the interaction of magnetic islands with perturbation fields. Theoretically, the occurrence of a shielding current results in the processes of mode penetration and mode unlocking. ECE-Imaging is able to measure two parameters playing an important role in theory: the island width and the phase difference between the island and the field perturbation. The known and controllable perturbation field of the DED and ECE-Imaging are used to answer the following questions:

- Are mode penetration and unlocking observed in the experiment, and are the thresholds in accordance with theory?
- Is the island growth after penetration in accordance with the Rutherford equation?
- Can we see and understand (changes in) the expected phase difference between the perturbation field and the actual island?

In chapter 9, DED induced islands are locally heated with ECRH to suppress them. The resulting temperature peaking and suppression rate is measured with ECE-Imaging and compared with theory to answer the following main questions:

- Is the energy confinement inside magnetic islands high enough to maintain a large enough temperature peaking?
- Is the expected suppression of magnetic islands due to this peaked temperature actually observed?
- Is suppression by heating of importance for the suppression of NTMs in a reactor?

Before describing the experimental results, in chapter 2 the theory of (the evolution of) magnetic islands is given. The ‘hardware’ used in this Thesis (TEXTOR, DED, diagnostics) is described in chapter 3. Finally, the theory of ECE as a temperature diagnostic is treated in chapter 4, along with the description of the ECE-Imaging system.

## 1.5 List of publications

Below is a list of publications related to my work on TEXTOR. Publications directly related to this thesis are marked with an asterisk (\*).

### • Journal publications

\*I.G.J. Classen, E. Westerhof, C.W. Domier, A.J.H. Donn , R.J.E. Jaspers, N.C. Luhmann Jr., H.K. Park, M.J. van de Pol, G.W. Spakman, M.W. Jakubowski and TEXTOR team,

‘Effect of heating on the suppression of tearing modes in tokamaks’,  
*Physical Review Letters* **98**, 35001 (2007)

\*I.G.J. Classen, R.J.E. Jaspers, H.K. Park, G.W. Spakman, M.J. van de Pol, C.W. Domier, A.J.H. Donn , N.C. Luhmann Jr., E. Westerhof and TEXTOR team,

‘Imaging meso-scale structures in TEXTOR with 2D-ECE’,  
*accepted for publication: Japan Journal: Plasma and Fusion Research*

\*I.G.J. Classen, M.F.M. de Bock et al.,

‘Dynamics of tearing modes in the presence of a perturbation field’  
submitted to *Nuclear Fusion*

\*M.F.M. de Bock, I.G.J. Classen et al.,

‘The interaction between plasma rotation, stochastic fields and tearing mode excitation by external perturbation fields’  
submitted to *Nuclear Fusion*

\*E.Westerhof, A. Lazaros, E. Farshi, M.R. de Baar, M.F.M. de Bock, I.G.J. Classen, R.J.E. Jaspers, G.M.D. Hogewij, H.R. Koslowski, A. Kr mer-Flecken, Y. Liang, N.J. Lopes Cardozo and O. Zimmermann,

‘Tearing mode stabilization by electron cyclotron resonance heating demonstrated in the TEXTOR tokamak and the implication for ITER’,  
*Nuclear Fusion* **47** 85 (2007)

H.K. Park, N.C. Luhmann, A.J.H. Donn , I.G.J. Classen, C.W. Domier, E. Mazzucato, T. Munsat, M.J. van de Pol, Z. Xia and TEXTOR team,

‘Observation of high-field-side crash and heat transfer during sawtooth oscillation in magnetically confined plasmas’,  
*Physical Review Letters* **96**, 195003 (2006)

H.K. Park, A.J.H. Donn , N.C. Luhmann, I.G.J. Classen, C.W. Domier, E. Mazzucato, T. Munsat, M.J. van de Pol, Z. Xia and TEXTOR team,

‘Comparison study of 2D images of temperature fluctuations during sawtooth oscillation with theoretical models’,  
*Physical Review Letters* **96**, 195004 (2006)

H.K. Park, E. Mazzucato, N.C. Luhmann, C.W. Domier, Z. Xia, T. Munsat, A.J.H. Donné, I.G.J. Classen, M.J. van de Pol and TEXTOR team,  
'Self-organized T-e redistribution during driven reconnection processes in high-temperature plasmas',  
*Physics of Plasmas* **13**, 055907 (2006)

B.P. van Milligen, I.G.J. Classen, C.J. Barth,  
'Revision of TV Thomson scattering data analysis and detection of profile structure'  
*Review of Scientific Instruments* **74** 3998 (2003)

N.J. Lopes Cardozo, I.G.J. Classen, C.J. Barth, C.C. Chu, A.J.H. Donné, R. Jaspers, J. Lok, A.A.M. Oomens, F.J. Pijper, F.C. Schuller,  
'Erratum: Plasma filamentation in the Rijnhuizen tokamak RTP'  
*Physical Review Letters* **90**, 149901 (2003)

\*H.R. Koslowski, E. Westerhof, M. de Bock, I. Classen, R. Jaspers, Y. Kikuchi, A. Kramer-Flecken, A. Lazaros, Y. Liang, K. Lowenbruck, S. Varshney, M. von Hellermann, R. Wolf, O. Zimmermann, and TEXTOR team,  
'Tearing mode physics studies applying the dynamic ergodic divertor on TEXTOR',  
*Plasma Physics and Controlled Fusion* **48**, B53 (2006)

\*K.H. Finken, S. Abdullaev, W. Biel, M.F.M. de Bock, S. Brezinsek, C. Busch, I. Classen *et al.*,  
'Overview of experiments with the dynamic ergodic divertor on TEXTOR',  
*Contributions to Plasma Physics* **46**, 515 (2006).

\*M. Lehnen, S. Abdullaev, W. Biel, M.F.M. de Bock, S. Brezinsek, C. Busch, I. Classen *et al.*,  
'Transport and divertor properties of the dynamic ergodic divertor',  
*Plasma Physics and Controlled Fusion* **47** B237 (2005)

K.H. Finken, S.S. Abdullaev, W. Biel *et al.*, among them I.G.J. Classen,  
'The dynamic ergodic divertor in the TEXTOR tokamak: plasma response to dynamic helical magnetic field perturbations'  
*Plasma Physics and Controlled Fusion* **46**, B143 (2004)

C.W. Domier, Z.G. Xia, P. Zhang, N.C. Luhmann, H.K. Park, E. Mazzucato, M.J. van de Pol, I.G.J. Classen, A.J.H. Donné, R. Jaspers,  
'Upgrades to the TEXTOR electron cyclotron emission imaging diagnostic',  
*Review of Scientific Instruments* **77**, 10E924 (2006)

\*T. Munsat, E. Mazzucato, H. Park, C.W. Domier, M. Johnson, N.C. Luhmann, J. Wang, Z. Xia, I.G.J. Classen, A.J.H. Donné, M.J. van de Pol,  
'2D imaging of electron temperature in tokamak plasmas',  
*IEEE Transactions on Plasma Science* **33**, 466 (2005)

A.J.H. Donné, M.F.M. De Bock, I.G.J. Classen *et al.*,  
'Overview of core diagnostics for TEXTOR',  
*Fusion Science and Technology* **47**, 220 (2005)

## 1 Introduction

---

\*H. Park, E. Mazzucato, T. Munsat, C.W. Domier, M. Johnson, N.C. Luhmann, J. Wang, Z. Xia, I.G.J. Classen, A.J.H. Donne, M.J. van de Pol, 'Simultaneous microwave imaging system for density and temperature fluctuation measurements on TEXTOR', *Review of Scientific Instruments* **75**, 3787 (2004)

\*J. Wang, C.W. Domier, Z.G. Xia, Y. Liang, N.C. Luhmann, H. Park, T. Munsat, E. Mazzucato, M.J. van de Pol, I.G.J. Classen, A.J.H. Donn , 'Two-dimensional electron cyclotron emission imaging diagnostic for TEXTOR', *Review of Scientific Instruments* **75**, 3875 (2004)

### • Conference contributions

\*I.G.J. Classen, E. Westerhof, C.W. Domier, A.J.H. Donn , R. Jaspers, N.C. Luhmann Jr., J.W. Oosterbeek, H.K. Park, M.J. van de Pol, G.W. Spakman and TEXTOR team, '2D ECE Temperature Measurements Inside Tearing Modes, Revealing the Suppression Mechanism by ECRH at TEXTOR', Invited Oral: *In proceedings of the 14<sup>th</sup> Joint Workshop on Electron Cyclotron Emission and Electron Cyclotron Resonance Heating (EC-14)*, Santorini, p134 (2006)

\*I.G.J. Classen, M.J. van de Pol, S. Leerink, A.J.H. Donn , C.W. Domier, N.C. Luhmann, Jr., E. Mazzucato, T. Munsat, H.K. Park, and the TEXTOR team, 'ECE correlation measurements of electron temperature fluctuations on TEXTOR using the new 2D ECE-imaging diagnostic', *In proceedings of the 13<sup>th</sup> Joint Workshop on Electron Cyclotron Emission and Electron Cyclotron Resonance Heating (EC-14)*, Nizhny Novgorod, p108 (2005)

I.G.J. Classen, S.K. Varshney, C.J. Barth and the TEXTOR team, 'Improved analysis of TEXTOR Thomson Scattering data, taking account of the effects of the Instrument Function' *30<sup>th</sup> EPS conf. on Contr. Fusion and Plasma Physics*, St. Petersburg P-2.132 (2003)

\*I.G.J. Classen, M.J. van de Pol, S. Leerink, A.J.H. Donn , C.W. Domier, N.C. Luhmann Jr., E. Mazzucato, T. Munsat, H. Park, A. Kr mer-Flecken and TEXTOR team, 'Fluctuation measurements with the 2D ECE Imaging system on TEXTOR' *31<sup>st</sup> EPS conference on Contr. Fusion and Plasma Physics*, London P-1.121 (2004)

\*I.G.J. Classen, M.W. Jakubowski, A.J.H. Donn , M.J. van de Pol, C.W. Domier, H.K. Park and TEXTOR team, '2D temperature profiles of DED structures using ECE-Imaging in TEXTOR', *32<sup>nd</sup> EPS conference on Contr. Fusion and Plasma Physics*, Tarragona P-2.041 (2005)

\*I.G.J. Classen, E. Westerhof, C.W. Domier, A.J.H. Donn , R. Jaspers, N.C. Luhmann Jr., J.W. Oosterbeek, H.K. Park, M.J. van de Pol, G.W. Spakman and TEXTOR team<sup>4</sup>, '2D ECE Temperature Measurements inside Tearing Modes, Revealing the Suppression Mechanism by ECRH at TEXTOR', *33<sup>rd</sup> EPS conference on Contr. Fusion and Plasma Physics*, Rome P2.169 (2006)

## 2 The theory of magnetic islands

Most of this thesis deals with magnetic islands (or more formally: tearing modes). In chapter 8, experiments will be described in which islands will be created using perturbation fields. In chapter 9, local heating by ECRH will be used to suppress them. Magnetic islands are one of the most common instabilities in a tokamak plasma. Larger magnetic islands have a negative effect on the ability of a plasma to confine energy and particles, and should hence generally be avoided. Very large islands (or the simultaneous occurrence of more than one island) can even lead to a rapid loss of the confinement in a so called disruption.

In this chapter the theory of magnetic islands is reviewed. The emphasis lies on the effects leading to a growth or a suppression of magnetic islands. The evolution of the island width, described in a modified version of the Rutherford equation, is mainly determined by the various parallel currents that are present in the island region. Each type of current corresponds to a different mechanism that can be used to suppress or destabilize magnetic islands. In particular the effects of external perturbation fields (described in [Fitzpatrick 1993/95/98]) and local heating are important for this thesis.

For some equations, in particular for those concerning torques, the sign is important. As this depends on the definition of the coordinate system, Figure 2-1 shows the right handed  $(r, \phi, \theta)$  coordinate system used throughout this thesis.

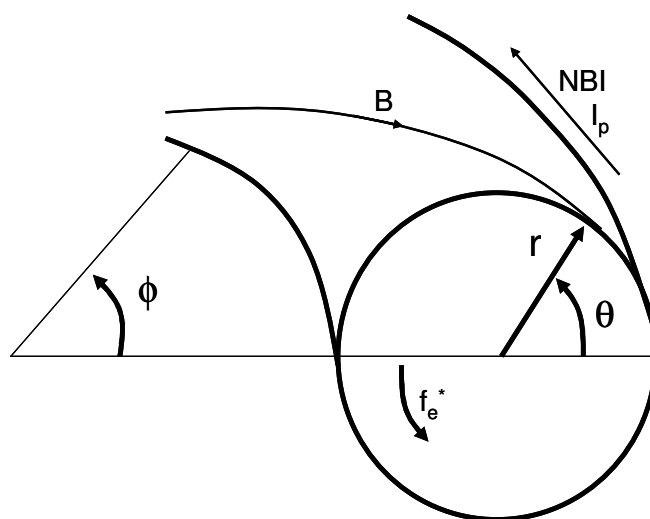


**Figure 2-1:** The definition of the  $(r, \phi, \theta)$  coordinate system. The directions of the magnetic field, co-NBI injection and diamagnetic drift are indicated for a normal TEXTOR discharge.

## 2.1 The island topology

Magnetic islands form when a perturbed radial magnetic field with a certain mode structure  $(m,n)$  is present, on top of the equilibrium magnetic field (whose radial component is zero, for simplicity assuming the equilibrium flux surfaces to be perfectly circular). In the presence of this perturbed field, the ideal magnetic topology of nested flux surfaces breaks down and the typical island structure forms on the  $q=m/n$  resonant surface. An island can be seen as a closed helical flux tube, closing on itself after going  $m$  times around the torus while going  $n$  times around poloidally. The island flux tube is bounded by the separatrix, with its typical X-point in the poloidal cross section. The O-point is the magnetic axis of the island flux tube. Individual field lines in the island make large radial excursions, offering a shortcut for the radial transport of energy and particles. To compare, a typical large island in TEXTOR has a width  $w$  of about 10cm, which is much larger than the typical gyro-radii  $\rho_e=0.05\text{mm}$  and  $\rho_i=2\text{mm}$  (which are the step sizes for classical, collisional transport).

The radial excursion of a field line caused by the perturbed  $m/n$  radial magnetic field is negligible unless the field line lies close to the rational  $q$  surface  $q=m/n$ , resonant with the perturbation. It is common to introduce a new (helical) coordinate

$$\xi = \theta - \frac{n}{m}\phi \quad \text{Eq. 2-1}$$

which is directed perpendicular to the equilibrium field lines at the  $m/n$  surface. The perturbed radial magnetic field can then be written as

$$B_r = B_{r,0}(r) \sin(m\xi - \omega t) \quad \text{Eq. 2-2}$$

where  $\omega$  is the mode frequency. The resulting island topology (for positive  $dq/dr$ , assumed throughout this chapter), which is a superposition of the perturbed radial field  $B_r$  and the equilibrium field, is given by ([Fitzpatrick 1993],[Hegna 1997],[Wilson 2004])

$$y = \frac{w}{2\sqrt{2}} \sqrt{\Omega + \cos(m\xi - \omega t)} \quad \text{Eq. 2-3}$$

$$w = 4 \sqrt{\frac{rqB_{r,0}}{mB_\theta |dq/dr|}} \quad \text{Eq. 2-4}$$

where  $y = r - r_s$  is the radial distance to the rational  $q=m/n$  surface at minor radius  $r_s$ ,  $w$  is the full island width and  $\Omega$  is a label of the perturbed flux surfaces acting as a radial coordinate inside the island, ranging from -1 at the O-point, to +1 at the separatrix. At  $t=0$  (assumed throughout this chapter), the O-points of the island chain are located at  $m\xi=0 \text{ mod}(2\pi)$ . Figure 2-2 shows the geometry given by Eq. 2-3 for a 2/1 island in the  $\xi$ - $y$  plane. Note that only the component of the equilibrium field in this  $\xi$ - $y$  plane ( $B^*$ ) plays a role in the construction of the island. Due to the (assumed constant) magnetic shear,  $B^*$  (which is in the  $\xi$ -direction) changes linearly with  $y$  and changes sign over the resonant surface (where it is zero). The lines, representing flux surfaces, are contour

lines of  $\Omega$ . Note that already very small radial field perturbations lead to considerable island sizes. For typical TEXTOR parameters ( $B_\phi=2.25\text{T}$ ,  $q=m=2$ ,  $dq/dr=6$ ), already  $B_{r,0} = 10^{-4} B_\phi$  gives a  $m/n=2/1$  island with  $w=3\text{cm}$ .

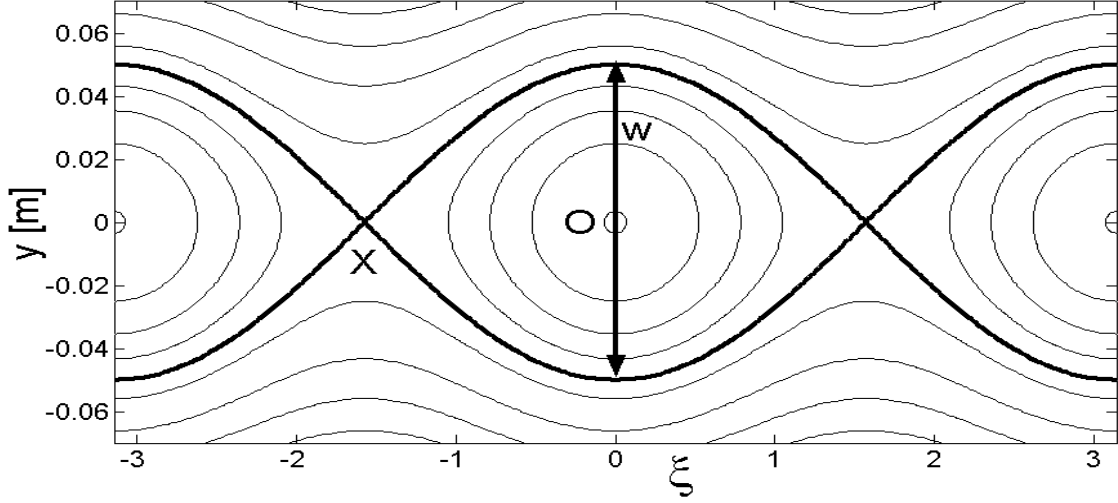


**Figure 2-2:** Contour plot of  $\Omega$  for a  $m/n=2/1$  island in the  $\xi$ - $y$  plane. The O-point, the X-point and the (full) island width  $w$  are indicated. The separatrix is shown as a thick black line.

It should be noted that Figure 2-2 only represents the flux surfaces, not the magnetic field lines themselves. The (in this case)  $m/n=2/1$  component of the magnetic field lines (directed ‘into the paper’) is much larger than the component perpendicular to the  $2/1$  component (in the plane of the figure). So in reality the magnetic field lines deviate only slightly from the unperturbed topology. For a particle gyrating around and travelling along these field lines the island structure only becomes apparent after travelling a long way along the field line, many times around the torus. Here, a second winding number  $q_{im}=m_{im}/n_{im}$  can be introduced describing the helicity of the field lines inside the island with respect to magnetic axis of the island (so the O-point). The field lines inside the island rotate  $n_{im}$  times around the O-point after travelling  $m_{im}$  times around the torus, whereas the island flux tube as a whole has a (normal)  $q=m/n$  structure. Close to the island separatrix,  $q_{im}$  goes to infinity.

Instead of the perturbed poloidal magnetic field ( $\tilde{B}$ , with radial component  $B_r$ ), it is practical to use the perturbed poloidal flux function  $\psi$  (in units of  $\text{Tm}^2$ ), defined as<sup>1</sup>

$$\tilde{B} = \nabla \phi \times \nabla \psi \quad \text{Eq. 2-5}$$

Assuming the perturbed flux to have the form

$$\psi = \psi_0 \cos(m\xi - \omega t) \quad \text{Eq. 2-6}$$

<sup>1</sup> In literature (in particular in the often referred to articles of Fitzpatrick), often a slightly different definition for the poloidal flux function is encountered which has units of  $[\text{Tm}]$ , defined by  $\tilde{B} = \hat{z} \times \nabla \psi$ , where  $\hat{z}$  is the unit vector in toroidal direction. One can convert this definition to the one used in this thesis by simply multiplying by  $R_0$ .

## 2 The theory of magnetic islands

---

gives a perturbed poloidal magnetic field in radial direction:

$$B_{r,0} = \frac{m\psi_0}{rR} \quad \text{Eq. 2-7}$$

where  $\psi_0$  has been assumed constant over the island region. This so called ‘constant  $\psi$  approximation’, already used in the derivation of Eq. 2-3, is common in literature and results in symmetric islands. From Eq. 2-4 and Eq. 2-7 follows the relationship between the amplitude of the perturbed flux  $\psi_0$  and the full island width  $w$ :

$$\psi_0 = \frac{B_\theta \left| \frac{dq}{dr} \right| R}{16q} w^2 = \frac{r_s B_\phi \left| \frac{dq}{dr} \right|}{16q^2} w^2 \equiv Cw^2 \quad \text{Eq. 2-8}$$

where the proportionality constant  $C$ , containing the equilibrium parameters, is introduced.

### 2.2 The effect of an island on $T_e$ and $n_e$

Whether a magnetic island has a large effect on the profiles of electron temperature  $T_e$  and density  $n_e$  depends on the ratio between perpendicular and parallel transport. Due to the fact that parallel transport is orders of magnitude larger than perpendicular transport,  $T_e$  and  $n_e$  can normally be assumed flux functions. Any gradient parallel to a flux surface is quickly removed by the large parallel transport. For a magnetic island, this would mean that the inner and outer separatrix have equal  $T_e$  and  $n_e$ , and (in the absence of significant heat sources or sinks inside the separatrix) that the profiles inside the separatrix are flat. Parallel transport offers a radial shortcut for the transport of energy and particles over the island. The assumption that  $T_e$  and  $n_e$  (and hence also the pressure  $p$ ) are flux functions is justified on all flux surfaces where the transport from one location on that surface to another is dominated by parallel transport. This is, however, not the case on (flux surfaces close to) the separatrix, where the individual field lines have (almost) the same helicity as the island itself. After  $m$  toroidal turns, a field line on the separatrix gets back to its starting point. Moreover, as the local island winding number  $q_m$  approaches infinity the field line has not made any radial excursion during these  $m$  turns. As a result of this ‘field line stagnation’, transport from one location on the separatrix to another is only possible through perpendicular transport. For flux surfaces *close to* the separatrix, a large number of toroidal turn is needed for an individual field line to ‘migrate’ from one location on that flux surface to another. So, although the transport parallel to these field lines is orders of magnitude larger than the perpendicular transport, also the parallel distance connecting two points on their flux surfaces is orders of magnitude larger than the perpendicular distance. So on flux surfaces close to the separatrix, the parallel and perpendicular transport channels compete, making gradients parallel to the flux surfaces possible.

A consequence of this conclusion, drawn from transport arguments, is that in the vicinity of the island separatrix, the standard MHD momentum equation  $j \times B = \nabla p$ , implying the absence of a pressure gradient parallel to  $B$ , is no longer completely valid, although the deviations are very small because the component of  $B$  parallel to



the pressure gradient is very small (even zero at the separatrix). A more general form of the momentum equation is given by [Friedberg 1987]:

$$\rho \frac{dv}{dt} - j \times B + \nabla p = -\nabla \cdot (\mathbf{\Pi}_i + \mathbf{\Pi}_e) \quad \text{Eq. 2-9}$$

where  $d/dt = \partial/\partial t + v \cdot \nabla$  represents the convective derivative and  $\mathbf{\Pi}_i$  is the anisotropic pressure tensor, mainly including viscosity. So either the right hand side of this equation, or the inertial term on the left hand side, can cause (small) parallel pressure gradients. In MHD theory, the right hand side is neglected as it is assumed that the pressure is always equilibrated (isotropic). Close to the island separatrix, however, the very long connection length between different points on the flux surfaces results in long pressure equilibration times [Milligen 1993][Hegna 1998] (going to infinity at the separatrix itself), making the assumption of equilibrated pressure difficult to hold.

The equilibration of  $T_e$  along a field line can be described by writing the electron heat flow as

$$q_e = -\kappa_{//} \nabla_{//} T_e - \kappa_{\perp} \nabla_{\perp} T_e \quad \text{Eq. 2-10}$$

where  $q_e$  is the electron heat flux,  $\kappa = n_e \chi_e$  is the thermal conductivity ( $\chi_e$  is the electron heat diffusivity) and the subscripts  $//$  and  $\perp$  respectively denote the parallel and perpendicular components. Solving Eq. 2-10 around a magnetic island, a critical island width  $w_{c,T}$  can be found [Fitzpatrick 1995], below which the parallel transport can not guarantee  $T_e$  to be a flux function:

$$w_{c,T} = \left( \frac{\kappa_{\perp}}{\kappa_{//}} \right)^{1/4} \left( \frac{R_0 r_s}{s_s n} \right)^{1/2} \quad \text{Eq. 2-11}$$

where  $s_s = \frac{r}{q} \frac{dq}{dr}$  is the local magnetic shear. Analogously, for  $n_e$  a critical island width  $w_{c,n}$  is found by replacing the thermal conductivities by the particle diffusion coefficients  $D$ :

$$w_{c,n} = \left( \frac{D_{\perp}}{D_{//}} \right)^{1/4} \left( \frac{R_0 r_s}{s_s n} \right)^{1/2} \quad \text{Eq. 2-12}$$

This critical width for  $n_e$  is typically a few times larger than the one for  $T_e$  (In [Fitzpatrick 1995] a factor 3.9 is mentioned), mainly due to the smaller parallel transport. When a magnetic island is much smaller than these critical widths, no significant flattening of the profiles occurs. The magnetic island, although present as a magnetic perturbation, is hence not visible in the  $T_e$  and  $n_e$  profiles.

For islands larger than the critical widths, there exists a layer, centred on the separatrix, where parallel gradients in  $n_e$  and/or  $T_e$  are possible, see Figure 2-3. The width of this layer is largest, about  $w_c$ , around the X-point. Half way between the X-points its width is about  $w_c^2/w$ . In the interior of the island, the profiles flatten if there is no significant local heat or particle source. Heat or particle fluxes flowing across the island (so radially out from the centre of the plasma towards the edge), do not

enter the interior of the island, but are conveyed through the X-point by the parallel gradients on the boundary layer.

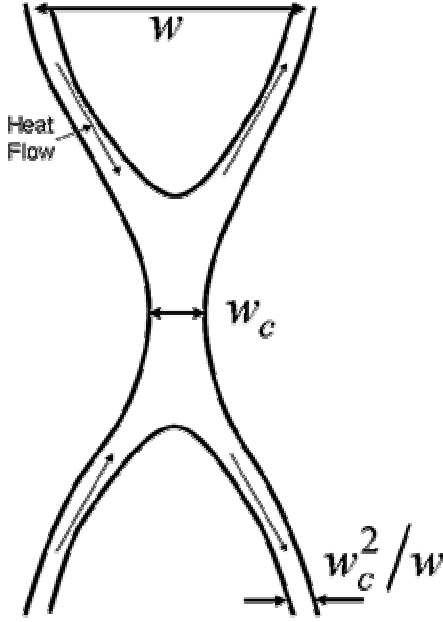


**Figure 2-3:** The layer in which  $T_e$  and  $n_e$  can not be considered flux functions. Islands smaller than the critical width  $w_c$  do not result in significantly flattened profiles. This critical island width is larger for  $n_e$  as for  $T_e$ . For islands larger than  $w_c$ , there is a layer around the separatrix where parallel gradients of  $T_e$  and  $n_e$  are possible. This layer, which channels the heat flux across the island, is widest across the X-point. Further inside the island,  $T_e$  and  $n_e$  are flux functions. If there is no significant heat source or sink inside this region, the profiles are flat. In the presence of a local heat source, this region (with its nested flux surfaces) can confine heat and particles, resulting in peaked profiles.

To find a quantitative value for the critical widths, the parallel and perpendicular transport coefficients are needed. Perpendicular (anomalous) transport for both energy and particles is comparable in amplitude and can be easily estimated from the energy and particle confinement times. Various models for the parallel transport can be found in literature ([Fitzpatrick 1995],[Hazeltine 1997],[Zohm 2001]), leading to a critical island width  $w_{c,T}$  of around 2cm for typical TEXTOR parameters.

### 2.3 The island evolution equation

The various types of currents in the plasma (and its boundary) all influence the dynamics of magnetic islands. The natural stability of magnetic islands is determined by the equilibrium toroidal current profile. The evolution of magnetic islands on the other hand, is governed by the perturbed parallel helical currents in the island region.

Ampere's law relates the second radial derivative of  $\psi$  to the parallel current density  $j_{||}$ :

$$\frac{1}{R_0} \frac{d^2\psi}{dr^2} = \mu_0 j_{||} \tag{Eq. 2-13}$$

here the island is assumed to be small, so that, despite the change in the second radial derivative,  $\psi$  itself changes only slightly over the island radius (constant  $\psi$  assumption) Integrated over the (assumed narrow) island region, Eq. 2-13 gives the basic equation for island evolution ([Rutherford 1973],[Hegna 1997],[Wilson 2004]):

$$\Delta' \psi_0 = 2\mu_0 R \int_{r_s-w/2}^{r_s+w/2} dy \int j_{||} \cos(m\xi) r_s d\xi \tag{Eq. 2-14}$$

where the parameter  $\Delta'$  ('delta prime') is introduced:

$$\Delta' = \frac{1}{\psi} \left[ \frac{d\psi}{dr} \right]_{r_s-w/2}^{r_s+w/2} = \left[ \frac{d[\ln(rB_r)]}{dr} \right]_{r_s-w/2}^{r_s+w/2} \quad \text{Eq. 2-15}$$

So  $\Delta'\psi$  is the step in the radial derivative of  $\psi$  over the island region and is a direct measure for the total perturbed parallel current in the island region. Notice that only current distributions with a  $\cos(m\xi)$  component contribute to the integral (so the equilibrium parallel current doesn't contribute). The positive current direction is in the direction of the equilibrium parallel current.

The value of  $\Delta'$  is a property of the plasma equilibrium (toroidal current profile) and has to be evaluated by matching the ideal MHD solution of  $\psi$  for the region  $0 < r < (r_s+w/2)$  to the solution for  $(r_s-w/2) < r < \infty$ . This will generally give a jump in  $d\psi/dr$  at the rational surface.

Neglecting plasma flow and resistivity, a plasma in force balance obeys  $j \times B = \nabla p$ . As the curl of a gradient equals zero, it follows that:

$$\nabla \times j \times B = 0 \quad \text{Eq. 2-16}$$

Linearization of the perturbed toroidal component of this equation then gives the differential equation governing the radial dependence of  $\psi$  ([Wesson 1997], [Fitzpatrick 1993]):

$$\frac{1}{r} \frac{d}{dr} r \frac{d\psi}{dr} - \frac{m^2}{r^2} \psi - \frac{dj_\phi/dr}{\frac{B_\theta}{\mu_0} \left( 1 - \frac{nq}{m} \right)} \psi = 0 \quad \text{Eq. 2-17}$$

The step in  $\psi$  is found by integrating Eq. 2-17 (from the centre of the plasma outward, and from 'infinity' inward to the resonant surface), using appropriate boundary conditions [  $\psi(0) = \psi(\infty) = 0$  ]. As the solutions to Eq. 2-17 are linear, it is only the normalized step in the flux function (definition of  $\Delta'$ ) that is determined. So in principle,  $\Delta'$  describes the matching criteria for magnetic islands of all sizes. Applied in a region of the plasma where the toroidal current can be neglected (for instance near the plasma edge), Eq. 2-17 predicts a perturbed flux function that falls off with  $(r/r_s)^{-m}$  for  $r > r_s$ , and  $(r/r_s)^m$  for  $r < r_s$  where  $r_s$  is the radius of the current carrying resonant surface. Notice that Eq. 2-17 has a singularity at the rational surface, as a result of neglecting the resistivity. So, inside the island region, this equation is not valid.

One can interpret  $\Delta'$  as a measure for the free energy available in the plasma to drive a tearing mode. The change in magnetic energy in the presence of an island is given by [Hegna 1994]:

$$\delta W_{mag} = -\frac{1}{4} r_s \psi_0^2 \Delta' \quad \text{Eq. 2-18}$$

So a positive  $\Delta'$  means that in the presence of an island, the plasma is in a lower (more favorable) energy state.

### 2.3.1 The Rutherford equation

Equation Eq. 2-14 tells us how much current is flowing in the island, but doesn't directly reveal how an island evolves in time. This time evolution only becomes apparent if we specify the mechanisms responsible for the perturbed parallel current. One mechanism that is always present is the current that is induced by the time derivative of  $\psi$  (and hence  $dw/dt$ ) ([Hegna 1997],[Wilson 2004]):

$$j_{\parallel growth} = \frac{1}{\eta} \frac{\partial \psi_0}{\partial t} \langle \cos(m\xi) \rangle \quad \text{Eq. 2-19}$$

where  $\eta$  is the resistivity (at  $r_s$ ) and  $\langle \rangle$  denotes an average over the helical flux surfaces. If this induced current is the only current contributing to  $j_{\parallel}$ , equation Eq. 2-14 reduces to the classical Rutherford equation for island evolution [Rutherford 1973]:

$$0.82 \cdot \tau_r \frac{dw}{dt} = r_s^2 \Delta' \quad \text{Eq. 2-20}$$

where  $\tau_r = \mu_0 r_s^2 / \eta$  is the current diffusion time. So a positive  $\Delta'$  means a growing island, as expected from the interpretation of  $\Delta'$  as the available free energy. If  $\Delta'$  is negative, the island is naturally stable; no island will develop. For small islands ( $w \ll a$ )  $\Delta'$  is often considered independent of  $w$ , so the Rutherford equation predicts unstable islands to grow exponentially. Bigger islands ( $w$  in the order of  $a$ ) considerably alter the toroidal current distribution, and hence a dependence of  $\Delta'$  on  $w$  is expected ( $\Delta'$  becoming smaller as the island grows; free energy is being used up). This effect can be approximated by writing

$$\Delta'(w) = \Delta'_0 \left( 1 - \frac{w}{w_{sat}} \right) \quad \text{Eq. 2-21}$$

where  $w_{sat}$  is the (experimentally determined) saturated island width. So the initially linearly growing island finally saturates at width  $w_{sat}$  when  $\Delta'(w) = 0$ .

A more precise derivation of the evolution equation, including the effects of plasma flows, results in a slightly different form of the Rutherford equation [Wesson 1997]:

$$0.82 \cdot \tau_r \frac{dw}{dt} = r_s^2 (\Delta'(w) - \alpha w) \quad \text{Eq. 2-22}$$

where  $\alpha$  is related to the local plasma parameters ( $\Delta'$  per definition only contains current profile effects). In the remainder of this thesis, when writing  $\Delta'(w)$ , actually  $(\Delta'(w) - \alpha w)$  is meant.

Introduction of other currents than the inductive current in the island region results in modifications to the Rutherford equation. These are described in the next paragraph.

## 2.4 Other contributions to the helical current

The introduction of other currents (with a  $\cos(m\xi)$  component) in the island region alters the evolution equation. A modified version of the Rutherford equation can be found by substituting the sum of all contributions to  $j_{||}$  into equation Eq. 2-14, repeated here.

$$\Delta' \psi_0 = 2\mu_0 R \int_{r_s-w/2}^{r_s+w/2} dy \oint j_{||} \cos(m\xi) r_s d\xi$$

In general, extra current inside the island in the same direction as the equilibrium parallel current (co-current) stabilizes the mode, and extra current in the other direction is destabilizing. The total current in the island region is fixed by the left hand side of Eq. 2-14, so extra current in the co-direction replaces the induced current due to island growth. So due to the extra co-current, Eq. 2-14 can now be satisfied without the need of island growth to maintain the prescribed total current.

The modifications to the island evolution equation due to the following extra (helical) currents are treated in this paragraph:

- The perturbed bootstrap current, leading to neoclassical tearing modes (NTMs).
- Shielding currents due to external perturbation fields.
- Currents caused by O-point heating.
- Currents due to direct non-inductive current drive

### 2.4.1 Perturbed bootstrap current: Neoclassical Tearing Modes

By introducing the perturbation in the bootstrap current due to the island, the mechanism of the so called neoclassical tearing mode (NTM) becomes apparent. The bootstrap current is a non-inductive current, which (in a simplified picture) is proportional to the radial gradient in the plasma pressure [Wesson 1997]. Because pressure is approximately a flux function for big enough islands [Fitzpatrick 1995], the pressure gradient is effectively removed from the island region, leaving a 'hole' in the bootstrap current profile with the necessary  $\cos(m\xi)$  component to influence the island evolution. For negative  $dp/dr$  and positive  $dq/dr$  (true in common tokamak regimes) this current perturbation opposes the induced current of the island, and hence is destabilizing. So, even islands with a negative  $\Delta'$  can be destabilized. The inclusion of the perturbed bootstrap current in Eq. 2-14 leads to a modified Rutherford equation of the form [La Haye 2006]:

$$0.82\tau_r \frac{dw}{dt} = r_s^2 \Delta'(w) + M_{bootstrap} \tag{Eq. 2-23}$$

$$M_{bootstrap} \approx -\epsilon^{1/2} \frac{L_q}{L_p} \frac{\beta_\theta}{w}$$

## 2 The theory of magnetic islands

---

where  $\varepsilon = r/R_0$  is the local inverse aspect ratio,  $L_q = q/(dq/dr)$  the magnetic shear length,  $L_p = p/(dp/dr)$  the pressure gradient length and  $\beta_\theta = 2\mu_0 p/B_\theta^2$  the poloidal  $\beta$ . Naturally stable (negative  $\Delta'$ ) islands destabilized by the perturbed bootstrap current are called neoclassical tearing modes (NTMs).

If Eq. 2-23 would be the whole story, the  $w^{-1}$  dependence of  $M_{bootstrap}$  would always destabilize an NTM. This would be catastrophic for the stable operation of tokamaks, and is in contradiction with experimental findings. Experimentally, NTMs are only destabilized above a certain threshold island width. So a ‘seeding’ island of sufficient width is needed. Seeding islands can be provided by any (coincidental) distortion of the plasma, for instance by the error field of a sawtooth precursor.

One correction on Eq. 2-23 is provided by the effects already described in paragraph 2.2. For small islands, temperature and density are not necessarily flux functions, and hence the flattening of the pressure profile assumed in Eq. 2-23 does not occur. Taking this effect into account results in [La Haye 2006]:

$$M_{bootstrap} \approx -\varepsilon^{1/2} \frac{L_q}{L_p} \beta_p \frac{w}{w^2 + w_c^2} \quad \text{Eq. 2-24}$$

where the critical width for pressure flattening  $w_c$  is closely related to the ones for temperature and density, Eq. 2-11 and Eq. 2-12.

A second effect leading to a threshold for island growth is the polarization current correction [Waelbroeck 2001], resulting from a difference in response of electrons and ions in a rotating island. This (complicated) correction results in a further ‘fine-tuning’ of  $M_{bootstrap}$ :

$$M_{bootstrap} \approx -\varepsilon^{1/2} \frac{L_q}{L_p} \beta_p \frac{r_s}{w} \left[ \frac{w^2}{w^2 + w_c^2} - \frac{w_{pol}^2}{w^2} \right] \quad \text{Eq. 2-25}$$

where the typical threshold island width due to the polarization current correction is approximately given by

$$w_{pol} \approx (L_q/L_p)^{1/2} w_b \quad \text{Eq. 2-26}$$

where  $w_b$  is the banana orbit width. This width also depends on collisionality and island frequency.

With the inclusion of the threshold island widths in  $M_{bootstrap}$ , it now describes the typical NTM behaviour. It should be noted that in TEXTOR the bootstrap current fraction is generally small. TEXTOR magnetic islands are therefore generally of classical origin (positive  $\Delta'$ ). TEXTOR, however, has a tool to destabilize otherwise naturally stable tearing modes: the resonant perturbation field of the Dynamic Ergodic Divertor, treated in the next paragraph.

## 2.4.2 The effect of an external perturbation field

Resonant magnetic perturbation fields, generated by currents flowing outside the island region, have a large influence on the stability of magnetic islands. On TEXTOR, the Dynamic Ergodic Divertor (DED) is used to generate such a perturbed field. In chapter 8, experiments investigating the effect of the DED field on magnetic islands are presented.

Currents flowing in external coils generate a perturbation field with a certain mode spectrum. This magnetic perturbation field can again be described by a perturbed poloidal flux function. At the position of the external coils this flux function will have a jump in the radial derivative, proportional to the current in the coils, analogous to the jump in  $\psi$  at the resonant surface described in Eq. 2-14 and Eq. 2-15. In the absence of a conducting plasma, this flux function will result in an island at the  $q=m/n$  surface in the vacuum magnetic field (which is the superposition of the perturbation field and the equilibrium field), with a width  $w_{vac}$  and corresponding perturbed flux  $\psi_{vac} = \psi_{vac,0} \cos(m\xi - \omega_{ext}t)$ , where  $\omega_{ext}$  is the mode frequency of the externally applied field. The perturbed flux  $\psi_{vac}$  scales linearly with the external coil current amplitude. The ideal MHD response of the plasma to this perturbed flux function will be to generate a current at the rational surface that cancels the effect of the external coil currents ([Fitzpatrick 1993],[Kikuchi 2006]). This shielding current has two important effects: it alters the stability of  $m/n$  tearing modes, described by a modified version of the Rutherford equation, and it exerts an electromagnetic torque on  $m/n$  modes.

The modified version of the Rutherford equation is again found by including the  $\cos(m\xi)$  component of the shielding current (expressed in terms of the vacuum island width) in Eq. 2-14, leading to ([Fitzpatrick 1991], [Fitzpatrick 1993], [Fitzpatrick 1998], [Morris 1992a])

$$0.82\tau_R \frac{dw}{dt} = r_s^2 \Delta'(w) + M_{ext} \quad \text{Eq. 2-27}$$

$$M_{ext} = 2mr_s \left( \frac{w_{vac}}{w} \right)^2 \cos(\Delta(m\xi))$$

where  $\Delta(m\xi) = m(\xi_{O,plasma} - \xi_{O,vacuum})$  is the phase difference between the O-points of the plasma island and the vacuum island. Notice that this modification is largest when the plasma island is small, and when the island is aligned with the external perturbation field (vacuum island).

The  $\sin(m\xi)$  component of the shielding current doesn't influence the evolution of the island width, but results in an electromagnetic torque  $T_{EM}$  in the direction of  $\xi$  on the island, trying to align the plasma island with the vacuum island. The origin of this torque is the net  $j \times B$  force attributable to the shielding current and the radial magnetic field of the island. The toroidal and poloidal components of this torque are given by ([Fitzpatrick 1993], [Fitzpatrick 1998], [Fitzpatrick 1991]):

$$T_{\phi,EM} = -\frac{n}{m} T_{\theta,EM} = -4\pi^2 \frac{mn}{\mu_0 R_0} C^2 w_{vac}^2 w^2 \sin(\Delta(m\xi)) \quad \text{Eq. 2-28}$$

## 2 The theory of magnetic islands

---

Because poloidal flow damping of the ions effectively prohibits any significant ion rotation in poloidal direction [Stix 1973], only the toroidal component of this torque is important.

If the MHD frequency  $\omega$  is equal to the frequency of the externally applied perturbation field  $\omega_{ext}$  (as is the case for a locked island), Eq. 2-28 can be directly applied. If, however, there is a difference in frequency, referred to as the ‘slip’ frequency

$$\Delta\omega = \omega - \omega_{ext} \quad \text{Eq. 2-29}$$

one has to distinguish between two different cases, depending on the size of the (induced) plasma islands. For both cases (referred to as the ‘non-linear’ and ‘linear’ cases), Eq. 2-28 is valid, but the expression for the time averaged electromagnetic torque in terms of the slip frequency  $\Delta\omega$ , takes different forms.

### 2.4.2.1 The electromagnetic torque in the non-linear regime.

Large, ‘non-linear’, islands always rotate at the MHD frequency. The island is not allowed to slip through the electron fluid. In this case, a non-zero  $\Delta\omega$  results in a plasma island that is alternately dragged in and out of phase with the perturbation field, giving a periodic growth and decay of the island and a fluctuating electromagnetic torque. Assuming the island rotation is not significantly altered by the fluctuating torque, and that the  $\Delta'$  term in the modified Rutherford equation (Eq. 2-27) is negligible with respect to the large perturbation field term (which is the case for small island widths), one can analytically solve the Rutherford equation, yielding the fluctuating island width [Fitzpatrick 1998]

$$w(t) = w_0 |\sin(\Delta\omega t)|^{1/3} \quad \text{Eq. 2-30}$$

$$w_0 = 1.939m^{1/3} \left( \frac{w_{vac}^2 / r_s^2}{\Delta\omega\tau_R} \right)^{1/3} r_s$$

where  $w_0$  is the maximum island size during one fluctuation. The time averaged electromagnetic torque acting on the island in the non-linear regime can now (by combining Eq. 2-30 and Eq. 2-28) be expressed as

$$\langle T_{\phi,EM} \rangle_{\text{non-linear}} = -\text{sign}(\Delta\omega) \cdot 0.5356 \cdot 4\pi^2 \frac{mn}{\mu_0 R_0} C^2 w_{vac}^2 w_0^2 \quad \text{Eq. 2-31}$$

which is proportional to  $\Delta\omega^{2/3}$  and in the direction to decrease  $\Delta\omega$ . Note that the  $\Delta\omega$  dependence is hidden in  $w_0$ .

### 2.4.2.2 The electromagnetic torque in the linear regime.

For very small islands, the island does not necessarily rotate at the same angular velocity as the electron fluid, but slips through it to some extent. This effect is caused by the viscosity between the island and the plasma ‘flowing around’ it. This viscosity



arises in a thin layer (with thickness of the order of the linear layer mentioned in [Fitzpatrick 1993], [Fitzpatrick 1998]), where an exchange of particles between the island and the surrounding plasma occurs. The rotation frequency of  $\psi$  (so the induced plasma island) can now slip with respect to the MHD frequency. In fact,  $\psi$  will now rotate at the frequency of the external perturbation field, but with a phase lag, resulting in a non-fluctuating torque and mode amplitude. For these experiments, the linear layer is in the ‘visco-resistive’ regime treated in ([Fitzpatrick 1993], [Fitzpatrick 1998]) (meaning that viscosity and resistivity are important, but inertia is negligible, valid for  $\Delta\omega \ll \tau_V^{1/3} \tau_H^{-2/3} \tau_R^{-2/3}$ ). The expression for the (visco-resistive) linear layer width is given by:

$$\delta_{VR} = \frac{\tau_H^{1/3}}{\tau_R^{1/6} \tau_V^{1/6}} r_s \quad \text{Eq. 2-32}$$

and is typically 3 mm in the experiments treated here. The hydromagnetic and viscous time scales are given by

$$\begin{aligned} \tau_H &= \frac{R_0 \sqrt{\mu_0 \rho}}{B_\phi} \frac{1}{ns} \\ \tau_V &= \frac{r_s^2}{D} \end{aligned} \quad \text{Eq. 2-33}$$

where  $\rho$  is the plasma mass density,  $D$  the effective momentum diffusion coefficient and  $s = \frac{r}{q} \frac{dq}{dr}$  the magnetic shear.

When the driven island width is larger than the linear layer width, the non-linear description is appropriate. When however the island widths are comparable to, or smaller than the linear layer width (as is usually the case during the early stages of mode penetration), the following linear theory is needed.

In the visco-resistive limit, the *steady* torque, island width and phase lag are given by: [Fitzpatrick 1993]

$$T_{\phi,EM,linear} = -4\pi^2 \frac{2m^2 n}{\mu_0 R_0 |\Delta'_0 r_s|} \frac{\Delta\omega \tau_{rec}}{1 + (\Delta\omega \tau_{rec})^2} C^2 w_{vac}^4 \quad \text{Eq. 2-34}$$

$$w^2 = \frac{1}{\sqrt{1 + (\Delta\omega \tau_{rec})^2}} \frac{2m}{|\Delta'_0 r_s|} w_{vac}^2 \quad \text{Eq. 2-35}$$

$$\Delta(m\xi) = \tan^{-1}(\Delta\omega \tau_{rec}) \quad \text{Eq. 2-36}$$

where  $\Delta_0'$  is the stability parameter at zero island width for the mode in question and

$$\tau_{rec} = \frac{2.1036}{|\Delta'_0 r_s|} \frac{\tau_H^{1/3} \tau_R^{5/6}}{\tau_V^{1/6}} \quad \text{Eq. 2-37}$$

is the typical reconnection time scale in the visco-resistive limit. Figure 2-4 gives an example of both the non-linear and linear theory for typical TEXTOR parameters. The two theories are very similar (both showing the resonance at the perturbation field frequency and similar torque amplitudes) despite the somewhat different parametric dependencies. The fact that the curve for the linear theory passes through 0, and the non-linear doesn't, is due to the fact that in the non-linear curve  $\Delta'$  is fully neglected. If a finite  $\Delta'$  would have been assumed, the resemblance between linear and non-linear would have been even greater. The most important difference however, is that the linear theory describes constant torques, whereas the non-linear theory deals with oscillating torques.

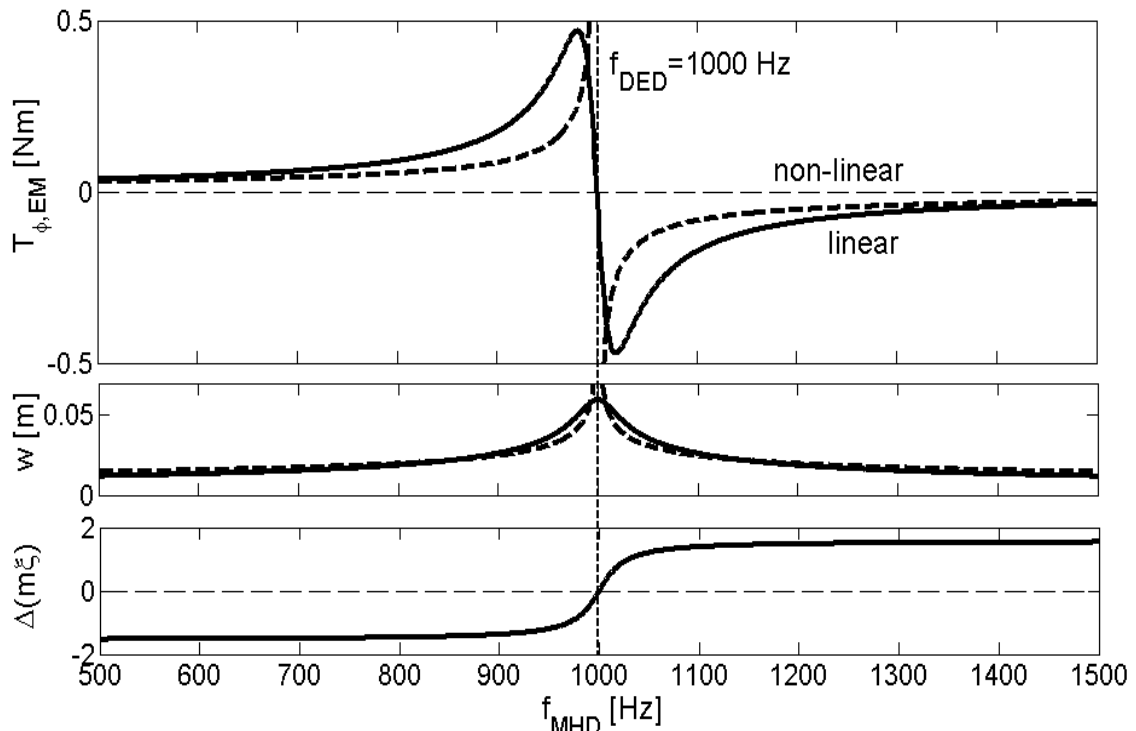


**Figure 2-4:** Example of the electromagnetic torque, island width and phase difference for both linear (solid) and non-linear (dashed) theory for typical TEXTOR parameters, using the DED to create the perturbed field. The perturbation field rotates at 1 kHz. The resonant character of the torque (trying to arrest the mode rotation) is apparent. The induced island widths are only large when the mode frequency is close to the perturbation field frequency. The phase difference is only shown for the non-oscillating linear theory.

### 2.4.3 Heating and current drive

Two more methods of generating helical currents in the island region are local heating and non-inductive current drive. But, before discussing these two methods to control the evolution of magnetic islands, it is practical to deduce a general form of the modified Rutherford equation, which can be derived from Eq. 2-14, Eq. 2-19 and Eq. 2-8 without any further assumptions on the nature of the extra currents ( $j_{//,1,2,\dots}$ ). The 'raw' form of any modification term in the Rutherford equation is given by:

$$0.82 \cdot \tau_r \frac{dw}{dt} = r_s^2 \Delta'(w) - M \quad \text{Eq. 2-38}$$

$$M = \frac{2\mu_0 R r_s^2}{Cw^2} \int_{r_s-w/2}^{r_s+w/2} dy \oint (j_{\parallel,1} + j_{\parallel,2} + \dots) \cos(m\xi) r_s d\xi$$

By specifying the spatial distribution of the extra current and integrating over the island region, more practical (but less general) expressions are found, as was (implicitly) done for  $M_{bootstrap}$  and  $M_{ext}$  in the previous paragraphs.

By introducing significant heating power in the island (for instance by Electron Cyclotron Resonance Heating, ECRH), a temperature peaking of the O-point with respect to the separatrix is created (if the island is big enough). As the resistivity is a function of  $T_e$ , the Ohmic current gets a  $\cos(m\xi)$  component and contributes to the island evolution. Assuming neoclassical resistivity [Wesson 1997]:

$$\eta \approx 2.8 \cdot 10^{-8} \frac{Z_{eff}}{T_e^{3/2}} (1 - \epsilon^{1/2})^2 \quad \text{Eq. 2-39}$$

and a  $T_e$  profile  $T_e(\Omega)$  in the island region, the Ohmic current has the form:

$$j_{Ohmic}(\Omega) = j_{sep} \left( \frac{T_e(\Omega)}{T_{e,sep}} \right)^{3/2} \quad \text{Eq. 2-40}$$

where a constant effective ion charge  $Z_{eff}$  is assumed. The subscript ‘sep’ refers to the value at the island separatrix  $\Omega=1$ . Inclusion of this perturbed Ohmic current and any directly driven non-inductive parallel current  $j_{\parallel,CD}$  in equation Eq. 2-38, gives the final two modifications:

$$0.82 \cdot \tau_r \frac{dw}{dt} = r_s^2 \Delta'(w) - M_{heating} - M_{currentdrive}$$

$$M_{heating} = \frac{2\mu_0 R r_s^2}{Cw^2} \cdot \frac{j_{sep}}{T_{e,sep}^{3/2}} \int_{r_s-w/2}^{r_s+w/2} dy \oint T_e^{3/2} \cos(m\xi) r_s d\xi \quad \text{Eq. 2-41}$$

$$M_{currentdrive} = \frac{2\mu_0 R r_s^2}{Cw^2} \int_{r_s-w/2}^{r_s+w/2} dy \oint j_{\parallel,CD} \cos(m\xi) r_s d\xi$$

So, O-point heating (having a positive  $\cos(m\xi)$  component) is stabilizing.

Non-inductive current drive, for instance by Electron Cyclotron Current Drive (ECCD), can be both stabilizing and destabilizing, depending on the direction of the driven current. Driving current in the same direction as the equilibrium current (co-current) is stabilizing, counter-current drive is destabilizing.

Eq. 2-41 suggests that current drive only influences island evolution if the current is driven preferentially at the O-points (by modulating the power). It is however not necessary to ‘aim’ at the O-points to get the desired  $\cos(m\xi)$  distribution of the driven

## 2 The theory of magnetic islands

---

current. When current is driven evenly over the island region (CW power), the rapid redistribution of the current over the island flux surfaces automatically results in the helical distribution. Of course, modulation does result in a more efficient island suppression, as it also results in the desired peaked current distribution at the O-point, without ‘spilling’ current outside the island (where it redistributes evenly, and does not contribute to Eq. 2-41).

Driving current by ECCD without also simultaneously heating the plasma by ECRH is not possible. The ratio of current drive to heating, the current drive efficiency, is for the TEXTOR case typically 0.1 A/W [Westerhof 1987].

The modifications in Eq. 2-41 are still in their almost raw form. In chapter 9 the effect of heating on tearing mode suppression is investigated. As the temperature profile over the island is directly measured in these experiments, Eq. 2-41 can be directly applied, and there is no need for assumptions on the shape of the  $T_e$  profile. In literature one can find a variety of simplified expressions for different assumptions on the temperature [Hegna 1997] and current ([Hegna 1997],[Morris 1992a],[Zohm 1997],[Zohm 2001]) distribution.

### 2.5 Mode rotation

In paragraph 2.4.2 the island rotation frequency played an important role. The rotation of an island should not be confused with the rotation of the plasma. The mode (or MHD) frequency  $\omega$ , refers to the frequency at which the magnetic field topology (island) rotates. Note that one cannot differentiate between toroidal and poloidal mode rotation, they are coupled through  $q$ . When talking about ‘plasma rotation’, normally the ion rotation in toroidal direction is meant. In steady state, the poloidal ion rotation is normally negligible, due to strong poloidal flow damping [Stix 1973]. The rotation of the electrons (which does have a poloidal component) differs from the ion rotation, giving rise to the plasma current. Since parallel (ion or electron) flows do not influence the magnetic topology, only the perpendicular flows play a role in the mode rotation. Islands are observed to always rotate with the perpendicular electron velocity [Klüber 1991]. The difference between electron and ion perpendicular velocity corresponds to the diamagnetic drift, resulting in a perpendicular current responsible for the confinement of the plasma via  $j \times B = \nabla p$  [Wesson 1997]. So, neglecting ion poloidal rotation and the (small) toroidal component of the diamagnetic drift, the relation between the MHD frequency  $\omega$  and toroidal ion rotation frequency  $\Omega_\phi$  is given by:

$$\omega \approx 2\pi n f_e^* - n \Omega_\phi$$

$$f_e^* = -\frac{1}{2\pi e n_e B_\phi r} \frac{\partial p}{\partial r}$$
Eq. 2-42

where  $f_e^*$  is the electron diamagnetic frequency (positive for these experiments, see Figure 2-1).

## 2.6 Conclusion

The evolution of magnetic islands is governed by a generalized form of the Rutherford equation, where each modification arises from the inclusion of a helical current in the island region. Collecting all modifications treated in this chapter gives:

$$0.82 \cdot \tau_r \frac{dw}{dt} = r_s^2 \Delta' + M_{bootstrap} + M_{ext} - M_{heating} - M_{currentdrive} \quad \text{Eq. 2-43}$$

where each modification  $M_*$  is defined such that it is (under normal circumstances) positive. So the sign indicates which terms are normally stabilizing (-) or destabilizing (+). Co-current drive and heating are stabilizing (for positive shear). Counter-current drive, perturbation fields and the loss of bootstrap current are normally destabilizing.

In paragraph 2.4, the ‘control’ of magnetic islands emphasized on changing the helical currents in the island region, so on changing the right hand side of Eq. 2-14. Alternatively, one can control the stability of islands by changing the left hand side of that equation, so by tailoring the equilibrium toroidal current profile represented by  $\Delta'$  (paragraph 2.3) ([Westerhof 1987],[Westerhof 1990]).

So, although magnetic islands (in particular the NTMs in larger tokamaks) represent a limitation of the parameter regime for stable operation of a tokamak, the physics of these instabilities offers a large number of possibilities to control them. In this thesis, the effects of external perturbation fields and heating will be used to manipulate islands.



## 3 TEXTOR and its auxiliary systems

In this chapter, a brief description of the hardware used in this thesis is given. The experiments reported in this thesis are performed on TEXTOR, a medium sized, circular, limiter tokamak. TEXTOR is well equipped with heating systems, diagnostics and a set of perturbation field coils: the Dynamic Ergodic Divertor (DED). The tokamak and its auxiliary systems are briefly introduced. Among them are the main tools used in this thesis: ECE-Imaging, the DED and the 140GHz gyrotron. A more in depth discussion of the ECE-Imaging system can be found in the next chapter (paragraph 4.3).

### 3.1 The TEXTOR tokamak

TEXTOR (the Tokamak Experiment for Technology Oriented Research) is a medium sized limiter tokamak with major radius  $R_0=1.75\text{m}$  and minor radius  $a=0.47\text{m}$  (an up to date overview of the design features can be found in [Neubauer 2005]). The plasmas in TEXTOR have a circular cross section and last for up to 10s. Magnetic fields of up to 3T and plasma currents up to 800kA are possible, although the typical values are 2.25T and 400kA. Table 3-1 lists the main parameters of TEXTOR.

**Table 3-1:** *Main parameters of TEXTOR*

Major radius $R_0$	1.75m
Minor radius $a$	0.47m
Toroidal magnetic field $B_T$	<3T
Plasma current $I_p$	<800kA
Pulse length	<10s
Total auxiliary heating power	8MW
Maximum NBI power	two beams with 1.5MW each
Maximum ECRH power	two gyrotrons: 800kA+200kA
Maximum ICRH power	4MW
Central plasma temperature (electron/ion)	typically 1keV
Central density $n_e$	typically $3 \cdot 10^{19} \text{ m}^{-3}$

The toroidal magnetic field is produced by a set of 16 toroidal field coils. The plasma current is produced by the iron core transformer, having 6 yokes and the Ohmic coils wound around the central leg. Two Vertical field coils compensate the hoop force on

the plasma, and four position control coils can produce both horizontal and vertical magnetic fields to keep the plasma at the desired position.

TEXTOR has three different types of limiters. The carbon tiles covering the DED perturbation field coils at the high field side of the vacuum vessel form a toroidal belt limiter, protecting about 30% of the poloidal circumference for the energy fluxes during a disruption. During DED operation these carbon tiles act as divertor target plates. The second type of limiters, the main limiters, are located at certain toroidal positions (at the top, bottom or low field side of the plasma) and can be moved in and out for plasma shaping and material testing. Thirdly, a pumped toroidal belt limiter, the Advanced Limiter Test II (ALT-II) limiter, mounted 45 degrees below the equatorial plane at the low field side, is designed to cope with the full 8MW of installed heating power for up to 10s.

## 3.2 Auxiliary heating systems

Apart from the Ohmic heating, TEXTOR has a total of about 8MW of additional heating power installed. Three types of auxiliary heating systems are available: two neutral beam injectors (NBI), two gyrotrons for electron cyclotron resonance heating (ECRH) and two ion cyclotron resonance heating (ICRH) antennae. The two systems used in this thesis, NBI and ECRH, are briefly introduced below. For a description of the ICRH system, not used in this thesis, see [Koch 2005].

### 3.2.1 The neutral beam injectors

Two tangential neutral beam injectors [Neubauer 2005] provide up to 1.5MW of additional heating power each. One injector, NBI1, is oriented in the same direction as the plasma current (co-direction) and hence provides (apart from heating power) momentum to the plasma in that direction. The second injector, NBI2, is directed in the opposite direction (counter-injection). So, the two injectors are a tool to influence the plasma rotation in both the co and counter-directions. By injecting equal amounts of power from both beams (balanced injection), no net momentum is transferred to the plasma. The two systems can inject neutral  $H_2$ ,  $D_2$ ,  $^3He$  or  $^4He$  particles with energies up to 60keV into the plasma. In the plasma, the neutral particles are ionised by charge exchange reactions with the plasma ions, and subsequently transfer their energy to the plasma electrons and ions through collisions. The beams are produced by first ionising the gas to accelerate it. About 50% of the ions are subsequently neutralised in a gas cell (neutraliser). The remaining ions are deflected by a magnet, and the beam of neutral particles passes through a so called V-target before entering the plasma. By adjusting the aperture of the V-target, collimating the beam, the injected power can be regulated.

### 3.2.2 ECRH

Two gyrotrons [Westerhof 2003], one at 110GHz and one at 140GHz, are available to inject X-mode microwave radiation into the plasma, heating the electrons by the resonant absorption of the waves at the 2<sup>nd</sup> harmonic of the electron cyclotron resonance (ECRH, electron cyclotron resonance heating). The 110GHz gyrotron has a



maximum output power of 500kW and a pulse length of 200ms. In this thesis, however, only use has been made of the 140GHz gyrotron, capable of producing 800kW of heating power and pulse lengths exceeding 3s.

The angle under which the power is injected into the plasma can be selected by rotating the front mirror of the steerable launcher. In this way, the angle of injection can be varied by  $\pm 25$  degrees vertically (elevation) and  $\pm 35$  degrees horizontally (rotation). A horizontal rotation results in non-inductive current drive (ECCD, electron cyclotron current drive). Depending on toroidal injection angle, temperature and density, non-inductive currents up to 50kA can be driven.

Main advantage of ECRH over other heating systems is the localised deposition profile. The radial deposition profile has a width in the order of a cm, enabling to accurately position the heating power and driven current at the desired radius, for example inside a magnetic island.

### 3.3 Main diagnostics used in this thesis

On TEXTOR, about 50 diagnostics are available [Donné 2005]. The most important ones for the work presented in chapters 5 till 9 are introduced in this chapter. Apart from ECE-Imaging used throughout the thesis, the charge exchange recombination spectroscopy system is used in chapter 8 to measure the ion rotation profile. The Thomson scattering system is used in chapters 8 and 9 to calibrate the ECE-Imaging system, and the density fluctuation measurements of the O-mode reflectometer are used in chapter 6 to compare with the ECE-Imaging temperature fluctuation measurements.

#### 3.3.1 ECE-Imaging

The main diagnostic used in this thesis is the Electron Cyclotron Emission Imaging (ECE-Imaging) system [Park 2003]. This 2D ECE diagnostic enables high spatial and temporal resolution measurements of the electron temperature. ECE-Imaging uses wide aperture optics to image the ECE radiation from the plasma onto a vertical 1-D array of 16 receivers. Each receiver is treated as a conventional 2<sup>nd</sup> harmonic X-mode ECE radiometer with 8 frequency channels, giving an 8 (radially) by 16 (vertically) array of sampling volumes, representing about 7 by 16 cm<sup>2</sup> in the poloidal plane of the plasma, centered on the equatorial plane. The position of the observation volume can be shifted radially. With the ECE-Imaging system one can directly explore the two-dimensional nature of plasma structures in a single measurement with a time resolution of up to 500 kHz. A detailed description of the system will be given in paragraph 4.3.

#### 3.3.2 Charge exchange recombination spectroscopy

The profile of toroidal ion rotation can be measured with the Charge Exchange Recombination Spectroscopy (CXRS) system on TEXTOR [De Bock 2007]. The

### 3 TEXTOR and its auxiliary systems

---

Doppler shift of the 529 nm  $C^{5+}$  line is a measure for the toroidal (main) ion velocity. This line is emitted by impurity carbon ions that undergo a charge exchange reaction with the neutral particles of the tangential neutral beam injector (NBI1) in the co-direction. So, CXRS data is only available when NBI is on. The time resolution of the system is limited to 50ms. The radial coverage is from the centre of the plasma to about 60% of the minor radius (at the low field side).

Apart from the toroidal ion velocity, also the ion temperature and the impurity content can be determined using this diagnostic. The width of the spectral line is a measure of the ion temperature, the intensity a measure for the density of the emitting impurity ions and, as said, the Doppler shift gives the ion velocity in the direction of the line of sight (toroidal direction).

#### 3.3.3 Thomson Scattering

The Thomson scattering diagnostic [Kantor 2001] measures the profiles of both the electron density and temperature. The light from a ruby laser, shot vertically through the plasma, is scattered by the electrons in the plasma. The spectrum of the scattered light as a function of vertical position along the laser chord is analysed. The intensity of the spectra is a measure for the electron density, the width a measure for the electron temperature.

The laser chord is horizontally offset by 9cm from the centre of the tokamak, so normally the system misses the plasma centre. The system can be used both for core and edge measurements. During core measurements, the full 90 cm laser chord is imaged onto the spectrometer, giving a spatial resolution of 7.5mm. For edge measurements, only the outer (upper) 16cm of the laser chord are imaged, with a spatial resolution of 1.7mm. In this thesis only the core system is used.

The system is designed to measure at a maximum of 10kHz during up to 3 bursts of 5 to 10ms. The current multi-pulse capability is however limited to only one burst with typically 40 laser pulses with a laser energy of about 15J each.

#### 3.3.4 O-mode reflectometer

The O-mode reflectometer on TEXTOR [Krämer-Flecken 2004] measures density fluctuations with a sampling frequency of 500 kHz. Reflectometry is based on the reflection of microwaves from a cut-off surface in the plasma. For O-mode radiation, this reflection occurs at the layer where the frequency of the probing beam equals the plasma frequency. As the plasma frequency depends on the electron density, fluctuations of the position of the cut-off surface correspond to density fluctuations. Also, by changing the frequency of the probing beam, the density (and hence the minor radius) of the reflecting layer can be selected. The TEXTOR O-mode reflectometer is tuneable between 26GHz and 37GHz, corresponding to electron densities ranging from  $0.8 \cdot 10^{19} m^{-3}$  to  $1.7 \cdot 10^{19} m^{-3}$ . The heterodyne detection system is capable of measuring both the amplitude and the phase of the received signals.

A set of five horn antennae, all positioned in the same poloidal cross section of TEXTOR, is used. Three antennae are located near the equatorial plane, 5.75 degrees poloidally apart. The middle of these three is used as the launching antenna and the other two as receivers. Two more antennae are located at the top of the vessel; one launching and one receiving antenna. The time delay of the fluctuations measured with different receiving horns can be used to derive the poloidal rotation velocity of the fluctuations.

### 3.4 The Dynamic Ergodic Divertor

TEXTOR is equipped with a tool to generate magnetic perturbation fields with known mode spectrum, amplitude and phase: the Dynamic Ergodic Divertor (DED) [Special Issue 1997]. The main motivation for building the DED was the control of the plasma-wall interaction [Finken 1997]. The DED as a divertor concept is designed to:

- Distribute the energy flux from the plasma over a large area target plate.
- Shield the plasma from impurities originating from the wall.
- More effectively exhaust particles (helium and impurities) from the plasma.

Later, it was recognised that the DED is also an ideal tool to study and control MHD instabilities like tearing modes and Edge Localised Modes (ELMs).

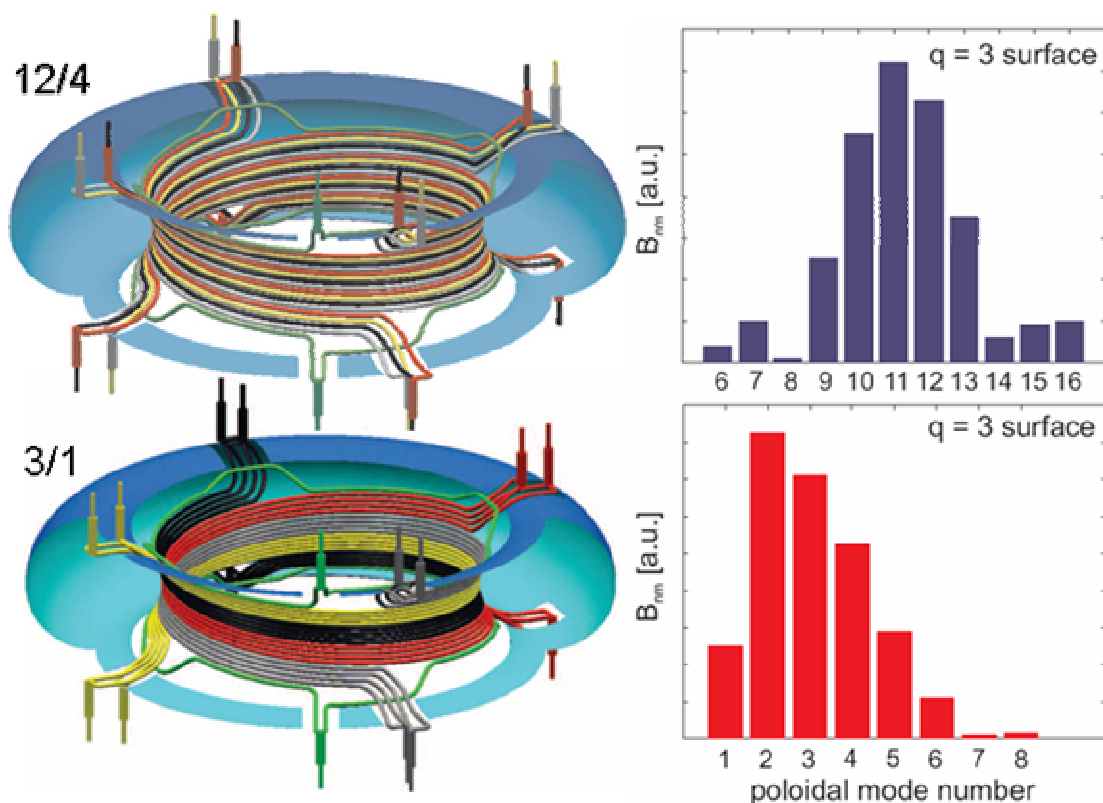


**Figure 3-1:** The DED coil configurations in the 12/4 and 3/1 modes and the corresponding mode spectra. The 16 helical perturbation field coils are located at the inboard side of the vacuum vessel. The four colours (grey, red, black and yellow) represent the four differently phased coil currents. The two compensation coils are shown in green.

### 3 TEXTOR and its auxiliary systems

---

The DED consists of 16 helical perturbation field coils, mounted on the inboard side of the vacuum vessel, see Figure 3-1. The coils are aligned with the magnetic field lines of the  $q=3$  surface. Each of the 16 coils make a full toroidal turn around the tokamak, while completing about 30% of a poloidal turn. Two more coils, the compensation coils located above and below the 16 perturbation field coils, are installed to minimize the stray field of the cable feedthroughs. At the plasma side, the coils are covered with carbon tiles, acting as divertor target plates [Giesen 1997].

The 16 coils are fed by a 4-phase current (0, 90, 180 and 270 degree phases) with a maximum amplitude of 15kA. The way the 16 coils are connected to these four differently phased currents determines the base component of the perturbation field. Three different coil configurations are possible: the so called 3/1, 12/4 and 6/2 modes, having respectively a base  $m/n=3/1$ , 12/4 and 6/2 perturbation field component. Figure 3-1 shows the coil configurations for both the 12/4 mode (upper-left) and the 3/1 mode (lower-left). In the 3/1 mode, used in chapters 8 and 9, clusters of four neighbouring coils all carry the same current. The current in the next cluster is phase shifted by 90 degrees. In the 12/4 mode, used in chapter 5, each individual coil is phase shifted by 90 degrees with respect to its neighbouring coils. The 6/2 mode is not used in this thesis, but has clusters of two coils. As the coils only cover about 30% of the poloidal circumference, the perturbation fields do not only consist of the base  $m/n$  component, but have strong side bands at other poloidal mode numbers close to  $m$ . The mode spectra for the 12/4 and 3/1 modes are shown in Figure 3-1 (upper and lower right respectively).

The DED can be operated both in DC and in AC mode. In DC mode, the perturbation field is static, while in AC mode the field rotates. Various frequencies for the AC coil currents are possible (between 2Hz and 10kHz, subject to change). In this thesis, only the DC and 1kHz options are used. Also the direction of rotation can be changed. In the so called AC<sup>+</sup> operation the field rotates toroidally clockwise, while in AC<sup>-</sup> operation it rotates counter-clockwise [de Bock 2007]. It should be noted that the DED frequency  $f_{DED}$  refers to the mode frequency, not to the rotation frequency. All components of the DED perturbation field have the same mode frequency  $f_{DED}$ , but (assuming only  $m$  differs) different poloidal rotation frequencies  $f_{\theta}=f_{DED}/m$ . The toroidal rotation frequency is  $f_{\phi}=f_{DED}/n$ , and is the same for all field components (as the base  $n$  dominates the mode spectra).

The vacuum perturbation field strength decays with decreasing minor radius, strongly depending on the poloidal mode number  $m$ : It decays like  $(r/r_{coil})^m$  for  $r < r_{coil}$ , where  $r_{coil}$  is the radius of the DED coils (see Eq. 2-17). As a result, the DED field in the 3/1 mode penetrates much deeper into the plasma as the field in the 12/4 mode. This makes the 3/1 mode (where the field has strong  $m/n=1/1$ , 2/1 and 3/1 components) most suited to study magnetic islands, see chapters 8 and 9. The 12/4 mode will have no effect further into the plasma (no islands) and is hence ideally suited for the study of the DED effects at the plasma edge, see chapter 5.

## 4 Electron Cyclotron Emission

As for this thesis ECE-Imaging is the main diagnostic, this chapter discusses the application of electron cyclotron radiation as a  $T_e$  diagnostic. After introducing the basic properties of ECE radiation in paragraph 4.1, the general principle of a heterodyne ECE radiometer is described in paragraph 4.2. Subsequently, a detailed description of the ECE-Imaging diagnostic, which can basically be regarded as an array of 16 heterodyne radiometers, is given in paragraph 4.3. The radial resolution of ECE diagnostics and their (thermal) noise levels are treated in paragraphs 4.4 and 4.5. Finally, in paragraph 4.6, a discussion on possible deviations of the measured (radiation) temperature from the electron temperature is given.

### 4.1 ECE as a local electron temperature measurement

In the presence of a magnetic field  $B$ , electrons gyrate around the field lines with the electron cyclotron frequency  $\omega_{ce}$ :

$$\omega_{ce} = \frac{eB}{m_e} \quad \text{Eq. 4-1}$$

so,  $f_{ce} = \omega_{ce} / 2\pi \approx 28 \cdot B[T] \text{ GHz}$ . The electrons emit (and absorb) electromagnetic radiation at this frequency and its higher harmonics  $n\omega_{ce}$  [Bornatici 1983]. As in a tokamak the (mainly toroidal) magnetic field  $B$  is a function of radius  $B=(B_0R_0)/R$ , also  $\omega_{ce}$  has this  $1/R$  dependence. At the  $n^{\text{th}}$  harmonic, the location of the emitting layer at frequency  $\omega$  is given by

$$R = \frac{neB_0R_0}{m_e\omega} \quad \text{Eq. 4-2}$$

Ideally (in the limit of an optically thick plasma, see paragraph 4.6), the intensity of the emitted radiation is equal to the radiation of a black body at temperature  $T_e$ . In the limit  $\hbar\omega_{ce} \ll T_e$  ( $T_e$  in J), valid for tokamaks, this intensity is given by the Rayleigh-Jeans approximation (classical limit) of Planck's radiation formula:

$$I_{BB}(\omega) = \frac{\omega^2 T_e}{8\pi^2 c^2} \quad \text{Eq. 4-3}$$

Both the spatial dependence of  $\omega_{ce}$  and the linearity of the radiation intensity with  $T_e$  offer the possibility to use ECE as a local  $T_e$  diagnostic.

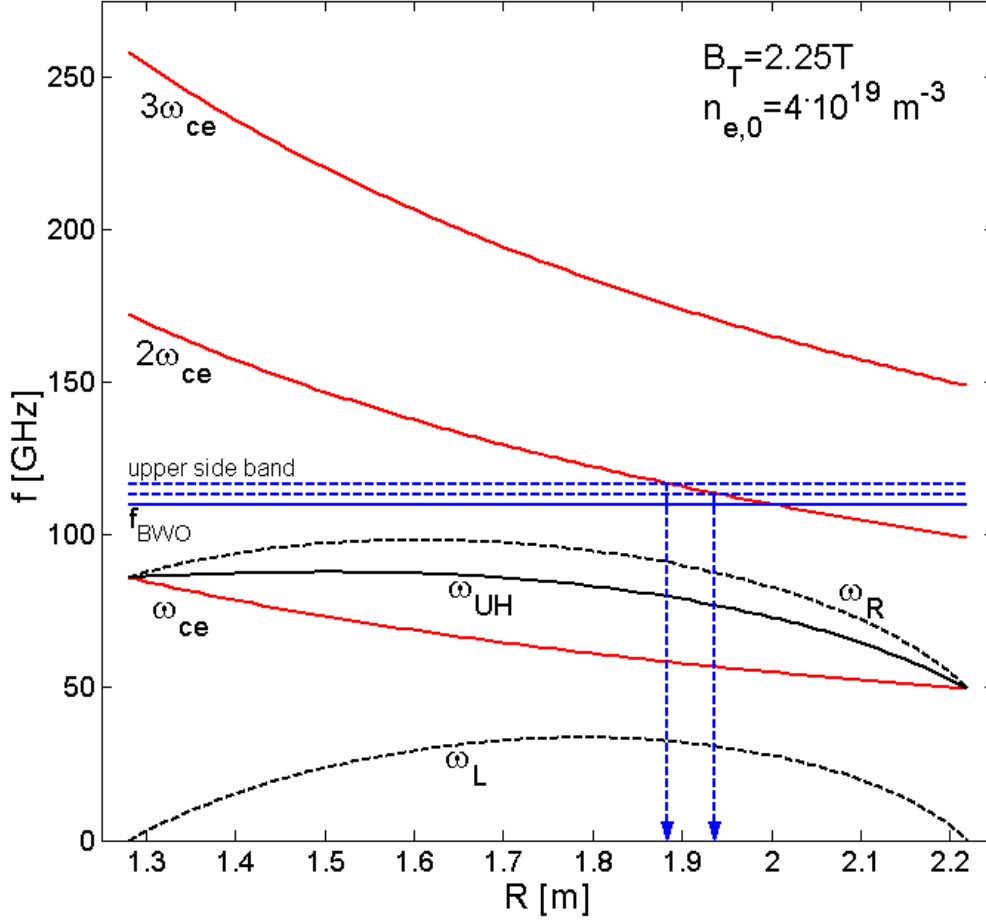


**Figure 4-1:** The characteristic frequencies for typical TEXTOR parameters ( $B_T=2.25T$ ,  $n_e=4 \cdot 10^{19} m^{-3}$ ). The  $1/R$  dependence of the ECE radiation makes a local temperature measurement possible. The first, second and third harmonic ECE radiation are shown, along with the two cut-offs ( $\omega_L$  and  $\omega_R$ ) and the resonance  $\omega_{UH}$  of X-mode radiation. X-mode radiation can not propagate below  $\omega_L$ , and between  $\omega_{UH}$  and  $\omega_R$ . An example of the frequency band (upper side band, dashed blue lines) of ECE-Imaging is shown for a local oscillator frequency  $f_{BWO}$  of 110GHz (solid blue line). In this example, the radiation of the 2<sup>nd</sup> harmonic ECE radiation from around  $R=1.9m$  can propagate freely to the observer on the low field side.

Two complications to the above discussion (which will be treated in detail in paragraph 4.4) should be mentioned:

- Plasmas are not always optically thick, leading to deviations from Eq. 4-3 and a sensitivity to density.
- The ECE emission line is broadened (mainly) by two effects; Doppler and relativistic broadening. Due to these two line broadening effects, an electron at velocity  $v$  emits and absorbs radiation with frequency [Bornatici 1983]:

$$\omega = \frac{n\omega_{ce}}{\gamma} + k_{||}v_{||} \quad \text{Eq. 4-4}$$

here  $\gamma = (1 - (v/c)^2)^{-1/2}$  is the relativistic factor, and  $k_{||}$  the parallel wave vector.

Apart from these two complications, for practical application of ECE radiation as a temperature diagnostic, the waves have to be able to propagate freely from the emitting layer to the observation point. The propagation of electromagnetic radiation in a magnetized plasma is (in the ‘cold plasma approximation’) described by the Appleton-Hartree equation, giving the real part of the refractive index  $N$  [Bornatici 1983][Hutchinson 1987]:

$$N_{O/X}^2 = 1 - \left( \frac{\omega_p}{\omega} \right)^2 \frac{2(\omega^2 - \omega_p^2)}{2(\omega^2 - \omega_p^2) - \omega_{ce}^2 (\sin^2 \theta \mp \rho)} \quad \text{Eq. 4-5}$$

$$\text{with } \rho^2 \equiv \sin^4 \theta + 4 \left( \frac{\omega^2 - \omega_p^2}{\omega \omega_{ce}} \right)^2 \cos^2 \theta.$$

Here  $\theta$  is the angle between the direction of wave propagation and the magnetic field, and the plasma frequency  $\omega_p$  is given by:

$$\omega_p = \sqrt{\frac{n_e e^2}{\epsilon_0 m_e}} \quad \text{Eq. 4-6}$$

One has to distinguish between O-mode radiation, whose electric field is oriented parallel to  $B$  (minus sign in Eq. 4-5), and X-mode radiation, whose electric field is oriented perpendicular to  $B$  (plus sign). For O-mode radiation, the electrons are induced to oscillate parallel to  $B$ , making them insensitive to  $B$ . For perpendicular propagation  $\theta = \pi/2$ , Eq. 4-5 for the O-mode reduces to:

$$N_{O,\perp}^2 = 1 - \left( \frac{\omega_p}{\omega} \right)^2 \quad \text{Eq. 4-7}$$

Like in a plasma without magnetic field, O-mode radiation has only one cut-off (where  $N$  goes to zero) at the plasma frequency  $\omega_p$ . At a cut-off surface in the plasma, radiation is reflected. No propagation is possible at frequencies below  $\omega_p$  where  $N < 0$ .

For X-mode radiation, the electrons are induced to oscillate perpendicular to  $B$ . Hence, apart from the plasma frequency  $\omega_p$ , here also the cyclotron frequency  $\omega_{ce}$  plays a role in the dispersion relation. For perpendicular propagation  $\theta = \pi/2$ , Eq. 4-5 for the X-mode reduces to:

$$N_{X,\perp}^2 = 1 - \left( \frac{\omega_p}{\omega} \right)^2 \frac{\omega^2 - \omega_p^2}{\omega^2 - \omega_{ce}^2 - \omega_p^2} \quad \text{Eq. 4-8}$$

X-mode radiation has two cut-offs  $\omega_L$  and  $\omega_R$ :

$$\omega_R = \frac{1}{2} \cdot \left[ \omega_{ce} + \left( \omega_{ce}^2 + 4\omega_p^2 \right)^{1/2} \right] \quad \text{Eq. 4-9}$$

$$\omega_L = \frac{1}{2} \cdot \left[ -\omega_{ce} + \left( \omega_{ce}^2 + 4\omega_p^2 \right)^{1/2} \right]$$

and one resonance (where  $N$  goes to infinity and radiation is either absorbed or converted to a non-propagating electrostatic oscillation) at the (upper) hybrid frequency  $\omega_{UH}$ .

$$\omega_{UH}^2 = \omega_{ce}^2 + \omega_p^2 \quad \text{Eq. 4-10}$$

X-mode radiation does not propagate at frequencies between  $\omega_{UH}$  and  $\omega_R$ , and below  $\omega_L$ . In Figure 4-1 the characteristic frequencies for perpendicular X-mode radiation are shown for typical TEXTOR parameters.

For practical application of ECE radiation as a temperature diagnostic, the waves have to be able to propagate freely from the emitting layer to the observation point (normally at the low field side), and there should be only one harmonic in the plasma emitting at that frequency. For 2<sup>nd</sup> harmonic X-mode radiation in TEXTOR (used by ECE-Imaging at frequencies between 85 and 130GHz), this means that one should stay above  $\omega_R$ , and avoid measurements very close to the high field side edge, as then the 2<sup>nd</sup> and 3<sup>rd</sup> harmonics of  $\omega_{ce}$  overlap in frequency. In Figure 4-1 an example of the situation with ECE-Imaging tuned to 110GHz is shown.

Note that for  $\omega > \omega_p$  for O-mode, and  $\omega > \omega_R$  for X-mode radiation, the index of refraction has values in the range  $0 < N < 1$  (phase velocities larger than the velocity of light), meaning the plasma bends the lines of sight slightly outward.

### 4.2 The principle of an ECE radiometer

Before describing the ECE-Imaging system, first the principle of a conventional ECE radiometer is discussed. The electronics of ECE-Imaging are basically the same as those of such a conventional radiometer. A simple (fictive) heterodyne radiometer is described in order to introduce the basic concepts like downconversion and the bandwidths  $B_{IF}$  and  $B_V$ , important for ECE-Imaging.

An ECE radiometer measures the intensity of the (microwave) radiation from the plasma in a certain frequency band. The central frequency of this band determines the location of the emitting layer in the plasma, and (to first order) the bandwidth determines the radial extent of this layer. The output signal is a measure of the intensity of the radiation in this frequency band, and is linear with  $T_e$ . By measuring the ECE intensity in a number of frequency bands (corresponding to different radii  $R$ ), the  $T_e$  profile can be determined. Wave accessibility and optical thickness normally limit the possibilities for practical application of ECE as a  $T_e$  diagnostic to only the first harmonic O-mode and second harmonic X-mode ECE radiation. For typical tokamak magnetic fields, this radiation has a frequency in the order of 100GHz. At such high frequencies, (electronic) signal processing is difficult. Therefore, the (radio frequency, RF) radiation from the plasma is downconverted to a lower frequency (intermediate frequency, IF) before further processing. A radiometer that uses such a downconversion is called a 'heterodyne' radiometer [Hartfuss 1997].

In Figure 4-2 a schematic representation of a (one channel) heterodyne ECE radiometer is shown (from [Hartfuss 1997]). The radiation from the plasma is



downconverted by mixing it with the radiation of a so called local oscillator ( $LO$ ) with frequency  $f_{LO}$ . In the mixer ( $M$ ), the sum and difference frequencies of the two sources are generated. The subsequent electronics are only sensitive to the (much) lower difference frequency. This process does not differentiate between a positive and a negative frequency difference, so a certain frequency  $f$  in the downconverted signal, corresponds to two frequencies  $f_{LO}+f$  and  $f_{LO}-f$  in the plasma (RF) signal. In Figure 4-2 (bottom right) the two side bands (upper and lower side bands) are shown, that result after band pass filtering the downconverted signal with a filter at central frequency  $f_{IF}$  and bandwidth  $B_{IF}$ . To guarantee a measurement of  $T_e$  at only one radius, one of these frequency bands generally has to be filtered out (by a side band filter  $SBF$ ) before mixing the plasma and  $LO$  signals. The bandwidth  $B_{IF}$  of the remaining side band then determines (to first order, see paragraph 4.4) the radial extent of the emitting layer in the plasma. The detector ( $S_V$ ) is basically a rectifier, converting the high frequency  $IF$  signal to a signal that is a measure for the power in the  $IF$  frequency band (the so called video signal). Finally, the signal is low pass filtered with a (video) bandwidth  $B_V$ , determining the time resolution of the radiometer. The higher frequency fluctuations in the detector signal are averaged out (resulting in a smaller noise level) to adapt the signal to the sampling frequency of the data acquisition system.

The above radiometer only measures one frequency band. Normally, radiometers have more channels, each detecting a different frequency band. This can be done by for instance splitting the signal before the  $IF$  filter  $B_{IF}$ , and filter the separate branches with different  $IF$  filters. ECE-Imaging uses a second downconversion step, mixing the  $IF$  signal with eight different  $LO$  signals, to select eight frequency bands, see the next paragraph.

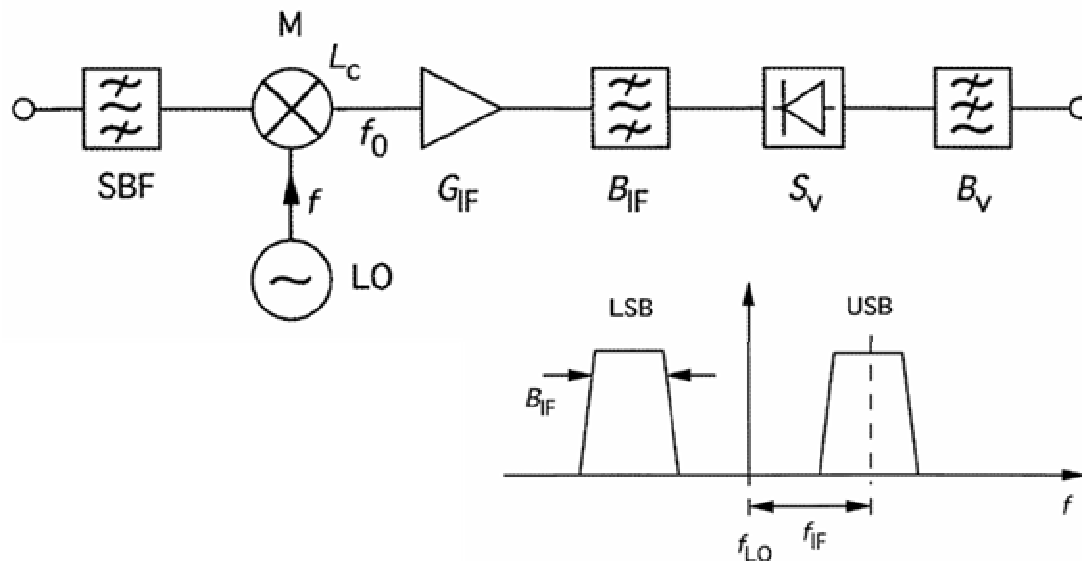


**Figure 4-2:** Schematic representation of an ECE radiometer (reproduced from [Hartfuss 1997]). The input ECE signal is mixed ( $M$ ) with the radiation of a local oscillator ( $LO$  with frequency  $f_{LO}$ ), after (optionally) filtering out one of the two side bands with a filter ( $SBF$ ). Subsequent filtering of the downconverted signal with a band pass filter with bandwidth  $B_{IF}$  and central frequency  $f_{IF}$  determines the width and frequency of the frequency band to which the radiometer is sensitive. The output of the detector ( $S_V$ ) is a measure for the power in this frequency band. Finally, the signal is low pass filtered with a bandwidth  $B_V$ , determining the time resolution of the radiometer.

### 4.3 ECE-Imaging

A conventional ECE radiometer generally consists of a horn antenna at the low field side plasma edge, receiving the ECE radiation of a single horizontal line of sight. Neglecting broadening effects, the different frequencies of this ECE radiation originate from different major radii in the plasma, due to the  $1/R$  dependence of the toroidal magnetic field. So by separating the ECE radiation into different frequency bands (of bandwidth  $B_{IF}$ ), the radiometer measures the local  $T_e$  at different radial locations along the line of sight.

The ECE-Imaging diagnostic at TEXTOR ([Park 2003],[Park 2004],[Wang 2004]) yields real time 2D measurements of the local  $T_e$ . This 2D capability is achieved by replacing the single antenna of a conventional radiometer by a vertically aligned array of 16 antennae, each observing a different horizontal line of sight (about 1cm apart) in the poloidal plane of the plasma. Each of the 16 antennae is subsequently treated as a conventional 8 channel (heterodyne) radiometer, resulting in a 2D array of 8 (radially) by 16 (vertically) sampling volumes in the poloidal plane, representing an area of approximately 7 by 16 cm.

Figure 4-3 shows the schematic setup of an ECE-Imaging system. Contrary to a conventional radiometer, the ECE-Imaging antenna array is located outside the tokamak. The ECE radiation from the plasma is observed through a large aperture vacuum window, and imaged onto the array by (refractive or reflective) optics. To facilitate the further processing of the signals, the radio frequency (rf) ECE radiation is downconverted by mixing it with the radiation of a local oscillator, resulting in a signal at the (lower) difference frequency. The local oscillator illuminates the antenna array from the back.

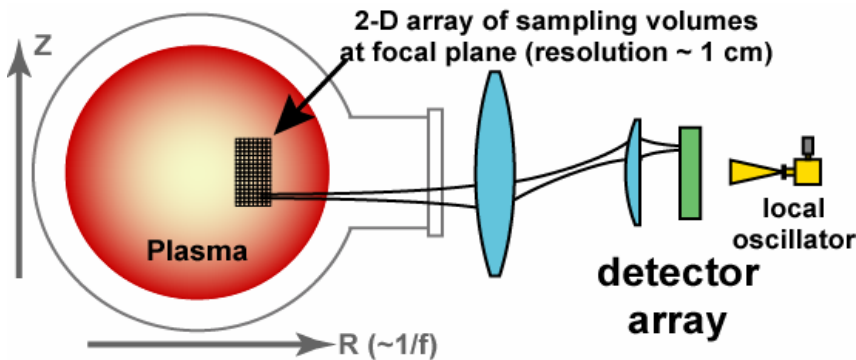


**Figure 4-3:** Schematic overview of a 2D ECE-Imaging system. An optical system images the ECE radiation from the plasma onto a vertically aligned (1-D) array of detectors. Each detector views a different horizontal line of sight in the poloidal plane of the plasma. From the back, the detectors are illuminated by a local oscillator to downconvert the signal. By treating each detector as a conventional ECE radiometer, the signals of each horizontal line of sight are split into radially separated observation volumes.

The TEXTOR ECE-Imaging system is shown in Figure 4-4. The system observes the plasma through a 42cm high, 30cm wide vacuum window, which is shared with the Thomson scattering system. The optical path of the ECE radiation is shown by the red

line. Two large cylindrical mirrors, one planar mirror and 4 lenses image the radiation onto the array. To assure the system is always in focus, the position of the focal plane in the plasma can be radially adjusted by translating the lens before the array (indicated by \*). Also, on top of this lens, a (quasi-optical) notch filter can be placed to protect the array against 140GHz stray radiation coming from the gyrotron. As local oscillator, a so called backward wave oscillator (BWO) with a tuneable frequency  $f_{BWO}$  is used. The optical path of the local oscillator radiation is shown in blue. The system is designed to observe the second harmonic X-mode ECE radiation in a 4 GHz wide frequency band (at central frequency  $f_{BWO}+5$  GHz), representing a radial section of about 7 cm in the plasma (depending on the local magnetic field gradient). By changing  $f_{BWO}$ , the ECE-Imaging system is tuneable over a frequency range of about 85 to 130 GHz. Changing  $f_{BWO}$  shifts the observation volume radially. Under normal TEXTOR operation ( $B_T=2.25$  T) this provides access to the centre and the low field side of the plasma.

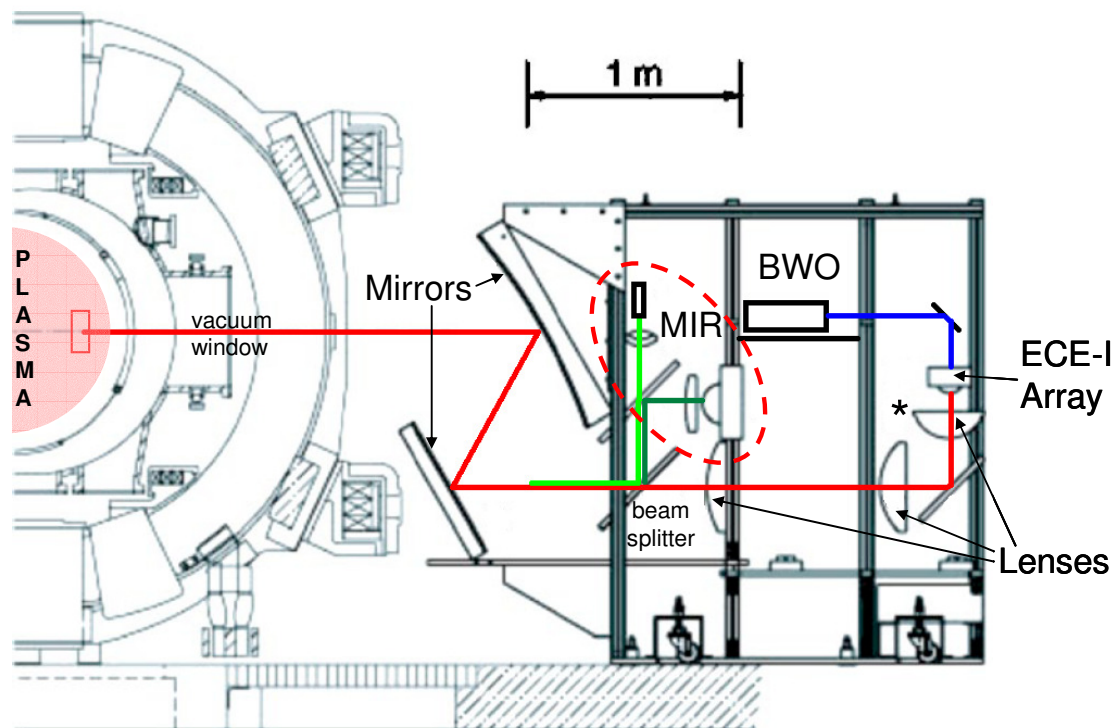


**Figure 4-4:** Layout of the combined ECE-Imaging/MIR system on TEXTOR. The optical system consists of two large cylindrical mirrors and a set of lenses. The optical paths of ECE-Imaging (red) and MIR (probing beam light green, reflected beam dark green) are separated using a beam splitter. The ECE-Imaging array is illuminated from the back (blue line) by a tuneable backward wave oscillator (BWO), which is used as local oscillator. By vertically translating the lens indicated by the asterisk (\*), the radial position of the ECE-Imaging focal plane in the plasma can be adjusted.

The two large cylindrical mirrors are shared with a second diagnostic, the Microwave Imaging Reflectometer (MIR) [Mazzucato 2001], mounted in the same frame. The optical paths of ECE-Imaging (red) and MIR (light and dark green) are separated by a beam splitter (which is normally removed if only ECE-Imaging is operated). Contrary to ECE-Imaging, MIR is an *active* microwave diagnostic; a 89 GHz probing beam

(light green) is sent into the plasma and reflected by a cut-off surface ( $\omega_R$ ), whose position in the plasma depends on both  $B$  and  $n_e$ . The reflected beam (dark green) is detected by a vertical array of 16 antennae, similar to the ECE-Imaging array. The variation of the phase of the reflected signal (with respect to the probing beam) contains information of the density fluctuations at the cut-off surface. The two cylindrical mirrors are designed to adapt the curvature of the probing beam wave front to the curvature of the cut-off surface. In this thesis, no use has been made of the MIR system, whose data proved to be difficult to interpret and very sensitive to deviations in the system alignment. Note that without the MIR system, the optical system for ECE-Imaging could have been significantly less complicated.

The spatial resolution perpendicular to the line of sight and the vertical inter-channel spacing are determined by the optics. Figure 4-5 shows the vertical focal plane patterns (vertical position with respect to the equatorial plane and width of the 16 lines of sight at the focal plane) of ECE-Imaging (measured at 115 GHz and normalised). The vertical inter-channel spacing of 11mm gives a total vertical extent of the observation volume of 16cm. This is observed to be independent of the radial position of the focal plane in the plasma, but can be influenced by refraction effect in the plasma (bending of the sight lines) as most lines of sight are located off-axis. The spot size, determining the vertical spatial resolution, is 12mm full width at half maximum for most channels. Toroidally, the spot sizes are about 9mm (FWHM) in the focal plane. It should be noted that in toroidal direction, the even channels are offset by about 8mm from the odd ones, due to the zigzag positioning of the (dual dipole) antennae on the array.

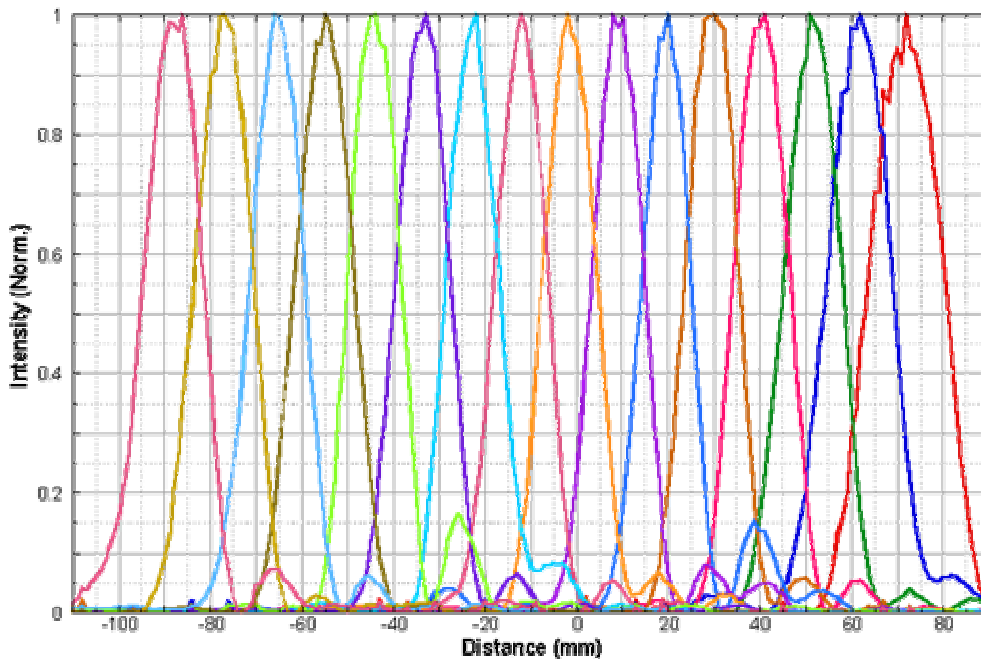


**Figure 4-5:** Vertical focal plane patterns of ECE-Imaging. The vertical inter-channel spacing is 11mm. The spot size, determining the vertical spatial resolution, is 12mm full width at half maximum for most channels.

The radial inter-channel spacing is not determined by the optics, but by the frequency difference between the adjacent ECE-Imaging channels. The radial spatial resolution

(spot size) is determined by both the bandwidth  $B_{IF}$  of the ECE radiation selected per channel, and broadening and absorption effects in the plasma described in the next paragraph. The IF bandwidth  $B_{IF}$  of 300 MHz, along with broadening effects in the plasma, leads to a radial resolution of about 1 cm.

In Figure 4-6 a schematic layout of the ECE-Imaging electronics of a single antenna is shown. The signal is downconverted two times. The first time at the array, by mixing the plasma and BWO signals. This downconverted signal is transmitted out of the TEXTOR bunker for further processing. After dividing the signal into 8 portions, these are mixed with 8 local oscillator signals (at  $f_{LO}$ =3.2, 3.8, 4.3, 4.8, 5.3, 5.8, 6.3, and 6.8 GHz) in the second downconversion step. The frequency difference between these local oscillators determines the radial inter-channel spacing of ECE-Imaging and is hence 0.5GHz. This corresponds to typically 1cm in the plasma, depending on the gradient of  $B$ . The resulting signals are band pass filtered (BPF, double sideband 5-150MHz), determining the bandwidth  $B_{IF}$  (effectively 300MHz) of the ECE radiation selected by each channel, which is important for the radial resolution of ECE-Imaging. As only the amplitude of the signal is of interest (not the frequency of the carrier wave), they are rectified by the detectors and low pass filtered (LPF). This filtering (adjustable between 70Hz and 240kHz), determines the (video) bandwidth  $B_V$  and hence the time resolution of ECE-Imaging. The bandwidth  $B_V$  corresponds to the maximum detectable fluctuation frequency. The sampling frequency is normally set to twice  $B_V$ . Finally, the signals are converted to a digital signal by 12 bit ADCs, capable of storing 2Msample per channel.

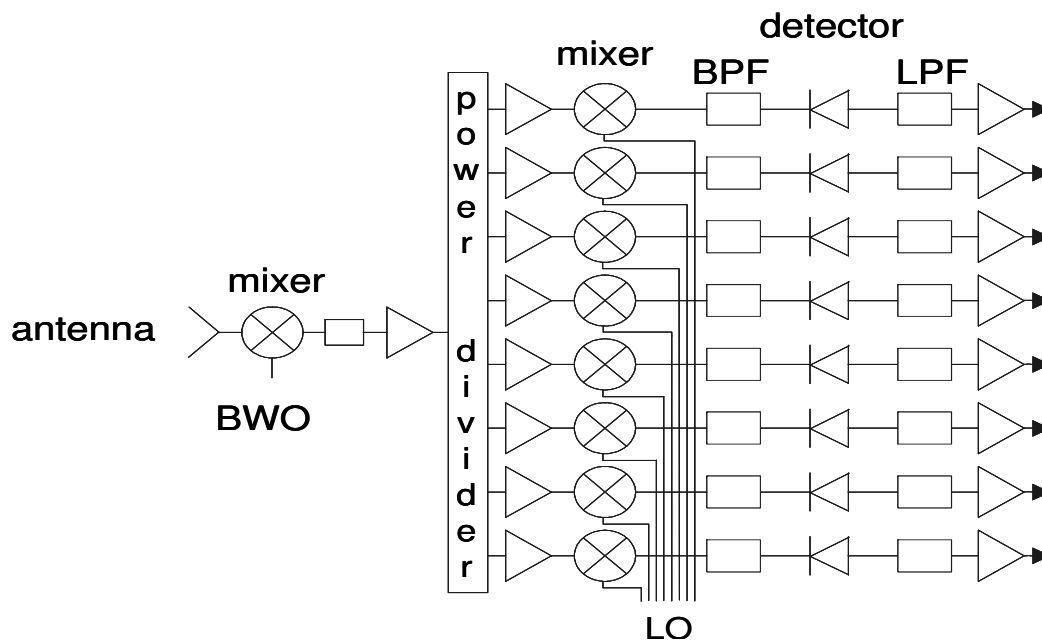


**Figure 4-6:** Schematic layout of the ECE-Imaging electronics of a single antenna. The signal is downconverted two times. The first time at the array, by mixing the plasma (antenna) and BWO signals. After dividing the signal into 8 portions, these are mixed with 8 local oscillator signals (at 3.2, 3.8, 4.3, 4.8, 5.3, 5.8, 6.3, and 6.8 GHz) in the second downconversion step. The resulting signals are band pass filtered (BPF), determining the bandwidth  $B_{IF}$  (effectively 300MHz) and hence the radial resolution of ECE-Imaging. After detection, the signals are low pass filtered (LPF), determining the (video) bandwidth  $B_V$  and hence the time resolution of ECE-Imaging.

During the second downconversion step, in principle both the signal at frequency  $f_{BWO+f_{LO}}$  (upper side-band) and  $f_{BWO-f_{LO}}$  (lower side-band) is selected. The radiation in these two side-bands originates from different regions in the plasma. This would mean that the ECE-Imaging signal would represent the average  $T_e$  over these two (radially separated) regions, which is of course unwanted. To avoid this, the lower side band is blocked by a dichroic plate (a quasi-optical high pass filter) in front of the array, with cut off frequency between  $f_{BWO}-3.2\text{GHz}$  and  $f_{BWO}+3.2\text{GHz}$ , so only the radiation in the upper side-band with frequency  $f_{BWO+f_{LO}}$  is selected.

## 4.4 Radial resolution of an ECE diagnostic

The radial resolution of an ECE radiometer is determined by both the bandwidth  $B_{IF}$  of the detected ECE radiation, and by the radial width of the (not re-absorbed part of the) emission profile. The emission profile  $j(R)$  (or  $j(\omega)$ ) is not a delta function as suggested by Eq. 4-2, but is broadened by both relativistic and Doppler broadening.

The non-zero bandwidth  $B_{IF}$ , (300 MHz for ECE-Imaging channels) results in an emitting layer of width  $\Delta R$ , determined by:

$$B_{IF} = \Delta\omega = \frac{neB_0R_0}{m_e(R + \Delta R)} - \frac{neB_0R_0}{m_eR} \approx -\frac{neB_0R_0}{m_eR^2} \Delta R \quad \text{Eq. 4-11}$$

For ECE-Imaging this is about 0.5cm. The width of the broadened emission profile  $j(\omega)$  due to Doppler  $\Delta\omega_D$  and relativistic  $\Delta\omega_{rel}$  broadening is given by [Bornatici 1983]:

$$\Delta\omega_D \approx n\omega_{ce} \frac{v_{th}}{c} |N \cos(\theta)| \quad \text{Eq. 4-12}$$

$$\Delta\omega_{rel} \approx n\omega_{ce} \left( \frac{v_{th}}{c} \right)^2 \quad \text{Eq. 4-13}$$

where  $v_{th}$  is the thermal velocity  $v_{th} = \sqrt{2T_e/m_e}$  ( $T_e$  in J). Doppler broadening also occurs for perpendicular observation  $\theta = \pi/2$ , contrary to what is suggested by Eq. 4-12, as every radiometer has a finite sensitivity to parallel radiation. Alternatively one can regard Doppler broadening for perpendicular observation as the natural line width of the ECE radiation caused by the finite transit time of an emitting electron through the observation volume. An alternative equation for  $\Delta\omega_D$ , more relevant for perpendicular observation, is given by [Sattler 1993]:

$$\Delta\omega_D \approx \frac{2\sqrt{2} \ln 2}{w_0} v_{th} \quad \text{Eq. 4-14}$$

where  $w_0$  is the waist of the Gaussian beam at the location of the resonance.

In Figure 4-7 the emission profiles  $j(\omega)$  for both Doppler and relativistic broadening are shown for  $T_e=1\text{keV}$  and  $w_0=12\text{mm}$  (which is the typical spot size of ECE-Imaging). Expressions for the line shapes are taken from [Hutchinson 1987]. Due to

the high spatial resolution of ECE-Imaging, the Doppler broadening is not negligible compared to relativistic broadening (as for many other ECE radiometers with less focused Gaussian beams). Analogously, instead of  $j(\omega)$  at fixed  $R$ , one can regard  $j(R)$  at fixed  $\omega$ . For ECE-Imaging, Doppler and relativistic broadening result in radial emission profiles with a full width at half maximum of about 1cm and 2cm respectively. As in reality the two broadening effects occur simultaneous, a total radial line width of about 3cm results.

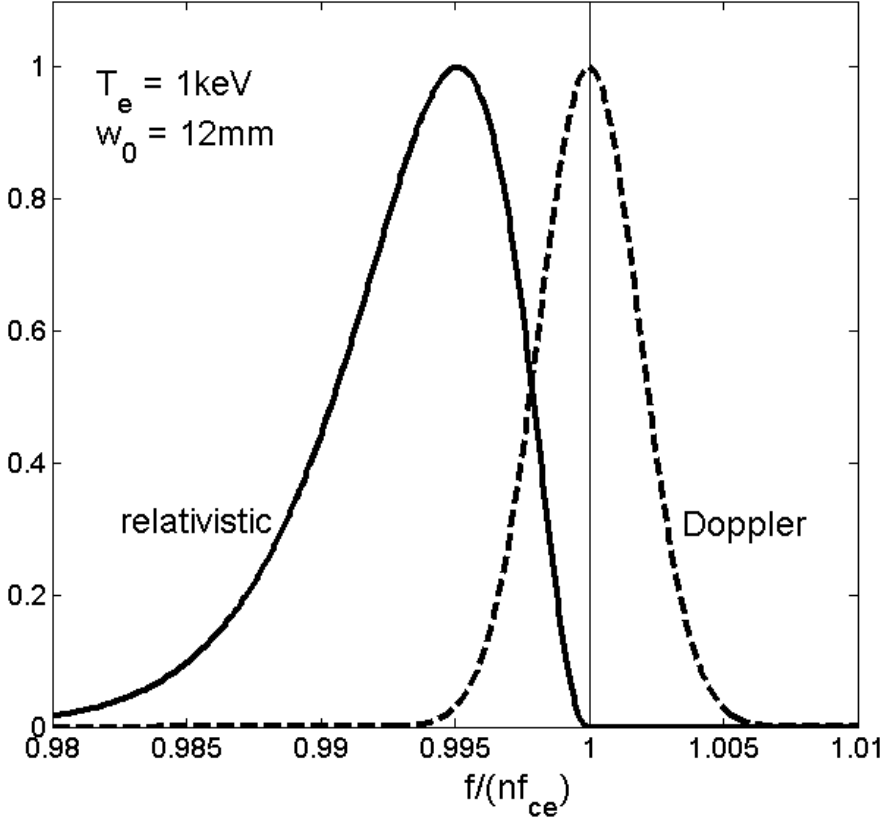


**Figure 4-7:** Relativistic and Doppler broadening of the ECE radiation for  $T_e = 1\text{keV}$  as a function of (normalised) frequency. For the Doppler broadening, the ECE-Imaging spot size  $w_0=12\text{mm}$  is used. Relativistic broadening always shifts the frequency down. Doppler broadening results in a symmetric profile with respect to  $nf_{ce}$ . In reality, both effects occur simultaneous.

To determine the radial resolution of an ECE radiometer, another effect has to be taken into account; the re-absorption of the emitted radiation. The radial resolution of an ECE radiometer (neglecting  $B_{IF}$ ) is not determined by the width of the emission profile  $j(R)$ , but by the much narrower profile of radiation that actually reaches the observer. The radiation emitted at the far side of the emission profile is largely absorbed before it reaches the observer (generally at the low field side). The radiation transport is governed by the following differential equation [Bekefi 1966]:

$$N^2 \frac{d}{ds} \left( \frac{I(\omega)}{N^2} \right) = j(\omega) - \alpha(\omega)I(\omega) \quad \text{Eq. 4-15}$$

## 4 Electron Cyclotron Emission

where  $\alpha(\omega)$  is the absorption coefficient. In thermal equilibrium, the intensity  $I(\omega)$  is equal to the black body intensity  $I_{BB}$ . So, the emission and absorption coefficients are related by [Hutchinson 1987]

$$\frac{j(\omega)}{\alpha(\omega)} = I_{BB}(\omega) \quad \text{Eq. 4-16}$$

known as Kirchhoff's law. So the absorption profile has the same shape as the emission profile (also radially, assuming the variation in  $T_e$  over the emission profile is negligible).

A measure for the total absorption of the plasma is the optical thickness  $\tau$ , defined as [Bornatici 1982]:

$$\tau(\omega) = \int_0^l \alpha(\omega) ds \quad \text{Eq. 4-17}$$

where the integration goes over the full length  $l$  of the line of sight through the plasma. If  $\tau \gg 1$ , the plasma is fully absorbing, and the emitted radiation is equal to the black body radiation. If  $\tau$  is small, the emitted intensity is reduced to  $I_{BB}(1 - \exp(-\tau))$ , and the plasma no longer fully absorbs the incident radiation but only attenuates it by a factor  $\exp(-\tau)$ . The optical thickness is an important parameter for the interpretation of ECE measurements, see paragraph 4.6. For perpendicular observation ( $\theta = \pi/2$ ), the optical thickness for both O and X-modes are given in Table 4-1 [Bornatici 1982]. Note that  $\tau$  is both a function of  $T_e$  and  $n_e$  (through  $\omega_p$ ).

**Table 4-1:** Optical thickness for perpendicular observation ( $\theta = \pi/2$ ,  $T_e$  in J).

X-mode 1 <sup>st</sup> harm.	$\tau_1^X = \frac{5\pi}{\sqrt{2}} \left( \frac{\omega_{ce}}{\omega_p} \right)^2 \left( \frac{T_e}{mc^2} \right)^2 \frac{\omega_{ce} R}{c}$
X-mode nth harm. $n \geq 2$	$\tau_n^X = \frac{\pi n^{2(n-1)}}{2^n (n-1)!} \left( \frac{\omega_p}{\omega_{ce}} \right)^2 \left( \frac{T_e}{mc^2} \right)^{n-1} (N_{X,\perp})^{2n-3} \left[ 1 + \frac{(\omega_p / \omega_{ce})^2}{n[n^2 - 1 - (\omega_p / \omega_{ce})^2]} \right]^2 \frac{\omega_{ce} R}{c}$
O-mode nth harm.	$\tau_n^O = \frac{\pi n^{2(n-1)}}{2^n (n-1)!} \left[ 1 - \left( \frac{\omega_p}{n\omega_{ce}} \right)^2 \right]^{n-1/2} \left( \frac{\omega_p}{\omega_{ce}} \right)^2 \left( \frac{T_e}{mc^2} \right)^n \frac{\omega_{ce} R}{c}$

To determine the portion of the emission profile  $j(R)$  that reaches the observer, a parameter closely related to  $\tau$  is useful,  $\tau(R)$ , defined as

$$\tau(R) = \int_{R_{\text{observer}}}^R \alpha ds \quad \text{Eq. 4-18}$$

where the integration goes from the location of the observer to  $R$ . The radial profile of the radiation that reaches the observer is now given by  $j(R)e^{-\tau(R)}$ . Figure 4-8 shows the construction of this 'last layer', which is typically less than 1cm wide for a wide range of plasma parameters [Sattler 1993]. An approximate expression for the width



$\Delta R_{last}$  of the last layer, valid for 2<sup>nd</sup> harmonic X-mode radiation and  $\tau_2^X > 3$  is given by [Clark 1983]:

$$\Delta R_{last} = F(\tau_2^X) \frac{T_e}{m_e c^2} R \quad \text{Eq. 4-19}$$

$$F(\tau_2^X) = \frac{1.814}{(\tau_2^X)^{2/7}} + \frac{0.804}{(\tau_2^X)^{4/7}} + \frac{0.57}{(\tau_2^X)^{6/7}}$$

The overall radial resolution of an ECE radiometer is now given by the convolution of the broadened profiles due to the finite  $B_{IF}$  (width  $\Delta R$ ) and the last layer (width  $\Delta R_{last}$ ). For ECE-Imaging, both normally have a width of the order of 0.5cm, resulting in a typical radial resolution better than 1cm. Note that at low  $\tau$ , the radial resolution will get worse, as the last layer becomes broader.

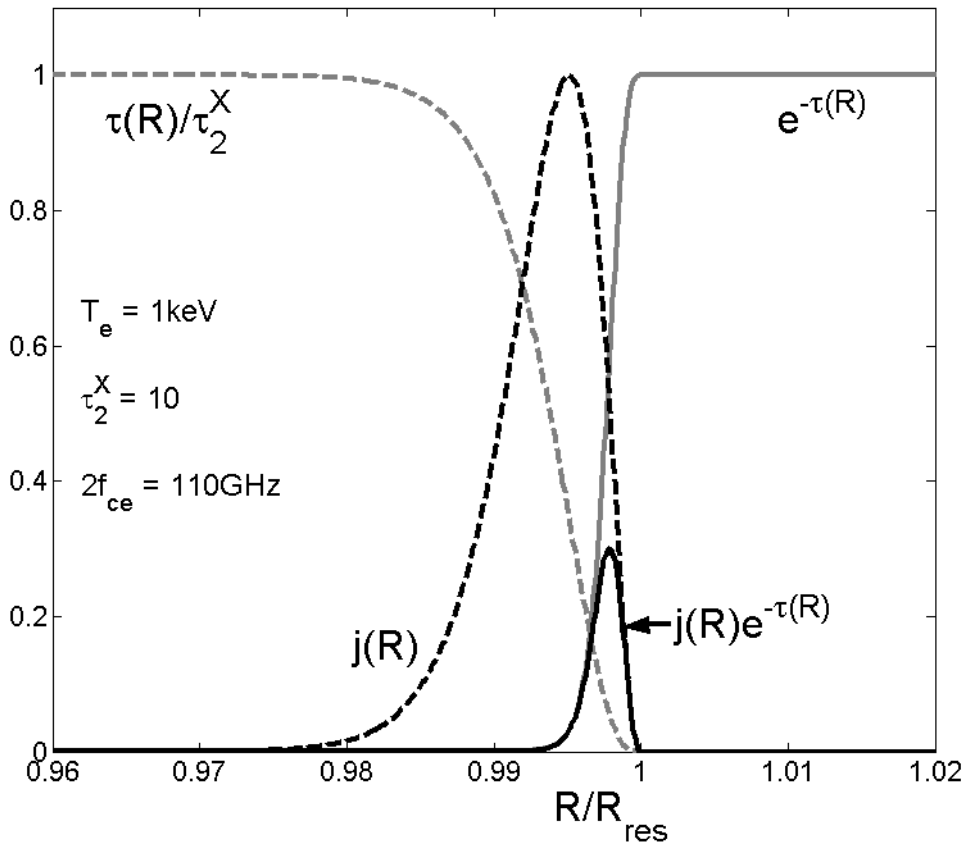


**Figure 4-8:** Construction of the ‘last layer’. The radial resolution of an ECE diagnostic is not determined by the width of the total emission profile  $j(R)$  (dashed black line, here only showing the relativistic broadening), but by the part of  $j(R)$  that actually reaches the observer. The part of  $j(R)$  furthest away from the observer is largely reabsorbed, by a factor  $1 - \exp[-\tau(R)]$ . The dashed gray line gives (the normalised)  $\tau(R)$ , the solid grey line  $e^{-\tau(R)}$ . For a wide range of plasma parameters (here  $T_e = 1\text{keV}$ ,  $\tau_2^X = 10$  at  $2f_{ce} = 110\text{GHz}$ ), the width of the last layer  $j(R)e^{-\tau(R)}$  is less than 1cm (solid black line).

## 4.5 Thermal noise

The signal of an ECE radiometer always fluctuates, due to the statistical nature of the emission process. The ECE radiation consists of a large number of incoherent waves, emitted by a plasma in thermal equilibrium. The beating of these waves results in the so called ‘thermal’ noise, which is unavoidable and an intrinsic property of ECE radiation. Normally, this noise dominates over all other noise sources caused by (imperfections of) the diagnostic. The thermal noise level is primarily determined by the bandwidths  $B_V$  and  $B_{IF}$  of the ECE radiometer [Bekefi 1966],[Hartfuss 1997]:

$$\frac{\sqrt{\langle dT_R^2 \rangle}}{\langle T_R \rangle} = \sqrt{\frac{2B_V}{B_{IF}}} \quad \text{Eq. 4-20}$$

Remember that  $B_V$  determines the time resolution of an ECE radiometer and that the radial resolution is (primarily) determined by  $B_{IF}$ . So there is a trade-off between spatiotemporal resolution and noise level. Increasing  $B_V$  (better time resolution) or decreasing  $B_{IF}$  (better spatial resolution) increases the relative thermal noise level.

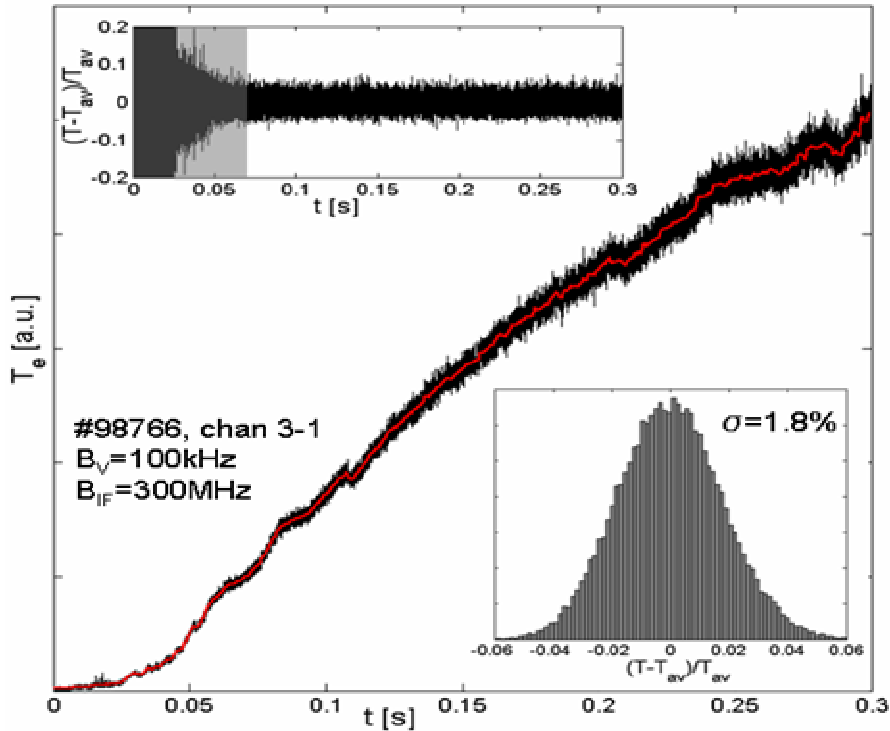


**Figure 4-9:** The experimentally observed thermal noise level of ECE-Imaging. The relative noise level  $[(T - T_{av})/T_{av}]$  shown in the upper left graph is independent of the signal level, as seen here during the first 0.3s of TEXTOR discharge 98766 (a ‘normal-shot’, using ECE-Imaging channel 3-1). Only at very low signal level (first 0.05s), the relative noise level is enhanced due to a small base noise level of the ECE-Imaging electronics (grey shaded area). During this first 0.3s no mode activity was detected, so the fluctuations are predominantly due to the thermal noise. The relative fluctuations (for  $0.1s < t < 0.3s$ ) have the expected Gaussian distribution around the central  $T_e$  (red line), as shown by the lower right histogram. The root-mean-square value of the relative fluctuations is 1.8%. This is somewhat less than the expected value of 2.5% from Eq. 4-20.

Note that the thermal noise is a purely classical effect and is not caused by shot noise due to the limited number of photons. Shot noise would result in a relative noise level that becomes smaller at higher ECE intensities. Thermal noise, however, results in a noise level that is independent of the signal level. This is also clearly seen in the experimental ECE-Imaging data, of which Figure 4-9 gives an example. No (clear) mode activity was observable in this time trace, so the fluctuations around the moving average  $T_{av}$  (red line) can be assumed to be due to the thermal noise. The relative noise level  $[(T-T_{av})/T_{av}]$  shown in the upper left graph] is independent of the signal level, except for very low signal levels where the relative noise level is enhanced due to a small base noise level of the ECE-Imaging electronics (grey shaded area). The relative fluctuations (for  $0.1s < t < 0.3s$ ) have the expected Gaussian distribution around the central  $T_{av}$ , as shown by the lower right histogram. The experimentally observed noise level of 1.8% is somewhat smaller than the prediction of 2.5% of Eq. 4-20 taking  $B_{IF}=300$  MHz and  $B_V=100$  kHz. The discrepancy could be caused by the non-ideal video filter  $B_V$ , which is only a first order filter and deviates significantly from the sharp filter assumed in the derivation of Eq. 4-20.

### 4.6 Radiation temperature versus electron temperature

Ideally, the measured ECE intensity is a direct measure for the local  $T_e$ . In reality, a number of effects can lead to deviations between the measured radiation temperature  $T_R$  and the electron temperature  $T_e$ . The effects of a non-fully absorbing plasma (so small  $\tau$ ) are described, important for the interpretation of the experimental results presented in chapters 5 and 6. Finally, some other possible sources of deviations are shortly mentioned.

Only in optically thick plasmas ( $\tau \gg 1$ ) does the measured radiation intensity reach the Rayleigh-Jeans intensity, and is consequently only a function of electron temperature. In optically thin plasmas the measured radiation temperature  $T_R$  can be expressed as [Bornatici 1983]:

$$T_R = T_e \frac{1 - e^{-\tau}}{1 - R_W e^{-\tau}} \quad \text{Eq. 4-21}$$

where  $R_W$  is the wall reflection coefficient. Radiation reflected from the back wall of the tokamak passes through the resonant layer again and contributes to the radiation intensity  $I$ . Note that this reflected wall component consists of radiation originating from the full vertical extent of the radiating layer, and hence represents a vertically averaged  $T_e$  [Bornatici 1983]. On TEXTOR, the wall reflectivity  $R_W$  is measured to be about 0.7 [Udintsev 2003], although it should be noted that the (stainless steel) inner tokamak wall has been covered by carbon tiles in the mean time, probably having a smaller  $R_W$ .

If one is only interested in the average value of  $T_e$ , a plasma can be called optically thick if  $\tau \gg 2$ . For *fluctuations* of  $T_e$ , a higher value of  $\tau$  is desirable. Since the optical thickness  $\tau$  is a function of both  $n_e$  and  $T_e$ , not only temperature fluctuations  $dT_e$ , but also density fluctuations  $dn_e$  will result in fluctuations of  $T_R$ . Neglecting wall

## 4 Electron Cyclotron Emission

---

reflections for simplicity ( $R_W=0$ ) and assuming  $T_R = (T_e + dT_e)(1 - e^{-\tau})$  and  $\tau \sim (n_e + dn_e)T_e$ , the contributions from  $dT_e$  and  $dn_e$  to the measured fluctuations  $dT_R$  can be estimated. A first order approximation gives [Sattler 1993]:

$$\frac{dT_R}{\langle T_R \rangle} = (1 + a) \frac{dT_e}{\langle T_e \rangle} + a \frac{dn_e}{\langle n_e \rangle} \quad \text{with} \quad a = \frac{\tau \cdot \exp(-\tau)}{1 - \exp(-\tau)} \quad \text{Eq. 4-22}$$

here  $\langle \rangle$  denotes an average and the factor  $a$  is always positive. For example, for  $\tau=2$   $a=0.31$  so about 30% of the density fluctuation level is seen in  $T_R$ . For  $\tau > 6$  density fluctuations hardly influence  $T_R$ . If the density and temperature fluctuations are in phase, the fluctuation amplitude inferred from  $T_R$  is an overestimation of the electron temperature fluctuation amplitude. So for fluctuations, a more stringent lower limit  $\tau > 6$  should be utilised to regard a plasma as being optically thick.

Apart from optical thickness effects, deviations of  $T_R$  from  $T_e$  can be caused by e.g.:

- **Finite sampling volume size:**  $T_R$  is an average of  $T_e$  over the sampling volume. Also, fluctuations with a wavelength comparable to or smaller than the sampling volume size will be attenuated.
- **Velocity distribution effects:** An ECE radiometer is sensitive only to a selection of the full (ideally Maxwellian) electron velocity distribution, because part of the radiation is absorbed before reaching the observer. Deviations from a Maxwellian velocity distribution (for instance due to the presence of a suprathermal electron population) then lead to deviations between  $T_R$  and  $T_e$ . The radiation of a population of fast electron can also be downshifted in frequency so much that it overlaps with the next lower harmonic.
- **Line bending:** Outward bending of the observation line occurs due to the variation in refractive index ( $0 < N < 1$ , see paragraph 4.1) Changes in the density profile can lead to vertical oscillations in the position of the observation volume, leading to fluctuations in  $T_R$  (see for instance [Clark 1983]).
- **Magnetic field fluctuations:** Fluctuations in  $B$  lead to a radially fluctuating position of the sampling volume, resulting in  $T_R$  fluctuations (see for instance [Sattler 1993]). This effect is normally negligible.

## 5 2D edge temperature profile during DED 12/4 operation

### 5.1 Introduction

In chapters 8 and 9, the Dynamic Ergodic Divertor (DED) will be used as a tool to generate and influence magnetic islands. The DED was however mainly built as a tool to influence the magnetic field at the plasma edge in order to control the flow of heat and particles towards the wall. The application of the DED perturbation field results in the creation of the so called ergodic and laminar regions in the vacuum magnetic field at the plasma edge. In the ergodic region, the magnetic field lines display chaotic behaviour, no longer staying on a flux surface, but filling up a volume. The laminar zone is located directly at the edge, where the perturbed field lines intersect the wall. Here, the field lines have a short wall-to-wall connection length and don't stay in the plasma long enough to display the chaotic behaviour as in the ergodic region. In the laminar zone a very complex structure of interwoven flux tubes with different wall-to-wall connection lengths exists.

In this chapter, 2D ECE-Imaging measurements of the edge electron temperature during DED 12/4 operation are presented. In the 12/4 DED coil configuration, each of the 16 DED coils at the high field side carry currents that are 90 degrees phase shifted with respect to the neighbouring coils. This current configuration results in a perturbation field with a base  $m=12$ ,  $n=4$  mode structure. Due to the limited poloidal extent of the DED coils, the perturbation field has strong side bands at other  $m$  values close to 12. Because perturbation fields (in vacuum) decay as  $(r/r_{coil})^m$  for  $r < r_{coil}$ , the 12/4 perturbation field is only noticeable near the plasma edge (in contrast to the low  $m$  perturbation field in the DED 3/1 configuration used in chapters 8 and 9). Both DC and AC DED currents are possible.

The 2D capability of ECE-Imaging is used to investigate the edge temperature profile during DED operation. The questions to be answered in this chapter are:

- Do we see an effect of the DED on the edge temperature profile? More specific, do we see a 2D structure as expected from calculations of the edge magnetic field? If yes, do experiment and theory show the same structures?
- How has the edge transport changed due to the DED, so how have the temperature gradients changed?
- How controllable is the edge temperature profile? Do we see the expected strong influence of the value of  $q$  at the edge ( $q_a$ )?

If the last question can be positively answered, this would confirm the value of the DED as a versatile tool to control and investigate the plasma surface interaction. To answer these questions, two types of plasma discharges are used. For the investigation

of the transport changes, the DED and non-DED phases were compared in plasmas with otherwise constant plasma parameters. For the investigation of the 2D structure of the edge (and its evolution), discharges with a ramped plasma current were used.

## 5.2 The vacuum field edge properties.

This paragraph reviews the literature on the properties of the plasma edge during DED operation. Based on the calculations of the magnetic field structure using the Atlas code [Jakubowski 2004], one can differentiate between three regions in the plasma: the laminar, ergodic and regular regions.

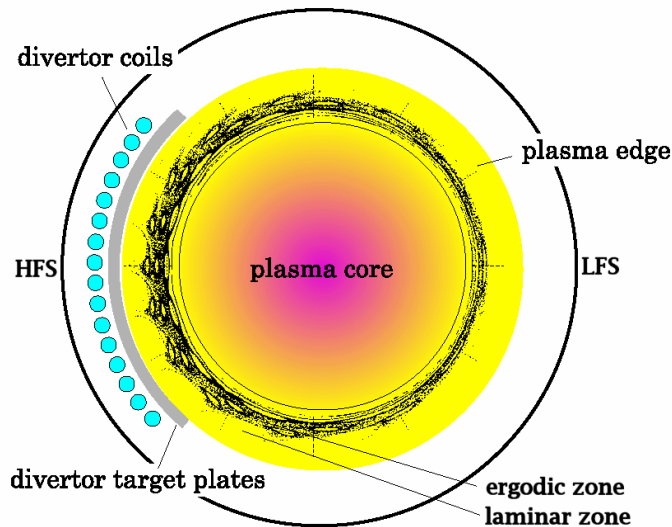


**Figure 5-1:** Schematic representation of the DED coils and the main plasma regions. In the 12/4 configuration, the 16 coils at the high field side carry currents with 90 degree phase increments with respect to the neighbouring coils. This coil arrangement results in a perturbation field with a main  $m/n=12/4$  component (resonant with  $q=3$ ). Because the coils only cover part of the poloidal circumference, also strong components at different poloidal mode numbers  $m$  are generated (mainly  $m=9, 10, 11, 13$  and  $14$ ). Deeper in the plasma, magnetic islands in the vacuum field are created at the resonant  $q$  surfaces. If the islands on two neighbouring resonant surfaces (for instance  $q=10/4$  and  $11/4$ ) are big enough to overlap, the magnetic field becomes chaotic. This region is called the ergodic zone. Closer to the edge in the laminar region, the field lines intersect the wall (the divertor target plates). Inside the plasma core, the perturbation field in the 12/4 configuration (decaying with  $r^m$ ) has no noticeable influence anymore. (Adapted from [Jakubowski 2004]).

In Figure 5-1, a schematic representation of the DED coils and the main plasma regions during DED 12/4 operation is shown. When the DED is switched on, the vacuum magnetic field topology changes drastically. At the resonant surfaces ( $q=10/4, 11/4, \dots$ ) island chains appear in the vacuum field. These islands grow with increasing DED coil current [ $w$  scales with  $(I_{DED})^{1/2}$ ]. When neighbouring island chains start to overlap, the field lines start to behave chaotically, no longer staying on one flux surface, but filling up a volume. This plasma region is referred to as the ergodic region. The amount of overlap between two island chains can be quantified by

the Chirikov parameter [Chirikov 1979] which is simply defined as the average width of the two island chains divided by the distance between the two island chains. Ergodicity of the field lines arises when the Chirikov parameter is larger than about 1.

Closer to the edge, the near field of the DED coils is dominant, resulting in perturbed field lines that intersect the wall (the divertor target plates). These open field lines have short wall-to-wall connection lengths  $L_C$ , defined as the length of a field line in the plasma between the two points where it intersects the wall, normally given in units of poloidal turns (which is  $q2\pi R_0$  m). A complicated interwoven structure of flux tubes with different  $L_C$  exists. This plasma region is referred to as the laminar zone.

Deeper inside the plasma, the effect of the DED is no longer noticeable. This region will be referred to as the regular zone.

In terms of field line topology, the laminar and ergodic regions can be defined by the ratio of the connection length  $L_C$  to the Kolmogorov length  $L_K$ . The latter is a characteristic length for the divergence of neighbouring field lines. Starting with two field lines a distance  $d$  apart, after moving one Kolmogorov length parallel along these field lines, the distance has (on average) increased to  $e$  times  $d$ . In the laminar zone  $L_C \ll L_K$ , inhibiting ergodic field line behaviour. In the ergodic region  $L_C$  is of the same order of, or longer than,  $L_K$ , making the magnetic topology ergodic.  $L_K$  can be determined by field line tracing, see below, and is found to be typically 15m (at a Chirikov parameter of 1) [Kobayashi 2004].

So called Poincaré and laminar plots are used to visualise the ergodic and laminar regions. These plots are generated using a set of computational tools called the ‘Atlas code’ [Abdullaev 2003],[Jakubowski 2004]. This code calculates the trajectories of individual field lines in the perturbed magnetic field configuration. For this purpose, the field line equation in Hamiltonian form is used. The trajectory of a field line is determined by

$$\frac{dx}{d\tau} = \frac{\mathbf{B}}{|\mathbf{B}|} \quad \text{Eq. 5-1}$$

where  $\mathbf{x}(\tau) = (r(\tau), \theta(\tau), \phi(\tau))$ , and  $\tau$  is a distance along the field line. Following [Abdullaev 2003], this equation can be reformulated in Hamiltonian form by introducing a new coordinate system, such that  $\mathbf{x} = \mathbf{x}(\psi, \vartheta, \phi)$ . Instead of the minor radius, now the toroidal flux  $\psi$  is used. The intrinsic poloidal angle  $\vartheta$ , is defined such that the pitch angle of a field line is constant over the flux surface. The magnetic field is given by:

$$\mathbf{B} = \nabla\psi \times \nabla\vartheta + \nabla\phi \times \nabla H \quad \text{Eq. 5-2}$$

and the field line equation Eq. 5-1 can now be expressed as:

$$\frac{d\vartheta}{d\phi} = \frac{\partial H}{\partial \psi}, \quad \frac{d\psi}{d\phi} = -\frac{\partial H}{\partial \vartheta} \quad \text{Eq. 5-3}$$

where  $H$  is the Hamiltonian. The equilibrium magnetic field is described by a Hamiltonian  $H_0$  that is only a function of  $\psi$ . The full Hamiltonian describing the perturbed magnetic field can be expressed as:

$$H = H_0(\psi) + \varepsilon H_1(\psi, \vartheta, \phi) \tag{Eq. 5-4}$$

where  $H_1$  is the perturbed Hamiltonian describing the DED perturbation field.  $H_1$  is periodic in both  $\vartheta$  and  $\phi$ , and  $\varepsilon$  is a small dimensionless parameter.

The magnetic field structure can be visualised in a Poincaré plot. Such a plot is generated by selecting a poloidal cross section and a collection of (starting points of) magnetic field lines. These field lines are followed on their numerous toroidal turns around the torus, and every time a field line intersects the poloidal cross section, this is marked by a point. Instead of calculating the entire field line trajectories by integrating the field line equation Eq. 5-3, a more practical (so called symplectic) mapping has been developed [Abdullaev 2003]. Figure 5-2 gives an example of such a Poincaré plot. Poincaré plots are ideal to visualise the ergodic regions, showing the island chains and ergodic field lines.

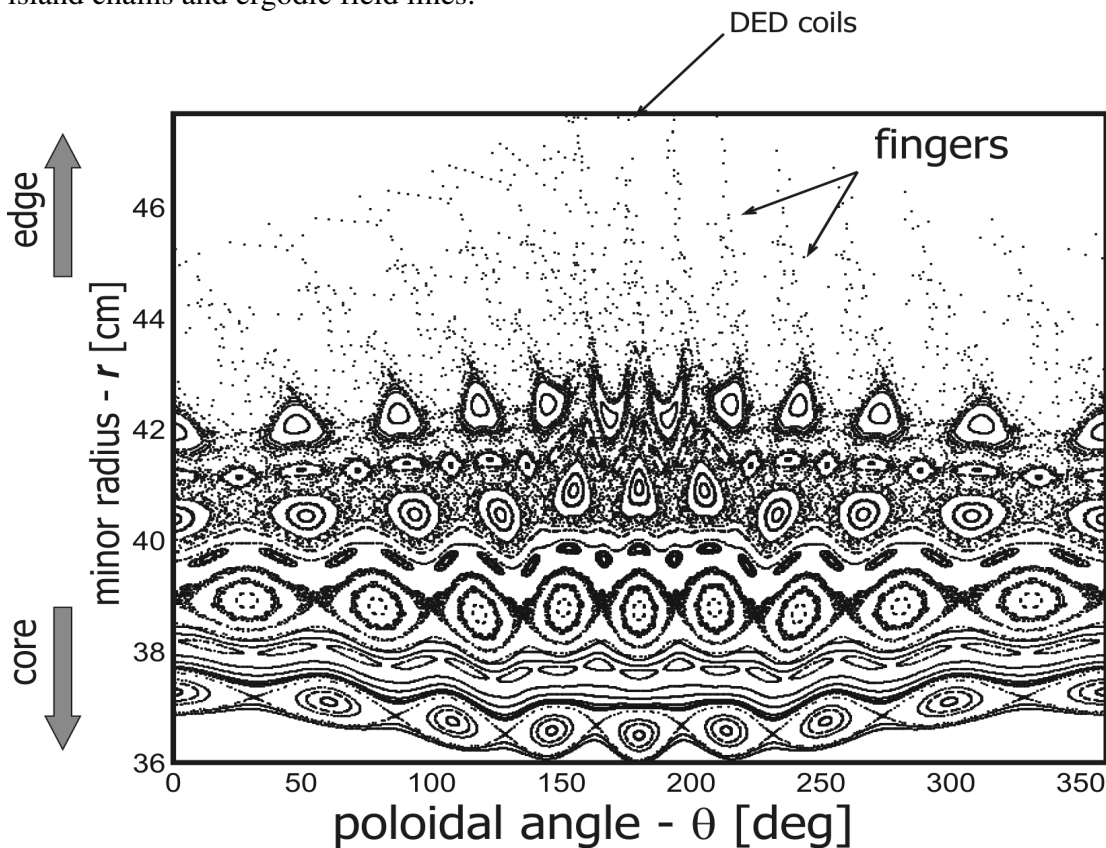


**Figure 5-2:** Example of a Poincaré plot, clearly showing the chains of magnetic islands at the various resonant surfaces. In the regions of overlap (here in particular around  $r=41\text{cm}$ ) the field lines fill up a volume. In the laminar region not a lot of points are visible, as they leave the plasma after a small number of poloidal turns. The laminar zone is characterized by finger-like structures of relatively long connection length (Adapted from [Jakubowski 2004]).

The laminar region is not clearly visible in a Poincaré plot, because the field lines in this region leave the plasma after a small number of toroidal turns, and hence leave only a few points on a Poincaré plot. To visualise the laminar region, so called laminar plots are used. These laminar plots are derived directly from the Poincaré



plots. They show the wall-to-wall connection length  $L_C$  (in units of poloidal turns) of the traced field lines. The distribution of the regions with different connection lengths in the poloidal cross section is represented by marking these regions with different colours. Examples of such laminar plots can be seen in Figure 5-3(e-h).

The topology of the DED induced structures and the level of ergodisation are mainly determined by the  $q$ -profile (positions of the resonant surfaces  $q_a$ ) and the plasma pressure, expressed in  $\beta_{pol}$ . With increasing  $\beta_{pol}$  the Shafranov shift enlarges the distance between resonant surfaces on the HFS near the DED coils. This leads to less overlap between the DED induced island chains (smaller Chirikov parameter), and hence less ergodisation. Also,  $\beta_{pol}$  influences the pitch angle of the field lines.

The existence of an ergodic region where the field lines behave chaotically and fill up a volume depends on the presence of overlapping island chains. In the vacuum magnetic field, represented by Poincaré plots, indeed overlapping islands and chaotic field lines can be seen. However, the magnetic field topology in the presence of a (conducting) plasma can be, and probably is, significantly different from the vacuum topology. This will also be seen in chapter 8, where only above a certain threshold in DED current a  $m/n=2/1$  magnetic island is seen to be destabilized. Before destabilization, no island is present, despite the fact that the vacuum field has an island. Even after destabilization, the island differs from the vacuum island; it is larger and has a (small) phase shift. The reason for this discrepancy is the shielding current at the rational surface, which tries to cancel the externally applied perturbation field. This current totally shields the inside of the rational surface for the perturbed field. Whether an island is destabilized or not, depends on the relative rotation between the plasma and the perturbation field. If the difference in rotation becomes zero, the island is destabilized and growth to a width determined by the stability parameter  $\Delta'$  (can be both larger and smaller than the vacuum island width). So the conclusion is that in the presence of a plasma, the vacuum field plots can not be expected to give a realistic picture of the actual magnetic field structure. All components of the DED field that have a corresponding (intact) resonant surface in the plasma will generate a shielding current. As long as there is a difference in rotation, the chains of vacuum islands, as seen in Poincaré plots will be suppressed. Ergodic regions in the plasma *can* occur, but only when the *actual* magnetic field structure has overlapping island chains.

In the laminar zone the field is dominated by the near field of the DED coils, resulting in field lines that intersect the wall. Here, no shielding currents are possible and the actual magnetic field can be expected to be close to the vacuum field. So it can be expected that the vacuum field calculations give a good impression of the laminar region. It is in the laminar region, where the most pronounced effects of the perturbed field on transport are expected.

### 5.3 Edge transport during DED operation

The transport of heat and particles in the perturbed region is a balance between perpendicular (collisional or turbulent) transport and parallel transport (convection/conduction along field lines). As the perturbed magnetic field lines have a radial component, both parallel and perpendicular transport can cause a radial loss of

heat and particles. The very complex structure of the edge magnetic field makes it difficult to (analytically) estimate the transport levels. The plasma edge during DED has a complicated (fractal) magnetic structure with entwined field lines of short and long connection length. In particular, long thin ergodic ‘fingers’ (see Figure 5-2), surrounded by laminar regions, connect the ergodic region with the wall. Whether a plasma region behaves ergodic, laminar or regular is determined by the ratios between the three parallel length scales that play a role:

- The Collision length,  $\lambda_e \approx \lambda_i \approx 850(T_e^2/n_e)$ , ( $T_e$  in keV,  $n_e$  in  $10^{19}\text{m}^{-3}$ ) [Wesson 1997], typically 10m (at  $T_e=100\text{eV}$  and  $n_e=1\cdot 10^{19}\text{m}^{-3}$ ).
- The Connection length  $L_C$ , known from laminar plots, about 30m per poloidal turn.
- The Kolmogorov length  $L_K$ , typically about 15m.

In the regular region, both  $L_K$  and  $L_C$  are negligible compared to  $\lambda$ , so the particles collide before they notice that they are on an ergodic or open field line. For ergodicity to have an effect on transport,  $L_K$  should be of the same order or smaller than  $\lambda$ . The divergence of the field lines then contributes to the radial transport, and competes with the radial step-size in a collision ( $\rho_e$  or  $\rho_i$ ).

For transport to be effected by open field lines (the laminar region),  $L_C$  should be of the same order or smaller than the collision length  $\lambda_e$ , so particles that (diffusively) enter the laminar zone almost certainly flow to the wall, making the laminar zone an effective heat sink. It should be noted that the field lines in a region of the laminar zone with equal  $L_C$ , form a flux tube in which all field lines hit the wall at about the same location. Hence, after a single collision, a particle is probably still inside that same flux tube. So a number of collisions are needed for the particle to ‘jump’ to a flux tube with a different  $L_C$ . This number depends on the width of the individual flux tubes.

Numerical modelling using the 3D plasma edge transport code EMC3-EIRENE [Kobayashi 2004], predicts that electron temperature and density follow the connection length profile, so in the fingers a higher  $T_e$  is expected. This model is a Monte Carlo fluid simulation, and uses the vacuum magnetic field topology as input. Also the heat deposition profile on the divertor target plates (footprint) is predicted to follow the structure of these long connection length fingers. Experimentally, both a raised temperature and density in the fingers and the footprints are observed ([Lehnen 2005], [Finken 2006]). Note that both effects are attributable to the laminar region, where the calculations (based on the vacuum field) are expected to be valid.

### 5.4 Experimental results

To investigate whether, and how, the temperature profile at the plasma edge during DED operation depends on  $q_a$ , a ramp of the plasma current with otherwise constant plasma parameters is used. In Figure 5-3(a-d), ECE-Imaging measurements at the low field side plasma edge during a shot with DC DED ( $I_{DED}=11.5\text{ kA}$ ,  $B_T=1.91\text{ T}$ ) are presented. The evolution of the main plasma parameters is shown in Figure 5-4. During this shot the plasma current was ramped down from  $I_p=450$  to 200 kA. As  $B_T$  was kept constant, this means that the value of  $q$  at the edge ( $q_a$ ) was ramped up. The

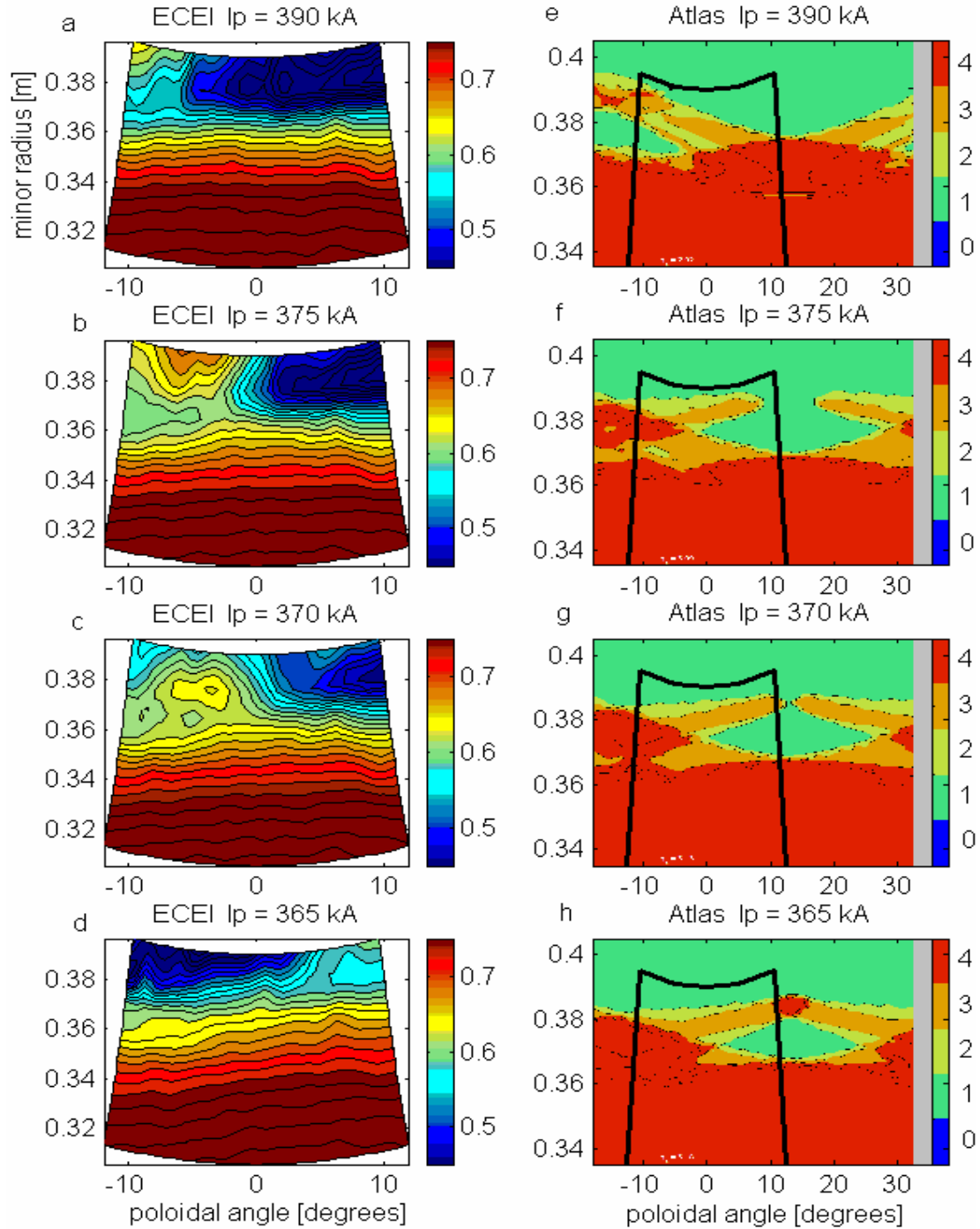
data in Figure 5-3 is normalised to the temperature at  $t=1.5$ s, before switching on the DED, and hence reflects the relative change in temperature during DED and the current ramp. To reduce the thermal noise, the data is filtered using singular value decomposition (a discussion of this filtering method is postponed to paragraph 7.1). The data in Figure 5-3 represents only part of the current ramp and is taken between  $t=2.5$  and  $2.75$ s. Figure 5-4 shows that during this time period, the central  $n_e$  and  $T_e$  are almost unaffected by the DED and the current ramp, so the relative changes in  $T_e$  shown in Figure 5-3 (up to 50%) are limited to the plasma edge.

Figure 5-3(e-h) gives the corresponding laminar plots, as calculated with the Atlas code [Jakubowski 2004]. Although the transition between laminar and ergodic regions is hard to define, it is safe to assume that the 1 poloidal turn field lines belong to the laminar zone and the 4 (or more) poloidal turn field lines belong to the ergodic (or regular) zones. As the 2 and 3 turn field lines constitute only a thin layer, the boundary between laminar and ergodic zones can be estimated fairly accurately. The black contour indicates the approximate position of the observation volume of ECE-Imaging. Due to uncertainties in both plasma position and ECE-Imaging alignment, deviations are possible.

After switching on the DED, the temperature drops over the entire observation volume of ECE-Imaging (all normalised temperatures below 1), which is a clear sign of an enhanced transport level. The relative  $T_e$  drop is largest near the edge. Apart from the overall drop in  $T_e$ , the measurements in Figure 5-3 show a clear 2D structure, despite the fact that ECE-Imaging measured at the low field side, opposite to the position of the DED coils. The main observations regarding the 2D structures are:

- The bottom half of the ECE-Imaging observation volume shows a poloidally symmetric  $T_e$  profile, while the top half (closest to the edge) shows a pronounced poloidal asymmetry.
- The poloidally asymmetric part shows a ‘bulge’ of higher  $T_e$  at the left hand side, separated from the poloidally symmetric region. The poloidal position of this bulge stays about the same during the current ( $q$ ) ramp.
- The radial position of the bulge depends on  $q$ . It migrates radially inward with decreasing plasma current. Due to the changing  $q$  profile, the DED induced structures are expected to evolve; the resonant  $q$  surfaces migrate inward during the ramp.
- The bulge merges with the poloidally symmetric region at a plasma current of about 365 kA (Figure 5-3d).

The Atlas calculations in Figure 5-3(e-h) show very similar structures. They also show a structure (a long  $L_C$  region in the upper left, where two ‘fingers’ cross) which migrates inward. In Figure 5-3(h) this structure connects to the main ergodic region at the same time as the bulge in the ECE-Imaging measurements merges with the poloidally symmetric main plasma. The laminar plots show a new structure arising just to the right of the ECE-Imaging observation volume. Also in the ECE-Imaging data,  $T_e$  is now observed to be higher on the right hand side. So the bulges seen with ECE-Imaging corresponds to the long  $L_C$  regions at the position where two fingers cross, which is also confirmed by measurements with the He beam diagnostic [Schmitz 2006],[Jakubowski 2006]. The poloidally symmetric region at  $r<35$ cm observed with ECE-Imaging corresponds to the  $L_C>=4$  poloidal turn region, located at about the same radius.



**Figure 5-3:** Comparison of ECE-Imaging temperature measurements (a-d) with the laminar plots (e-h) during a plasma current ramp down (TEXTOR discharge #96419). The ECE-Imaging data is normalized to the  $T_e$  before the DED phase, and hence shows the relative  $T_e$  drop in the poloidal plane. The laminar plots (Atlas calculations) show the wall-to-wall connection length (in terms of the number of poloidal turns) for the various (strongly deformed) flux tubes in the poloidal cross section. The ergodic region is represented by the red, more than four poloidal turn field lines. The thick black contours indicate the (approximate) position of the ECE-Imaging observation volume. As the current ramps down, the resonant  $q$  surfaces shift inward (down). Both the ECE-Imaging measurements and the laminar plots show an inward migrating (high  $T_e$  / long connection length) structure, joining the poloidally symmetric region at about  $I_p=365$  kA.

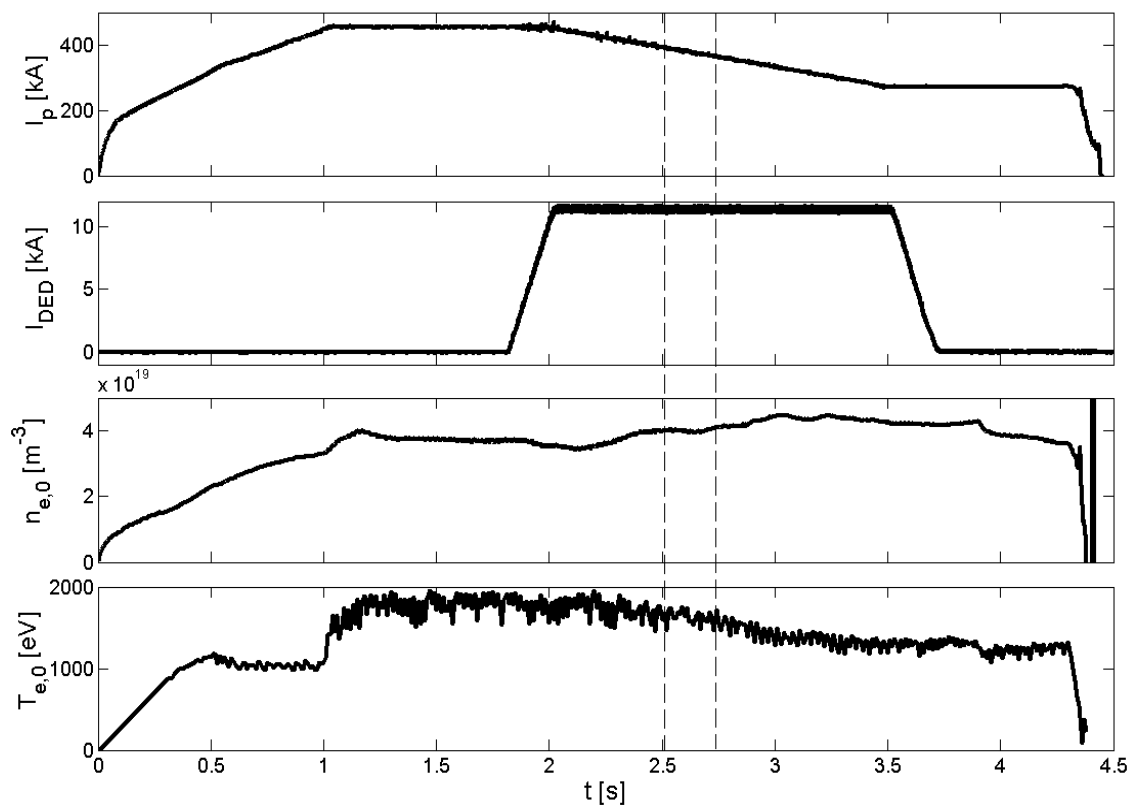


**Figure 5-4:** Overview of TEXTOR discharge #96419. The plasma current is ramped down from 450 to 200 kA (at constant  $B_T=1.91T$ ) to vary  $q_a$ . The 12/4 DC DED is switched on between 2 and 3.5 s at 11.5 kA. The ECE-Imaging data is normalized to the (radiation) temperature at 1.5s. The data of Figure 5-3 is taken between 2.5 and 2.75s (dashed lines). In this time interval the central  $T_e$  and  $n_e$  are still close to the values at the moment of ECE-Imaging normalization and show no clear effect of the DED.

To investigate the change in transport in the edge, a comparison is made between the DED phase and the non-DED phase in a plasma with otherwise constant plasma parameters ( $I_p=350$  kA,  $n_e \approx 1.5 \cdot 10^{19}$  m<sup>-3</sup>,  $B_T=1.9T$ ). As, apart from the DED current, these phases are identical, the observed changes can be directly attributed to the DED. In Figure 5-5a (normalised) ECE-Imaging data from a shot with DC DED ( $I_{DED}=12$ kA) is shown. The data again clearly shows a relatively hot bulge, separated from the main plasma by a colder region, similar to the structure in Figure 5-3. The corresponding laminar plot is shown in Figure 5-5b. In Figure 5-5c, estimates of the absolute temperature profiles at cross sections 1 and 2 indicated in Figure 5-5a are shown, along with the poloidally averaged profile and the non-DED reference case. ECE-Imaging is not absolutely calibrated and has to rely on cross calibration or profile shape assumptions. The absolute temperature values presented in Figure 5-5c are derived from measurements with a different, calibrated ECE system, and the edge profile shape (in the non-DED reference case) is estimated from He beam measurements [Schmitz 2006]. The profile is taken linear inside the last closed flux surface (at approximately  $R=2.11$ m), and exponentially decaying with an e-folding length of 4cm outside the last closed flux surface.

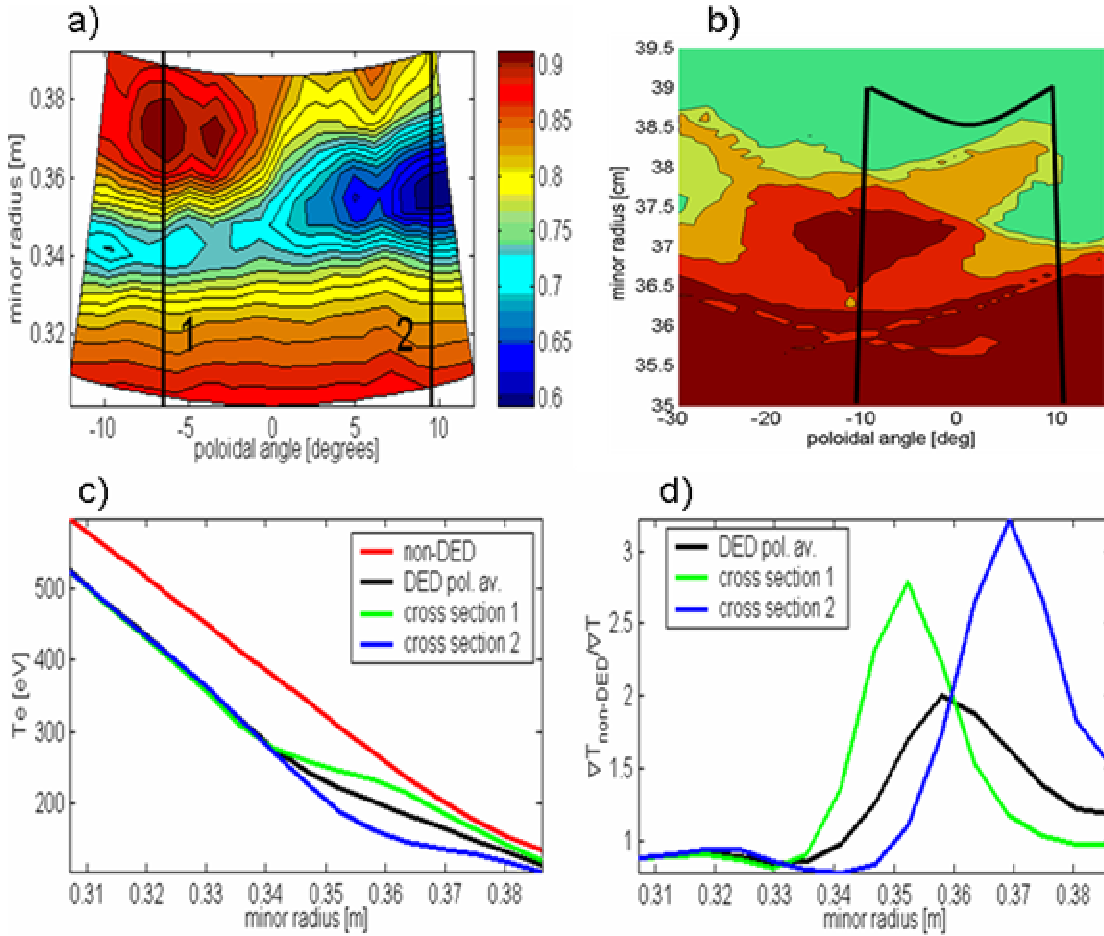


**Figure 5-5:**  $T_e$  profile during DED compared with non-DED reference (TEXTOR discharge #96454). In a) the relative  $T_e$  profile, normalized to the pre-DED profile, shows a pronounced ‘relatively hot-spot’ and a ‘relatively cold channel’ separating it from the main plasma. The laminar plot in b) shows a spot of high  $L_c$  at the same position as the hot-spot [note that the radial coverage in figure a) is about twice as large as in b)]. Assuming an unperturbed  $T_e$  profile shape as shown in c) by the red line, an estimate of the ‘absolutely calibrated’ profiles during DED is obtained. The black line represents the poloidally averaged profile, the green and blue lines are the profiles through respectively cross sections 1 and 2 in a). The flattening of these profiles indicates enhanced transport. In d) the ratio between the observed  $T_e$  gradients and the non-DED reference is plotted, showing an increase in gradient of about a factor of 3 inside the ‘cold channel’.

The profiles clearly show the overall drop in temperature and the large poloidal variation in profile shape during DED. The extent of the DED affected region is clearest seen in Figure 5-5d, where the ratio between the temperature gradient in the non-DED reference case and the temperature gradient during DED is plotted. Assuming heat flux and density profiles stay the same (which is an oversimplification, certainly for the two poloidal cross section profiles due to poloidal redistribution of heat flux) this ratio is a measure for the enhancement of the heat transport during DED [Kobayashi 2004]:

$$\frac{\nabla T_{e,non-DED}}{\nabla T_{e,DED}} \approx \frac{\chi_{erg}}{\chi_{\perp}} \quad \text{Eq. 5-5}$$

Where  $\chi_{\perp}$  is the effective perpendicular diffusion coefficient in the unperturbed case and  $\chi_{\text{erg}}$  is the (poloidally averaged) effective heat diffusion coefficient in the perturbed magnetic field (containing both perpendicular and parallel transport and hence is not a true diffusion coefficient). In Figure 5-5d, the poloidally averaged  $T_e$  gradient is observed to reduce by about a factor of two in the laminar region, meaning that here the heat transport doubled (assuming the relative  $n_e$  change was small compared to the relative change in  $T_e$  gradient). The two local temperature profiles indicate a significant transport enhancement in the plasma regions where from Atlas calculations the laminar zone is expected, here the gradients reduced by up to a factor of three. In the regions corresponding to the ergodic region in the laminar plots (so both the poloidally symmetric main plasma and the hot bulge), no significant enhancement of heat transport is found. These local gradient changes are, however, more difficult to link to changes in heat transport, as it can be expected that the heat flux also has a poloidal variation (largest where the smallest  $T_e$  gradients are observed).

Caution is needed in quantitatively interpreting the ECE-Imaging edge measurements due to two difficulties. First due to the lack of an absolute calibration and second, due to the low optical thickness near the edge (typically,  $\tau=0.5$ ), meaning that not only  $T_e$ , but also  $n_e$  changes are reflected in the measurements. As  $n_e$  is seen to change in a similar way as  $T_e$  [Schmitz 2006], the relative temperature drop during DED is overestimated (by about 30%). Qualitatively, the presented results are, however, not sensitive to these two difficulties.

## 5.5 Summary and discussion

During DED 12/4 operation, an overall drop in  $T_e$  is observed near the plasma edge. Using the 2D capability of ECE-Imaging, a large poloidal variation in the  $T_e$  profile is observed. Moreover, these structures in the 2D  $T_e$  profile depended on the value of  $q_a$ . The most prominent structure, a hot ‘bulge’ with relatively high  $T_e$ , was seen to migrate inward until it merged with the main, poloidally symmetric plasma. A comparison of the ECE-Imaging data with the theoretical vacuum magnetic field structure (laminar plots) shows that the hot bulge corresponds to a region in the laminar zone of relatively large connection length at the position where two ‘fingers’ cross. The moment at which the bulge merges with the main plasma corresponds to the moment at which the large connection length region connects to the ergodic region, which has equally large connection lengths. The region in which ECE-Imaging measures strong poloidal variations of  $T_e$  is limited to the (small connection length) laminar region.

The observed (overall) drop in  $T_e$  is a clear sign of an enhanced heat transport in the plasma edge during DED 12/4 operation. The relative change in  $T_e$  gradient can be used to estimate the relative change in heat conductivity. The poloidally averaged  $T_e$  gradient is observed to reduce by about a factor of two in the laminar region, meaning that here the heat transport doubled. Inside the hot bulge, and in the poloidally symmetric region, the transport levels are close to the unperturbed values.

## 5 2D edge temperature profile during DED 12/4 operation

---

The resemblance between the ECE-Imaging data and the laminar plots is not perfect, which could be caused by inaccuracies in the reconstruction of the plasma equilibrium going into the calculation of the laminar plot. In particular, the exact value of  $q_a$ , and hence the radial position of the large  $L_C$  region, depends on the size and position of the plasma. More general, one can not expect the two to be identical: ECE-Imaging shows a temperature while the laminar plots show a connection length. The connection length is probably more related to the gradient in  $T_e$  than to  $T_e$  itself.

So, it is observed that the DED has a large influence on  $T_e$  profile and heat transport at the plasma edge. Moreover, the exact edge topology can be selected by changing the positions of the resonant surfaces near the edge. This makes the DED a flexible tool to investigate the plasma-wall interaction.



## 6 Fluctuation measurements with ECE-Imaging

The experimentally determined transport levels in tokamak plasmas are one to two orders of magnitude higher than predicted by neoclassical transport theory. This discrepancy is generally ascribed to electrostatic plasma turbulence. Fluctuations of the plasma electron temperature  $T_e$ , electron density  $n_e$  and electric field  $E$  can result in additional radial heat ( $q_e$ ) and particle ( $\Gamma_e$ ) fluxes according to [Cima 1995]:

$$\Gamma_e^{ES} = \langle \tilde{n}_e \tilde{E}_\theta \rangle / B \quad \text{Eq. 6-1}$$

$$q_e^{ES} = \frac{3}{2} n_e \langle \tilde{T}_e \tilde{E}_\theta \rangle / B + \frac{3}{2} T_e \Gamma_e^{ES}$$

So not only the fluctuation levels, but also the phase relations between the various fluctuating quantities are important. A wide variety of candidate (electrostatic) turbulent modes, like the ion (electron) temperature gradient ITG (ETG) and trapped electron modes (TEM), have been discussed in the literature, see [Horton 1999] for a review. Apart from electrostatic turbulence, also imperfections of the magnetic field topology can give rise to enhanced transport

Experimentally, many observations of broadband fluctuations with frequencies between 50 and 500 kHz, and wave numbers  $k=2\pi/\lambda$  between 1 and 15 cm<sup>-1</sup> [Horton 1999] are reported, mainly as density fluctuations. Experiments on TEXT-U [Cima 1995] provided the first evidence of broadband  $T_e$  fluctuations using correlation ECE. Later, similar measurements were reported from other tokamaks. The reported  $T_e$  fluctuation spectra show a broad peak, typically around 100 kHz. The observed amplitudes increase with radius, typically ranging from about 0.5% near the plasma centre to up to 10% at the edge. The limited spatial resolution of ECE diagnostics generally restricts the measurements to wave numbers smaller than about 2 cm<sup>-1</sup>.

Assuming also on TEXTOR broadband fluctuations are responsible for the anomalous transport, ECE-Imaging should be able to measure them using correlation techniques to suppress the thermal noise. The 2D character of ECE-Imaging would enable both the radial and poloidal wave numbers and correlation lengths to be determined. This chapter explores the capabilities of ECE-Imaging as a fluctuation diagnostic. To illustrate the analysis techniques, two examples of fluctuation measurements will be discussed: The so-called quasi-coherent mode [Krämer-Flecken 2003] near the plasma edge and the ‘Alfvén-like’ mode [Zimmermann 2005] deeper into the plasma core. The question whether or not broadband turbulence is present in TEXTOR, comparable to the observations in other tokamaks, is addressed.

## 6.1 Noise reduction by correlation

The ability of ECE-Imaging to detect high frequency fluctuations depends on the signal to noise ratio, the time resolution and (for small wavelength fluctuations) the spatial resolution. The main source of noise is the thermal noise inherent to any ECE measurement. The thermal noise level depends on both the spatial and temporal resolutions of the ECE measurement. Repeating some points from chapter 4:

- The spatial resolution in the direction perpendicular to the line of sight is determined by the optics and is typically 12 mm vertically and 9 mm toroidally (FWHM) in the focal plane (that can be shifted to ensure that the observation volume is always in focus). The spatial resolution in the radial direction is determined by the bandwidth of the ECE radiation selected by each channel ( $B_{IF}$ ) and by the optical depth (which is a function of the plasma parameters). The IF bandwidth  $B_{IF}$  of 300 MHz, along with broadening effects in the plasma, leads to a radial resolution below 1 cm for optically thick plasmas.
- The time resolution is determined by the video bandwidth  $B_V$  of the system. The maximum  $B_V$ , and hence the maximum detectable fluctuation frequency, can be varied, and is normally set to 100 kHz. The sampling frequency is normally set to twice the video bandwidth.
- The accuracy of the  $T_e$  measurements is determined by the thermal noise level, which forms a fundamental limitation of ECE measurements. Increasing  $B_V$  (better time resolution) or decreasing  $B_{IF}$  (better spatial resolution) increases the relative thermal noise level according to [Bekefi 1966]:

$$\frac{\sqrt{\langle dT_R^2 \rangle}}{\langle T_R \rangle} = \sqrt{\frac{2B_V}{B_{IF}}} \quad \text{Eq. 6-2}$$

Taking  $B_{IF}=300$  MHz and  $B_V=100$  kHz gives a thermal noise level of about 2.5%. This value is close to the experimentally observed noise levels of ECE-Imaging, see chapter 4.

For a (periodic) structure in the plasma to be visible by ECE-Imaging, of course its wavelength has to be at least twice as large as the spatial resolution. Also, the fluctuation amplitude has to be big enough not to be ‘swamped’ by the thermal noise. In ‘raw’ ECE data, normally only the largest plasma oscillations (magnetic islands and the sawtooth oscillation) are visible. To detect fluctuations with smaller amplitudes, the thermal noise has to be suppressed. Correlation (or the closely related coherence) offers an effective method to do this.

Mathematically, the cross-correlation is the expectation value of the product of two random processes  $S_1(t)$  and  $S_2(t)$  (two ECE signals in our case), both being functions of  $t$  (time in our case), with one process shifted in  $t$  with a certain (time)lag  $l$ .

$$C_{1,2}(l) = \langle S_1(t)S_2(t-l) \rangle \quad \text{Eq. 6-3}$$

where  $\langle \rangle$  denotes the expectation value. In practice, only having finite time segments of length  $N$  of discrete signals  $S(n)$ , one can estimate the cross-correlation by:

$$C_{1,2}(l) = \begin{cases} \frac{1}{N} \sum_{n=0}^{N-l-1} S_1(n+l)S_2(n) & l \geq 0 \\ C_{2,1}(-l) & l < 0 \end{cases} \quad \text{Eq. 6-4}$$

$C_{1,2}(l)$  can be seen as the dot product between  $S_1$  and  $S_2$ , shifted by a time lag  $l$ . Alternatively, the cross-correlation function can be obtained by convolving the two signals with one of them reversed in time.

$$C_{1,2}(l) = \frac{1}{N} [S_1(t) * S_2(-t)] \quad \text{Eq. 6-5}$$

Normally, the signals are ‘mean removed’, so only the fluctuating parts  $\tilde{S} = S - \bar{S}$  are used in the cross-correlation. In this case one also speaks of the cross-covariance. If  $S_1=S_2$  one speaks of the auto-correlation function. The amplitude of the (correlated part of the) fluctuations is found by taking the square root of the amplitude in  $C_{1,2}$ . Correlated broadband phenomena with bandwidth  $B_w$  cause decaying contributions (with increasing time lag) to  $C_{1,2}$  that fall off with a decay time [Sattler 1993]

$$\tau_{1/2} = \sqrt{\frac{\ln 2}{\pi} \cdot \frac{1}{B_w}} \quad \text{Eq. 6-6}$$

A special case is the correlated (broadband) thermal noise in an auto-correlation, resulting in a sharp peak at zero time lag.

Figure 6-1 gives examples of (auto-)correlation functions for some idealized synthetic signals. In real ECE signals, normally a mixture of different fluctuation types is present (like sawtooth oscillations and magnetic islands). Suppose the signal consists of fluctuations  $A$  and  $B$ , then  $C_{1,2}$  can be written as:

$$C_{1,2}(l) = \langle S_1(t)S_2(t-l) \rangle = \langle A_1(t)A_2(t-l) \rangle + \langle B_1(t)B_2(t-l) \rangle + \langle A_1(t)B_2(t-l) \rangle + \langle B_1(t)A_2(t-l) \rangle \quad \text{Eq. 6-7}$$

If the various fluctuation types are mutually uncorrelated, the last two cross terms vanish and the resulting correlation function is the sum of the contributions from the individual fluctuation types (for long enough data segments).

It should be noted that the correlation function represents the average behaviour over the integration period. If a certain fluctuation is only present during part of this period, the amplitude in the correlation function will be correspondingly smaller, leading to an underestimation of the fluctuation amplitude. It is also difficult to differentiate between a fluctuation with an irregular frequency (of certain bandwidth), or a highly coherent (constant frequency) fluctuation whose frequency gradually changes over the integration period. So caution is needed in interpreting correlation functions.

As the cross-correlation of uncorrelated fluctuations is zero (at least in the mathematical definition Eq. 6-3), the thermal noise can be suppressed by cross-correlating two signals with independent noise. For two signals consisting of

correlated  $T_e$  fluctuations and uncorrelated noise,  $S = \tilde{T} + \tilde{N}$ , the cross-correlation can be written as:

$$C_{1,2}(l) = \langle S_1(t)S_2(t-l) \rangle = \langle \tilde{T}_1(t)\tilde{T}_2(t-l) \rangle + \langle \tilde{N}_1(t)\tilde{N}_2(t-l) \rangle + \langle \tilde{T}_1(t)\tilde{N}_2(t-l) \rangle + \langle \tilde{N}_1(t)\tilde{T}_2(t-l) \rangle \quad \text{Eq. 6-8}$$

The last three terms represent correlations of uncorrelated fluctuation, and are hence zero, only leaving the wanted  $T_e$  fluctuations. For finite data segments, however, the second (noise) term is only approximately zero (for sub-noise  $T_e$  fluctuations the last two ‘cross’ terms are negligible compared to the second). Correlating (discrete) signals of length  $N$  reduces the noise by a factor of  $N^{1/2}$ . Because fluctuations are contained quadratically in  $C_{12}$ , the minimal detectable fluctuation level scales with  $N^{-1/4}$  and can be written as:

$$\frac{\sqrt{\langle dT_R^2(t) \rangle}}{\langle T_R(t) \rangle} = N^{-1/4} \sqrt{\frac{B_V}{B_{IF}}} \quad \text{Eq. 6-9}$$

For ECE-Imaging data at maximal sampling rate, taking 2s of data ( $10^6$  data points), this theoretically leads to a minimal detectable fluctuation level of about 0.1 %.

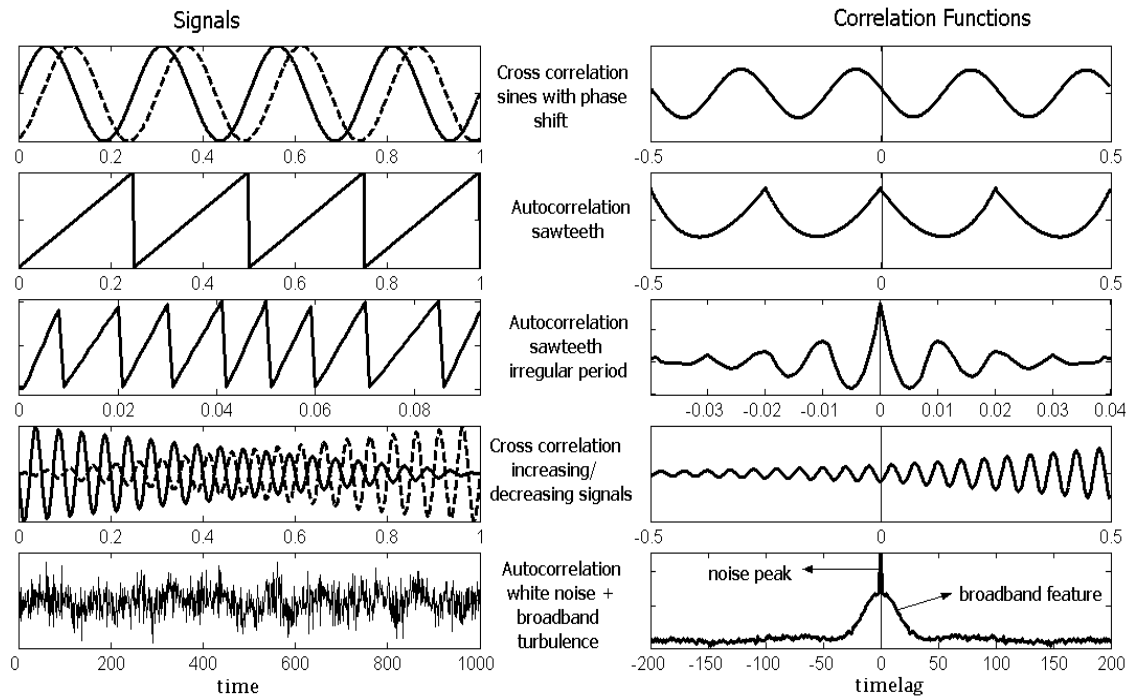


**Figure 6-1:** Examples of correlation functions for typical signals. a) Correlating two equal frequency harmonic functions with a phase shift results in a cosine of the same frequency with a phase shifted maximum. b) (Auto-)correlating an oscillation which is asymmetric in time (like a sawtooth), results in time symmetric oscillation in the correlation function. c) Signals with irregular frequency result in a correlation function with decaying amplitude for larger time lags. d) Signals with a different time evolution of the amplitude result in an asymmetric amplitude of the correlation function. e) Broadband fluctuations (bandwidth  $\geq$  frequency) result in a single decaying peak, larger bandwidths (for instance ‘white noise’) giving narrower peaks.

As an alternative to the cross-correlation itself, one can use the cross spectral density  $D_{1,2}$ , which can be determined by either taking the Fourier transform of  $C_{1,2}$ , or by taking the product of the Fourier transforms of the individual signals:

$$D_{1,2}(f) = F(S_1)F(S_2) = N \cdot F(C_{1,2}) \quad \text{Eq. 6-10}$$

$D_{1,2}$  is a complex quantity, containing both phase (the so called cross phase) and amplitude information. If one is only interested in the amplitude information, normally the coherence  $H$  is used, which is a normalized version of the cross spectral density, and takes values between 0 and 1:

$$H_{1,2}(f) = \frac{|F_{1,2}(f)|^2}{F_{1,1}(f)F_{2,2}(f)} \quad \text{Eq. 6-11}$$

The coherence is a powerful tool in analyzing coherent fluctuations. Broadband fluctuations, however, are more easily detected using the cross-correlation function.

## 6.2 The Quasi Coherent mode

As a first example of high frequency, small scale fluctuation measurements with ECE-Imaging, observations of the so called quasi-coherent mode are described. On TEXTOR, this mode is first observed with the TEXTOR O-mode reflectometer ([Krämer-Flecken 2003],[Krämer-Flecken 2004]), but it is also observed with similar experimental setup in FTU and T10 ([Vershkov 2001],[Vershkov 1999]). These density fluctuations have a typical frequency of 50-100 kHz, amplitudes of up to a few percent (highest near the plasma edge) and high poloidal mode number (around  $m=50$ ). The physical origin of this fluctuation is not yet conclusively resolved, although in [Krämer-Flecken 2004] the ion temperature gradient mode (thought responsible for the anomalous transport) is mentioned as a possible candidate.

The quasi coherent mode is also observed with ECE-Imaging, tuned to measure close to the low field side plasma edge. In TEXTOR discharge #95097 ( $B_T=2.25T$ ,  $I_p=400kA$ ,  $n_{e,1a}=2.7 \cdot 10^{19} \text{ m}^{-3}$ ,  $P_{ECRH}=800kW$ ) both ECE-Imaging and the reflectometer simultaneously observed the mode. Figure 6-2 shows Fourier spectra of the reflectometer data during this discharge (around  $t=3.6s$ ). The quasi coherent mode is visible as a broad peak (on top of a much broader background) around 80 kHz, with a bandwidth of roughly 50 kHz. The fact that the bandwidth of this fluctuation is almost as large as its frequency provided its name.

With cross-correlation, using a second of data, the quasi coherent mode is also visible with ECE-Imaging. The cross-correlation function shown in Figure 6-3 of two neighbouring channels around  $R=2.17m$  (about 8 cm from the plasma edge), shows a clear 90 kHz oscillation around zero time lag (superimposed on the sawtooth oscillation and a weak 5 kHz fluctuation at larger time lags). From the decay of the fluctuation amplitude with increasing time lag, a bandwidth of around 50 kHz can be derived (Eq. 6-6), in good agreement with the simultaneous reflectometer measurements at the same radius (Figure 6-2). The amplitude of the quasi-coherent fluctuation in Figure 6-3 is about 1.5%. The smallest fluctuation amplitudes still detectable using cross-correlation (for channels at smaller radii) were about 0.2% (see

## 6 Fluctuation measurements with ECE-Imaging

also Figure 6-5), proving that the minimum fluctuation levels predicted by Eq. 6-9 are really accessible.

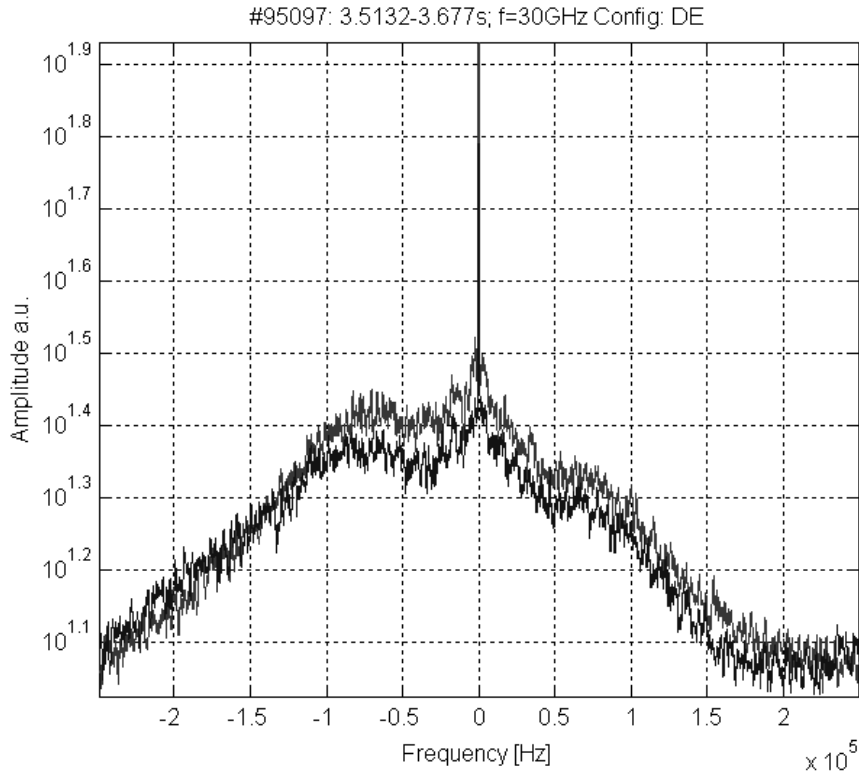


**Figure 6-2:** Double sided Fourier amplitude spectra of the fluctuations measured by two channels of the O-mode reflectometer for TEXTOR discharge #95097. Apart from the low frequency peak ( $<10\text{kHz}$ ), a broad peak around  $80\text{kHz}$  dominates the spectrum. As the bandwidth of this peak (about  $50\text{kHz}$ ) is comparable to its frequency, these fluctuations are called ‘quasi-coherent’. The slight asymmetry in the spectra is probably caused by a combination of toroidal plasma rotation and small misalignments of the (probing or receiving) antennae [Krämer-Flecken 2004].

The contour plots in Figure 6-4 show the cross-correlation function as a function of channel separation  $\Delta s$  (relative to a reference channel, channel 11-2, 3 cm below the equatorial plane). In the cross-correlation function of poloidally separated channels a phase shift is observed, increasing linearly with  $\Delta s$ . From this phase shift as a function of  $\Delta s$ , a poloidal phase velocity of about  $6\text{ km/s}$  can be deduced. From the  $\Delta s$  needed to get a phase shift of  $2\pi$  the poloidal wavelength can be estimated to be around  $7\text{ cm}$  (or alternatively:  $\lambda_{pol}=v_{pol}/f$ ), from which a poloidal mode number around  $m=40$  is found. Since the analogous contour plot for radial separations does not show any phase shift, it can be concluded that the radial velocity is zero (or too large to resolve, as the phase shift is largest for slow propagating fluctuations).

The observed structures are periodic in poloidal, but not in radial direction. The correlation drops quickly with increasing radial channel separation, giving a radial correlation length in the order of  $2\text{cm}$ . Part of this is however due to the drop in fluctuation amplitude with decreasing radius. A poloidal correlation length is less obvious to determine, due to the rotation in that direction. For a channel separation of  $(-7\text{cm})$ , so one wavelength, in Figure 6-4 almost no correlation is observed at zero

time lag, so the poloidal correlation length is at least smaller than 7cm. Note that at the same channel separation the phase shifted maximum at a time lag of about  $1 \cdot 10^{-5}$ s is still clearly visible. This means that the life-time of the rotating fluctuations (the decorrelation time) is at least longer than  $1 \cdot 10^{-5}$ s.

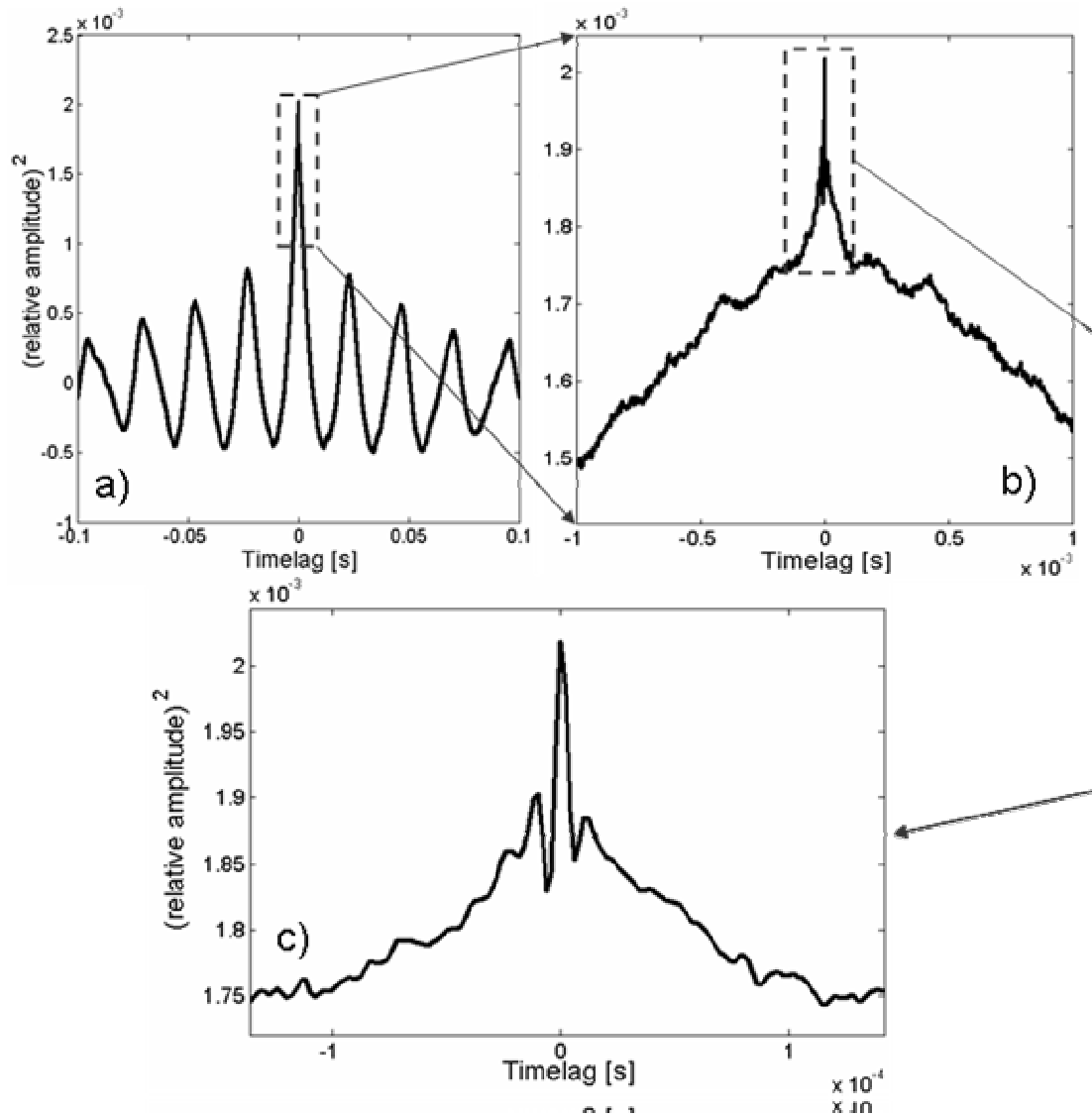


**Figure 6-3:** Cross-correlation function of two [normalized and mean-removed  $(S - \bar{S})/\bar{S}$ ] ECE-Imaging channels (channels 11\_1 and 11\_2) for the same TEXTOR discharge as in Figure 6-2 (#95097). This correlation function represents a second of data ( $t=3-4$ s). The low frequencies are dominated by the sawtooth oscillations. ‘Zooming in’ around zero time lag, first a weak, coherent (so also visible at larger time lags) oscillation of about 5 kHz is visible. Zooming in further to even smaller time lags reveals the high frequency (about 90 kHz), ‘quasi-coherent’ oscillation. Quasi-coherent here means that the decay time of the oscillation is only slightly longer than its oscillation period, so only a few oscillations can be discerned in the correlation function. The relative fluctuation amplitudes (square root of the amplitudes in the correlation function) are about 5% for the sawtooth and 1.5% for both the 5kHz and the quasi-coherent oscillations.

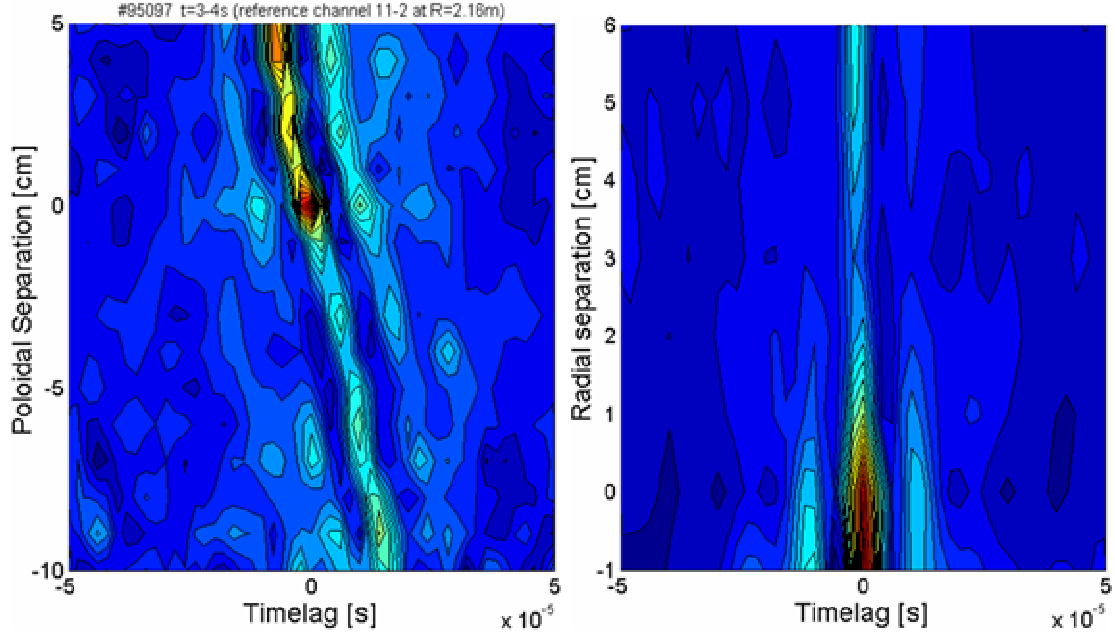


**Figure 6-4:** Contour plots of the correlation function of two spatially separated ECE-Imaging channels, as a function of (poloidal or radial) separation. For both plots a fixed reference channel (channel 11\_2) is chosen. The left plot shows the correlation function of this reference channel with poloidally separated channels. An increasing phase shift with increasing channel separation is observed. From this phase shift a poloidal rotation velocity of about 6km/s can be deduced. Furthermore, a poloidal wavelength of about 7 cm (corresponding to a poloidal mode number close to  $m=40$ ) can be found from the figure as the poloidal separation between two maxima at constant time lag. The right plot shows the correlation function of the reference channel with radially separated channels. No phase shift is visible, meaning either that the fluctuations do not propagate radially or that the propagation velocity is too high to resolve.

The measured radial dependence of the fluctuation amplitude is given in Figure 6-5 (red curve). Because near the plasma edge a low optical thickness can be expected, this amplitude cannot be directly interpreted as the temperature fluctuation amplitude. For 2<sup>nd</sup> harmonic X-mode radiation well below the cut-off frequency the optical thickness  $\tau_0^{2X}$  is [Bornatici 1983]:

$$\tau_0^{2X} = \frac{\pi k_B e}{\epsilon_0 m_e c^3} \cdot n_e T_e \cdot \frac{R^2}{B_0 R_0} \quad \text{Eq. 6-12}$$

In optically thin plasmas (neglecting the possible influences of suprathermal radiation and wall reflections) the measured radiation temperature  $T_R$  can be expressed as:

$$T_R = T_e (1 - e^{-\tau}) \quad \text{Eq. 6-13}$$

Since the optical thickness  $\tau$  is a function of both  $n_e$  and  $T_e$ , not only  $T_e$  fluctuations, but also  $n_e$  fluctuations will result in fluctuations of  $T_R$ . Assuming  $dT_e$  and  $dn_e$  have the same phase, a first order approximation gives [Sattler 1994]:



$$\frac{dT_R}{\langle T_R \rangle} = (1 + a) \frac{dT_e}{\langle T_e \rangle} + a \frac{dn_e}{\langle n_e \rangle} \quad \text{with} \quad a = \frac{\tau \cdot \exp(-\tau)}{1 - \exp(-\tau)} \quad \text{Eq. 6-14}$$

From the  $T_e$  and  $n_e$  profiles, the optical thickness  $\tau$  and the parameter  $a$  of Eq. 6-14 can be calculated. The optical thickness is found to be about 1.5 at the outboard side of the ECE-Imaging observation volume, rapidly increasing towards the plasma centre. The general radial dependence of the density fluctuation amplitude (dashed line in Figure 6-5) is known from reflectometer measurements [Krämer-Flecken 2003], so the  $n_e$  fluctuation contribution to the measured  $T_R$  fluctuations can be estimated ( $a \cdot dn/n$ ) and is given by the blue line in Figure 6-5, which lies well below the  $T_R$  fluctuation amplitude. The shaded area indicates  $(1+a)$  times the estimated  $T_e$  fluctuation amplitude. So, despite all uncertainties, it is likely that the quasi coherent mode is both a density and a temperature fluctuation. Figure 6-5 suggests comparable amplitudes for both  $dT_e/T_e$  and  $dn_e/n_e$ . Note that a possible phase difference between  $dT_e/T_e$  and  $dn_e/n_e$  results in a larger estimate for  $dT_e/T_e$ .

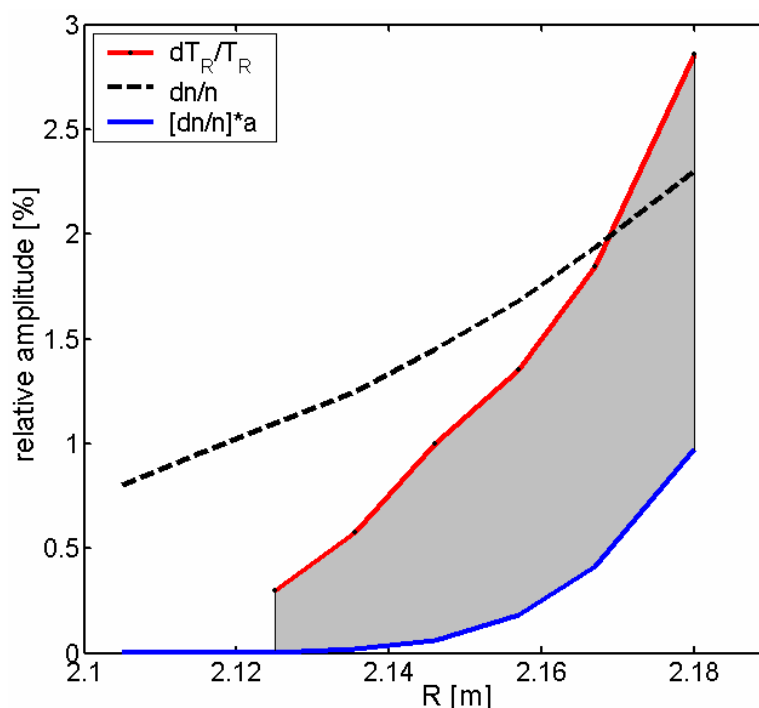


**Figure 6-5:** The radial dependence of the relative fluctuation amplitudes for the quasi-coherent mode. The red line corresponds to the fluctuation amplitude of the radiation temperature as measured with ECE-Imaging (derived from the auto-correlation functions of discharge #95097) and can contain  $T_e$  as well as  $n_e$  fluctuations. The dashed black line shows the average radial dependence of the density fluctuation amplitude as it is measured by the O-mode reflectometer over a large number of ohmic and neutral beam heated plasmas (always showing approximately the same dependence) [Krämer-Flecken 2003]. The blue line is the amount of parasitic density fluctuations in the ECE-Imaging signal expected from  $dn/n$  and the optical thickness. As this curve lies well below the fluctuation amplitudes measured by ECE-Imaging, this suggests a significant contribution of  $dT_e/T_e$  (the size of the shaded gray area if there is no phase difference between the  $n_e$  and  $T_e$  fluctuations).

### 6.3 Alfvén-like modes

An example of a high frequency fluctuation in the plasma core is the so called ‘Alfvén-like mode’. This fluctuation, normally associated with the simultaneous presence of a magnetic island, was first reported by ([Zimmermann 2005], [Zimmermann 2006]) on TEXTOR and [Buratti 2005] on FTU using magnetic pick-up (Mirnov) coils. Again, there is little known about the physical origin of this mode. As the frequency of this mode is observed to scale with the Alfvén velocity  $v_A = B_0/\sqrt{\mu_0 n_e}$  (but well below the typical TAE frequency), it is called the Alfvén-like mode. Figure 6-6 shows the spectrogram of a pick-up coil signal for a discharge (#97215,  $B_T=2.25\text{T}$ ,  $I_p=270\text{kA}$ ,  $P_{NBI}=1.3\text{MW}$ ) with two phases of Alfvén-like mode activity. During the first phase, from about 0.55s to 0.7s, two bands of high frequency fluctuations, at 25kHz and 43kHz, are visible. The second phase, from 2.3s onwards, shows only the lower, 25kHz band which now shows a clear substructure. During both phases, also a 2/1 tearing mode, with a frequency around 1kHz, was present.

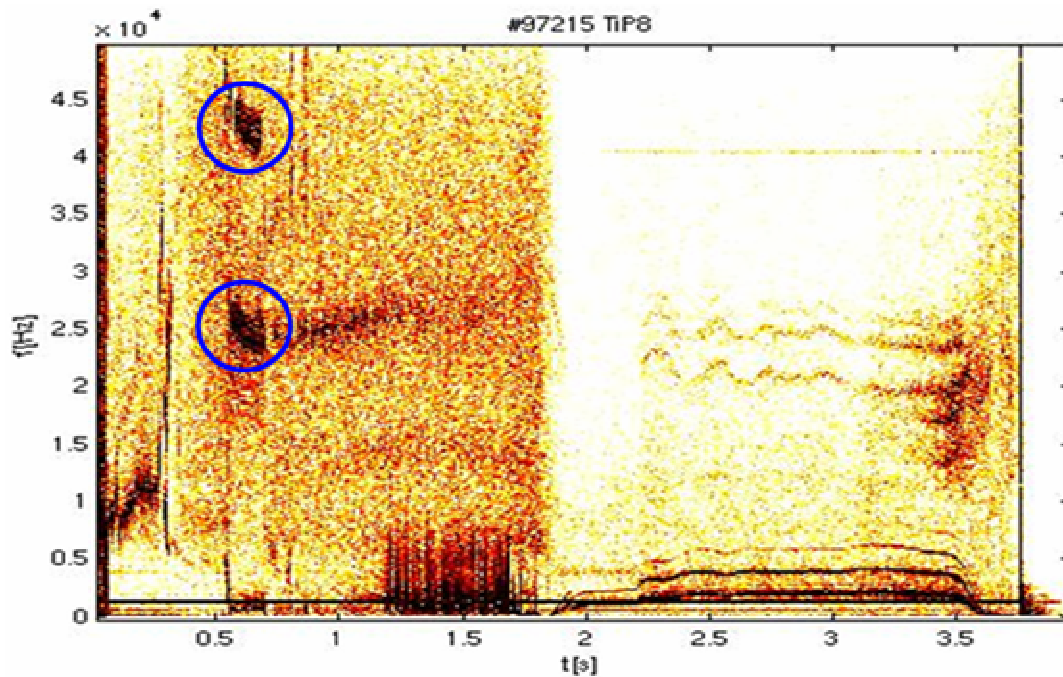


**Figure 6-6:** Spectrogram of a magnetic pick-up coil showing two phases with ‘Alfvén-like’ modes, one from 0.55 to 0.7s (with two bands at 25 and 43 kHz, highlighted by blue circles) and another from 2.2 to 3.5s (with only the lower band, now clearly split into two branches) [Zimmermann 2005]. With ECE-Imaging only the first phase is visible.

A mode number analysis of the pick-up coil data [Zimmermann 2005], showed that these Alfvén-like modes have low mode numbers (2/1 or 3/1) and that the two strongest bands in the substructure (during the second phase) rotate in opposite directions and differ in frequency by exactly twice the 2/1 tearing mode frequency. The first phase doesn’t show a clear splitting of the bands, which might be due to the lower frequency of the 2/1 tearing mode. Further, the central  $n_e$  during the first phase ( $1.5 \cdot 10^{19} \text{m}^{-3}$ ) is about twice as low as in the second phase ( $3.5 \cdot 10^{19} \text{m}^{-3}$ ), whereas the central  $T_e$  is a bit higher (2keV in the first phase, 1.5keV in the second).

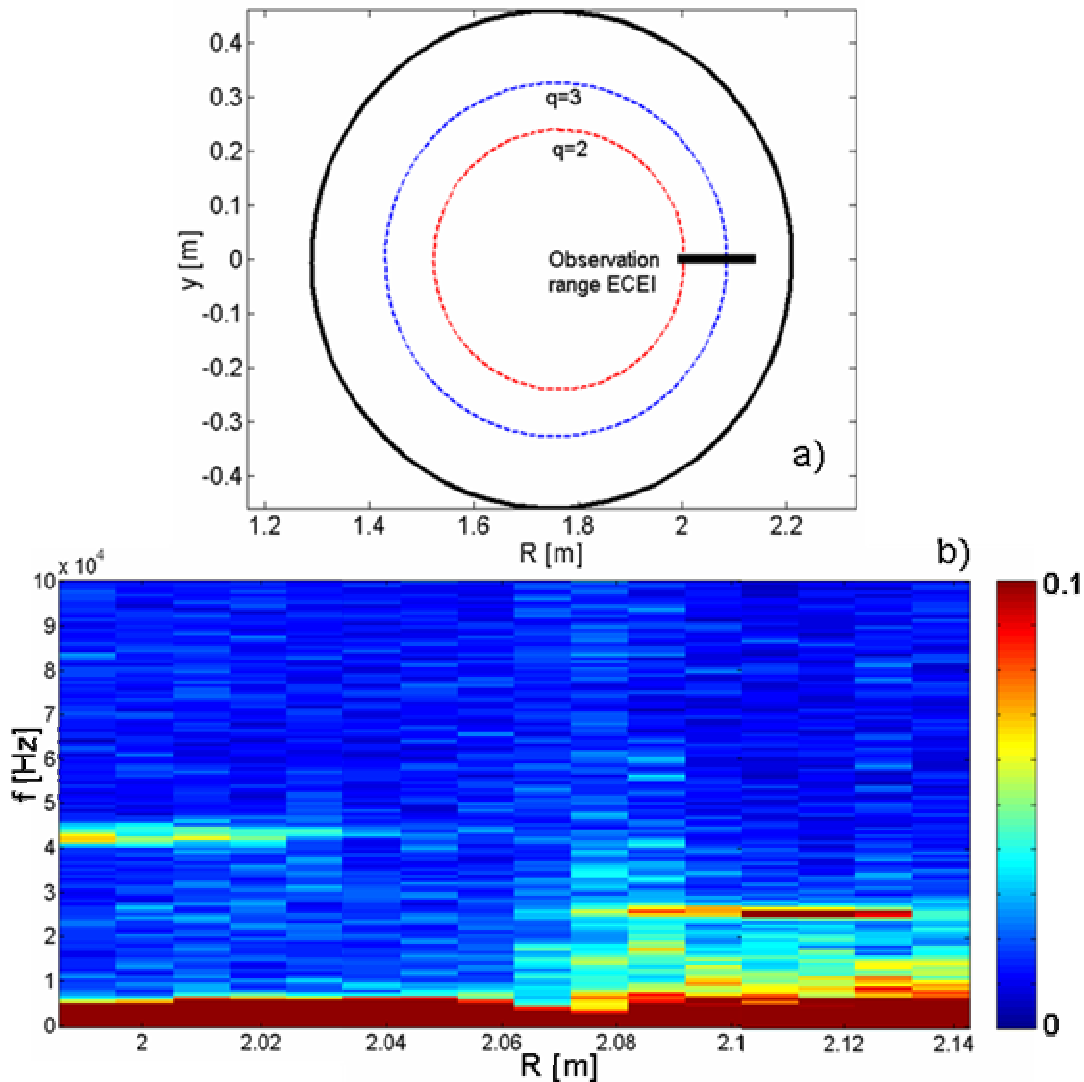


**Figure 6-7:** ECE-Imaging measurements showing a contour plot of the coherence as a function of radius. The data of three identical discharges (#97211, #97213 and #97215) is used to expand the radial range of ECE-Imaging to 15 cm as shown in a), where the locations of the  $q=2$  and 3 surfaces are estimated assuming a parabolic current profile. In b), the coherence as a function of radius is shown, revealing that the 25 and 43 kHz modes are spatially separated, most likely linked to the rational surfaces. To improve statistics, for each radius the coherence (calculated over the time interval 0.55-0.68s) of 15 neighboring pairs (1-2, 2-3, 3-4....15-16) of the 16 ECE-Imaging channels in poloidal direction is averaged.

With ECE-Imaging, only the fluctuations during the first phase are detectible. Figure 6-7 shows a contour plot of the coherence as a function of radius. For this plot, the data of three identical discharges (#97211, #97213 and #97215), but with different BWO frequency tuning of ECE-Imaging, was used to extend the radial range (see the upper plot, also showing the estimated positions of the  $q=2$  and 3 surfaces). For each radius, the coherence is calculated using the data of neighboring channel pairs in vertical (poloidal) direction. To improve statistics, the coherence functions of the 15 possible pairs for each radius (so pairs 1-2, 2-3, ..., 15-16) are averaged. So, with an

integration time of 0.13s (0.55 to 0.68s) and a sampling rate of 200kHz, effectively  $4 \cdot 10^5$  data points are used for each coherence function.

Figure 6-7 shows that the two bands of Alfvén-like modes at 25 and 43kHz originate from radially separated locations. The estimated locations of the  $q=2$  and 3 resonant surfaces (assuming a parabolic current profile) suggest that the 43kHz mode is associated with  $q=2$  and the 25kHz with  $q=3$ . The relative fluctuation amplitude is about 0.3% for both bands (determined using cross-correlation), although the coherence is somewhat higher for the low-frequency band (about 0.1).

During the second phase (>2.3s), the Alfvén-like modes were not visible with ECE-Imaging. Possibly, because the amplitude is too small (suggested by the weaker pick-up coil signal). Again, caution is needed in interpreting the fluctuations as  $T_e$  fluctuations. Due to the relatively low density during the first phase, the optical thickness ranged from about 1 for the outermost channels to 6 for the innermost. So, although for the innermost channels the parasitic  $n_e$  fluctuations can safely be neglected, for the outermost channels  $a$  (Eq. 6-14) is about 0.5.

### 6.4 Conclusions and discussion

The two examples of fluctuation measurements show that the detection of fluctuations with amplitudes significantly (more than an order of magnitude) lower than the thermal noise level is possible using cross-correlation techniques. The lowest detected fluctuation amplitude of about 0.2% is close to the predicted sensitivity for correlation techniques.

The most pronounced example of a high frequency fluctuation is the quasi coherent mode at the plasma edge. The amplitude of this mode, about 3% at the very edge, decreases rapidly with decreasing radius until it is no longer detectable by ECE-Imaging. The ECE-Imaging measurements suggest  $n_e$  and  $T_e$  fluctuations are comparable in amplitude for this mode. Radial and poloidal correlation length of a few cm and a decorrelation time of about  $1 \cdot 10^{-5}$ s are observed. The measurements of the quasi-coherent mode demonstrated that ECE-Imaging is (at least) sensitive to fluctuations with  $f \leq 100\text{kHz}$ ,  $\lambda \geq 0.07\text{m}$  ( $k \leq 1\text{cm}^{-1}$ ), and relative amplitude larger than 0.2%

Deeper into the plasma core, the observation of high frequency  $T_e$  fluctuations with ECE-Imaging is rare. The Alfvén-like mode is an example of a high frequency, low mode number fluctuation that is visible. The ECE-Imaging data shows that the different branches of this fluctuation originate from different radii, and are probably related to the rational  $q$  surfaces.

Can ECE-Imaging observe the broadband turbulence responsible for the anomalous transport? In [Krämer-Flecken 2003/2004] it is argued that the quasi-coherent fluctuation is the ITG mode. Indeed the ECE-Imaging data of this mode is very reminiscent of the broadband turbulence measured by for instance [Cima 1995]. Frequency, bandwidth, wave number and the radial dependence of the amplitude are all comparable. Only the absolute value of the amplitude is somewhat smaller (0.2% in the centre instead of 0.5%), causing the fluctuations to drop below the statistical

noise level. It is however known from the O-mode reflectometer measurements that the mode is also present deeper into the plasma core with density fluctuation levels of about 0.3% at half radius [Krämer-Flecken 2003]. These measurements also show that further inside the plasma, the wavelength of the mode decreases, the wave numbers increasing from about  $1 \text{ cm}^{-1}$  at the edge up to about  $3 \text{ cm}^{-1}$  at  $\rho=0.4$ . For reference, ECE-Imaging is designed to be sensitive for  $k < 2.8 \text{ cm}^{-1}$  [Park 2003]. So, both the smaller wavelength and the smaller amplitude make the fluctuations harder to measure with ECE-Imaging. In [Cima 1995] it was already demonstrated that the fluctuation levels depend very critically on the focussing (transverse spatial resolution) of the ECE channels, indicating a large part of the fluctuation amplitude is attributable to higher  $k$  components. So it can be concluded that the broadband fluctuations are at the edge of the capabilities of ECE-Imaging; visible at the edge, but not in the centre.



## 7 Experimental determination of the island parameters

ECE-Imaging produces large amounts of data, which, in its raw form, is often hard to interpret. For the analysis of magnetic islands, described in chapters 8 and 9, parameters like island width and  $T_e$  profile are needed, which cannot be directly extracted from the raw ECE-imaging data. Data of the time history of one full island rotation period is used to make a 2D poloidal reconstruction of the island. This way of visualizing the ECE-imaging data greatly facilitates the interpretation and analysis of (nearly) constant frequency magnetic islands. The procedure to extract the island parameters is described in this chapter.

### 7.1 Calibration and filtering

Before constructing the poloidal reconstruction, the ECE-Imaging data is (cross) calibrated on Thomson scattering and filtered using Singular Value Decomposition.

The ECE-Imaging system itself is not calibrated. The 128 channels all have different sensitivities (Volts per keV) and offsets. For a meaningful 2D visualization of the data, some kind of calibration is necessary. Often, a relative calibration (for instance by normalizing the channels to their average value) is sufficient, which doesn't require another calibrated  $T_e$  diagnostic. If, however, the absolute value of  $T_e$ , or the shape (mainly the radial gradient) of the  $T_e$  profile are important, the ECE-Imaging data has to be cross-calibrated with a different calibrated  $T_e$  diagnostic. For the study of magnetic islands, the ECE-Imaging system is cross-calibrated with the Thomson scattering diagnostic. Thomson scattering measures the  $T_e$  profile during one or more (typically 10) short pulses along a vertical chord in the plasma slightly displaced from the plasma centre, see chapter 3. By estimating the shape of the magnetic flux surfaces in equilibrium (mainly the Shafranov shift), the Thomson  $T_e$  profile can be projected on the equatorial plane and directly applied to calibrate ECE-Imaging. The ECE-Imaging channels are cross calibrated by setting the measured average  $T_e$  during (a small time window around) the Thomson pulses equal to the (projected) Thomson  $T_e$  at the corresponding minor radius. As  $m/n=2/1$  islands are roughly located at half radius, this procedure is not very sensitive to uncertainties in the position of the plasma centre. Also,  $n_e$  and  $T_e$  are large enough for the plasma to be optically thick, so the ECE-Imaging signal does not contain a parasitic  $n_e$  contribution.

To reduce the thermal noise inherent to all ECE diagnostics, the 2D data is filtered using Singular Value Decomposition (SVD), a standard mathematical technique to decompose matrices into biorthogonal pairs of eigenvectors. SVD is a powerful tool in analyzing data of diagnostics with a large number of spatial channels, all

representing comparable data ([Nardone 1992],[Dudok 1994]). The ECE-Imaging data of  $N$  time samples from the 128 channels builds an  $N$  by 128 matrix. SVD splits this data into 128 pairs of orthogonal space and time eigenvectors of respectively length 128 and  $N$ , the so called *topos-chronos* pairs, which are specific for the given data set. The eigenvalues of these eigenvector pairs are called the ‘singular values’. One can compare SVD to Fourier analysis. The Fourier components are the analogues to the singular values. The difference is that Fourier analysis expands the data in the orthogonal basis of harmonic functions, whilst SVD expands the data in the orthogonal basis of eigenvector pairs specific for the data set under consideration. This can be a large advantage: An infinite number of Fourier components is needed to describe a sawtooth, while in SVD only one *chronos* is needed. Also, if data *can* be represented by only one eigenvector pair, SVD *does* represent it by only one pair with (large) nonzero eigenvalue. If, on the other hand, the data is totally incoherent (uncorrelated white noise on all channels), SVD needs all 128 eigenvector pairs, all with comparable (low) eigenvalue, to describe the data.

By only keeping the eigenvectors with the largest eigenvalues, the data is filtered. The more redundancy (so double information) in the data, the less eigenvector pairs SVD needs to accurately describe the data and the more accurate these eigenvectors are. There is a large amount of redundancy in the ECE-Imaging data of islands. Because the islands rotate poloidally, all information is seen 16 times by the 16 vertical channels, only slightly phase-shifted. Also the data from the 8 radial channels display large similarities. It can hence be expected that the (coherent part of) this data can be described by a small number of eigenvector pairs. To avoid throwing away physics, the number of SVD components kept, is taken larger than strictly necessary. Typically the highest 30 of 128 eigenvector pairs are kept for describing magnetic island data. So the SVD filtering throws away most noise (roughly three quarters), and keeps practically all (coherent) physics, without limiting the space or time resolution of the signals (as is the case in ‘smoothing’).

## 7.2 Poloidal reconstruction of the island

To visualize the ECE-Imaging data in an easily interpretable way, a poloidal reconstruction is used. From this reconstruction of the ‘full’  $2/1$  island, the main island parameters like island width and  $T_e$  profile are extracted. Figure 7-1 gives a typical example of ECE-Imaging data of a  $2/1$  magnetic island. The observation volume of ECE-Imaging is about 8 by 16 cm, for the island experiments located at the  $q=2$  surface at the low field side of TEXTOR, see Figure 7-1b. The minor radius of the  $q=2$  surface is typically 30 cm (the TEXTOR minor radius is 47 cm), so ECE-Imaging covers less than 10 % of the poloidal circumference of the  $q=2$  surface. It is therefore hard to get a comprehensive view of the mode structure from the ‘raw’ data, as at any time only a small part of the island is observed by ECE-Imaging. The plasma around the  $q=2$  surface is assumed to rotate like a rigid rotator (constant velocity as a function of minor radius), which is confirmed by the phase velocity as a function of radius measured by ECE-Imaging. It is therefore possible to map the data for one full island rotation period onto a poloidal shell to visualize the entire poloidal mode structure (see Figure 7-2). In this mapping, time takes over the role of the poloidal angle. As every part of a rotating magnetic island is measured by more than one ECE-Imaging channel, there is a large amount of redundancy in the data (the 16 vertical



channels of each column see the same part of the island, only time shifted). Using only one radial row of 8 channels for the reconstruction already gives a good result, because the (redundant) information of the other 15 rows is already used in the Singular Value Decomposition to determine the spatiotemporal eigenvectors, and the statistics for all 128 channels is hence contained in the SVD filtered signal for this one row of 8 channels. So although the 2D character of ECE-Imaging is not directly used, the analysis does profit from the large number of available channels. The rotational reconstruction is a representation of the mode structure of the island as observed at the low field side, assuming a constant rotation velocity around a perfectly circular poloidal shell. In reality the rotation velocity can vary around this shell, as long as the mode frequency stays constant (so a higher poloidal velocity has to be cancelled by a larger poloidal wavelength). Also, the real island probably has a different shape at the high field side (more symmetrical with respect to the  $q=2$  surface). The reconstruction, however, is mainly used to derive the width of the island (at the low field side), which is insensitive to these effects and the exact shape ( $q=2$  surface might be slightly noncircular) and radius of the reconstructed shell. A reconstruction contains data of a full poloidal rotation period (2 ms), and the derived island parameters are hence an average over this period. So, the procedure is only valid if the changes in the mode structure are slow compared to the rotation period.

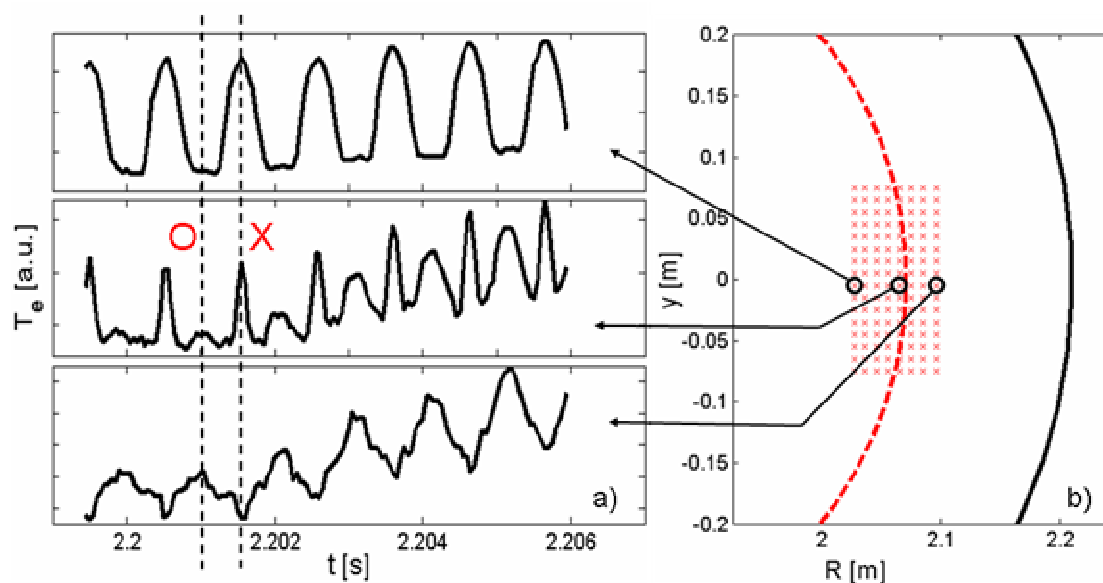


**Figure 7-1:** *a) Typical ECE-Imaging  $T_e$  time traces of a 2/1 magnetic island (#99183). At 2.2s a local heating source (ECRH) is introduced inside the island. b) The position of the three channels with respect to the  $q=2$  surface. For channels inside the island radius, the maxima in the signal correspond to the time at which the X-point passes by the observation volume. Channels outside the island radius show maxima if the O-point passes by. So there is a phase inversion between the inner and outer channels. Note the increasing O-point  $T_e$  peaking in the central channel after ECRH switch on.*

Two typical examples of poloidal island reconstructions are shown in Figure 7-2. Without a large heat source, the  $T_e$  profile inside the island is (almost) flat, as in the left reconstruction. The elliptically deformed plasma centre is clearly visible. If, as is

shown in the right reconstruction, heat is deposited inside the island (here by ECRH), the  $T_e$  profile becomes peaked at the O-point, revealing the full island structure.

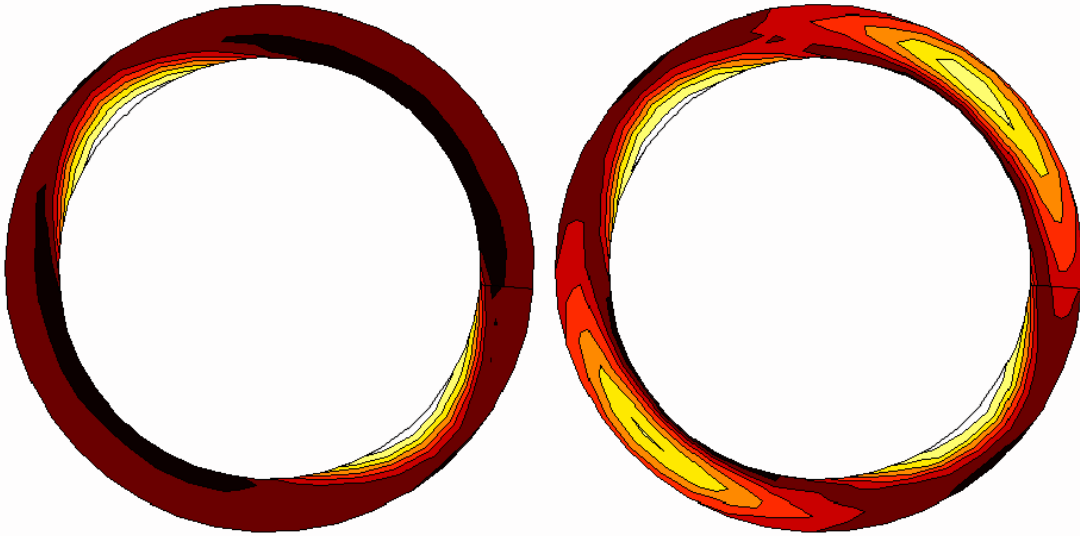


**Figure 7-2:** Typical examples of poloidal island reconstructions. The left plot shows an island with a flat  $T_e$  profile. The hotter plasma centre is approximately elliptically deformed. At the right, a (ECRH) heated island with a peaked  $T_e$  profile is shown. The maximum of this peaking corresponds to the O-point.

### 7.3 The fitting procedure

An algorithm is used to extract the main island parameters from the poloidally reconstructed ECE-Imaging data. This enables to analyze the large amount of data in an objective way. To determine the island width, an ellipse (at temperature  $T_{ell}$ ) is fitted to the data, see Figure 7-3. A standard least mean squares fit, minimizing the  $T_e$  deviation between the ellipse and the data, is used to fit the ellipse to the data, which is regarded as a surface in the 3D  $(r, \theta, T)$  space (in the 2D projection in Figure 7-3, the  $T_e$  direction is colour coded). The fitted ellipse has four free parameters: major radius  $a$ , minor radius  $b$ , orientation angle  $\theta_{ell}$  and temperature  $T_{ell}$ . The difference between the major radius  $a$ , and minor radius  $b$  of this ellipse gives the displacement (radial excursion) of the fitted  $T_e$  contour, and is a measure for the width of the island. This method works for islands with and without a peaked  $T_e$ . Also, not the entire island has to be visible (which is often the case due to the limited radial extent of the ECE-Imaging channels). The four free parameters of the ellipse are too much to be fitted in one step, so first a ‘trial’ ellipse with fixed  $[a, b]$  is fitted to find the  $[\theta_{ell}, T_{ell}]$ .

The minor radius  $a$  of the ellipse is chosen such that the ellipse is slightly smaller than the inner separatrix of the island, to ensure it lies in the steep  $T_e$  gradient of the hot central plasma. If the fitted ellipse is chosen too large (too close to, or even larger than the inner island separatrix), the flat  $T_e$  gradient inside the (unheated) island separatrix causes the fit to behave unstably (the deviation between ellipse and data becomes independent of  $b$ ). The wanted value of  $a-b$  is insensitive to the exact size of the ellipse, as long it is close to the size of the inner separatrix. Also,  $a-b$  is only meant as

a *measure* for  $w$ , which is also true if the fitted ellipse is smaller than the island separatrix.

For islands with a peaked  $T_e$  profile (ECRH heated), the O-point position ( $r_{max}$ ) and temperature ( $T_{max}$ ) are found by looking for the  $T_e$  maximum on the minor axis of the fitted ellipse. Also, the exact position of (a point of) the inner separatrix can be determined by finding the minimum  $T_e$  between the O-point and the fitted ellipse.

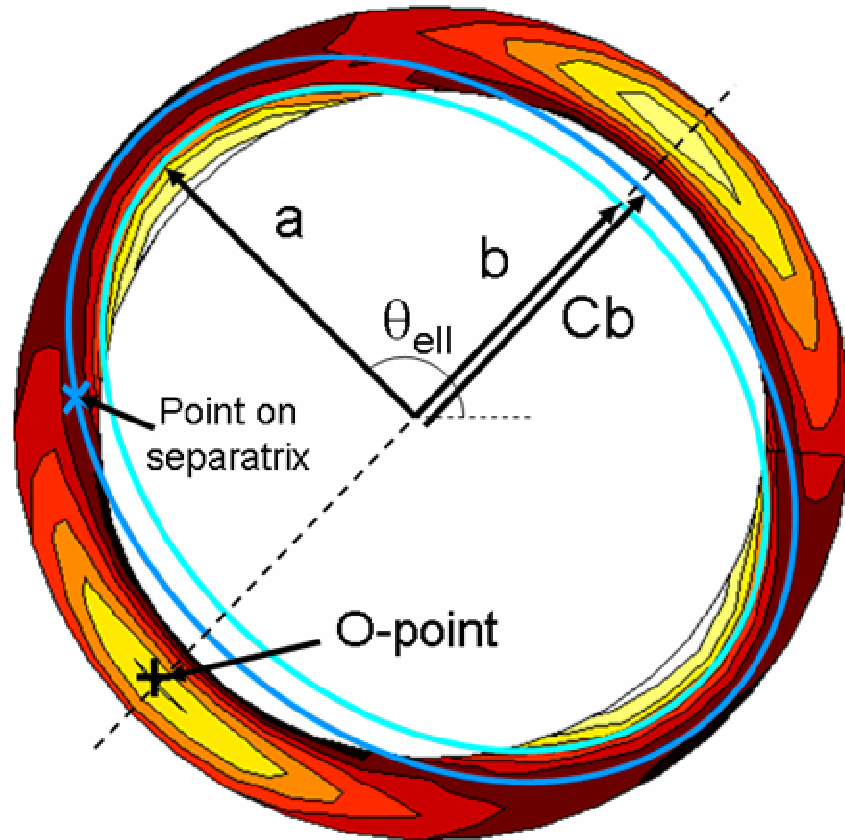


**Figure 7-3:** Overview of the various parameters that are determined by the fitting procedure, being the four free parameters  $[a, b, \theta, T]_{ell}$  of the ellipse, the radius and  $T_e$  of the O-point, the position of a point on the separatrix and the correction factor  $C$  needed to overlay the ellipse with this point on the separatrix.

As mentioned, the fitted ellipse is too small to represent the (inner) separatrix. This can be corrected for by introducing a correction factor  $C$ , defined such that  $Ca$  and  $Cb$  are the major and minor radii of the ellipse passing through the found separatrix position.

Two definitions of the full island width  $w$  can be used, see Eq. 7-1. First, the difference between major and minor radii of the fitted ellipse is a measure for the island width, with an unknown proportionality constant  $A$ . Second, twice the difference in radius between O-point and (corrected) minor radius of the ellipse. The second definition is a direct measure for the island width, but is only useable for heated (peaked) islands. The second definition can be used to calibrate the first method, yielding a typical proportionality constant  $A$  of 1.5 (the exact value has to be determined from experiment to experiment).

$$w \approx A(a - b) \approx 2(r_{\max} - Cb) \quad \text{Eq. 7-1}$$

The  $T_e$  profile inside the island is evaluated on a circle through the O-point (see Figure 7-4). In this way the (relative)  $T_e$  profile is independent of any (relative) calibration errors, since all points on a circle are measured by the same ECE-Imaging channel(s). An example of a  $T_e$  profile inside an island is shown in Figure 7-4 (the red line). The  $T_e$  is plotted versus the normalized effective island radius  $\rho^*$ , related to the island flux surface label  $\Omega$  (see chapter 2) as

$$\rho^* = \sqrt{\frac{\Omega + 1}{2}} \quad \text{Eq. 7-2}$$

Going once around the circle through the O-point, the  $T_e$  profile is seen four times (the four black lines in Figure 7-4) as the values of  $\Omega$  repeat themselves. The  $T_e$  profile used in the analysis is the average of these four profiles (the red line). As the islands are generally slightly asymmetric, the O and X-points lie on slightly different minor radii, and part of the  $T_e$  outside the island ( $\Omega > 1$ ) is visible on the circle through the O-point. The separatrix corresponds to the minimum  $T_e$  on the  $T_e$  profile, fixing  $\rho^* = \Omega = 1$ . The  $T_e$  peaking  $\Delta T_e$  is defined as the difference between O-point and separatrix  $T_e$ .

In the next two chapters, the island parameters derived as described here play a central role.

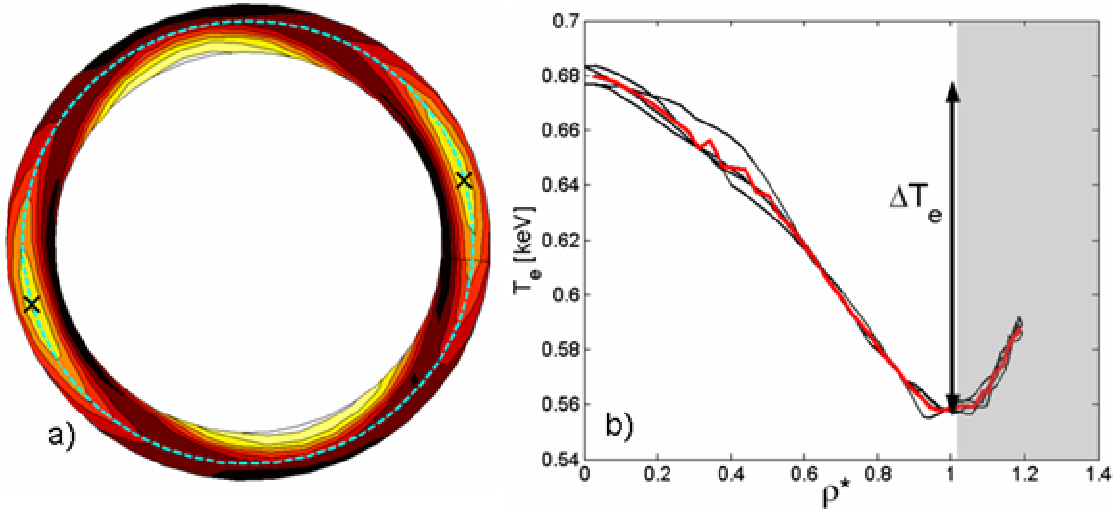


**Figure 7-4:** a) Circle on which the  $T_e$  profile is evaluated. As all data points on the circle are measured by the same ECE-Imaging channels, this  $T_e$  profile is insensitive to relative calibration errors. b) Example of a  $T_e$  profile inside an island as a function of the normalized island radius  $\rho^*$ . Going once around the circle, the  $T_e$  profile is observed four times. The minimum in the average profile determines the position of the separatrix. The part outside the separatrix (grey area) is discarded. The difference between O-point and X-point  $T_e$  is referred to as  $\Delta T_e$ .

## 8 Dynamics of tearing modes in the presence of a perturbation field\*

**Abstract.** The influence of a magnetic perturbation field on the dynamics of tearing modes in the TEXTOR tokamak is investigated. A set of experiments is performed to quantitatively test the generally accepted theory, mainly developed by Fitzpatrick. The perturbation field is generated by the Dynamic Ergodic Divertor (DED). This perturbation field causes shielding currents to flow on the resonant  $q$  surfaces which have two effects: they alters the stability of tearing modes and exert a torque on the rational surfaces, influencing the plasma rotation. The rotation frequency and width of tearing modes, as well as the relative phase shift to the perturbation field are measured with the ECE-Imaging diagnostic. The evolution of the island width (determined by a modified version of the Rutherford equation) and the processes of mode penetration and unlocking (determined by the balance of all torques acting on the island) are compared with theory using a numerical simulation, giving satisfying agreement.

### 8.1 Introduction

The formation of tearing modes (or magnetic islands) in tokamaks decreases the global confinement of energy and particles, and hence should generally be avoided. Furthermore, large islands can lead to plasma disruptions. Magnetic perturbation fields resonant with the island are capable of both generating an island, and locking a pre-existing island. Although perturbation fields normally work destabilizing, they can also be used to suppress islands ([La Haye 2006], [Lazzaro 1988]). Perturbation fields are present in all tokamaks. Two examples are the stationary error field caused by deviations of the magnetic field from axisymmetry (for example due to coil misalignments and the field ripple), and the perturbation field a rotating island causes by inducing currents to flow in a conducting wall or on a different resonant surface. So the interaction of tearing modes with perturbed magnetic fields is of major importance for the understanding of tearing mode dynamics. Experimental investigation of this interaction is normally difficult, because the perturbation field is in general unknown and uncontrollable, enabling only a qualitative comparison with theory ([Morris 1992b], [Savrukhin 2000]). This paper describes a set of experiments on the TEXTOR tokamak, using the very controllable and fully known (rotating) perturbation field of the Dynamic Ergodic Divertor (DED) [Special Issue 1997]. In these experiments the DED perturbation field strength is increased until an  $m/n=2/1$  tearing mode (not present before) is destabilized ([Koslowski 2006], [Liang 2004]).

---

\* The work presented in this chapter is (in altered form) submitted to NF

This process is generally referred to as mode penetration, and occurs when the plasma rotation (more accurately, the perpendicular electron rotation) is forced to be equal to the perturbation field rotation (due to an electromagnetic torque on the plasma). The island is observed to grow to a saturated width of about 10 cm and is locked to the perturbation field, with only a very small phase difference between the (plasma) island and the vacuum island. The vacuum island is the fictive island in the ‘vacuum magnetic field’, defined as the superposition of the perturbation field and the equilibrium magnetic field. When the DED perturbation field strength is slowly decreased, first the locking becomes less strong, resulting in an increased phase difference between plasma and vacuum islands (but still equal rotation frequencies). Finally, at a perturbation field strength much smaller than the one required for mode penetration, the island unlocks and the mode rotation frequency relaxes to its ‘natural’ value (see Figure 8-1). Due to apparent changes in the tearing mode stability (probably related to the coupling with a mode at the  $q=1$  surface), the island doesn’t disappear after switching off the DED, but remains, without large changes in island width. Note that the sawtooth oscillations disappear approximately at the moment of penetration (or coupling with the  $q=1$  mode), and do not reappear after unlocking.

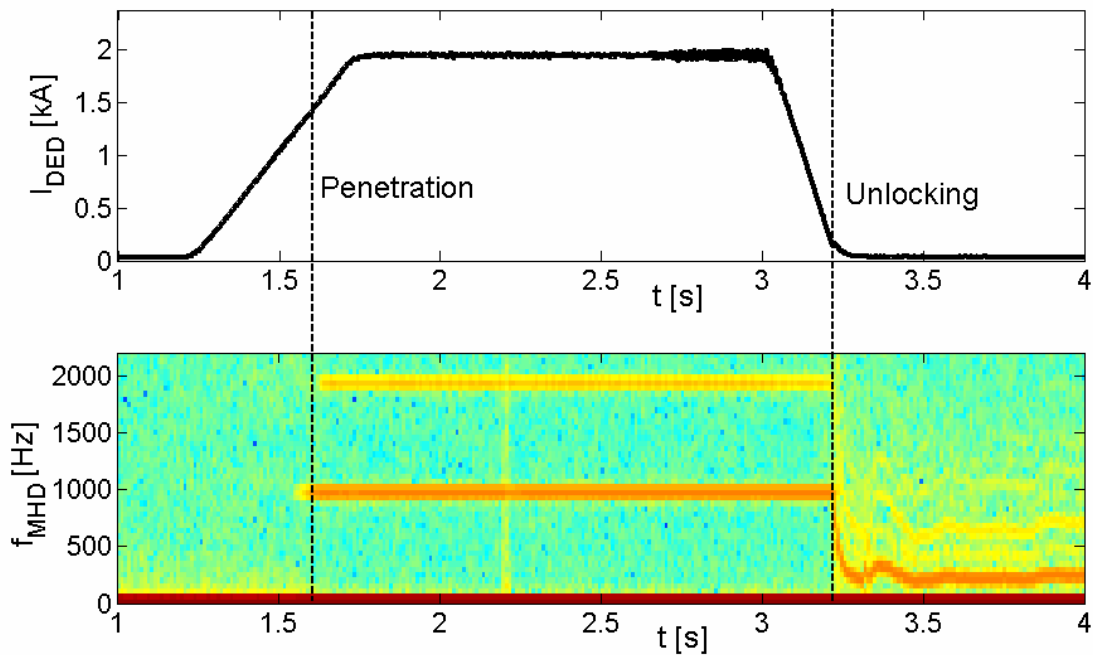


**Figure 8-1:** Penetration and unlocking of the  $m/n=2/1$  tearing mode. a) Dynamic Ergodic Divertor coil current amplitude. b) Spectrogram of an ECE-Imaging channel at the island position. Before switch on of the DED, no island is present. After penetration, the island frequency is locked to the 1 kHz rotation of the DED field. Unlocking occurs at a much lower DED current than the penetration threshold, after which the island frequency relaxes to its natural value.

The most important qualitative features predicted by theory that are to be experimentally verified are:

- The sudden growth of an island during penetration.
- The sudden stepwise change in  $d\omega/dt$  during unlocking.

Both representing jumps between two bifurcated states.

- The threshold perturbation field amplitude for unlocking being much smaller than the one for penetration (hysteresis).
- The change in phase difference between plasma and vacuum islands before unlocking.

Also a qualitative comparison between theory and experiment will be performed.

After describing the experimental setup in paragraph 8.2, the general theoretical framework of the interaction between tearing modes and perturbation fields, mainly developed by Fitzpatrick, will be summarized in paragraph 8.3. Paragraph 8.4 will apply this theory to the experimental result on the various phases of the interaction process, being the mode penetration, the mode growth, and the mode unlocking. A set of TEXTOR discharges with identical discharge parameters is used for the analysis. A numerical simulation, modelling the evolution of the island width and the plasma velocity profile, is used to take into account the various (electromagnetic, viscous and NBI) torques as realistic as possible for these discharge parameters. A discussion of the results is finally given in paragraph 8.5.

## 8.2 Experimental setup

### 8.2.1 The DED perturbation field

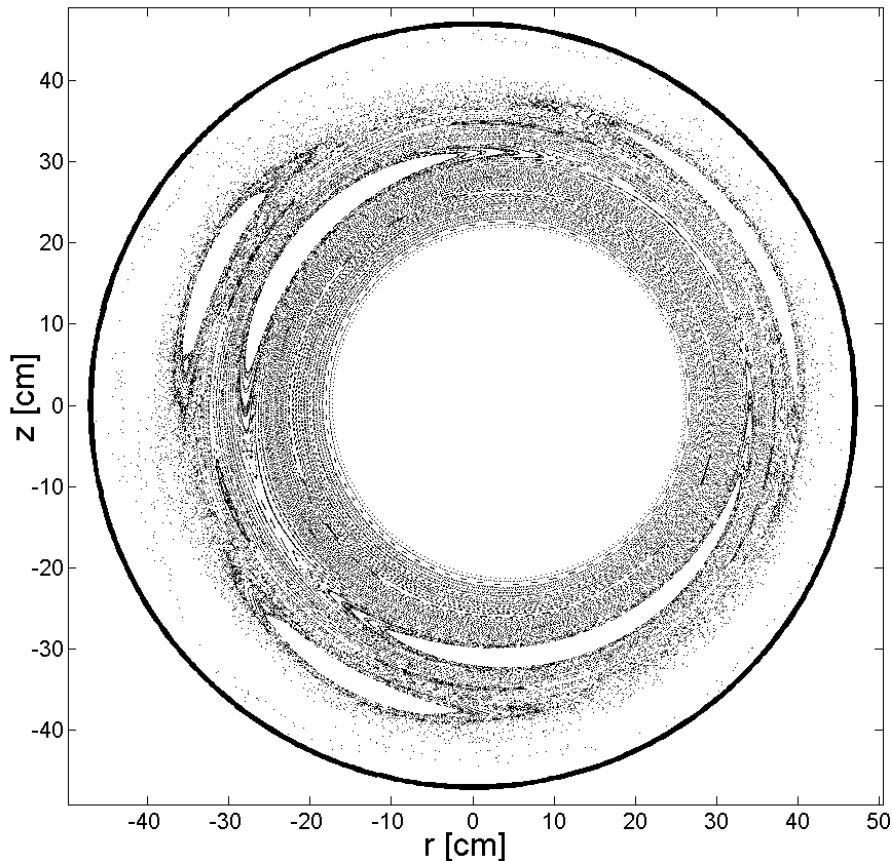
For these experiments, the Dynamic Ergodic Divertor (DED) [Special Issue 1997] is operated in the so called 3/1 DED mode. The currents through the DED coils are arranged such that they introduce a perturbation field with a base  $m=3$ ,  $n=1$  mode structure, with strong side bands at other mode numbers, in particular  $m/n=2/1$  and  $1/1$ .

Figure 8-2 shows the vacuum field for the experiments described in this paper, containing large 3/1 and 2/1 island chains ( $q=1$  surface is not shown). This field results from the superposition of the equilibrium magnetic field with the DED perturbation field. Both DC and AC DED currents are possible. In these experiments (+)1 kHz AC currents are used, resulting in a rotating vacuum field. Note that for an  $m/n$  structure in the vacuum field this means a poloidal rotation frequency of  $n/m$  times 1 kHz, and hence a different apparent poloidal rotation frequency for the different modes. When the current in the DED coils is increased, the vacuum islands become larger. For the 2/1 and 3/1 vacuum islands, both about 4 cm wide in Figure 8-2 (at 2 kA DED current), the relation between the vacuum island width  $w_{vac}$  and the DED coil current amplitude  $I_{DED}$  (in kA) is approximately given by

$$w_{vac}^2 \approx 8 \cdot 10^{-4} I_{DED} \quad \text{Eq. 8-1}$$

It must be stressed however, that Figure 8-2 only represents the magnetic field structure in the absence of a plasma response to the perturbation field. In the presence of a conducting plasma, the magnetic topology changes due to (shielding) currents that are generated on the rational  $q$  surfaces. These currents influence the stability of tearing modes. For these experiments, this results in a plasma in which a 2/1 island is destabilized when the current in the DED coils exceeds a certain threshold. Below this threshold, there is no island in the plasma as the shielding current on the  $q=2$  surface

acts to create a magnetic field that counters the 2/1 component of the DED field. So an island in the vacuum magnetic field doesn't always result in a destabilized tearing mode in the plasma. Nevertheless, the concept of a vacuum island is a useful representation of the topology of the perturbation field. It represents both the amplitude and phase of the perturbation field. In the following, the term 'vacuum island' always refers to the fictive island in the absence of a conducting plasma. In the presence of a plasma, it should only be interpreted as a representation of the perturbation field. If a real tearing mode in the plasma is meant, the term 'plasma island' is used.



**Figure 8-2:** *The vacuum magnetic field [Jakubowski 2004], resulting from the superposition of the DED perturbation field and the equilibrium magnetic field, for the plasma parameters used in these experiments ( $I_p=300$  kA,  $B_T=2.25$  T,  $I_{DED}=2$  kA). The large 2/1 and 3/1 vacuum islands, both with a width of about 4 cm, are clearly visible.*

### 8.2.2 Diagnostics: ECE-Imaging and CXRS

The properties of the plasma islands induced by the DED are measured using the ECE-Imaging (ECE-I) diagnostic [Park 2003]. In these experiments, the position of ECE-I was tuned to the  $q=2$  surface (the BWO frequency set to 102 GHz). For comprehensive visualization of the ECE-Imaging data, a poloidal reconstruction is used in which the data for one full rotation period is mapped onto a poloidal shell, assuming rigid plasma rotation within that thin shell. Note that the poloidal



reconstruction only represents the low field side structure of the island. Figure 8-3 shows two examples for a small (4.5 cm) and a big (about 11 cm) island. The hot, central plasma, approximately elliptically deformed by the island, is clearly visible. The interior of the island itself is visible as a flat temperature region.

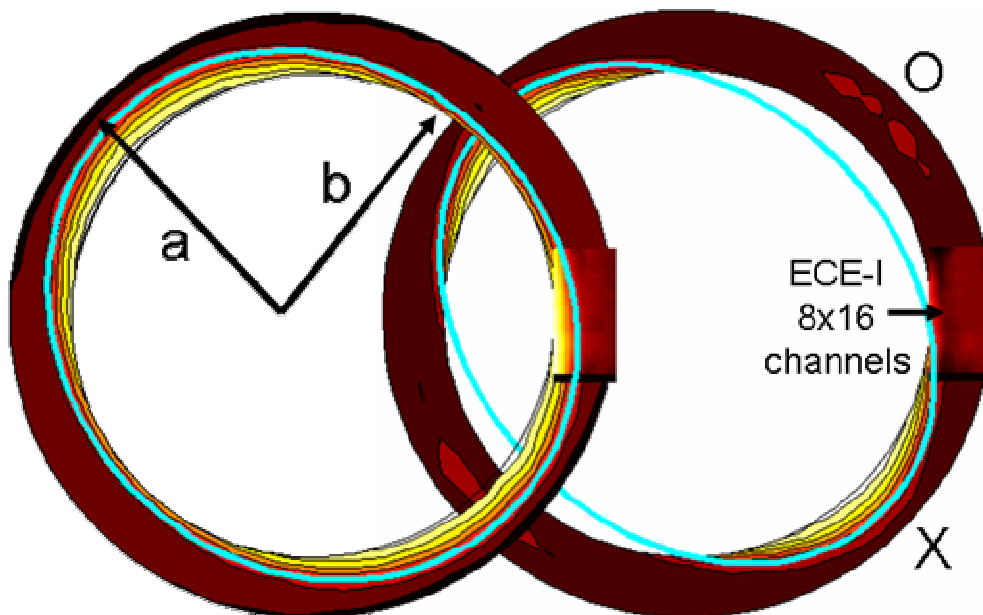


**Figure 8-3:** *The known rotation frequency of the 2/1 island enables a poloidal reconstruction of the island topology using ECE-Imaging. The left reconstruction shows the still small (4.5 cm) island just after penetration (TEXTOR discharge #99175  $t=1.595$  s). The right reconstruction shows the saturated island with a width of approximately 11 cm (at  $t=1.75$  s).*

The (toroidal) plasma rotation plays a crucial role in the interaction between perturbation fields and tearing modes. The profile of toroidal ion rotation can be measured with the charge exchange recombination spectroscopy (CXRS) system on TEXTOR [Donné 2005]. The Doppler shift of the 529 nm  $C^{5+}$  line is a measure for the toroidal (main) ion velocity. This line is emitted by impurity carbon ions that undergo a charge exchange reaction with the neutral particles of the tangential neutral beam injector (NBI) in the ‘co’ direction (positive toroidal direction in the same direction of the plasma current, see Figure 8-7). So, CXRS data is only available when NBI is on. The time resolution of the system is limited to 50 ms. The radial coverage is from the centre of the plasma to about 60% of the minor radius (at the low field side).

### 8.2.3 Discharge scenario and data analysis

The plasma discharges described in this paper all had the same discharge parameters. A toroidal magnetic field of 2.25 T, a plasma current of 300 kA, and a line averaged density of  $2 \cdot 10^{19} \text{ m}^{-3}$  were chosen. A small amount of unbalanced NBI (300 kW) was injected from  $t=1$  to 3.5 s, to allow for CXRS measurements. The DED coil current is

ramped up in about 0.5 s and ramped down again in about 0.25 s after 1.2 s of flat top at 2 kA, see Figure 8-1.

An automated algorithm, described in more detail in chapter 7, is used to extract the main island parameters from the reconstructed ECE-Imaging data. To determine the full island width  $w$  and the phase of the island, an ellipse is fitted to the data (see Figure 8-3). The difference between the major radius  $a$ , and minor radius  $b$  of this ellipse gives the displacement of the fitted temperature contour, and is a measure for the width of the island (The formula used is  $w \approx 1.5 (a - b)$ , where the factor 1.5 is based on experiments with a peaked temperature profile inside the island (by ECRH heating), see chapter 9. In these experiments, both the position of the O-point and the separatrix were accurately measured.).

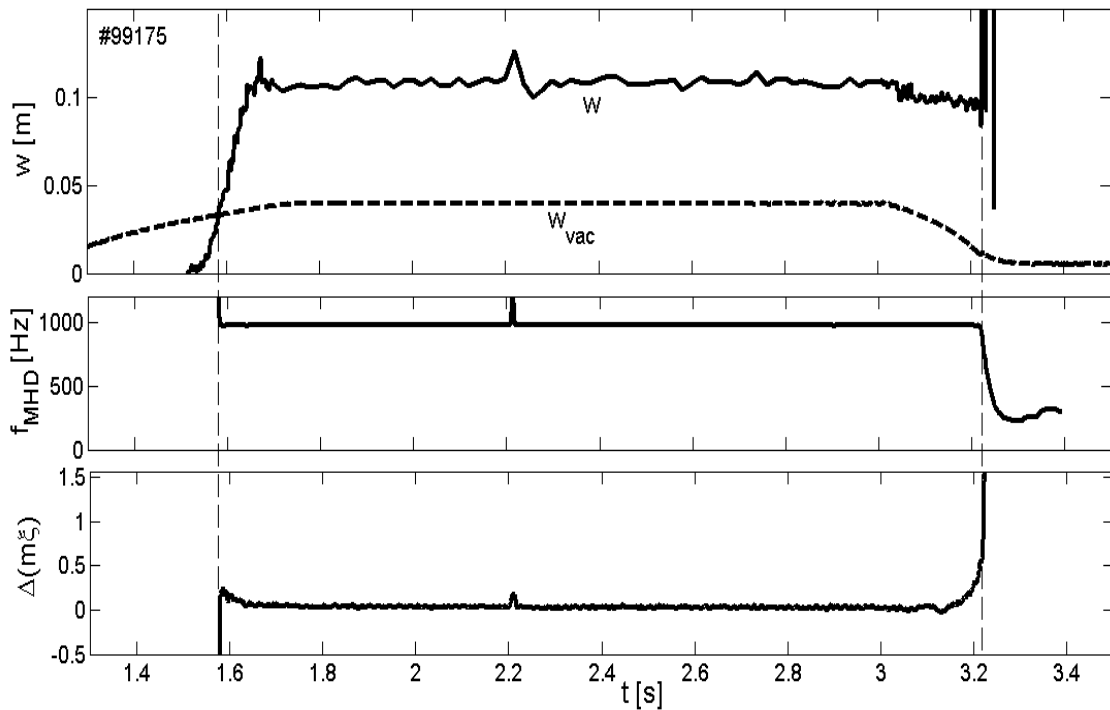


**Figure 8-4:** *The main island parameters: a) The (plasma) island width  $w$  and vacuum island width  $w_{vac}$ . The saturated plasma island width is significantly larger than the vacuum island. b) The MHD frequency, which is equal to the DED frequency during the locked phase. After unlocking it relaxes approximately exponential to the natural frequency. c) The phase difference  $\Delta(m\xi)$  between the plasma and vacuum islands.*

Figure 8-4 gives an overview of the most important (vacuum and plasma) island parameters for a typical discharge (TEXTOR discharge #99175, which is used throughout most of the paper). If the perturbation field (here shown in terms of  $w_{vac}$ ) becomes large enough, a 2/1 island is generated, whose width rapidly (in about 100 ms) increases to a saturated value of about 11 cm. The frequency of this mode is equal to the DED frequency. During the ramp down of the DED current, first the phase difference between the plasma and vacuum island increases, followed by the unlocking of the 2/1 mode. The unlocking is seen as a sudden decrease in rotation frequency, which relaxes approximately exponentially to the natural frequency. After

unlocking, the island remains, while its width is only slightly reduced\*. Note that penetration occurs at about  $w_{\text{vac}}=3\text{cm}$ , while for unlocking the vacuum island width has to be reduced to about 0.5 cm.

The phase of the vacuum island is not actually measured. To determine the phase difference between plasma and vacuum islands, use has been made of the exactly known, and constant, DED frequency. The phase of the vacuum island is given by  $(\omega_{\text{DED}}t + \varphi)$ , where  $\varphi$  is the unknown start phase. The phase difference [denoted as  $\Delta(m\xi)$ , which is  $m$  times the difference in helical angle, see paragraph 8.3.1] is now found by subtraction of this vacuum island phase from the measured phase of the plasma island, choosing  $\varphi$  such that the phase difference during the ‘strongly’ locked phase of the discharge is zero. The experimental determination of  $\varphi$  is hampered by the fact that the DED current is measured using a different timing system than ECE-I uses. The exact relationship between the two (slightly deviating) timing systems is not well enough known to yield a meaningful phase difference (note that a time inaccuracy of 0.00025 s already corresponds to a  $\pi/2$  phase inaccuracy). So, only changes in phase difference are directly experimentally measured. Setting the phase difference to zero during the locked phase is based on theory.

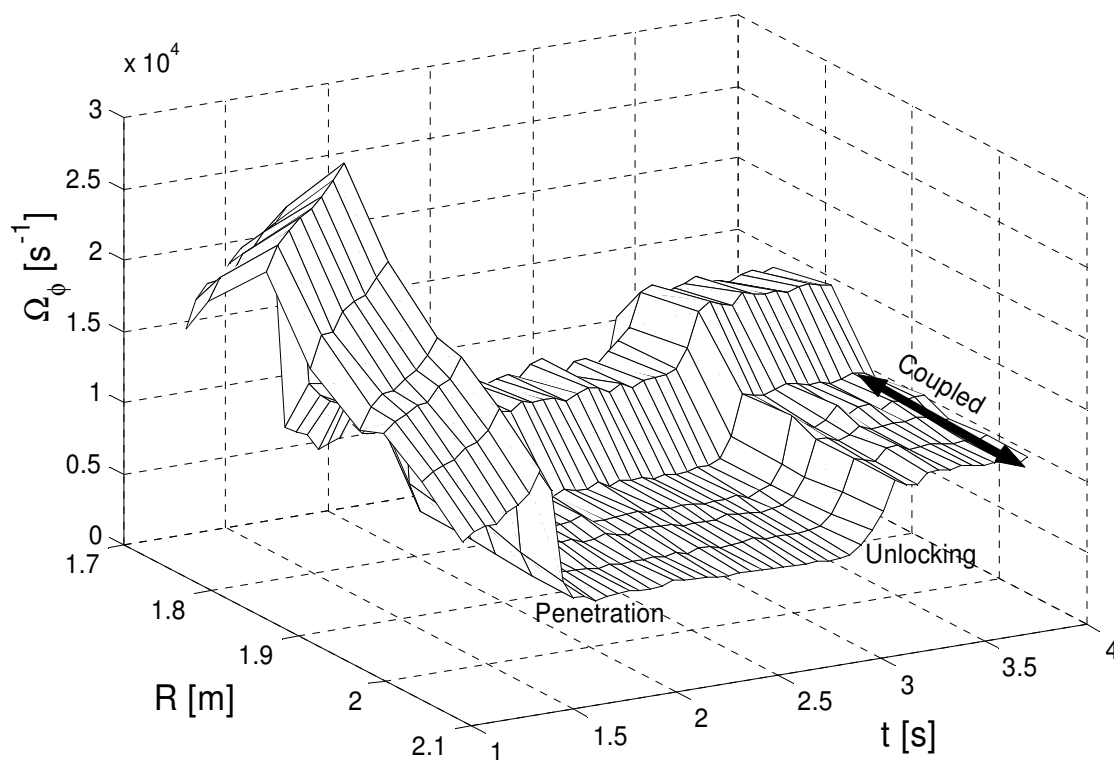


**Figure 8-5:** The radial ion rotation frequency profile (discharge #99175), measured by Charge Exchange Recombination Spectroscopy (CXRS). The data covers the central part of the plasma, up till just inside the  $q=2$  surface. The flat rotation profile after penetration indicates mode coupling between the  $2/1$  island and the  $q=1$  surface (or possible  $1/1$  mode). The mode coupling remains after the DED unlocking.

\* The data shown stops at the moment of unlocking, as the routine used to determine  $w$  fails due to the decreasing ECE fluctuation frequency. The amplitude of the ECE fluctuation however (also a measure for the island width) stays unchanged.

Figure 8-5 gives the toroidal ion rotation profile measured by CXRS. The  $q=2$  surface is located just outside the radial range. Note that a positive change in ion toroidal rotation corresponds to a change in the *negative* direction for the MHD frequency (more on this later, see Eq. 8-9), so penetration is seen as a rapid decrease in toroidal ion rotation, and unlocking as an increase. The natural rotation profile, seen before penetration, shows a peaked rotation profile in the direction of the NBI torque. After penetration, a broad flat region in the rotation profile is observed, rotating at the resonant DED frequency (corrected for the diamagnetic drift) [de Bock 2007]. This is interpreted as a coupling between the 2/1 island and a mode at the  $q=1$  surface (1/1 mode). This coupling remains after switch off of the DED, so that the modes at the  $q=1$  and 2 surfaces unlock simultaneously from the DED. Coupled  $m/n=1/1$  and 2/1 islands are common in TEXTOR, see for instance [de Vries 1997].

## 8.3 Theoretical framework

This paragraph summarizes the theoretical ingredients used in this chapter. See chapter 2 for a more thorough treatment.

### 8.3.1 The interaction of islands with a perturbation field

The shielding currents on the rational surfaces, caused by the (DED) perturbation field, have two important consequences for the dynamics of magnetic islands. The ‘in phase’ component of this shielding current influences the stability of the island, and the evolution of the island width. This is reflected in a modification to the Rutherford equation describing the growth of magnetic islands ([Fitzpatrick 1993], [Fitzpatrick 1998], [Fitzpatrick 1991], [Morris 1992a])

$$0.82\tau_R \frac{dw}{dt} = r_s^2 \Delta'(w) + 2mr_s \left( \frac{w_{vac}}{w} \right)^2 \cos(\Delta(m\xi)) \quad \text{Eq. 8-2}$$

where  $\Delta(m\xi) = m(\xi_{O,plasma} - \xi_{O,vacuum})$  is the phase difference between the O-points of the plasma island and the vacuum island. The helical angle  $\xi = \theta - \frac{n}{m}\phi$  is directed perpendicular to the equilibrium field lines at the  $q=m/n$  surface.

The component of the shielding current in ‘phase quadrature’ doesn’t influence the evolution of the island width, but results in an electromagnetic torque  $T_{EM}$  in the direction of  $\xi$  on the island, trying to reduce the phase difference between the plasma and vacuum islands. In practice it turns out that only the toroidal component of this torque is important, because poloidal flow damping of the ions effectively prohibits any significant ion rotation in poloidal direction [Stix 1973]. The toroidal component of this torque is given by ([Fitzpatrick 1993], [Fitzpatrick 1998], [Fitzpatrick 1991]):

$$T_{\phi,EM} = -4\pi^2 \frac{mn}{\mu_0 R_0} C^2 w_{vac}^2 w^2 \sin(\Delta(m\xi)) \quad \text{Eq. 8-3}$$

where the proportionality constant  $C$  (containing all plasma equilibrium dependent parameters) is given by

$$C = \frac{r_s B_\phi \left| \frac{dq}{dr} \right|}{16q^2} \quad \text{Eq. 8-4}$$

If the MHD frequency  $\omega$  is equal to the frequency of the externally applied perturbation field  $\omega_{\text{DED}}$  (as is the case for a locked island), Eq. 8-3 can be directly applied. If, however, there is a difference in frequency, referred to as the ‘slip’ frequency  $\Delta\omega = \omega - \omega_{\text{DED}}$ , one has to distinguish between two different cases, depending on the size of the (induced) plasma islands. For both cases (referred to as the ‘non-linear’ and ‘linear’ cases), Eq. 8-3 is valid, but the expression for the time averaged electromagnetic torque in terms of the slip frequency  $\Delta\omega$ , takes different forms.

Large, ‘non-linear’, islands always rotate at the MHD frequency. The electron fluid is not allowed to slip through the island. In this case, a non-zero  $\Delta\omega$  results in a plasma island that is alternately dragged in and out of phase with the perturbation field, giving a periodic growth and decay of the island and a fluctuating electromagnetic torque. Neglecting the  $\Delta'$  term in the modified Rutherford equation Eq. 8-2 one finds a time averaged electromagnetic torque

$$\langle T_{\phi, \text{EM}} \rangle_{\text{non-linear}} = -\text{sign}(\Delta\omega) \cdot 0.5356 \cdot 4\pi^2 \frac{mn}{\mu_0 R_0} C^2 w_{\text{vac}}^2 w_0^2 \quad \text{Eq. 8-5}$$

which is proportional to  $\Delta\omega^{2/3}$  and in the direction to decrease  $\Delta\omega$ . The maximum induced island size during one fluctuation (containing the  $\Delta\omega$  dependency) is given by:

$$w_0 = 1.939m^{1/3} \left( \frac{w_{\text{vac}}^2 / r_s^2}{\Delta\omega \tau_R} \right)^{1/3} r_s \quad \text{Eq. 8-6}$$

For very small islands, the plasma does not necessarily rotate at the same angular velocity as the island, but slips through it to some extent. This effect is caused by the viscosity between the island and the surrounding plasma ‘flowing around’ it. This viscosity arises in a thin layer (with a thickness of the order of the linear layer mentioned in [Fitzpatrick 1993], [Fitzpatrick 1998]), where an exchange of particles between plasma and island occurs. The rotation frequency of the induced plasma island can now slip with respect to the MHD frequency. In fact, it will now rotate at the frequency of the external perturbation field, but with a phase lag, resulting in a non-fluctuating torque and mode amplitude. For these experiments, the linear layer is in the ‘visco-resistive’ regime treated in ([Fitzpatrick 1993], [Fitzpatrick 1998]), with a typical (visco-resistive) linear layer width of 3 mm. If the driven island width is larger than the linear layer width, the non-linear description is appropriate. When however the island widths are comparable to, or smaller than the linear layer width (as is usually the case during the early stages of mode penetration), the following linear theory is needed. In the visco-resistive limit, the *steady* torque is given by [Fitzpatrick 1993]

$$T_{\phi,EM,linear} = -4\pi^2 \frac{2m^2 n}{\mu_0 R_0 |\Delta'_0 r_s|} \frac{\Delta\omega\tau_{rec}}{1 + (\Delta\omega\tau_{rec})^2} C^2 w_{vac}^4 \quad \text{Eq. 8-7}$$

where  $\Delta'_0$  is the stability parameter at zero island width for the mode in question and

$$\tau_{rec} = \frac{2.1036}{|\Delta'_0 r_s|} \frac{\tau_H^{1/3} \tau_R^{5/6}}{\tau_V^{1/6}} \quad \text{Eq. 8-8}$$

is the typical reconnection time scale in the visco-resistive limit. Figure 8-6 gives an example of both the non-linear and linear theory for typical TEXTOR parameters. The two theories are very similar (both showing the resonance at the perturbation field frequency and similar torque amplitudes) despite the somewhat different parametric dependencies and physical meaning.

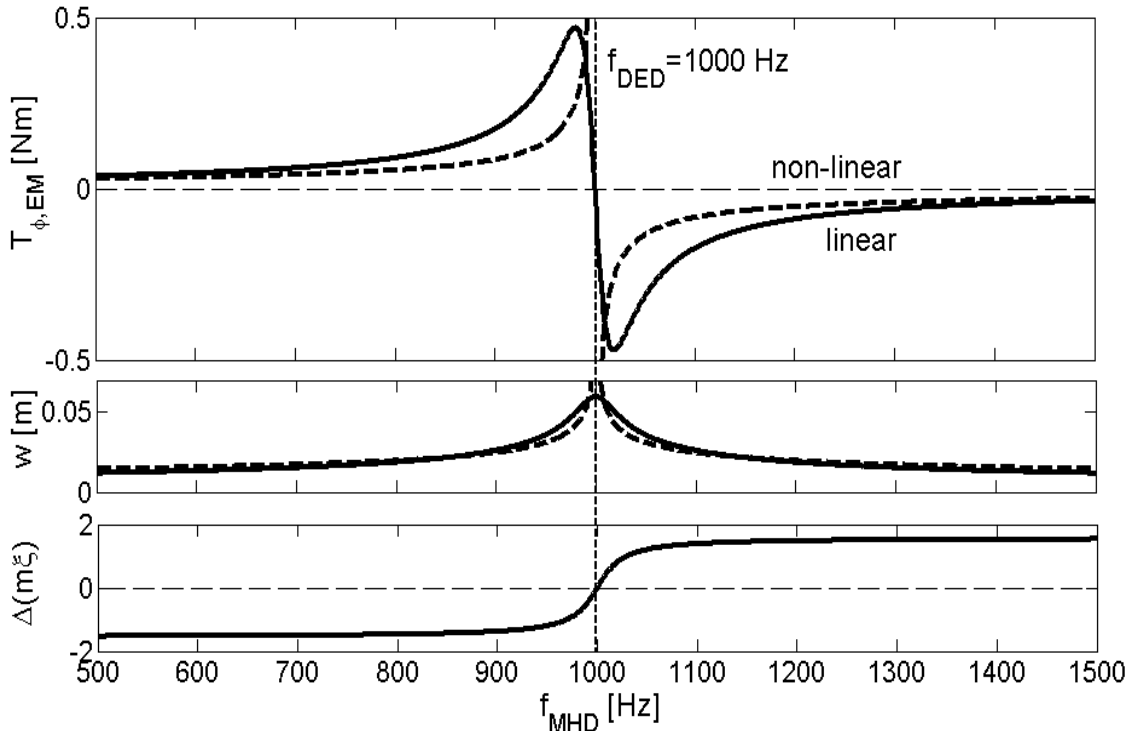


**Figure 8-6:** Example of the electromagnetic torque, island width and phase difference for both linear and non-linear theory for  $w_{vac}=0.03$  m. Use has been made of the  $q=2$  surface parameters listed in Table 8-1 and  $|\Delta'_0 r_s|=1$ .

### 8.3.2 Mode rotation

The mode (or MHD) frequency  $\omega$  refers to the frequency at which the magnetic field topology (island) rotates. This is the frequency that is directly measured by ECE-Imaging. The velocity profile measured by CXRS on the other hand corresponds to the ion rotation in toroidal direction. The poloidal ion rotation is assumed to be negligible, due to strong poloidal flow damping [Stix 1973]. The rotation of the electrons (which does have a poloidal component) differs from the ion rotation, giving

rise to the plasma current. Since parallel (ion or electron) flows do not influence the magnetic topology, only the perpendicular flows are important. Islands are observed to always rotate with the perpendicular electron velocity [Klüber 1991]. The difference between electron and ion perpendicular velocity corresponds to the diamagnetic drift, responsible for the confinement of the plasma via  $j \times B = \nabla p$  [Wesson 1997]. So, neglecting ion poloidal rotation and the (small) toroidal component of the diamagnetic drift, the relation between the MHD frequency  $\omega$  and toroidal ion rotation frequency  $\Omega_\phi$  is given by:

$$\begin{aligned} \omega &\approx 2\pi n f_e^* - n \Omega_\phi \\ f_e^* &= -\frac{1}{2\pi n e B_\phi r} \frac{\partial p}{\partial r} \end{aligned} \quad \text{Eq. 8-9}$$

where  $f_e^*$  is the electron diamagnetic frequency (positive for these experiments, see Figure 8-7). In the rest of the paper it is assumed that  $f_e^*$  is constant in time. So a change in the MHD frequency (as measured by ECE-Imaging) is matched by a (negative) change in toroidal ion rotation frequency (as measured by CXRS).

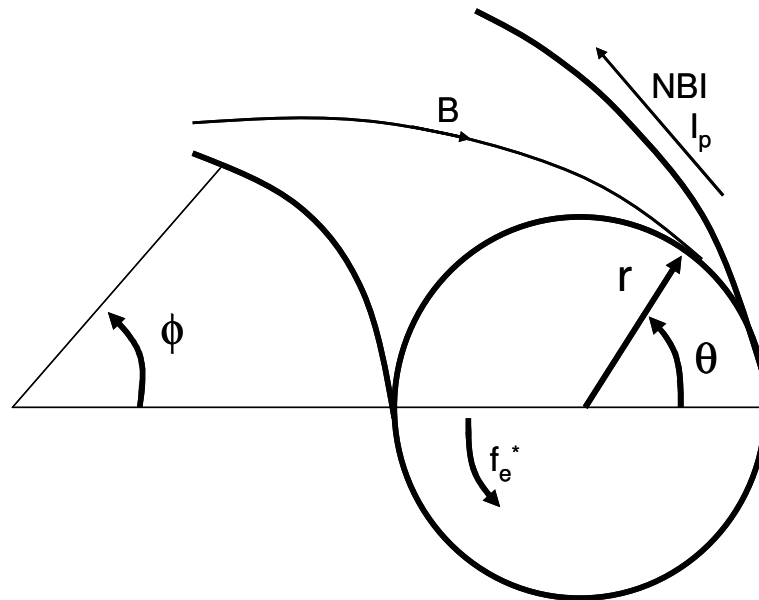


**Figure 8-7:** *The definition of the  $(r, \phi, \theta)$  coordinate system used in this paper. The directions of the magnetic field, NBI injection and diamagnetic drift are indicated.*

### 8.3.3 Torque balance and viscosity

In a steady state situation, all torques acting on the plasma (or island) must cancel out. Any net torque will be balanced against inertia, resulting in a change of frequency:

$$\sum T_\phi = m_{\text{plasma}} R_0^2 \frac{d\Omega_\phi}{dt} \quad \text{Eq. 8-10}$$

## 8 Dynamics of tearing modes in the presence of a perturbation field

Apart from the electromagnetic torque due to the DED, for the experiments described in this paper, the torque due to the unbalanced neutral beam injection (NBI) and the viscous torque are important. The toroidal viscous torque is given by

$$T_{\phi,VS} = 4\pi^2 R_0 \left[ (D\rho r R_0^2) \frac{\partial \Omega_\phi}{\partial r} \right]_{r-}^{r+} \quad \text{Eq. 8-11}$$

So a bend in the radial rotation frequency profile gives rise to a viscous torque in the direction to reduce this bend. Without perturbation field, the island rotates at its natural rotation frequency and all torques on it balance out. In these experiments, the natural rotation profile is mainly determined by the balance between NBI and viscous torques. In many situations, where only the (steady state) perturbed viscous torque due to deviations from the natural rotation frequency are of interest, the above expression can be approximated by

$$T_{\phi,VS} = A\Delta\Omega_\phi \quad \Delta\Omega_\phi = \Omega_\phi - \Omega_{\phi,0} \approx -\frac{1}{n}(\omega - \omega_0) \quad \text{Eq. 8-12}$$

where  $\Delta\Omega_\phi$  is the deviation from the natural rotation frequency and  $A$  is a constant depending on viscosity and the details of the natural rotation profile.

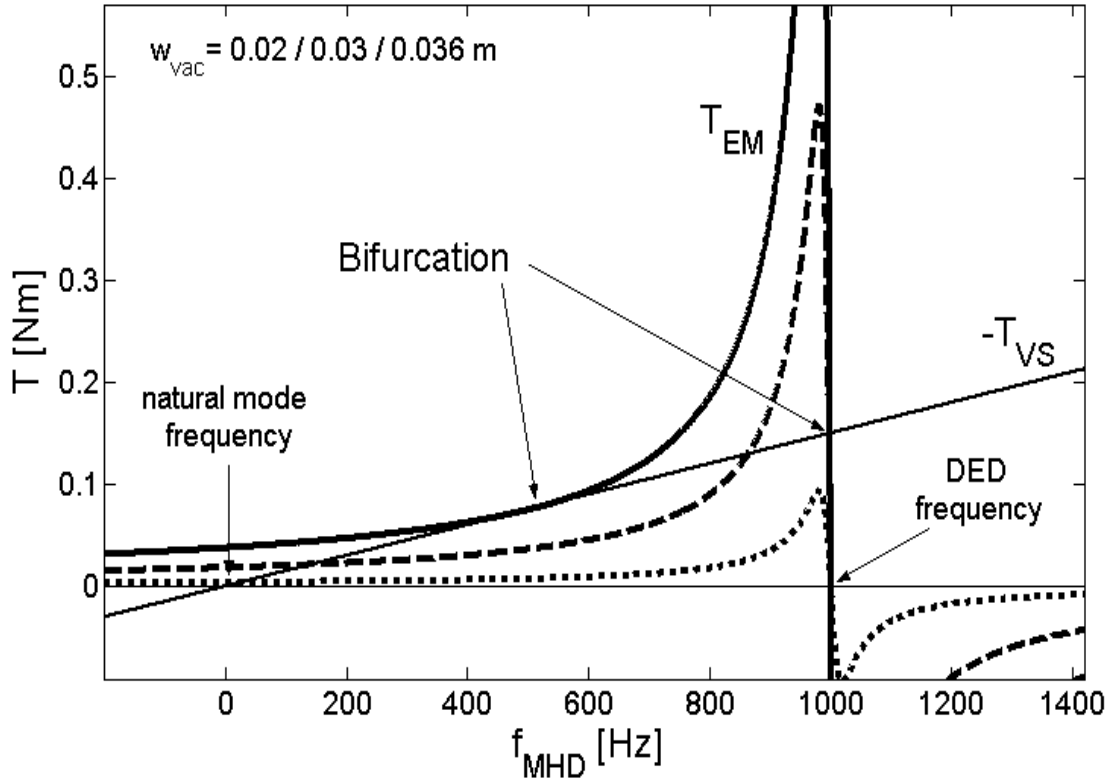


**Figure 8-8:** Schematic representation of mode penetration. Plotted is the (linear) electromagnetic torque for three values of  $w_{vac}$  (0.02, 0.03 and 0.036 m, respectively dotted, dashed and solid lines) and the viscous torque which increases linearly with the deviation from the natural mode frequency (here taken 0 Hz, by coincidence). Balance between the electromagnetic and viscous torques is reached at the intersections of  $T_{EM}$  and  $-T_{VS}$ .



Figure 8-8 shows how the balance between the electromagnetic and viscous torques leads to mode penetration when the perturbation field strength is gradually increased. Balance between the electromagnetic and viscous torques is reached at the intersections of  $T_{EM}$  and  $-T_{VS}$ . The situations for  $w_{vac}=0.03$  and  $0.036$  m show two stable balance points. For  $w_{vac}>0.036$  m, only one remains at  $f_{DED}=1$  kHz. So, starting at the natural mode frequency, with increasing perturbation field strength (increasing  $w_{vac}$ ), the balance point shifts in the direction of the perturbation field frequency. A critical point is reached when the viscous curve becomes tangent to the electromagnetic curve. In the linear theory this happens when the difference between mode and perturbation field frequencies is reduced to half of its natural value ( $2/5$  for the non-linear theory). If the perturbation field strength is further increased, balance between the viscous and electromagnetic torques can only be achieved for  $f_{MHD}=f_{DED}$ . This bifurcation is referred to as mode penetration.

### 8.3.4 Complications

There are a few effects that have to be taken into account to explain the experimental data that complicate the above general theory. First, the DED perturbation field does not solely exist of the  $2/1$  field component. Even though we are most interested in the dynamics of the observed  $2/1$  island, also the large  $3/1$  and  $1/1$  components of the DED field have a large influence (on the velocity profile), and have to be taken into account. The intrinsic error field of TEXTOR is neglected. It is assumed that the rotation frequency of the islands is always large enough for the torques due to this field to be negligible. The fact that the islands do not lock to the wall after switch off of the DED supports this assumption.

Second, a coupling between the  $2/1$  mode and a mode at the  $q=1$  surface is suggested by the CXRS data (Figure 8-5). This coupling is present during the unlocking, but not during the mode penetration. Both the electromagnetic torques on the various rational surfaces, and the mode coupling, can only be implemented by modelling the velocity profile. This also enables to model the viscosity realistically.

Third, there is another (type of) torque associated with the perturbation field of the DED, caused by the near field effects close to the plasma edge [Finken 2005], [Busch 2006]. This torque, acting at the plasma edge, is responsible for the initial increase in toroidal ion rotation just before penetration, seen in Figure 8-5. It raises the entire natural rotation profile. In this paper, for simplicity, this torque is neglected. Only the natural mode rotation frequency is corrected for the influence of this torque.

## 8.4 Comparison of experiment with theory

The theory described in the last paragraph has little or no free parameters; a consequence of the fact that they are almost directly derived from first principles like Maxwell's equations. All uncertainties are related to the exact plasma properties. To compare the theory with experiment, it is hence of crucial importance that the knowledge of the plasma parameters, mainly of the velocity profile, is as accurately as possible. To model the velocity profile as accurately as possible, a numerical

simulation is used. After describing this simulation, the various stages of the experiment, being mode penetration, mode growth and mode unlocking, will be compared to theory.

### 8.4.1 The numerical simulation

A numerical simulation is used to model the experiment as closely as possible. The simulation evaluates the evolution of the 2/1 island width and phase, as well as the velocity profile, including the viscous, electromagnetic (on  $q=1, 2$  and 3) and NBI torques.

The 2/1 island is treated as a non-linear island (so as an island that rotates at the same velocity as the plasma), using the Rutherford equation (Eq. 8-2) to determine the evolution of the island width, and Eq. 8-3 to determine the electromagnetic torque on the island. Early in the penetration process, the island is smaller than the linear layer width, and should actually be modelled using the linear theory (Eq. 8-7). During the important phase of the penetration however, close to the threshold, the 2/1 island is about 2 cm wide and clearly larger than the linear layer. Treating the island as a non-linear island throughout the entire penetration doesn't introduce a large error. The torque on the  $q=1$  and 3 surfaces on the other hand are evaluated using the linear theory (Eq. 8-7), assuming  $\Delta'$  for the 1/1 and 3/1 modes is negative enough to prohibit a growth of these modes into the non-linear regime.

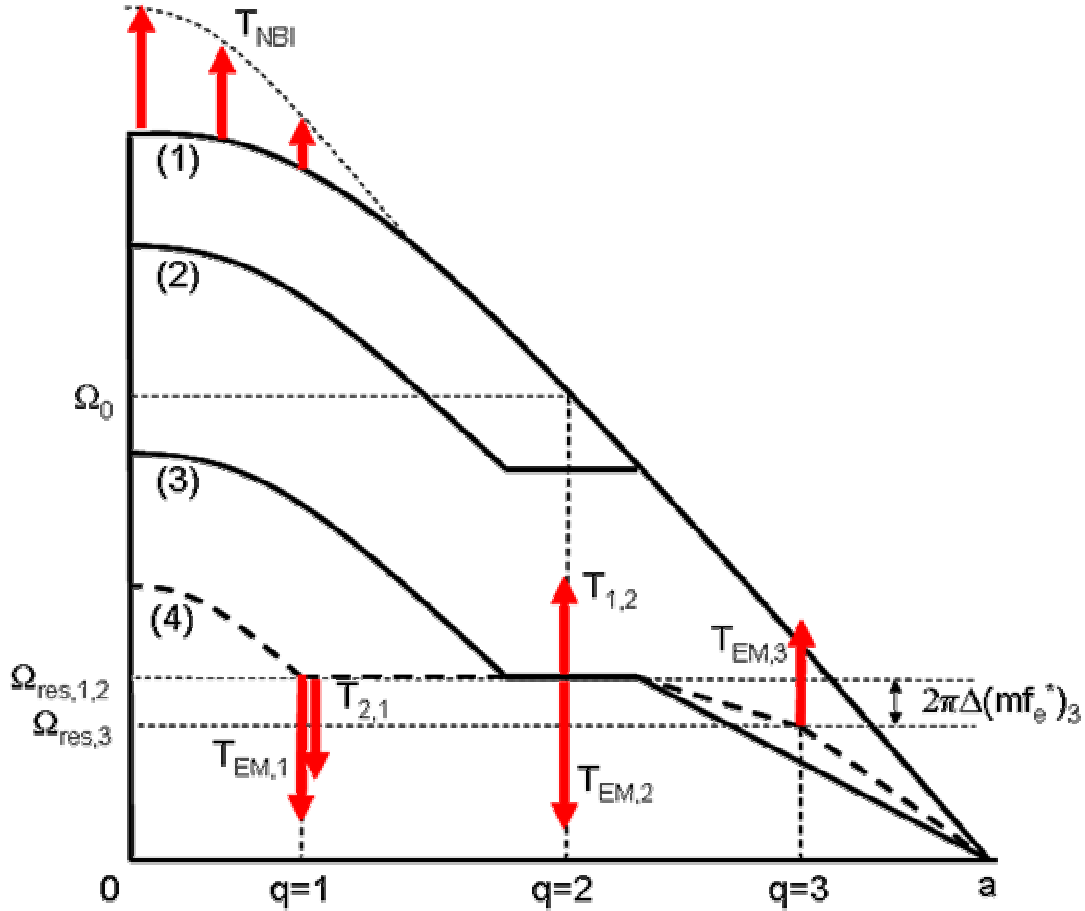
The modelled velocity profile (see Figure 8-9) is based on the toroidal ion rotation profile, as (partly) measured by CXRS. The natural profile is determined by balancing the neutral beam torque against viscosity. The neutral beam torque is known, and is about 0.2 Nm. The power deposition profile is assumed to be a Gaussian with full width at half maximum of 20 cm, centred on the magnetic axis. Good agreement between the simulated and experimentally measured natural rotation profiles is reached by taking the momentum diffusion coefficient  $D=1 \text{ m}^2/\text{s}$  (assumed constant for the entire plasma), using Eq. 8-11 for the viscous torque.

Table 8-1 lists the input parameters used in the simulation. They are determined using the measured density and temperature profiles, as well as the estimated current profile. The latter is estimated from the temperature profile (and loop voltage) assuming neoclassical resistivity. The time increment used in the simulation is  $5 \cdot 10^{-6} \text{ s}$  and the radial resolution of the simulated velocity profile about 0.02 m. Taking either a significantly (twice) smaller radial resolution, or a significantly larger time increment, results in numerical instability. The 2/1 island is treated as a rigid rotator of width  $w$ .

The resonant ion rotation frequencies depend on the diamagnetic drift frequency, and are generally different for  $q=1, 2$  and 3.

$$\Omega_{\text{res},q} = -\frac{\omega_{\text{DED}}}{n} + 2\pi \frac{m}{n} f_{e,q}^* \quad \text{Eq. 8-13}$$

The flat rotation profile measured by CXRS suggests an equal resonant frequency for  $q=1$  and 2. The resonance for the  $q=3$  surface is not measured, and hence a free parameter in the simulation  $\Omega_{\text{res},3} = \Omega_{\text{res},1,2} - 2\pi\Delta(mf_e^*)_3$ .



**Figure 8-9:** Schematic representation of the simulated ion rotation profile, and the various torques acting on it. The upper solid profile (1) represents the natural profile determined by the balance between the NBI and viscous torques in the absence of a mode, with the  $q=2$  surface rotating at  $\Omega_0$ . The 2/1 tearing mode is treated as a rigid rotator of width  $w$ , resulting in the natural rotation profile (2) in the presence of a mode. The DED perturbation field exerts electromagnetic torques  $T_{EM,q}$  on the  $q=1, 2$  and 3 surfaces. Profile (3) shows the situation where only the 2/1 mode is locked to the DED. Profile (4) (dashed) shows all surfaces locked. The observed mode coupling between the modes at the  $q=1$  and 2 surfaces is qualitatively taken into account by introducing two equal but opposite torques  $T_{1,2} = -T_{2,1}$  on the  $q=1$  and 2 surfaces.

**Table 8-1** Input parameters of the numerical simulation for the  $q=1, 2$  and 3 surfaces.

$q$	$r_s$ [m]	$C$ [T]	$w_{\text{vac}}$ [m]	$\tau_{\text{R}}$ [s]	$\tau_{\text{rec}}  \Delta'_0 r'_s $ [s]
1	0.105	0.043	0.06	0.24	0.013
2	0.285	0.09	0.04	0.4	0.0083
3	0.375	0.084	0.04	0.13	0.0024

The observed coupling between  $q=1$  and 2 is taken into account in a qualitative way by introducing two equal but opposite torques  $T_{1,2}=-T_{2,1}$  on the  $q=1$  and 2 surfaces. The amplitude of these torques has been taken linearly increasing with the rotation frequency difference between  $q=1$  and 2. The exact strength of these torques turns out to be unimportant, as long as they are strong enough to keep the  $q=1$  and 2 surfaces locked. Note that these torques are only meant to mimic the experimentally observed rotation profiles and mode coupling and are not an attempt to realistically model the mode coupling. These coupling torques are used for the modelling of the unlocking, but not for the penetration.

### 8.4.2 Mode penetration

Experimentally, mode penetration is observed at a vacuum island width of about 3 cm, see Figure 8-4. The plasma, initially rotating at frequency  $\omega_0 \approx 2\pi m f_e^* - n\Omega_0$  at the  $q=2$  surface, is forced to rotate at the DED resonance by the electromagnetic torques acting on it. To model this, it is necessary to estimate the initial velocity profile, and the resonant ion rotation frequencies for the  $q=1, 2$  and 3 surfaces (so the diamagnetic drifts) as accurately as possible.

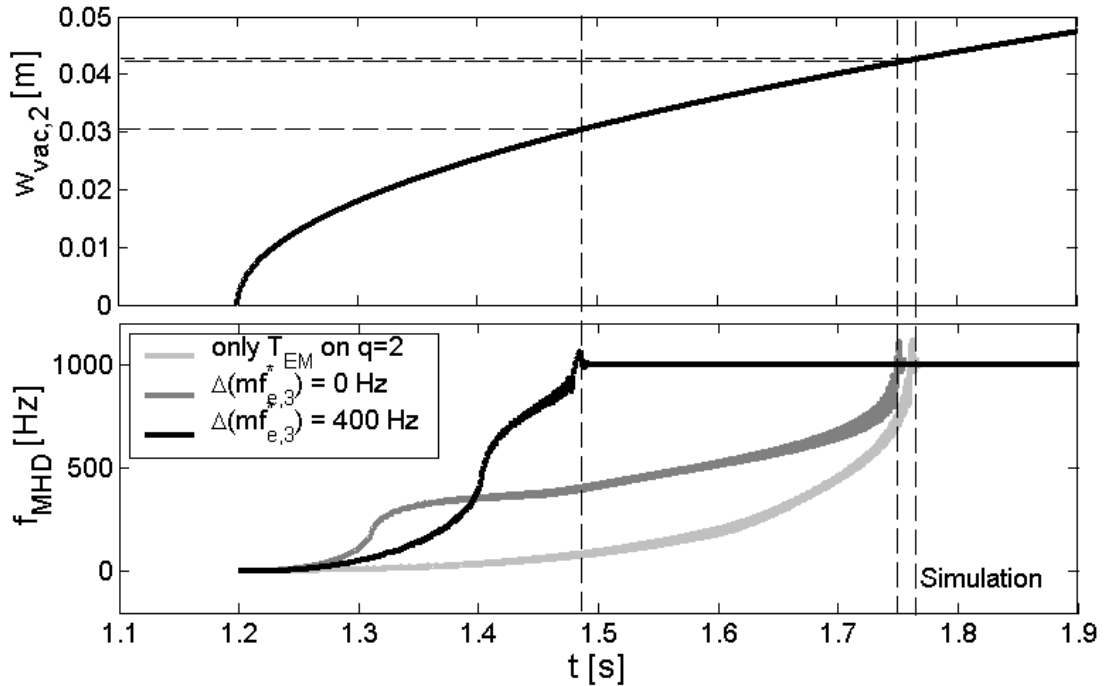


**Figure 8-10:** Simulation of the mode penetration with  $D=1 \text{ m}^2/\text{s}$ ,  $\omega_0=0 \text{ s}^{-1}$  and  $T_{NBI}=0.2 \text{ Nm}$ . If only the electromagnetic torque on the  $q=2$  surface is taken into account, locking occurs at a  $2/1$  vacuum island width that is about 50% larger than the experimentally observed value. Inclusion of the torques on the  $q=1$  and 3 surfaces results in a smaller penetration threshold because the  $q=3$  surface locks prior to the  $q=2$  surface, reducing  $\Delta\omega$  at  $q=2$ . The exact resonant frequency  $\Omega_{res,3}$  has a large influence on the penetration process.

Figure 8-10 shows the results of the simulation for three different situations. First, the simulation is done using only the electromagnetic torque on the  $q=2$  surface. The natural rotation profile is determined by taking  $D=1 \text{ m}^2/\text{s}$ ,  $T_{\text{NBI}}=0.2 \text{ Nm}$ , and  $\omega_0 = 0 \text{ s}^{-1}$ . With increasing perturbation field strength, it is seen that the rotation frequency of the  $q=2$  surface approaches the DED frequency (1 kHz), finally locking to it at a vacuum island width of about 4.3 cm, significantly higher than the experimental threshold. An earlier penetration would of course have been observed with a higher  $\omega_0$  or a smaller momentum diffusion coefficient. To reproduce the observed early penetration however, unrealistic values of (one of) these two parameters would be required. So more likely is that the electromagnetic torques on the  $q=1$  and 3 surfaces play a role in the penetration. To include these two torques, the resonant ion rotation frequencies  $\Omega_{res,1}$  at the  $q=1$  and  $\Omega_{res,3}$  at the  $q=3$  surface have to be estimated. The resonant frequency for the  $q=1$  surface is taken equal to the  $q=2$  surface resonance (from CXRS). Figure 8-10 shows the results for two different resonant frequencies of the  $q=3$  surface. Both cases show the locking of the  $q=3$  surface prior to the locking of the  $q=2$  surface. The locking of the  $q=3$  surface affects the rotation frequency of the  $q=2$  surface, bringing it closer to resonance, and hence decreasing the penetration threshold for the  $q=2$  surface. The exact resonant frequency  $\Omega_{res,3}$  has a large influence on the relative timing of the locking of  $q=2$  and 3 surfaces. Although the exact value of this resonance is unknown, all likely values led to a locking of the  $q=3$  surface in the simulation.

The torque on the  $q=1$  surface turned out to be too small to lead to a locking of the  $q=1$  surface, due to the large difference between natural and resonant rotation frequencies. So, only the torque due to the DED perturbation field is (at least in the simulation) not sufficient to explain the observed mode coupling. A direct coupling between the mode at the  $q=1$  surface and the (1/1 component of the) 2/1 island is hence likely.

### 8.4.3 Mode growth

After the rotation frequency of the  $q=2$  surface has locked to the DED frequency, the 2/1 island can grow to its saturated width. This island growth is governed by the modified Rutherford equation (Eq. 8-2). The various torques and the velocity profile do not play a significant role in this process, except for keeping the rotation of the  $q=2$  surface locked.

Figure 8-11 shows both the experimental and simulated evolution of the 2/1 island width plotted against  $(t-t_{\text{pen}})$ . Here, the time of penetration  $t_{\text{pen}}$  is defined as the time where  $f_{\text{MHD}}$  reaches  $f_{\text{DED}}$  (and the phase difference between plasma and vacuum islands reaches steady state). The simulation shows the oscillation in island width before penetration, characteristic for the non-linear theory. The island is dragged in and out of phase with the vacuum island by the difference in rotation frequency. For an island to be observed by ECE, it has to be larger than a critical width, determined by the competition between perpendicular and parallel transport, which for TEXTOR is of the order of 2 cm [Fitzpatrick 1995]. So, the fact that the oscillations are not observed experimentally doesn't mean they are not there.

Directly after penetration, which happens at a relatively large perturbation field amplitude, the phase difference between plasma and vacuum islands settles at a value close to zero. As the plasma island grows, the phase difference approaches zero even closer, because the electromagnetic torque increases quadratically with both plasma and vacuum island widths. But as long as the phase difference remains close to zero, it doesn't significantly influence the 2/1 mode growth. The two important parameters in the modified Rutherford equation are the current diffusion time  $\tau_R$  (which is estimated, see Table 8-1), and the unknown stability parameter  $\Delta'$ . In the simulation shown,  $\Delta'$  is neglected, except for island widths exceeding 0.1 m where  $\Delta'$  has been taken slightly negative to reproduce the observed saturated island width of 0.11 m (the same  $\Delta'$  is used as was found in the analysis of chapter 9). For small plasma islands,  $\Delta'$  can safely be neglected, as the perturbation field term of the Rutherford equation then dominates over the  $\Delta'$  term. For larger island widths,  $\Delta'$  does significantly influence the island growth after penetration, finally (in these experiments) leading to saturation. The fact that before switching on the DED, no natural island was present (hence negative  $\Delta'$ ), while after switching off the DED the island remains with an almost unaltered width of around 0.1 m (and hence  $\Delta'(w)=0$  for  $w=0.1$ m), it is assumed that  $\Delta'$  is close to zero during the entire process. The above observations are however hard to explain without an evolution of  $\Delta'$  (as a function of  $w$ ) during penetration. Despite neglecting  $\Delta'$  however, Figure 8-11 shows reasonable agreement between experiment and simulation.

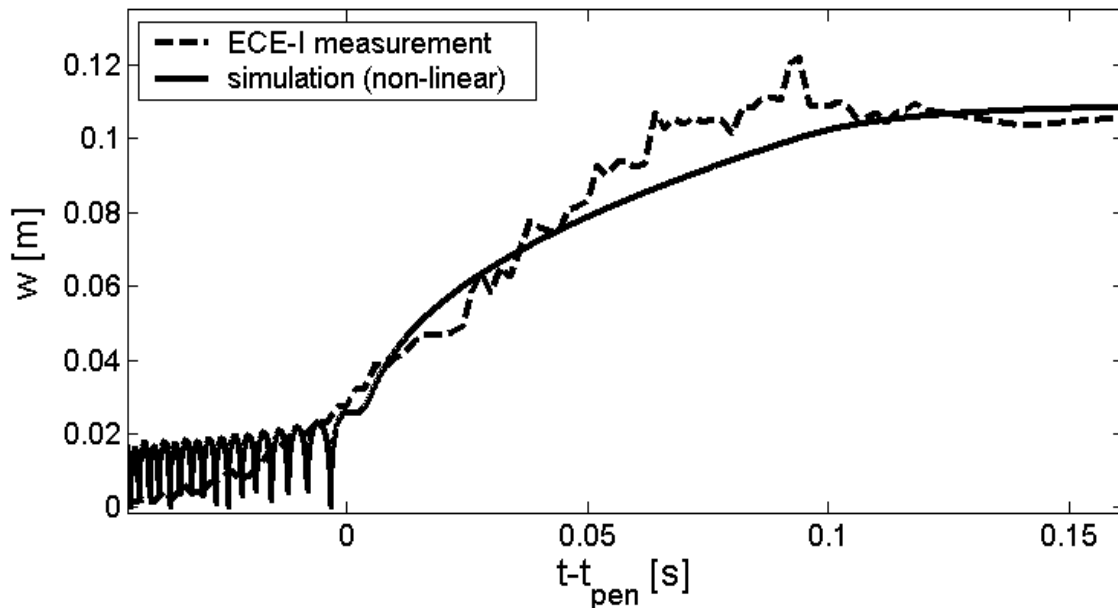


**Figure 8-11:** Comparison of the experimentally observed 2/1 island growth during penetration (#99175) with the simulation (using the non-linear theory). The time of penetration  $t_{pen}$  is defined as the time at which the rotation frequency has reached the resonant value. The simulation shows oscillations in  $w$  prior to locking (with maximum amplitude  $w_0$ ), characteristic for the non-linear theory. In the simulation,  $\Delta'$  is neglected for  $w < 0.1$  m, and slightly negative for larger islands, to reproduce the observed saturated island width.

### 8.4.4 Mode unlocking

During the locked phase (at full DED current), where the 2/1 island has its saturated island width, the phase difference between the plasma and vacuum islands is close to zero. The electromagnetic torque, which is linearly proportional to this phase difference (for small angles), settles at the value needed to balance all other torques on the 2/1 island. The maximum possible electromagnetic torque, at  $\Delta(m\xi) = \pi/2$ , is however much larger. During the ramp down of the DED current, the torque balance on the 2/1 island can hence be maintained by gradually increasing the phase difference, keeping the electromagnetic torque constant. Unlocking occurs when the phase difference has reached  $\pi/2$ , and the maximum electromagnetic torque is needed to balance all other torques (assuming the plasma island width stays the same, otherwise unlocking occurs already at a smaller angle, see [Fitzpatrick 1993]).

After unlocking, the electromagnetic torque is not sufficient anymore to keep torque balance, and the island rotation will start to deviate from the DED frequency (in the direction of the natural MHD frequency). Due to this frequency mismatch the remaining electromagnetic torque will rapidly loose influence, leaving the plasma free to relax back to the natural rotation profile. The initial rate of change of the 2/1 rotation frequency is determined by the sum of the torques on the island just after unlocking, which is equal but opposite to the electromagnetic torque that was still present just before unlocking. So the value of  $d\omega/dt$  just after unlocking is a direct measure for the electromagnetic torque during the entire locked phase, and in particular the maximum electromagnetic torque ( $\sin(\Delta(m\xi))=1$ ) at the moment of unlocking. The smaller the value of  $d\omega/dt$  after unlocking, the less the plasma opposes the locked state (either because the natural rotation is closer to the DED resonance or because viscosity is smaller), the easier the island can be kept locked by the perturbation field. So, as the perturbation field strength depends linearly on the DED coil current amplitude, a linear dependency between the observed  $d\omega/dt$  and the threshold  $I_{\text{DED}}$  for unlocking is expected. Figure 8-12 shows the MHD frequency during unlocking for four discharges. Although all discharges had identical settings, a variation in natural mode frequency and initial  $d\omega/dt$  is observed. As expected, the discharge with the largest  $d\omega/dt$  unlocks first, and the DED current at unlocking scales approximately linear with the observed  $d\omega/dt$ .

The difference in natural MHD frequency for the four discharges shown, might be caused by a difference in the momentum diffusion coefficient. Although only a factor of two variation in  $\Delta\Omega$  is observed in Figure 8-12, the variation in the observed  $d\omega/dt$  is about a factor of four. As a linear scaling of the viscous torque with  $\Delta\Omega$  is expected (see Eq. 8-12), this suggest a variation in momentum diffusion coefficient, the discharge with the highest  $d\omega/dt$  having a twice as high viscosity. Regardless of the value for  $D$  however, the initial  $d\omega/dt$  is still a direct measure for the torque imbalance after unlocking, see Eq. 8-10. For a direct application of this equation to the 2/1 island it is however not a priori clear which mass has to be taken (some ‘effective’ island mass, including the shell of plasma surrounding the island that moves along due to viscosity). The numerical simulation doesn’t have this problem, because the entire velocity profile is modelled, applying Eq. 8-10 to each radial increment of the velocity profile using their actual mass (from the measured density profile).

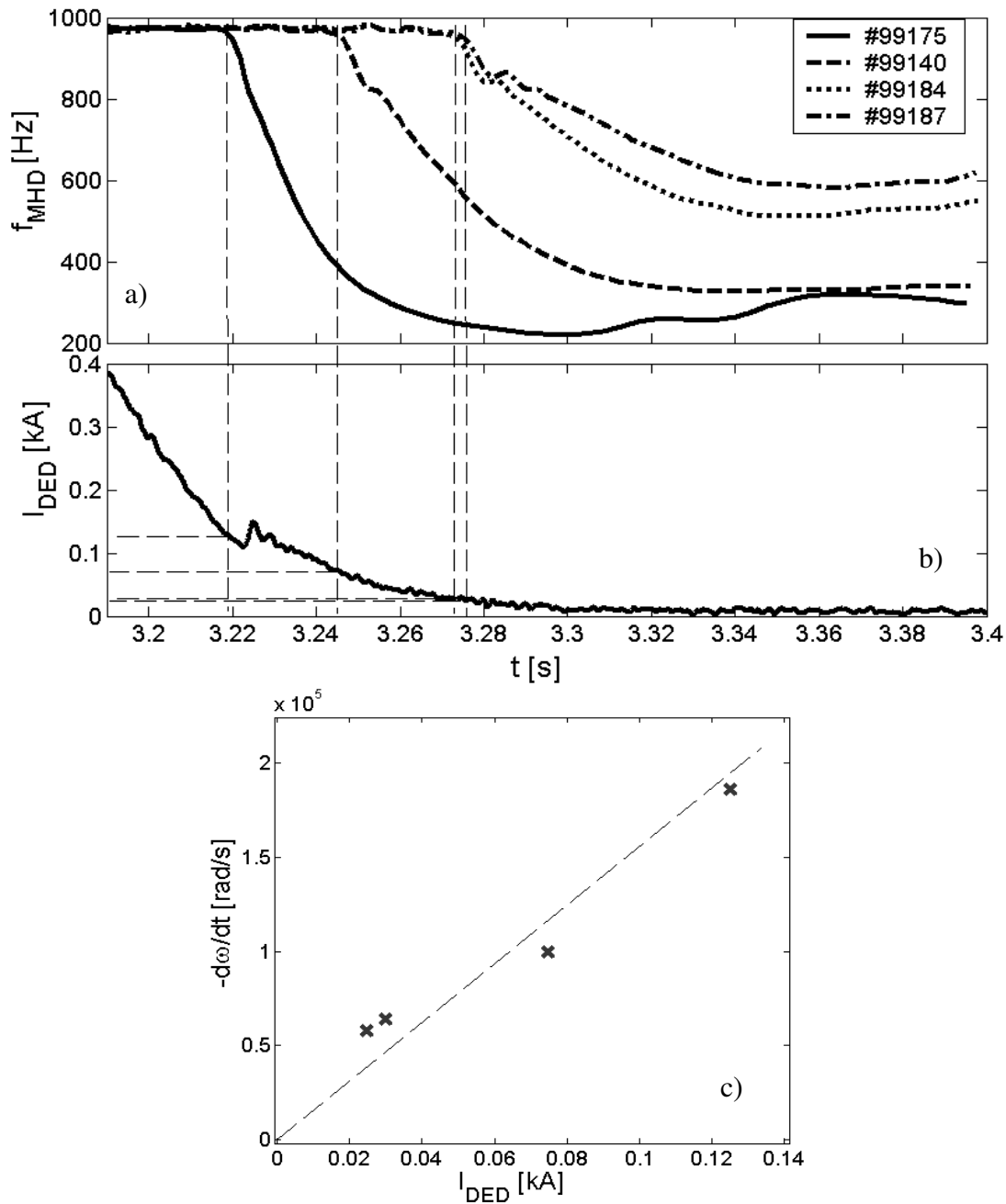


**Figure 8-12:** a) The experimentally observed MHD frequency during unlocking for four identical TEXTOR discharges and b) the corresponding DED current. The almost instantaneous drop to a large negative  $d\omega/dt$  during unlocking is due to the loss of the electromagnetic torque. The value of  $d\omega/dt$  just after unlocking is a measure for the (viscous) torque on the 2/1 island, and is equal in amplitude to the electromagnetic torque just before unlocking. The discharge with the largest viscous torque unlocks first. c) As expected, the DED current at unlocking scales approximately linearly with the viscous torque.

Figure 8-13 shows the results of the numerical simulation for the unlocking phase. Use has been made of the experimental DED current (vacuum island width),  $D=1 \text{ m}^2/\text{s}$ ,  $\omega_0=0 \text{ s}^{-1}$ ,  $T_{\text{NBI}}=0.2 \text{ Nm}$  and  $\Delta(mf_e^*)_3=0 \text{ Hz}$  as input parameters. The coupling



between the modes at the  $q=1$  and 2 surfaces is mimicked by the inclusion of two opposing torques. The simulation shows the expected increase in phase difference before unlocking (the wiggle is due to the step in the vacuum island width), and the resulting relaxation of the MHD frequency after unlocking (when the phase difference passes  $\pi/2$ ). The time trace of the electromagnetic torque on the  $q=2$  surface shows a more complex picture, with steps in the torque corresponding to the unlocking of one of the resonant  $q$  surfaces. First, the  $q=1$  surface is seen to ‘unlock’, leading to a larger torque on the  $q=2$  surface. Note that the coupling between the  $q=1$  and 2 modes remains. The rotation frequency of the  $q=1$  surface (almost) doesn’t change, but the DED torque on the  $q=1$  surface becomes negligible. The unlocking of the  $q=3$  surface leads to a decrease in torque on the  $q=2$  surface (transition of the dotted profile to profile 3 in Figure 8-9), resulting in a small bump on the phase difference time trace. Because of the large island width (hence large electromagnetic torque) the 2/1 mode is the last to unlock. So, just before unlocking only the electromagnetic torque on the 2/1 mode has to be taken into account. After unlocking, the electromagnetic torque on the 2/1 mode is seen to oscillate around zero, increasing in frequency as  $\Delta\omega$  increases.

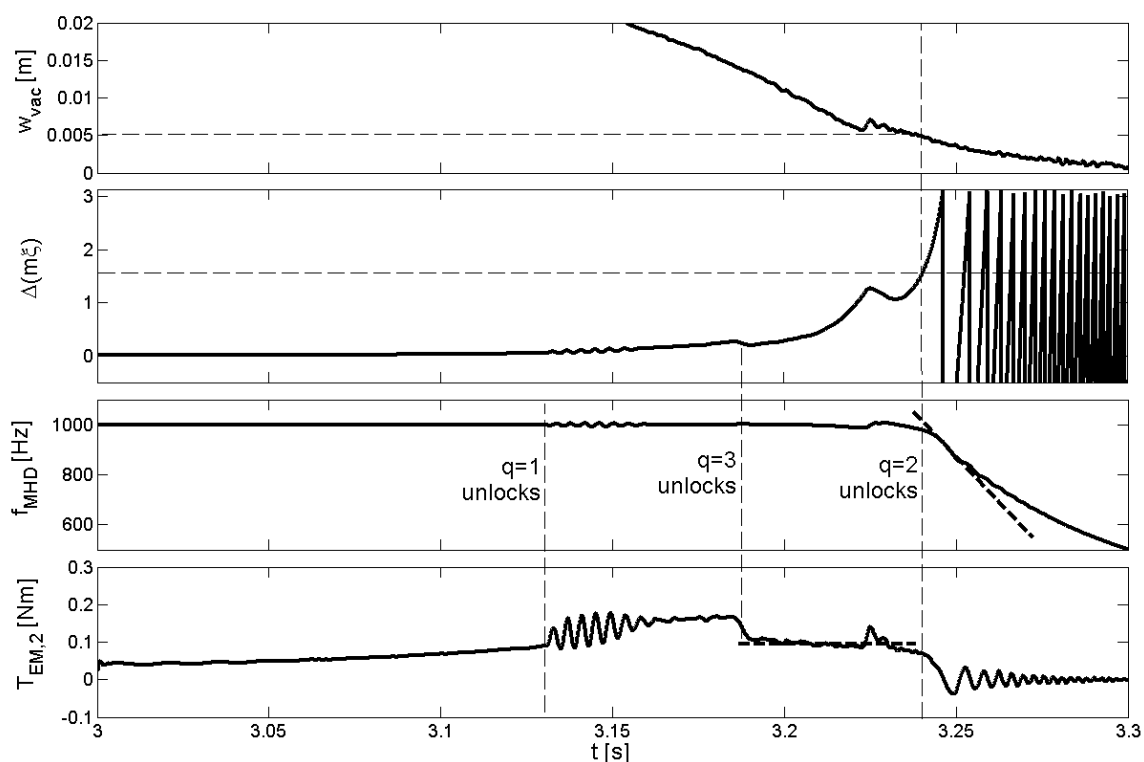


**Figure 8-13:** Simulation of the mode unlocking with  $D=1 \text{ m}^2/\text{s}$ ,  $\omega_0=0 \text{ s}^{-1}$ ,  $T_{NBI}= 0.2 \text{ Nm}$  and  $\Delta(mf_e^*)_3=0 \text{ Hz}$  including the coupling between the modes at the  $q=1$  and 2 surfaces. Use has been made of the experimentally observed vacuum island width. Unlocking of the 2/1 island occurs when the phase difference between plasma and vacuum islands exceeds  $\pi/2$ . Prior to the unlocking of the 2/1 island, both the  $q=1$  and 3 surfaces unlock (although  $q=1$  stays coupled to  $q=2$ ), as can be seen from the steps in  $T_{EM,2}$ . The electromagnetic torque on the 2/1 island prior to unlocking is about 0.1 Nm. After unlocking, the torque oscillates around zero. The loss of these 0.1 Nm results in a  $d\omega/dt$  of about  $1 \cdot 10^5 \text{ s}^{-2}$ .

Figure 8-14 shows the experimental MHD frequency and phase difference during unlocking. The expected increase in phase difference and subsequent frequency relaxation are observed. The behaviour of the  $q=1$  and 3 surfaces can not be seen from this data (although the small bump on the phase difference, better seen in Figure 8-4, might correspond to the unlocking of the  $q=3$  surface). The simulation however shows that it is safe to assume that the  $q=2$  surface is the last to unlock.

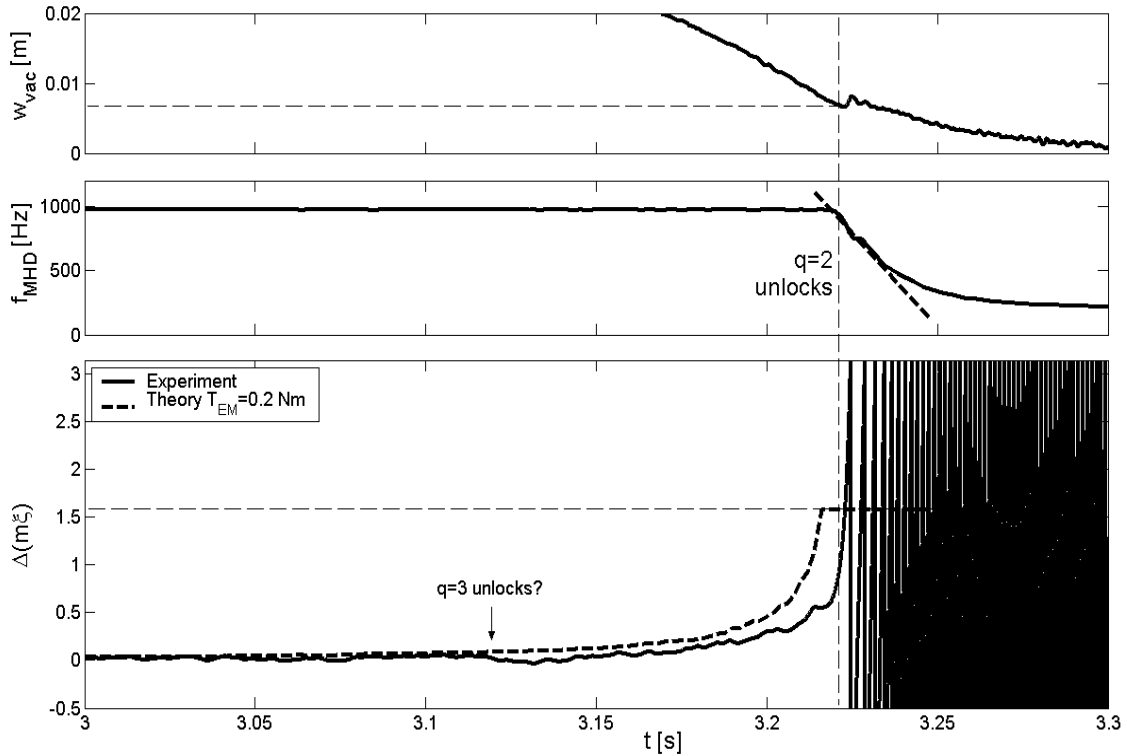


**Figure 8-14:** Experimental MHD frequency and phase difference during unlocking (#99175). After unlocking, a  $d\omega/dt$  of about  $2 \cdot 10^5 \text{ s}^{-2}$  is observed. According to the numerical simulation this corresponds to a viscous torque of about 0.2 Nm. The dashed line in the lower graph is the theoretical phase difference expected in a steady state situation, calculated from Eq. 8-3 using  $T_{EM}=0.2 \text{ Nm}$  and the experimental values for  $w$  and  $w_{vac}$ .

To link the observed  $d\omega/dt$  of about  $2 \cdot 10^5 \text{ s}^{-2}$  to a torque (using Eq. 8-10), the ‘effective’ island mass has to be known. In the numerical simulation, where this problem is avoided, the observed  $d\omega/dt$  was about  $1 \cdot 10^5 \text{ s}^{-2}$ , and corresponded to a torque of about 0.1 Nm (see Figure 8-13). This suggests that the experimentally observed  $d\omega/dt$  of about  $2 \cdot 10^5 \text{ s}^{-2}$  corresponds to a torque of about 0.2 Nm. The dotted line in Figure 8-14 gives the theoretically expected steady state phase difference, calculated with Eq. 8-3, using  $T_{EM}=0.2 \text{ Nm}$  and the experimental values for  $w$  and  $w_{vac}$ . This curve is indeed very close to the experimental one, predicting the unlocking only slightly too early.

Remember that the phase difference during the ‘strongly’ locked phase was synthetically set to zero, and hence the entire curve might be shifted up or down.

Experimentally, only the change in phase difference is measured, which is in agreement with the theoretically observed change.

### 8.5 Summary and discussion

Although the exact details of the experiment are hard to reconstruct, theory and experiment agree, qualitatively and to a large extent also quantitatively, on all accounts. The sudden growth of an island during penetration, and the sudden torque imbalance (leading to a stepwise change in  $d\omega/dt$ ) during unlocking are reproduced. Moreover, these bifurcations are observed at threshold perturbation field amplitudes close to the theoretical values, the threshold for unlocking being much smaller than the one for penetration. The predicted change in phase difference between plasma and vacuum islands before unlocking is actually observed, and in agreement with the (viscous) torque on the island, derived from the frequency relaxation after unlocking. Smaller viscous torques led to smaller thresholds for unlocking, approximately linear with the DED coil current amplitude. Only taking account of the electromagnetic torque on the  $q=2$  surface in the numerical simulation led to a threshold for 2/1 mode penetration of about 50% higher than experimentally observed. Inclusion of the electromagnetic torque on the  $q=1$  and, in particular, the  $q=3$  surface, resulted in a significantly lower penetration threshold. The observed threshold is most likely explained by the locking of the  $q=3$  surface prior to, or simultaneous with, the  $q=2$  surface. Finally, despite the unknown island stability parameter  $\Delta'$ , the growth of the 2/1 island after penetration is well reproduced in the numerical simulation.

Some questions remain. The 2/1 island is observed to be stable (negative  $\Delta'$ ) before the DED is switched on, but it doesn't disappear after switching off the DED. A threshold island width (as is the case for neoclassical tearing modes), might explain this. It is, however, unlikely that the 2/1 island is of neoclassical nature, due to the small bootstrap current fraction in these experiments. An evolution of the current profile leading to a less stable island is also hard to imagine. A growing island uses the free energy available in the current profile and should hence lead to a more stable current profile. Probably the stability has changed due to the coupling with the mode at the  $q=1$  surface, making the combined 2/1-1/1 system more unstable than the individual modes. Luckily, the theoretical predictions are not very sensitive to the exact value of  $\Delta'$  (for  $\Delta\omega \gg 1/\tau_{rec}$ ,  $\Delta'$  can even safely be neglected). The results of the numerical simulation are however very sensitive to, in particular, the chosen values for  $\omega_b$ ,  $\Omega_{res,3}$  and  $w_{vac}$ , leaving some room for variation.

The way the mode coupling between the 2/1 island and the mode at the  $q=1$  surface is treated in the simulation is very qualitative. Simply, two (strong enough) torques are introduced to mimic the observed velocity profile. It turns out however, that this coupling doesn't significantly affect the dynamics of the 2/1 island. The net torque the 2/1 island 'feels', is not changed by the inclusion of the two (cancelling) torques responsible for the coupling. A more realistic treatment of the mode coupling is hence beyond the scope of this thesis.

Finally, the question remains whether there actually are 1/1 and 3/1 modes in the plasma. Experimentally, no 3/1 mode is observed. The existence of a 1/1 mode is less important for the results presented in this paper, but is likely because of the observed

coupling. For an island to be experimentally observable (by for instance ECE), it should be large enough to affect the pressure profile. Its width has to be larger than a critical width, determined by the competition between perpendicular and parallel transport, which for TEXTOR is of the order of 2 cm [Fitzpatrick 1995]. In the simulation it is assumed that the  $\Delta'$  for these modes is negative enough to prohibit a growth of these modes into the 'non-linear' regime. So, the electromagnetic torques do not rely on the existence of an experimentally observable island. If, in reality, there are larger 1/1 or 3/1 islands ( $\Delta'$  less negative than assumed), then the role of the electromagnetic torques on these islands (scaling with  $w^2$ ) is underestimated, and the non-linear theory might have been necessary. Again, during penetration, the value of  $\Delta'$  is relatively unimportant as normally  $\Delta\omega \gg 1/\tau_{\text{rec}}$ .

Despite these questions regarding the details of the experiment, one can conclude that the theory (as mainly developed by Fitzpatrick) worked remarkably well to explain the observations, throughout the various stages of the experiment (mode penetration, growth and unlocking), both qualitatively and quantitatively. This gives confidence in the validity of predictions based on this theory, like for instance the tolerable error field in future devices like ITER. One should however make sure to include all important details of the experiment in question into the analysis. The experiments described here showed for instance, that in order to describe the behaviour of the  $q=2$  island, it was essential to include the effect of the other rational surfaces in the plasma.

## 9 The effect of heating on the suppression of tearing modes\*

I.G.J. Classen<sup>1</sup>, E. Westerhof<sup>1</sup>, C.W. Domier<sup>2</sup>, A.J.H. Donné<sup>1</sup>, R.J.E. Jaspers<sup>1</sup>,  
N.C. Luhmann Jr.<sup>2</sup>, H.K. Park<sup>3</sup>, M.J. van de Pol<sup>1</sup>, G.W. Spakman<sup>1</sup>,  
M.W. Jakubowski<sup>4</sup> and TEXTOR team<sup>4</sup>

<sup>1</sup> FOM-Institute for Plasma Physics Rijnhuizen, Association EURATOM-FOM, PO  
Box 1207, 3430 BE Nieuwegein, The Netherlands, [www.rijnh.nl](http://www.rijnh.nl)<sup>#</sup>

<sup>2</sup> University of California at Davis, Dept. of Applied Science, Davis, California,  
95616 U.S.A.

<sup>3</sup> Princeton Plasma Physics Laboratory, Princeton, New Jersey, 08543 U.S.A.

<sup>4</sup> Forschungszentrum Jülich GmbH, Institut für Plasmaphysik, Association  
EURATOM-FZJ, D-52425 Jülich, Germany<sup>#</sup>

<sup>#</sup>Partners in the Trilateral Euregio Cluster

**Abstract.** The suppression of (Neoclassical) Tearing Modes is of great importance for the success of future fusion reactors like ITER. Electron cyclotron waves can suppress islands, both by driving non-inductive current in the island region and by heating the island, causing a perturbation to the Ohmic plasma current. This Letter reports on experiments on the TEXTOR tokamak, investigating the effect of heating, which is usually neglected. The unique set of tools available on TEXTOR, notably the Dynamic Ergodic Divertor to create islands with a fully known driving term, and the electron cyclotron emission imaging (ECE-Imaging) diagnostic to provide detailed 2D electron temperature information, enables a detailed study of the suppression process and a comparison with theory.

52.55.Tn, 52.55.Fa, 52.25.Fi, 52.70.Gw

Tearing modes, and in particular neoclassical tearing modes (NTMs), have a deleterious effect on the performance and stability of tokamak plasmas. Larger tokamaks, like the proposed ITER tokamak, are more susceptible to the formation of NTMs. It is therefore important to develop techniques to control or suppress them and to gain understanding of the suppression process. Islands can be stabilized by driving a (helical) current perturbation inside the island region. Gyrotrons are an ideal tool for the localized generation of this current through the injection of radio frequency waves

---

\* The work presented in this chapter is published in this form in *Physical Review Letters* under the title 'Effect of heating on the suppression of tearing modes in tokamaks'.  
I.G.J. Classen *et al.*, *Phys. Rev. Lett.* **98**, 035001 (2007)

into the plasma. This current can either be directly driven non-inductively by Electron Cyclotron Current Drive (ECCD) [La Haye 2006] or indirectly by heating the island by Electron Cyclotron Resonance Heating (ECRH) ([Hoshino], [Sing 1993], [Kislov 1997]), causing a helical perturbation to the Ohmic current due to the temperature dependence of the plasma conductivity. ECCD is thought to be a more efficient way to suppress (neoclassical) islands. The tearing mode suppression by heating is often neglected. In this Letter, it will be shown that on TEXTOR the physical mechanism at work during heating can be clearly identified. It is demonstrated that also heating gives a sizeable suppression of the islands.

A set of tearing mode suppression experiments on the TEXTOR tokamak is described, that focuses on the suppression by heating (ECRH). In TEXTOR, suppression by ECRH dominates over ECCD [Westerhof 2006] due to the low current drive efficiency (low  $T_e$ ).

TEXTOR is a medium sized limiter tokamak with a circular plasma cross section ( $R_0=1.75$  m,  $a=0.46$  m) and is ideally suited for island suppression studies due to the unique combination of available tools. With the Dynamic Ergodic Divertor [Special Issue 1997], islands can be created and controlled with (in contrast to other tokamaks) a fully known driving term. The gyrotron can be used to apply highly localized heating or current drive inside the island. Finally, the process of suppression can be observed in detail by the 2D electron cyclotron emission imaging (ECE-Imaging) diagnostic [Park 2003].

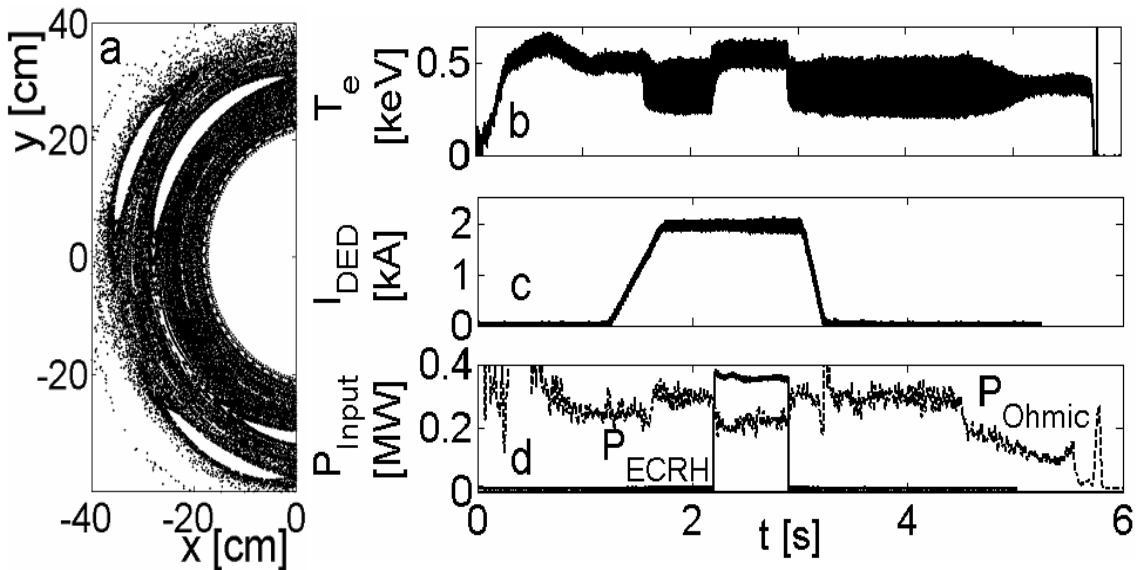


**Figure 9-1:** Overview of a typical discharge. a) DED vacuum magnetic field. b)  $T_e$  time trace from an ECE-Imaging channel just inside the island. c) Amplitude of the DED coil currents. d) Ohmic power and ECRH power.

The Dynamic Ergodic Divertor (DED) on TEXTOR is a perturbation field experiment consisting of 16 helical coils on the high field side, aligned with the  $q=3$  field lines. Figure 9-1a shows the vacuum field used for the experiments described in this Letter, containing large 3/1 and 2/1 island chains. In the presence of a plasma, the magnetic topology changes due to shielding currents that are generated on the rational  $q$

surfaces. For these experiments, this results in a plasma in which only a 2/1 island is destabilized when the current in the DED coils exceeds a threshold [Koslowski 2006]. In the underlying work, 1 kHz AC DED currents are used, resulting in a poloidal rotation of 500 Hz for the  $m/n = 2/1$  island which is locked to the rotating perturbation field.

An 800 kW, 140 GHz gyrotron is used to suppress the islands. The steerable launcher enables accurate positioning of the power on the resonant surface  $r_s$  (at the high field side for these experiments). Both continuous (CW) and modulated power is possible. The radial width of the (assumed Gaussian) power deposition profile is calculated to be 1.5 cm full width at half maximum.

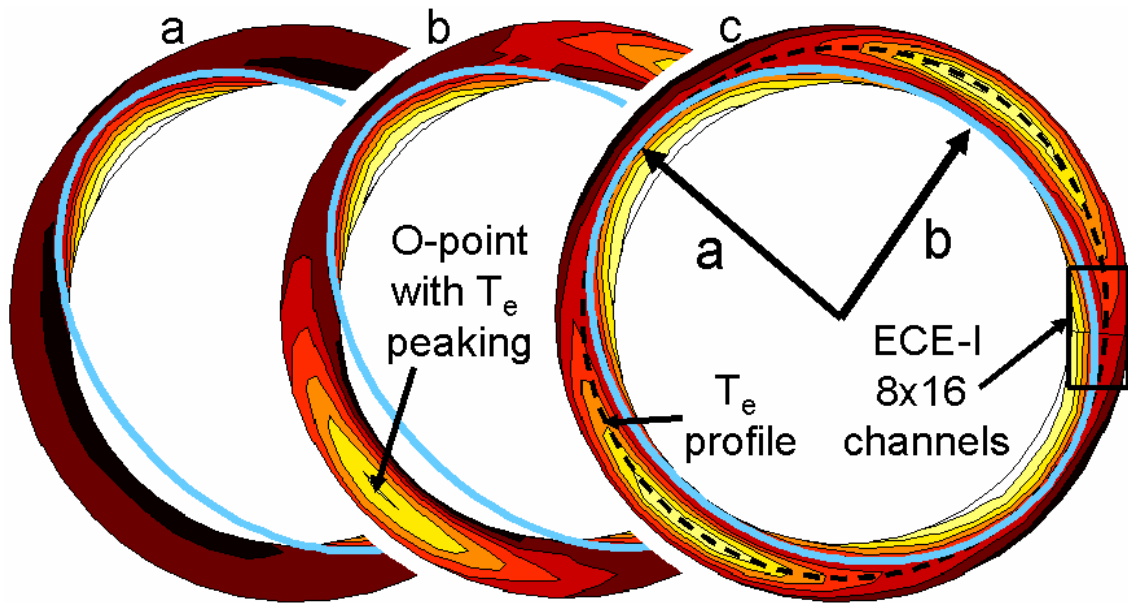
The ECE-Imaging diagnostic on TEXTOR measures the electron temperature in a 2D array of 8 (radially) by 16 (vertically) observation volumes in the poloidal plane, representing about 8 by 16 cm<sup>2</sup> in the plasma, centred on the equatorial plane. For these experiments, the field of view was adjusted to the  $q=2$  surface at the low field side, and the data were sampled at 200 kHz.

Figure 9-1 gives an overview of a typical discharge. All discharges have a toroidal magnetic field of 2.25 T, a toroidal plasma current of 300 kA and a line averaged density of about  $3 \cdot 10^{19} \text{ m}^{-3}$ . The DED coil current amplitude is ramped up, reaching a flat top of 2 kA (Figure 9-1c). A 2/1 tearing mode is destabilized when the DED current becomes sufficiently high, as can be seen on an ECE-Imaging temperature time trace from a channel just inside the island radius as a 1 kHz oscillation (Figure 9-1b). From 2.2 s to 2.9 s, ECRH is switched on (Figure 9-1d), either CW or modulated, with (for these experiments) 200, 300 or 400 kW of power. These power levels are comparable to the Ohmic input power. In this Letter, only data are presented for which the ECRH power was deposited directly on the resonant  $q=2$  surface. The appropriate launcher position is determined from a scan of the poloidal launcher angle, searching for optimum island suppression [Westerhof 2006].

For comprehensive visualization of the ECE-Imaging data, a poloidal reconstruction is used in which the data for one full rotation period are mapped onto a poloidal shell, assuming rigid plasma rotation. Note that the poloidal reconstruction only represents the low field side structure of the island. Figure 9-2 shows the reconstruction of the island during the three main stages of the suppression process. The first stage (Figure 9-2a) is the situation in which the island has been generated and has reached a saturated width of about 12 cm, but before ECRH application. In this phase, the temperature profile inside the island is still flat. The hot, central plasma, approximately elliptically deformed by the island, is clearly visible. The second reconstruction (Figure 9-2b), at about 10 ms after switch on of ECRH, shows a peaked  $T_e$  profile inside the island. Although an island degrades the global confinement of the plasma, the island itself can confine energy and particles. The third stage (Figure 9-2c) is the steady state situation long (more than 100 ms) after switch on of ECRH. The island is now suppressed to about half the initial size, the central plasma is less deformed and the peaked temperature region inside the island is narrower.

An automated algorithm is used to extract the main island parameters from the reconstructed ECE-Imaging data. To determine the full island width  $w$ , an ellipse is

fitted to the data (see Figure 9-2). The difference between the major radius  $a$ , and minor radius  $b$  of this ellipse gives the displacement of the fitted temperature contour, and is a measure for the width of the island ( $w \approx 1.5 (a - b)$  [Classen 2006]). The O-point position and temperature is found by looking for the temperature maximum along a line through the minor axis of the fitted ellipse. The exact position of the inner separatrix can be determined by finding the minimum temperature between the O-point and the ellipse. The temperature profile inside the island is evaluated on a circle through the O-point (dotted line in Figure 9-2c). In this way, the (relative) temperature profile is independent of any (relative) calibration errors, since all points on a circle are measured by the same ECE-Imaging channel(s). The temperature peaking  $\Delta T_e$  is defined as the difference between the O-point and separatrix temperatures.



**Figure 9-2:** Poloidal reconstructions of the island, showing the time evolution during the suppression process: a) flat island b) heated island c) suppressed island with schematic representation of various island parameters extracted from the poloidal reconstruction.

Figure 9-3 gives the typical time evolution of the full island width  $w$  and the relative temperature peaking, during the suppression process. Directly after switch on of ECRH, the temperature inside the island starts to peak, reaching a maximum peaking of typically  $\Delta T_e/T_e = 25\%$  after about 10 ms. After the  $T_e$  peaking has formed, the island starts to shrink to typically half the initial width after about 100 ms. The temperature peaking disappears almost immediately (within the local energy confinement time of the island) after switch off of ECRH. The island then relaxes back to the initial width.

The effectiveness in which a temperature peaking forms inside an island depends on the electron heat diffusivity  $\chi_e$  inside the island. The detailed knowledge of the temperature profile and the electron heat flux  $q_e$  due to ECRH enables a power



balance analysis. Applied to the island geometry, the standard formula for a steady state power balance  $q_e = -n_e \chi_e \nabla T_e$  can be written as

$$\langle q_e \rangle_S = -n_e \chi_{\perp,e} \frac{dT_e}{d\Omega} \langle \nabla \Omega \rangle_S \quad \text{Eq. 9-1}$$

where  $\langle \cdot \rangle_S$  denotes a flux surface average. The island flux surface label  $\Omega = 8(r - r_s)^2 w^{-2} - \cos(m\xi)$  (using the helical angle  $\xi = \theta - (n/m)\phi$ ) can be seen as a radial coordinate inside the island: in the O-point,  $\Omega = -1$ , on the separatrix,  $\Omega = 1$ .  $T_e$  and  $\chi_e$  are assumed to be flux functions. For simplicity,  $n_e$  is taken constant over the island. Inside the island, ECRH is the only significant heating source, and is assumed to be ideally aligned on  $r_s$  (for modulated power also centred on the O-point).

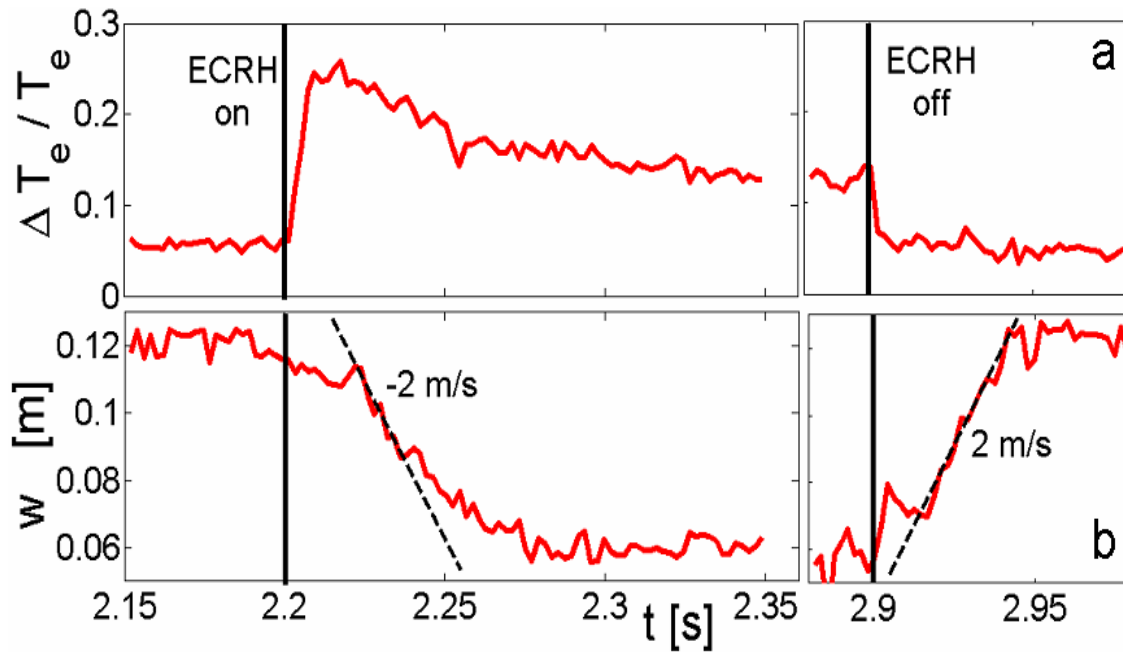


**Figure 9-3:** Typical time evolution of a) relative  $T_e$  peaking and b) island width.

The numerical evaluation of Eq. 9-1 has been performed in the fully suppressed island stage of the discharges. Figure 9-4 shows the results of the power balance analysis for three discharges with different CW ECRH input power (400, 300 and 200 kW). The temperature profiles for these three powers are shown in Figure 9-4a. The profiles of the electron thermal diffusivity (Figure 9-4b) show that over the largest part of the island,  $\chi_e$  is about 1 to 1.5  $\text{m}^2/\text{s}$ . Near the O-point, the uncertainty in the exact positioning of ECRH leads to deviations. Near the separatrix,  $\chi_e$  rises due to the fact that close to the separatrix the electron temperature can no longer be considered a flux function [Fitzpatrick 1995]. A power balance analysis of the entire plasma reveals that the transport in the ambient plasma is comparable to the transport inside the island. For the ambient plasma,  $\chi_e$  is typically 1  $\text{m}^2/\text{s}$  inside the deposition radius of ECRH and somewhat higher outside the deposition radius.

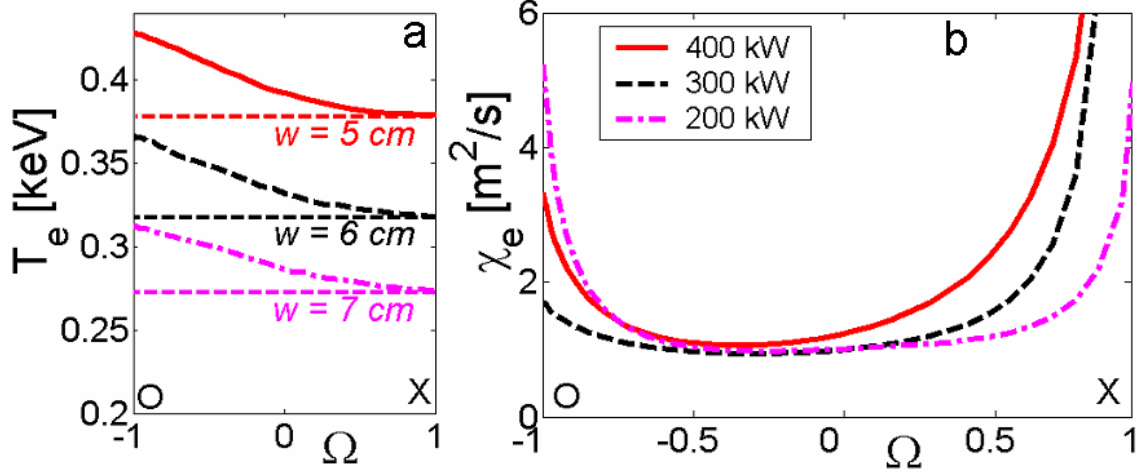


**Figure 9-4:** Power balance inside the island for three CW input powers. *a)* Temperature profiles inside the fully suppressed islands. Note the large effect the ECRH power has on the equilibrium (separatrix) temperature. *b)* Heat diffusion coefficients inside the islands.

Discharges with modulated ECRH show results very similar to the CW results. Similar relative temperature peakings and similar transport levels are observed. The only significant difference is that for modulated ECRH the equilibrium temperature (so the temperature of the island separatrix) rises less due to the lower total power input into the plasma. Consequently, modulation has advantages, since it doesn't spill power outside the island and disturbs the plasma less. Suppression works as long as there is power deposited inside the island.

The evolution of a tearing mode depends on the (helical) currents that flow inside the island region. The time evolution of the island width is governed by Eq. 9-2, relating the stability parameter  $\Delta'$  (the step in the poloidal flux function  $\psi$  over the island region) to the total helical current inside the island region [Wilson 2004].

$$\Delta' \tilde{\psi} = 2\mu_0 R \int_{r_s-w/2}^{r_s+w/2} dy \oint j_{||} \cos(m\xi) r_s d\xi \quad \text{Eq. 9-2}$$

If only the inductive current due to the growth of the island  $dw/dt$  is taken into account, Eq. 9-2 results in the classical Rutherford equation (Eq. 9-3, skipping the last two terms) [Rutherford 1973] where  $w$  is the full island width and  $\tau_r = \mu_0 r_s^2 / \eta$  is the current diffusion time. The inclusion of other contributions to the parallel current results in modifications to the classical Rutherford equation.

For these experiments, two modifications are important. First, a destabilizing contribution  $M_{DED}$  due to the shielding currents caused by the resonant external DED currents (Eq. 9-4, valid for strongly locked islands) ([Fitzpatrick 1993], [Fitzpatrick 1998], [Morris 1992a]). The DED sets up a perturbed magnetic field resonant with the island, causing currents to flow inside the island region that try to compensate this external field. Second, a stabilizing contribution  $M_{ECRH}$  due to the perturbed Ohmic current caused by temperature perturbations inside the island (Eq. 9-5) [Hegna 1997].

$$0.82 \cdot \tau_r \frac{dw}{dt} = r_s^2 \Delta'(w) + M_{DED} - M_{ECRH} \quad \text{Eq. 9-3}$$

$$M_{DED} = 2mr_s \left( \frac{w_{vac}}{w} \right)^2 \quad \text{Eq. 9-4}$$

$$M_{ECRH} = \frac{32q\mu_0 r_s^2}{B_\theta \left| \frac{dq}{dr} \right| w^2} \cdot \frac{j_{sep}}{T_{e,sep}^{3/2}} \int_{r_s-w/2}^{r_s+w/2} dy \int r_s d\xi T_e^{3/2} \cos(m\xi) \quad \text{Eq. 9-5}$$

In principle,  $\Delta'$  is unknown for the present experiments. Before the DED is switched on, there is no 2/1 island present (so the natural island is stable), but after switch off of the DED the island remains. Apparently the current profiles before and after the DED phase are not exactly the same, with  $\Delta'$  negative before the DED and positive after.

The DED term (Eq. 9-4) is fully known. The vacuum island width  $w_{vac} = 4$  cm, as can be seen from Figure 9-1a. In the DED phase of the discharges, before ECRH is switched on, the saturated (plasma) island width  $w_1$  is about 12 cm. Saturation is reached if all terms in Eq. 9-3 are in balance, thereby implying  $\Delta'(w_1) \approx -2$ .

The ECRH term  $M_{ECRH}$  can be evaluated numerically. The  $q$  profile and current density on the separatrix  $j_{sep}$  are estimated from the temperature profile. Figure 9-5a gives  $M_{ECRH}$  as a function of time, showing it is approximately constant at 1.2 m.

Directly after switch on (or switch off) of ECRH, coming from a steady state situation, the heating term  $M_{ECRH}$  is the only one contributing to  $dw/dt$ . Then, Eq. 9-3 predicts an initial suppression (or growth) rate of about 2 m/s, consistent with the experimentally observed values (see Figure 9-3).

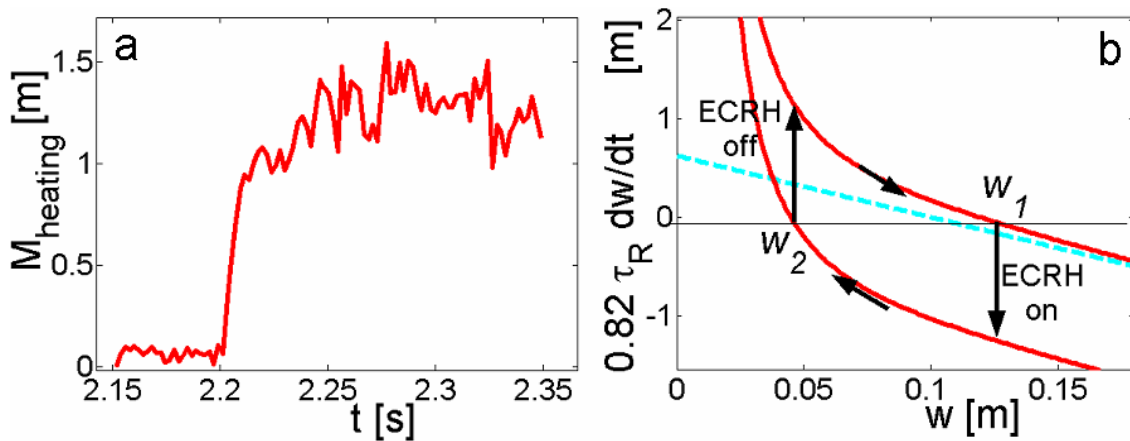


**Figure 9-5:** The suppression process: a) The heating term b) Overview of the various terms in the modified Rutherford equation.

The relaxation to the new saturated island width  $w_2$  (about 6 cm) is determined by the balance of  $M_{ECRH}$  with all other terms. Figure 9-5b gives an overview of the suppression process. Plotted is the right hand side of the modified Rutherford equation

(equals  $0.82 \tau_r dw/dt$ ) against  $w$ . The upper curve is composed of the  $\Delta'$  and DED terms. The lower curve includes the heating term (and is hence 1.2 m lower). To reproduce the observed saturated island widths, a  $\Delta'$  term of the form of the dashed line had to be introduced.

It should be noted that the stabilizing heating term in the Rutherford equation is the same for Neoclassical Tearing Modes (NTMs) which are driven unstable by the perturbed bootstrap current instead of the DED ([Fitzpatrick 1995], [Wilson 2004], [Hegna 1997]). In the presence of an island, the pressure gradient is removed, which results in a 'hole' in the bootstrap current distribution, which gives a destabilizing contribution to the Rutherford equation. In the ITER reference scenario, bootstrap current fractions of about 30% are expected [Sips 2005]. Therefore, to compensate this lost bootstrap current by the extra current due to a peaked temperature inside the NTM, a temperature peaking of about 20% is needed. In Eq. 9-6 the general scaling for the temperature peaking is given, assuming narrow islands and a power deposition width smaller than the island width.

$$q_e = -n\chi_e \nabla T_e \propto \frac{P_{ECRH}}{r_s R} \quad \frac{\Delta T_e}{T_e} \propto \frac{w \nabla T_e}{T_e} \propto \frac{w P_{ECRH}}{r_s R n \chi_e T_e} \quad \text{Eq. 9-6}$$

To get a 20% temperature peaking in ITER, Eq. 9-6 requires  $\chi_e < 0.2 \text{ m}^2/\text{s}$  inside the ITER islands, assuming 20 MW of ECRH power. Even if inside the ITER islands  $\chi_e \sim 0.5 \text{ m}^2/\text{s}$ , which is equal to the expected equilibrium  $\chi_e$  at the  $q = 3/2$  surface in ITER, the heating effect is still significant, and relaxes the gyrotron power requirements based only on current drive (ECCD).

This work, supported by the European Communities under the contract of Association between EURATOM/FOM, was carried out within the framework of the European Fusion Program together with the US Department of Energy. The views and opinions expressed herein do not necessarily reflect those of the European Commission.

## 10 Conclusions and Outlook

Making use of the ideal combination of tools available on TEXTOR, in particular ECE-Imaging, the DED and the 140 GHz gyrotron, experiments were conducted on three transport related topics, being magnetic islands, magnetic field perturbations at the plasma edge and high frequency temperature fluctuations.

To explore the capabilities of the ECE-Imaging diagnostic, experiments on the effects of a perturbation field on the edge temperature profile, and on high frequency (temperature) fluctuations were presented. The added value of having a 2D diagnostic was demonstrated in both these experiments. The edge temperature profile during DED 12/4 operation showed a pronounced 2D structure, and the measured fluctuations showed distinctly different behaviour in radial and poloidal directions. The capabilities of ECE-Imaging as a 2D fluctuation diagnostic were confirmed, encouraging a more in depth investigation of these topics in the future.

The main results presented in this thesis are the quantitative experimental verifications of two aspects of the dynamics of magnetic islands: The effects of a perturbation field and local heating. The known perturbation field of the DED and the accurate local power deposition of ECRH enabled an experimental verification of the heating and perturbation field terms in the modified Rutherford equation, governing island evolution.

### 10.1 2D structures and fluctuations

In chapter 5, 2D ECE-Imaging measurements of the edge electron temperature during DED 12/4 operation were presented. The effects on the temperature profile and transport were investigated.

During DED, the edge temperature profile developed a pronounced 2D structure. A poloidal asymmetry was observed close to the edge (relatively hot bulges in an otherwise cold region), but not further into the plasma. The relatively high temperature structures (bulges) at the edge could be linked to regions of long connection length (where two ‘fingers’ cross) in the theoretical calculations of the vacuum field topology (Atlas code). Also, the poloidally asymmetric part of the plasma could be identified as the laminar zone. Theory and experiment agree on (the evolution of) the position of these structures, giving confidence in the validity of the Atlas code, at least in the laminar region.

An overall drop in temperature is observed, which is a clear sign of enhanced transport. A transport enhancement of about a factor of two (poloidally averaged) in

the poloidally asymmetric region was observed. No notable change in transport in the poloidally symmetric part of the plasma and the hot bulges was found.

So, the DED has a large influence on the  $T_e$  profile and heat transport at the plasma edge. Moreover, a strong dependence of the observed 2D structure on the value of  $q$  at the edge is observed, making the edge structure controllable. These observations confirm that the DED is a flexible tool to control and investigate the plasma-wall interaction.

The experimental results on the DED edge structures show that ECE-Imaging is capable of direct 2D observation of structures in the temperature profile. To reduce the noise without sacrificing spatial or time resolution, effective use has been made of a filtering based on singular value decomposition. For high frequency, low amplitude fluctuations, a direct observation is not possible due to the thermal noise. However, by using correlation techniques, the time averaged properties of such fluctuation can be determined. ECE-Imaging enables correlations in both radial and poloidal directions, making it possible to reveal the 2D structure (propagation speed, wavelength and correlation length) of fluctuations.

In chapter 6, measurements of two types of high frequency fluctuations in TEXTOR were presented: the quasi-coherent (QC) mode and the Alfvén-like mode. The measurements of the QC mode demonstrated that ECE-Imaging is (at least) sensitive to fluctuations with  $f \leq 100\text{kHz}$ ,  $\lambda \geq 0.07\text{m}$  ( $k \leq 1\text{cm}^{-1}$ ), and relative amplitude larger than 0.2%. The following properties of the fluctuations could be derived:

- The amplitude of the QC mode was observed to depend on radius: about 3% at the edge to below 0.2% in the plasma centre.
- Temperature and density fluctuations were estimated to be comparable in amplitude for the QC mode.
- The radial and poloidal behaviour of the QC mode was distinctly different.
  - Poloidally, the QC mode was seen to propagate with a velocity of about 6 km/s. The poloidal wavelength was about 7cm, and the poloidal mode number  $m$  about 40.
  - Radially, the QC mode is not observed to propagate. The radial correlation length was about 2cm.
- The lifetime of the QC structures was about  $1 \cdot 10^{-5}\text{s}$ .
- The two frequency branches of the Alfvén-like mode originate from different minor radii, and are probably related to the  $q=2$  and 3 surfaces.

The question whether the QC mode can be identified as the ITG mode, as suggested in [Krämer-Flecken 2003], remains open. The measurements resemble measurements reported in literature from other fusion devices. The poloidal extent of the QC mode (wavelength of 7cm) is larger than the radial extent (correlation length of about 2cm). So, if the QC mode is the ITG mode, the radially extended finger-like structures typical for the ITG mode are not observed. This could, however, be caused by velocity shearing, decreasing the radial extent of the turbulent cells.

The experiments in chapters 5 and 6 lay the foundation of a more elaborate experimental investigation of the two topics in the future. Particularly interesting is the question whether the quasi-coherent mode can be identified as the ion temperature gradient (ITG) mode.

## 10.2 Magnetic islands

In general, any helical current in the island region, results in a modification to the Rutherford equation governing the evolution of the island width. The main goal of chapters 8 and 9 was an experimental check of two modifications to the Rutherford equation: the perturbation field term and the heating term, representing the effects of two currents of totally different origin; the shielding current and the perturbed Ohmic current respectively.

Apart from influencing the evolution of the island width, the shielding current also results in a torque on the island, balancing against all other (mainly viscous) torques on the island. Theoretically, the interplay between this torque balance and the (perturbation field term in the) modified Rutherford equation determines the dynamics of tearing modes in the presence of an external perturbation field. The experimental results presented in chapter 8, investigated the processes of mode penetration and mode unlocking. The experimental observations lead to the following answers to the questions posed in chapter 1:

- The mode penetration and unlocking are observed. The sudden growth of an island during penetration, and the sudden change in rotation frequency of the island during unlocking, are clear signs of the theoretically expected bifurcations.
- The threshold perturbation field amplitudes (for penetration and unlocking) were close to the theoretically predicted values, the threshold for unlocking being much smaller than the one for penetration.
- The expected phase difference between plasma and vacuum islands was observed and changed as predicted. Before unlocking, with decreasing perturbation field amplitude, the phase difference increased. The unlocking occurred when the phase difference exceeded 90 degrees.

So the overall conclusion is that theory and experiment agreed, not only qualitatively but also to a large extent quantitatively. As in theory both the island evolution and the torque are consequences of a shielding current, these experiments indirectly confirm the existence of such a current.

In chapter 9, the experiments on tearing mode suppression by local heating were presented. The modified Rutherford equation predicts that a peaked temperature profile inside the island works stabilising. The formation of this temperature peaking is determined by both the amount and distribution of the power being deposited inside the island, and the heat transport inside the island. The main results in this chapter were:

- Large relative temperature peakings inside the island of 25% could be reached. Inside the island, a typical  $\chi_e$  of 1.5 m<sup>2</sup>/s was found, comparable to the ambient plasma. Both modulated and CW ECRH gave comparable temperature peakings, however, modulated ECRH disturbed the plasma equilibrium less and spills less power outside the island separatrix.
- A significant suppression of the DED induced islands, typically to half their initial width, is observed, The measured suppression rates were consistent with theory.
- Scaling up the results for TEXTOR to ITER, it was concluded that in ITER the effect of heating is as large as the effect of current drive if  $\chi_e < 0.2$  m<sup>2</sup>/s inside the ITER islands. Even if  $\chi_e \sim 0.5$  m<sup>2</sup>/s, equal to expected equilibrium  $\chi_e$  at the  $q = 3/2$  surface in ITER, the heating effect is still significant.

Again, theory and experiment agree. Two totally different sources of helical current in the island region (shielding and perturbed Ohmic currents) resulted in the expected influence on island evolution. This does not only give confidence in the two modification terms tested directly, but also in the general Rutherford theory. If one knows the helical current inside the island region, Rutherford theory gives the effect on island evolution.

So the theory can be confidently applied to future fusion devices like ITER, where both Rutherford theory and shielding current torques play a large role in processes like:

- Tearing mode penetration due to the stationary error field.
- Locking of existing modes to the stationary error field, possibly leading to a disruption.
- Suppression of existing (neoclassical) tearing modes by ECRH and/or ECCD.

When driving current with ECCD, one automatically also heats the island. This effect is not negligible. Using conservative assumptions (equal heat diffusion coefficients inside and outside the island, for a 10cm island), still a 20% contribution is expected. This will result in a faster suppression, with less power consumption. Even though suppression by heating is less effective for small islands, heating alone could (help) keep NTMs at an acceptably small width.

### 10.3 Outlook

The work presented in chapters 8 and 9 showed that the influences of a peaked temperature and perturbation fields on magnetic island are well understood. This gives confidence in using the theory of these two effects in future fusion devices like ITER. As ITER has both gyrotrons, and (as every tokamak) an error field, both effects play a role.

The results presented in chapters 5 and 6, show that the 2D capability of ECE-Imaging can contribute to these fields of research. A further exploration of these topics is desirable. In particular, a more elaborate data set on the quasi coherent mode under various plasma conditions is of interest, as this mode might be the ion temperature gradient (ITG) mode, which is one of the turbulent modes thought responsible for the anomalously high transport in tokamaks.

Although ECE-Imaging already proved to be a good tool for 2D temperature measurements, progress is being made in further improving this diagnostic. The ECE-Imaging system has recently been upgraded [Domier 2006], increasing its radial coverage by about 50%. The limited radial coverage of about 7cm in the old setup was sometimes a disadvantage in the study of larger MHD instabilities like magnetic islands or the sawtooth crash, as most of the time ECE-Imaging only offered a partial view of the instability. The new system will hence facilitate the investigation of larger plasma structures. In particular one can think of:

- Magnetic islands: More accurate determination of the island width and temperature profile will be possible.
- Sawtooth crash: The behaviour at both sides of the sawtooth inversion radius ( $q=1$ ) can be visualised simultaneously.



- Edge Localised Modes (ELMs): In the limiter H-mode scenario on TEXTOR, the 2D capacity of ECE-Imaging could contribute to the understanding of the ELMs, responsible for the periodic collapse of the edge barrier.

So in summary, the work presented in this thesis showed that the influences of local heating and perturbation fields on magnetic island are well understood. The theory can be applied to future devices with confidence. Also, the ECE-Imaging diagnostic proved to be a valuable tool for 2D temperature (fluctuation) measurements that can contribute to a wide variety of physics experiments.



# Summary

In search for an alternative to fossil fuel, nuclear fusion is an environmentally friendly and inexhaustible option. By merging two light nuclei (Hydrogen isotopes) to a heavier (Helium) nucleus, energy is released. In order for this reaction to occur, however, the reacting particles have to be brought very close together to overcome the Coulomb repulsion. At very high temperatures, the particles' kinetic energy is sufficient to overcome this barrier. At the required temperature (in the order of 100 million K) the reacting 'gases' form a plasma. For an efficient reaction, it is necessary to confine this hot plasma. In the sun, confinement is provided by gravity. On earth, the most promising scheme to achieve nuclear fusion is the tokamak, which confines the plasma in a magnetic field.

In this thesis, the ideal combination of available tools on TEXTOR is used to study three phenomena influencing the quality of confinement in a tokamak, being magnetic islands, magnetic field perturbations at the plasma edge and high frequency temperature fluctuations. The main topic is the investigation of magnetic islands. The presence of this plasma instability deteriorates the confinement and can even lead to a total loss of the plasma (disruption). Larger tokamaks, like the future ITER tokamak, are more susceptible to a particularly dangerous type of island: the neoclassical tearing mode (NTM). For future large tokamaks to be successful, these islands have to be avoided. So the understanding and control of these instabilities is of vital importance. TEXTOR is an ideal tokamak for the study of magnetic islands, due to the unique combination of available tools: a high resolution 2D electron temperature diagnostic (ECE-Imaging), the Dynamic Ergodic Divertor (DED) to create islands in a very controllable way, and a gyrotron to inject radio frequency waves into the plasma for highly localized heating or current drive. The ECE-Imaging diagnostic enables to directly image the 2D electron temperature profile with a high spatial (1cm) and temporal (1 $\mu$ s) resolution. With ECE-Imaging one can directly explore the two-dimensional nature of plasma structures (like islands) in a single measurement.

Two aspects of the dynamics of magnetic islands are investigated: the effects of a perturbation field and suppression of magnetic islands by local heating. The known perturbation field of the DED and the accurate local power deposition by the gyrotron (Electron Cyclotron Resonance Heating, ECRH) enable an experimental verification of the heating and perturbation field terms in the modified Rutherford equation, governing island evolution.

The effect of the perturbation field of the DED is to generate a current in the plasma at the resonant magnetic flux surface. This shielding current tries to expel the perturbed field from the plasma and has two important effects: it influences the stability of magnetic islands and influences the plasma rotation by introducing a torque. When the perturbed DED field is strong enough, this results in the generation of an island at the

## Summary

---

resonant surface (so called mode penetration), whose frequency is equal to that of the external perturbation field (the island is 'locked'). So with the DED we can produce islands in a very controlled way. The interaction of islands with perturbation fields is a very important issue in all tokamaks, because it affects the island stability and rotation, possibly leading to a disruption. Perturbation fields (or error fields) are present in all tokamaks although their strength and mode spectrum are normally unknown. The known amplitude and phase of the DED perturbation field, along with the detailed knowledge of the island evolution from ECE-Imaging (island width, phase and frequency), enables a thorough investigation of the interaction between islands and perturbation fields. The experimental results presented in this thesis show that the processes of mode penetration and mode unlocking are well described by theory, both qualitatively and quantitatively.

The suppression of an already existing island can be achieved by locally injecting power into the island by the resonant absorption of radio frequency waves. The effect of these waves is to either (non-inductively) drive current, or to heat the island (ECRH). ECE-Imaging measurements of the island during their suppression by ECRH reveal a peaking of the temperature profile inside the island. The reduced resistivity due to this higher temperature leads to extra current inside the island, giving a suppression of the island. These measurements allow the determination of the transport properties inside the island, and a direct comparison of the observed suppression rates with the theory of island evolution. The results show that the DED induced islands have been suppressed to about half their original size, with a suppression rate consistent with the theoretical prediction by the modified Rutherford equation. The efficiency of island suppression by heating hinges on the heat confinement inside the island. A heat conductivity inside the island comparable to that of the surrounding plasma was found in these experiments. An extrapolation of the TEXTOR results to ITER shows that the often neglected effect of island suppression by heating is important for the suppression of NTMs in ITER.

Using the same tools, experiments on two other transport related topics were performed: magnetic field perturbations at the plasma edge and high frequency temperature fluctuations. The added value of having ECE-Imaging as a 2D diagnostic was demonstrated in both experiments.

The edge temperature profile during DED operation shows a pronounced 2D structure, with regions (the so called laminar zone) of enhanced heat transport. This observed 2D temperature structure could be successfully linked with the theoretical topology of the vacuum magnetic field. The 2D structure at the edge could be controlled by changing the plasma current profile. So the edge transport properties can be changed in a controllable way by the DED, making it a good tool to influence the plasma surface interaction.

The measured high frequency fluctuations showed distinctly different behaviour in radial and poloidal directions. The most pronounced high frequency fluctuation observed by ECE-Imaging is the 'quasi coherent' mode, a mode previously observed as a density fluctuation (reflectometer data). It was suggested that this mode is related to drift wave turbulence (ITG), which is generally thought responsible for the 'anomalously' high transport levels in tokamaks. With ECE-Imaging, both the radial and poloidal characteristics of this mode could be derived using correlation

techniques. Also, the data showed that the temperature and density fluctuations caused by this mode are comparable in amplitude. Due to its low amplitude and wavelength and its high frequency, the quasi coherent mode provided a test for ECE-Imaging, confirming its capabilities as a 2D fluctuation diagnostic.

So, the work presented in this thesis shows that the influences of local heating and perturbation fields on magnetic island are well understood. The theory can be applied to future devices with confidence. Also, the ECE-Imaging diagnostic proved to be a valuable tool for 2D temperature (fluctuation) measurements that can contribute to a wide variety of physics experiments.



# Samenvatting

In de zoektocht naar een alternatief voor fossiele brandstof is kernfusie een milieuvriendelijke en onuitputtelijke optie. Door twee lichte atoomkernen (waterstof isotopen) te versmelten tot een zwaardere (helium-) atoomkern komt energie vrij. Om deze reactie te laten verlopen moeten de reagerende deeltjes echter zeer dicht bij elkaar gebracht worden om de Coulomb-afstoting te overwinnen. Bij heel hoge temperatuur is de kinetische energie van de deeltjes voldoende om deze barriere te overwinnen. Bij deze hoge temperatuur, in de orde van 100 miljoen K, vormen de reagerende 'gassen' een plasma. Voor een efficiënte reactie is het nodig dit plasma op te sluiten. In de zon zorgt de zwaartekracht voor opsluiting; op aarde is de tokamak de meest veelbelovende methode om kernfusie mogelijk te maken. In een tokamak wordt het plasma door middel van een magneetveld opgesloten.

In dit proefschrift wordt de unieke combinatie van beschikbare instrumenten op TEXTOR benut om drie fenomenen te bestuderen die de kwaliteit van de plasma-opsluiting beïnvloeden. De drie fenomenen zijn magnetische eilanden, verstoringen van het magnetische veld aan de rand van het plasma en hoogfrequente temperatuursfluctuaties. Het hoofdonderwerp is de bestudering van magnetische eilanden. In de aanwezigheid van deze plasma-instabiliteit is de opsluiting verminderd en kan het plasma zelfs volledig verloren gaan in een zogenaamde disruptie. Grotere tokamaks, zoals de toekomstige ITER tokamak, zijn gevoelig voor een bijzondere soort van magnetisch eiland, de 'neoclassical tearing mode' (NTM). Om toekomstige grote tokamaks succesvol te laten zijn moeten deze NTMs vermeden worden. Het begrip en de controle van deze instabiliteiten is daarom van groot belang. TEXTOR is een ideale tokamak om magnetische eilanden te onderzoeken door de unieke combinatie van beschikbare instrumenten: een hoge-resolutie-, 2D-, electronen-temperatuursdiagnostiek (ECE-Imaging), de 'Dynamic Ergodic Divertor' (DED) om eilanden op gecontroleerde wijze te maken door middel van magnetische stoorvelden, en een gyrotron om radiofrequente golven het plasma in te zenden om zeer lokaal te verhitten en stroom te drijven. De ECE-Imaging diagnostiek maakt een directe opname van het 2D-profiel van de electronentemperatuur mogelijk, met een hoge plaats- (1cm) en tijdsresolutie (1 $\mu$ s). Met ECE-Imaging kan men het tweedimensionale karakter van plasmastructuren rechtstreeks onderzoeken in een enkele meting.

Twee aspecten van de dynamica van magnetische eilanden zijn onderzocht: de effecten van een magnetisch stoorveld en de onderdrukking door lokale verhitting. Het bekende stoorveld van de DED en de nauwkeurig gelocaliseerde depositie van vermogen door het gyrotron (electron cyclotron resonante verhitting, ECRH) maken een experimentele verificatie mogelijk van de verhittings- en stoorveld-termen in de vergelijking die eiland-evolutie beschrijft (de gemodificeerde Rutherford vergelijking).

## Samenvatting

---

Het effect van het stoorveld van de DED is het opwekken van een stroom in het plasma op de positie van het resonante magnetische-fluxoppervlak. Deze stroom probeert het plasma af te schermen voor het stoorveld en heeft twee belangrijke effecten: hij beïnvloedt de stabiliteit van magnetische eilanden en beïnvloedt de plasmarotatie doormiddel van een koppel. Als het DED-stoorveld sterk genoeg is resulteert dit in het ontstaan van een magnetisch eiland op het resonante fluxoppervlak (dit proces heet modepenetratie). De frequentie van dit eiland is gelijk aan de frequentie van het externe stoorveld. Met de DED kunnen we dus op zeer gecontroleerde wijze eilanden maken. Stoorvelden, en hun interactie met eilanden, zijn belangrijk voor alle tokamaks omdat deze de eiland stabiliteit en de plasmarotatie beïnvloeden en mogelijk zelfs een disruptie tot gevolg hebben. Stoorvelden komen voor in alle tokamaks, hoewel hun sterkte en spectrum normaal gesproken onbekend zijn. De bekende fase en sterkte van het DED-stoorveld, samen met de gedetailleerde kennis van de eiland-evolutie door ECE-Imaging (eiland breedte, fase en frequentie), maken een diepgaand onderzoek naar de interactie tussen stoorvelden en eilanden mogelijk. De in dit proefschrift gepresenteerde experimentele resultaten laten zien dat deze interactie (met name de modepenetratie bij toenemende stoorveldsterkte en de ont koppeling bij afnemende stoorveldsterkte) goed door de theorie beschreven wordt, zowel kwalitatief als kwantitatief.

De onderdrukking van een reeds bestaand magnetisch eiland kan bereikt worden door lokaal vermogen in het eiland te deponeren, door middel van de resonante absorptie van radiofrequente golven. Als gevolg van deze golven wordt het eiland verhit (ECRH) en eventueel wordt er een (niet-inductieve) stroom gedreven. De ECE-Imaging metingen van eilanden tijdens hun onderdrukking door middel van ECRH (dus enkel verhitting) laten een gepiekt temperatuurprofiel in het eiland zien. Door de verhoogde temperatuur is de elektrische weerstand in het eiland verminderd. Dit heeft een extra stroom in het eiland tot gevolg die voor de onderdrukking van het eiland verantwoordelijk is. De ECE-Imaging metingen maken de bepaling van de transport eigenschappen binnen het eiland mogelijk, alsmede een direct vergelijk tussen de waargenomen en theoretisch voorspelde snelheid waarmee het eiland kleiner wordt. De resultaten tonen dat de door de DED gemaakte eilanden tot ongeveer de helft van hun oorspronkelijke breedte onderdrukt zijn. De snelheid waarmee de eilanden kleiner worden komt overeen met de voorspellingen van de Rutherford vergelijking. De efficiëntie waarmee eilanden onderdrukt worden hangt grotendeels af van het vermogen van de eilanden om warmte vast te houden. De in deze experimenten gevonden warmtegeleiding in het eiland was vergelijkbaar met die buiten het eiland. Een extrapolatie van de TEXTOR-resultaten naar ITER laat zien dat het vaak verwaarloosde effect van eiland-onderdrukking door verhitting belangrijk is voor de onderdrukking van NTMs in ITER.

Gebruik makend van dezelfde instrumenten zijn er experimenten aan twee andere transportgerelateerde onderwerpen uitgevoerd: verstoringen van het magnetische veld aan de rand van het plasma en hoogfrequente temperatuursfluctuaties. De toegevoegde waarde van ECE-Imaging als een 2D-diagnostiek wordt door beide experimenten gedemonstreerd.

Het temperatuurprofiel aan de rand van het plasma gedurende DED-operatie toont een prominente 2D-structuur met gebieden waar het warmtetransport toegenomen is. Het verband tussen de waargenomen 2D-structuren en de theoretische topologie van



het vacuüm-magneetveld kan succesvol gelegd worden. Het 2D-temperatuursprofiel aan de rand kan aangepast worden door het profiel van de plasmastroom te veranderen. De transporteigenschappen kunnen zo dus gecontroleerd worden, wat de DED een goed instrument voor de beïnvloeding van de plasma-wand-interactie maakt.

De gemeten hoogfrequente fluctuaties vertonen een duidelijk afwijkend gedrag in de radiale en poloidale richtingen. De meest in het oog springende hoogfrequente temperatuursfluctuatie die door ECE-Imaging is waargenomen is de ‘quasi-coherente’ mode. Deze fluctuatie is reeds eerder waargenomen (met de reflectometer) als een fluctuatie in de dichtheid. Het is gesuggereerd dat deze fluctuatie gerelateerd is aan de turbulentie die algemeen verantwoordelijk wordt geacht voor het experimenteel waargenomen ‘anomaal’ hoge transportniveau in tokamaks. Met ECE-Imaging konden zowel de radiale als de poloidale eigenschappen van deze fluctuatie bepaald worden, gebruik makend van correlatietechnieken. De data toont aan dat de door deze instabiliteit veroorzaakte temperatuursfluctuaties in amplitude vergelijkbaar zijn met de dichtheidsfluctuaties. Door zijn kleine amplitude en golflengte en zijn hoge frequentie vormt de ‘quasi-coherente’ mode een test voor ECE-Imaging die bevestigt dat ECE-Imaging in staat is hoogfrequente fluctuaties twee-dimensionaal te meten.

Het in dit proefschrift gepresenteerde werk toont dus aan dat de invloeden van locale verhitting en stoorvelden op magnetische eilanden goed begrepen zijn. De theorie kan met vertrouwen toegepast worden op toekomstige machines als ITER. Voorts heeft ECE-Imaging bewezen een waardevolle diagnostiek voor 2D-metingen van de temperatuur (en temperatuursfluctuaties) te zijn, die kan bijdragen aan een veelvoud van fysische experimenten.



## Curriculum Vitae

I was born on October 12, 1978 in Herkenbosch in the Netherlands. I went to high school in Roermond, the ‘Stedelijke Scholengemeenschap’, and obtained my ‘Atheneum’ diploma in 1997. After that, I studied applied physics at the Eindhoven University of Technology (TU/e) where I graduated ‘cum laude’ as a M.Sc. in August 2002. Two traineeships were part of this study; A three month traineeship at Philips Research (NatLab) in Eindhoven, and a nine month traineeship at the Forschungszentrum Jülich (under contract with FOM Rijnhuizen) concerning the analysis of Thomson Scattering data on the TEXTOR tokamak.

In September 2002 I started working as a Ph.D. student at FOM Rijnhuizen. This work, presented in this thesis, was also carried out at the Forschungszentrum Jülich. After spending about one year on completing my work on Thomson Scattering, started during the traineeship, I concentrated on the ECE-Imaging diagnostic and its applications.



## Acknowledgements

Writing a thesis is only possible if you are surrounded by an inspiring team of people. As a FOM Rijnhuizen Ph.D. student located in Jülich, I was part of a team that did not only make writing this thesis possible, but that also made this a very pleasurable experience.

First, I thank the ‘wise men’ that guided me through the process of writing this thesis. The wealth of plasma physics knowledge of my promotors Niek Lopes Cardozo and Chris Schüller were of great help. Niek spent a lot of time proofreading this thesis, despite the fact that he was on ‘sabbatical’. His many suggestions and corrections gave structure to this thesis. My daily supervisors Tony Donné (during the first few years) and Roger Jaspers (supervisor during the last few years and co-promotor), were indispensable with their enthusiastic support.

The many discussions with Maarten de Bock on the effects of the DED were crucial for the understanding of this subject. Also, the expertise on magnetic islands of Egbert Westerhof was of great help.

Of course, running a tokamak is a group effort. So I thank the entire TEXTOR team and the high temperature plasma physics division of the Rijnhuizen team for their obvious, and less obvious, contributions to this work. I am thankful to the Thomson Scattering team (Rolie Barth, Hennie van der Meiden, Theo Oyevaar) in which I spent the first year of my Ph.D. period, and the ECE-Imaging team in which I conducted the work that is put down in this thesis. In the latter team, I am especially grateful to Marc van de Pol, Calvin Domier, Heyon Park and Tobin Munsat for keeping the system up and running.

I would not have enjoyed my period in Jülich without all the people responsible for the great, friendly atmosphere. The constantly changing group of colleagues at the coffee table is too large for everyone to be mentioned; I thank all of them. Outside the institute, the many Tuesday night beers with Maarten de Bock, Serge Brons, Cor Tito, John Scholten and Geert Willem Spakman at the ‘Liebevoll’ provided the necessary distraction. Finally, I would like to apologize myself for all those times I kept Maarten, Ben, Cor and Jurrian from working, whenever I was fed up with sitting behind my computer screen.

Most importantly, I thank my parents, who sadly both died during my period in Jülich, for always having loved and supported me. I wish they could have witnessed the completion of this work. Finally, thanks to my family and friends in the Netherlands, in particular Angelien and Wim who always welcomed me in the weekends and helped me when I needed it.



## Bibliography

- [Abdullaev 2003] S.S. Abdullaev *et al.*, *Nucl. Fusion* **43**, 299 (2003)
- [Bekefi 1966] G. Bekefi, “Radiation processes in Plasmas”, New York, Wiley (1966).
- [Bornatici 1982] M. Bornatici, *Plasma Physics* **24**, 629 (1982)
- [Bornatici 1983] M. Bornatici *et al.*, *Nucl. Fusion* **23**, 1153 (1983)
- [Buratti 2005] P. Buratti *et al.*, In proceeding of the 32nd EPS Conference on Plasma Phys. Tarragona, 27 June - 1 July 2005 ECA Vol.**29C**, P-5.055 (2005)
- [Busch 2006] C. Busch, ‘*Spectroscopische Untersuchung der poloidalen Plasmarotation unter dem Einfluss statischer und dynamischer Ergodisierung am Tokamak TEXTOR*’, PhD thesis, Heinrich-Heine-Universität Düsseldorf (2006)
- [Chirikov 1979] B.V. Chirikov, *Phys. Rep.* **52**, 265 (1979)
- [Classen 2006] I.G.J. Classen *et al.*, in Proceedings of the 14<sup>th</sup> Joint Workshop on Electron Cyclotron Emission and Electron Cyclotron heating, 9-12 May 2006, Santorini, Greece, edited by A. Lazaros, page 134
- [Clark 1983] W.H.M. Clark, *Plasma Physics* **25**, 1501 (1983)
- [Cima 1995] G. Cima *et al.*, *Phys. Plasmas* **2**, 720 (1995)
- [de Bock 2007] M.F.M. de Bock, ‘*Understanding and controlling plasma rotation in tokamaks*’, Ph.D. thesis, Technische Universiteit Eindhoven, (2007)
- [de Vries 1997] P.C. de Vries, ‘*Magnetic islands in tokamak plasmas*’, Ph.D. thesis, Universiteit Utrecht, (1997)
- [Domier 2006] C.W. Domier *et al.*, *Rev. Sci. Instrum.* **77**, 10E924 (2006)
- [Donné 2005] A.J.H. Donné *et al.*, *Fusion Science and Technology* **47**, 220 (2005)

## Bibliography

---

- [Dudok 1994] T. Dudok de Wit *et al.*, ‘The biorthogonal decomposition as a tool for investigating fluctuations in plasmas’, *Phys. Plasmas* **1**, 3288 (1994)
- [Finken 1997] K.H. Finken, G.H. Wolf, *Fusion Engineering and Design* **37**, 337 (1997)
- [Finken 2005] K.H. Finken *et al.*, *Phys. Rev. Lett.* **94**, 015003 (2005)
- [Finken 2006] K.H. Finken *et al.*, *Contrib. Plasma Phys.* **46**, 515 (2006)
- [Fitzpatrick 1991] R. Fitzpatrick and T.C. Hender, *Phys. Fluids B* **3**, 644 (1991)
- [Fitzpatrick 1993] R. Fitzpatrick, *Nucl. Fusion* **33**, 1049 (1993)
- [Fitzpatrick 1995] R. Fitzpatrick, *Phys. Plasmas* **2**, 825 (1995)
- [Fitzpatrick 1998] R. Fitzpatrick, *Phys. Plasmas* **5**, 3325 (1998)
- [Friedberg 1987] J.P. Friedberg, ‘*Ideal magneto hydrodynamics*’, Plenum Press, New York (1987)
- [Garbet 2004] X. Garbet *et al.*, *Plasma Phys. Contr. Fusion* **46**, 1351 (2004)
- [Giesen 1997] B. Giesen *et al.*, *Fusion Engineering and design* **37**, 341 (1997)
- [Hartfuss 1997] H.J. Hartfuss *et al.*, *Plasma Phys. Control. Fusion* **39**, 1693 (1997)
- [Hazeltine 1997] R.D. Hazeltine *et al.*, *Phys. Plasmas* **4**, 2920 (1997)
- [Hegna 1994] C.C. Hegna and J.D. Callen, *Phys. Plasmas* **1**, 2308 (1994)
- [Hegna 1997] C.C. Hegna and J.D. Callen, *Phys. Plasmas* **4**, 2940 (1997)
- [Hegna 1998] C.C. Hegna, *Phys. Plasmas* **5**, 1767 (1998)
- [Horton 1999] W. Horton, *Review of Modern Physics* **71**, 735 (1999)
- [Hoshino 1992] K. Hoshino *et al.*, *Phys. Rev. Letters* **69**, 2208 (1992).
- [Hutchinson 1987] I.H. Hutchinson, ‘*Principles of plasma diagnostics*’, Cambridge University Press (1987)
- [IPCC 2007] Intergovernmental Panel on Climate Change, ‘*Climate Change 2007: The Physical Science Basis. Summary for Policymakers*’, (2007) available at [www.ipcc.ch](http://www.ipcc.ch)
- [IEA 2003] International Energy Agency, ‘*Energy statistics 2003*’, (2003) available at [www.iea.org](http://www.iea.org)



- [IEA 2006] International Energy Agency, 'Key world energy statistics 2006', (2006) available at [www.iea.org](http://www.iea.org)
- [Jakubowski 2004] M.W. Jakubowski *et al.*, *Nucl. Fusion* **44**, S1 (2004)
- [Jakubowski 2006] M.W. Jakubowski *et al.*, *Phys. Rev. Letters* **96**, 035004 (2006)
- [Kantor 2001] M.Yu. Kantor *et al.*, *Rev. Sci. Instrum.* **72**, 1159 (2001)
- [Kikuchi 2006] Y. Kikuchi *et al.*, *Contrib. Plasma Phys.* **46**, 539 (2006)
- [Kislov 1997] D.A. Kislov *et al.*, *Nuclear Fusion* **37**, 339 (1997).
- [Klüber 1991] O. Klüber *et al.*, *Nucl. Fusion* **31**, 907 (1991)
- [Kobayashi 2004] M. Kobayashi *et al.*, *Nucl. Fusion* **44** S64 (2004)
- [Koch 2005] R. Koch *et al.*, *Fusion Science and Technology* **47**, 97 (2005)
- [Koslowski 2006] H.R. Koslowski *et al.*, *Nucl. Fusion* **46**, L1 (2006)
- [Krämer-Flecken 2003] A. Krämer-Flecken, EPS2003, ECA Vol 27A, P-2.135
- [Krämer-Flecken 2004] A. Krämer-Flecken *et al.*, *Nucl. Fusion* **44**, 1143 (2004)
- [La Haye 2006] R.J. La Haye, *Phys. Plasmas* **13**, 055501 (2006)
- [Lazzaro 1988] E. Lazzaro and F.F. Nave, *Phys. Fluids* **31**, 1623 (1988)
- [Lehnen 2005] M. Lehnen *et al.*, *Plasma Phys. Control. Fusion* **47**, B237 (2005)
- [Liang 2004] Y. Liang *et al.*, In proceeding of the 31st EPS Conference on Plasma Phys. London, 28 June - 2 July 2004 ECA Vol.28G, P-1.126 (2004)
- [Llewellyn-Smith 2005] C. Llewellyn-Smith, speech during dinner-debate on 'Energy for the coming generations; the role of fusion in the future energy mix' at the European Parliament (2005), available on [www.fusie-energie.nl](http://www.fusie-energie.nl)
- [Mazzucato 2001] E. Mazzucato, *Nucl. Fusion* **41**, 203 (2001)
- [Milligen 1993] B.P. van Milligen *et al.*, *Nuclear Fusion* **33**, 1119 (1993)
- [Morris 1992a] A.W. Morris *Plasma Physics and Controlled Fusion* **34**, 1871 (1992)
- [Morris 1992b] A.W. Morris *et al.*, *Phys. Fluids B* **4**, 413 (1992)
- [Nardone 1992] C. Nardone, *Plasma Phys. Contr. Fusion* **34**, 1447 (1992)

## Bibliography

---

- [Neubauer 2005] O. Neubauer *et al.*, *Fusion Science and Technology* **47**, 76 (2005)
- [Park 2003] H. Park *et al.* *Rev. Sci. Instrum.* **74** 4239-62 (2003)
- [Park 2004] H. Park *et al.*, *Rev. Sci. Instrum.* **75**, 3787 (2004)
- [Rutherford 1973] P.H. Rutherford, *Phys. Fluids* **16**, 1903 (1973)
- [Sattler 1993] S. Sattler, PhD thesis Max-Planck-Institut für Plasmaphysic, IPP III/193, (1993)
- [Sattler 1994] S. Sattler and H.J. Hartfuss, *Phys. Rev. Letters* **72**, 653 (1994)
- [Savrukhin 2000] P.V. Savrukhin, *Plasma Physics Reports* **26**, 633 (2000)
- [Schmitz 2006] O. Schmitz, Ph.D. Thesis, Heinrich-Heine-Universität, (2006)
- [Sing 1993] D.C. Sing *et al.*, *Phys. Fluids B* **5**, 3239 (1993).
- [Sips 2005] A.C.C. Sips, *Plasma Phys. Controlled Fusion* **47**, A19 (2005).
- [Special Issue 1997] Special Issue, *Fusion Eng. Design* **37**, 335 (1997), edited by K.H. Finken
- [Stix 1973] T.H. Stix, *Phys. Fluids* **16**, 1260 (1973)
- [Udintsev 2003] V.S. Udintsev, 'Electron Temperature Dynamics of TEXTOR Plasmas', Ph.D. thesis, Universiteit Utrecht, (2003)
- [Vershkov 1999] V.A. Vershkov *et al.*, *Rev. Sci. Instr.* **70** 1700-9 (1999)
- [Vershkov 2001] V.A. Vershkov *et al.*, In proceeding of the 28th EPS Conference on Plasma Phys., Madeira, 18-22 June 2001 P-1.011 (2001)
- [Wang 2004] J. Wang *et al.*, *Rev. Sci. Instrum.* **75**, 3875 (2004)
- [Waelbroeck 2001] F.L. Waelbroeck *et al.*, *Phys. Rev. Lett.* **87**, 215003 (2001)
- [Wesson 1997] J. Wesson 'Tokamaks' Oxford University Press, 2<sup>nd</sup> edition (1997)
- [Westerhof 1987] E. Westerhof, *Nucl. Fusion* **27**, 1929 (1987)
- [Westerhof 1990] E. Westerhof, *Nucl. Fusion* **30**, 1143 (1990)
- [Westerhof 2003] E. Westerhof *et al.*, *Nucl. Fusion* **43**, 1371 (2003)
- [Westerhof 2006] E. Westerhof *et al.*, *Nucl. Fusion* **47**, 85 (2007).
- [Wilson 2004] H.R. Wilson, *Fusion Science and Technology* **45**, 123 (2004)

- [Zimmermann 2005] O. Zimmermann *et al.*, In proceeding of the 32nd EPS Conference on Plasma Phys. Tarragona, 27 June - 1 July 2005 ECA Vol.**29C**, P-4.059 (2005)
- [Zimmermann 2006] O. Zimmermann *et al.*, In proceeding of the 33rd EPS Conference on Plasma Phys. (2006)
- [Zohm 1997] H. Zohm, *Phys. Plasmas* **4**, 3433 (1997)
- [Zohm 2001] H. Zohm *et al.*, *Phys. Plasmas* **8**, 2009 (2001)